Electrochemistry of Platinum Nanoparticles

A thesis submitted for the degree of Doctor of Philosophy
in Physical and Theoretical Chemistry

Xue Jiao
St John's College

Trinity Term 2018

Electrochemistry of Platinum Nanoparticles

A thesis submitted for the degree of Doctor of Philosophy
in Physical and Theoretical Chemistry

Xue Jiao
St John's College

Trinity Term 2018

Abstract

This thesis reports experimental work with two main aims: the first is the investigation of single nanoparticles with an emphasis on their porosity, and the second is to develop a more comprehensive understanding of their electrocatalytic behavior. The fundamental principles and techniques of electrochemistry are introduced in Chapter 1. Chapters 2 and 3 respectively summarize nanomaterials and their characterization methods. In particular, the technique of single particle electrochemical impacts, so-called "nanoimpacts", is used to study redox reactions at individual nanoparticles.

Chapters 4 and 5 report the porosity of platinum nanoparticles (PtNPs) *via* tag-redox coulometry (TRC) and surface platinum oxidation, respectively. In the former, thiol-tagged PtNPs are employed and current transients upon impacts with a cathode are detected. This is due to the nitro group reduction on individual PtNPs. The charge per spike is measured and the number of tag molecules can be calculated. Therefore, the "electroactive surface area" of the PtNPs is revealed. In the latter, oxidative transients upon direct impacts are observed. The charge per current spike is measured and attributed to the formation of surface platinum oxides. XPS shows PtO and PtO_2 in different amounts and an average oxidation state is deduced as a function of potential. Thus the number of platinum atoms oxidized per PtNP can be estimated. Both experiments allow

insight into extent to which the internal surface of the aggregate is "seen" by the solution and is electrochemically active, providing a fuller knowledge of the catalytic behavior of nanoparticles, as reflected from the reaction kinetics and the redox currents. Furthermore, results from Chapters 4 and 5 are in close agreement with each other, indicating the accuracy of the measurements in both studies.

With this appreciation of the internal nanoscale structure, Chapter 6 investigates the kinetics of the hydrogen oxidation reaction (HOR) on mesoporous particles. The steady-state current for HOR is measured on both individual platinum particles and PtNPs drop-casted substrates. The kinetic parameters are determined and contrasted between these two approaches. Nanoimpacts are required in order to correctly understand the electrochemical reaction catalyzed by nanoparticles, as the aggregation or loss of ensemble drop-casted particles leads to errors.

Chapter 7 further elaborates the role of nanomorphology of nanoparticles in catalyzing the HOR using individual mesoporous particles and low density random arrays of particles. At the single particle scale the activity of the platinum catalyst towards the hydrogen oxidation is potential dependent and exhibits two peaks, as reflected in the electrochemical current. This is due to the sensitivity of the reaction rate to the interfacial structure of PtNPs. The decrease in activity correlates directly with the potential at which the underpotential deposited hydrogen (H_{upd}) is removed from the catalytic interface. The contribution of the internal mesoporous nanoparticle structure towards the total particle catalytic activity is further corroborated through comparison of the current-time transients recorded for individual nanoparticles of differing morphology: solid vs mesoporous, and by evidencing the sensitivity of the single particle catalytic activity to the supporting electrolyte concentration.

In Chapter 8, the underpotential deposition and removal of hydrogen from a mesoporous PtNP surface is shown to quantify the electrochemically active surface area (ECSA) of an individual nanoparticle. This surface area of the particle is concomitantly correlated with its individual catalytic activity (current density) towards the hydrogen evolution reaction (HER). In addition, conclusions in this chapter are compared with the results in Chapters 4 and 5, showing consistency in all structural measurements of the particles.

Finally, Chapter 9 provides the main conclusions for the studies described in the thesis. The various discoveries in this thesis in respect of individual nanoparticles reflect generic methodological development, both fundamentally and applied, in studying electrochemistry at nanoscale. The overall major finding is that it is essential to recognize particle porosity to fully understand catalytic properties.

Acknowledgements

First and foremost, I would like to express my deep gratitude to my supervisor, Professor Richard G. Compton, for his invaluable guidance and inspiration throughout my DPhil, my Part II and summer projects over the past four years. I would like to thank him for his trust, support and encouragement as always. This thesis would not have been possible without his help.

The second thank you must go to Dr. Christopher Batchelor-McAuley who made huge contribution to my work. Thanks to his patience and generous advice to the projects, and for introducing me to the wonders of electrochemistry since my first day in this group.

Thank you to all the members of the Compton group, past and present, for making the lab and office such an enjoyable place to work in. In particular, thanks to Dr. Chuhong Lin and Dr. Enno Kätelhön for their collaborations on the simulations. To Dr. Eden E. L. Tanner for her help on interpreting the experimental results. To Dr. Stanislav V. Sokolov, Dr. Neil P. Young and Dr. Robert G. Palgrave for their precious assistance on TEM and XPS. Acknowledge also go to Dr. Xiuting Li who accompanied and took care of me during my DPhil. To Dr. Giorgia Zampardi who acts like a sister and gives me immeasurable suggestions to both of my work and life. To Yavor, Dia, Daisy, Lifu, Korbua, Haonan, Jake and Collin for being my lunch and sports buddies. And to every other colleague, thank you all for making my time working here so great. In addition, I would like to thank Ke for his understanding and for always being so supportive. Thank you for standing on my side through my difficult times.

Last but not the least, a very special thank you to my parents, for their endless love and care, and for working so hard to provide me all these wonderful opportunities. Thank you for being proud of me. I feel extremely lucky to have such a great family.

It has been a great journey for me to study and stay in Oxford for the past seven years. Thank you to all the amazing people who help me and see my growth in this lovely place.

Glossary

Roman Symbols

Symbol	Meaning	Unit
(ads)	adsorbed phase	
(aq)	aqueous phase	
a_i	activity of species i	mol m^{-3}
$a^{\ominus}$	standard activity (1 M)	mol m^{-3}
A	area	m^2
$\boldsymbol{A}$	absorbance	
$\boldsymbol{c}$	speed of light	m s^{-1}
c_i	concentration of species i	mol m^{-3}
c_i^*	bulk concentration of species i	mol m^{-3}
$c_i(z=0)$	surface concentration of species i	mol m^{-3}
c_S	electrolyte concentration	mol m^{-3}
$c^{\ominus}$	standard concentration (1 M)	mol m^{-3}
C_d	double layer capacitance	F m^{-2}
D_i	diffusion coefficient of species i	m^2 s^{-1}
D_∞	diffusion coefficient at infinite temperature	m^2 s^{-1}
e	electronic charge	C
E	electrode potential	V
$E_{1/2}$	half-wave potential	V
E_a	activation energy	J mol^{-1}
E_ini	initial switching potential	V
E_mid	midpoint potential	V
$E_\mathrm{p,b}$	backward peak potential	V
$E_\mathrm{p,f}$	forward peak potential	V
E_switch	switch potential	V
$E^{\ominus}$	standard electrode potential	V
$E_\mathrm{f}^{\ominus}$	formal potential	V
$E^{\ominus}_{\mathrm{H^+/H_2}}$	standard hydrogen electrode potential (0.00 V)	V

Symbol	Meaning	Unit
ΔE_p	peak-to-peak separation	V
f	frequency	Hz
F	Faraday constant (96485 C mol^{-1})	C mol^{-1}
$G_i^\ominus$	standard Gibbs energy of species i	J mol^{-1}
h	Planck constant (6.62×10^{-34} J s)	J s
ΔH_ads	enthalpy of adsorption	J mol^{-1}
$\Delta H_\mathrm{M\text{-}H}$	metal-hydrogen bond enthalpy	J mol^{-1}
i	species	
I	current	A
$\boldsymbol{I}$	transmitted intensity	W m^{-2}
$\boldsymbol{I_0}$	incident intensity	W m^{-2}
I_ad	adsorption-limited current	A
I_diff	diffusion-limited current	A
I_ox	oxidation current	A
$I_\mathrm{p,f}$	forward peak current	A
I_red	reduction current	A
I_ss	steady-state current	A
j_0	exchange current density	A m^{-2}
$j_{a,\mathrm{lim}}$	anodic limiting flux	mol m^{-2} s^{-1}
j_i	flux of species i	mol m^{-2} s^{-1}
$j_{\mathrm{c},i}$	convective flux of species i	mol m^{-2} s^{-1}
$j_{c,\mathrm{lim}}$	cathodic limiting flux	mol m^{-2} s^{-1}
$j_{\mathrm{d},i}$	diffusive flux of species i	mol m^{-2} s^{-1}
$j_{\mathrm{m},i}$	migratory flux of species i	mol m^{-2} s^{-1}
j_ox	oxidation flux	mol m^{-2} s^{-1}
j_red	reduction flux	mol m^{-2} s^{-1}
k_a	adsorption rate constant	m^5 mol^{-2} s^{-1}
k_B	Boltzmann constant (1.38×10^{-23} J K^{-1})	J K^{-1}
k_d	desorption rate constant	m^2 mol^{-1} s^{-1}
k_el	electron transfer rate constant	m^3 mol^{-1} s^{-1}

Symbol	Meaning	Unit
k_{ox}	oxidation rate constant	m s^{-1}
k_{re}	reduction rate constant	m s^{-1}
k_s	salt parameter	m^3 mol^{-1}
$k^{\ominus}$	standard electrochemical rate constant	m s^{-1}
$k^{\ominus}_{\mathrm{red}}$	standard oxidation rate constant	m s^{-1}
$k^{\ominus}_{\mathrm{ox}}$	standard reduction rate constant	m s^{-1}
K_i	Henry's law constant of species i	Pa m^3 mol^{-1}
L	path length	m
(m)	electrode metallic phase	
m	mass	g
m_{T}	mass transport coefficient	m s^{-1}
M	molar mass	g mol^{-1}
M	unoccupied adsorption site	
n	number of electrons transferred	
N_i	number of species i	
p_i	partial pressure of species i	Pa
$p^{\ominus}$	standard pressure (1 atm)	Pa
q_{d}	charge density of the diffuse layer	C m^{-2}
q_{i}	charge density of the specifically adsorbed ions	C m^{-2}
q_{m}	charge density of the metallic electrode	C m^{-2}
q_{s}	charge density of the solution	C m^{-2}
Q	charge	C
Q_{m}	charge of the metallic electrode	C
Q_{s}	charge of the solution	C
r, z	spatial coordinate	
r_{e}	electrode radius	m
r_i	radius of species i	m
R	Universal Gas Constant (8.314 J K^{-1} mol^{-1})	J K^{-1} mol^{-1}
$\boldsymbol{R}$	electrical resistance	Ω
S_i	surface area of species i	m^{-2}

Symbol	Meaning	Unit
t	time	s
t_{switch}	switch time of the sweep direction	s
T	absolute temperature	K
v	fluid velocity	m s^{-1}
V_i	volume of species i	m^3
x, y, z	Cartesian coordinate	
z_i	ionic charge of species i	

Greek Symbols

Symbol	Meaning	Unit
α	Butler–Volmer reductive transfer coefficient	
β	Butler–Volmer oxidative transfer coefficient	
γ_i	activity coefficient of species i	
$\Gamma_{\text{H}_{\text{ads}}}$	surface coverage of adsorbed hydrogen	mol m^{-2}
Γ_i	surface coverage of species i	mol m^{-2}
Γ_{max}	maximum surface coverage	mol m^{-2}
Γ_{M}	surface coverage of unoccupied adsorption site	mol m^{-2}
δ	diffusion layer thickness	m
Δ	difference in a quantity	
ε	extinction coefficient	m^2 mol^{-1}
η	dynamic viscosity	Pa s
η_0	overpotential	V
θ	dimensionless potential	
λ	radiation wavelength	m
μ_i	chemical potential of species i	J mol^{-1}
$\overline{\mu_i}$	electrochemical potential of species i	J mol^{-1}
$\mu_i^{\ominus}$	standard chemical potential of species i	J mol^{-1}
ν	scan rate	V s^{-1}
ρ_i	density of species i	g m^{-3}

Greek Symbols

Symbol	Meaning	Unit
τ	dimensionless time	
ϕ	electric potential	V
ϕ_{m}	electric potential of the metallic electrode	V
ϕ_{s}	electric potential of the solution	V
Φ	work function	J

Abbreviations

Symbol	Meaning
ADI	alternating direction implicit
BE	binding energy
BET	Brunauer–Emmett–Teller
CA	chronoamperogram
CAE	constant analyzer energy
CE	counter electrode
CV	cyclic voltammogram
DAQ	data acquisition
DF	dilution factor
erf	error function
ECSA	electrochemically active surface area
ESCA	electron spectroscopy for chemical analysis
GC	glassy carbon
$\mathrm{H}_{\mathrm{ads}}$	adsorbed hydrogen
$\mathrm{H}_{\mathrm{upd}}$	underpotential hydrogen deposition
HER	hydrogen evolution reaction
HOMO	highest occupied molecular orbital
HOR	hydrogen oxidation reaction
IHP	Inner Helmholtz Plane
KE	kinetic energy

Symbol	Meaning
LSPR	localised surface plasmon resonance
LSV	linear-sweep voltammetry
LUMO	lowest unoccupied molecular orbital
MSE	mercury/mercurous sulfate electrode
NP	nanoparticle
NTP	4-nitrothiophenol
OHP	Outer Helmholtz Plane
PtNP	platinum nanoparticle
PZC	potential of zero charge
RAG	redox active group
RDE	rotating disc electrode
RDS	rate-determining step
RE	reference electrode
RHE	reversible hydrogen electrode
SAM	self-assembled monolayer
SCE	saturated calomel electrode
SHE	standard hydrogen electrode
TEM	transmission electron microscopy
TRC	tag-redox coulometry
UPD	underpotential deposition
UV–vis	ultraviolet-visible spectroscopy
WE	working electrode
XPS	X-ray photoelectron spectroscopy

Contents

Chapter 1

Fundamentals of Electrochemistry

This chapter provides a fundamental introduction and overview of electrochemistry and associated techniques. These are essential in understanding the experiments and results reported later in this thesis. Topics covered in this chapter include electrochemical equilibrium, Faradaic and non-Faradaic processes, mass transport, macroelectrodes, microelectrodes and electrochemical techniques.

1.1 Electrochemical Equilibrium

1.1.1 Electron Transfer at the Electrode/Solution Interface

Electrochemical equilibrium can be established at the interface between a metal electrode (m) and a solution phase (aq), where transfer of charged particles and electrons are involved. Consider a general n-electron reduction of species A to B:

$$m\mathrm{A}_{(\mathrm{aq})} + n\mathrm{e}^-{}_{(\mathrm{m})} \underset{k_{\mathrm{ox}}}{\overset{k_{\mathrm{red}}}{\rightleftharpoons}} q\mathrm{B}_{(\mathrm{aq})} \tag{1.1}$$

where m, n and q are the stoichiometric coefficients, k_{red} and k_{ox} are the reduction and oxidation rate constants for the electron transfer. A piece of metal is inserted into the solution containing A and B to facilitate the electron transfer within this redox couple. A charge separation is likely to occur between the electrode and the solution at the point of

equilibrium. The amount of charge on each phase depends on the position of the reaction equilibrium. Given the charge separation, an electrode potential will be developed at the metal relative to the solution species. Note the electrochemical equilibrium is set up only if the rate of electron transfer at the electrode/solution interface is rapid. In other words, "fast electrode kinetics" is essential for a potential difference to be established.

For a potential determining equilibrium, the established electrode potentials can be understood by the energy of the electrons of the pertinent species, as shown in Figure 1.1. In the metallic electrode, the electrons filled up to form an continuous conduction band until an energy maximum, which is also known as the Fermi level. On the contrary, the electronic structure of the solution phase A and B are discrete. Suppose that before the electrons transfer, the Fermi level of the metal is relatively higher than the lowest

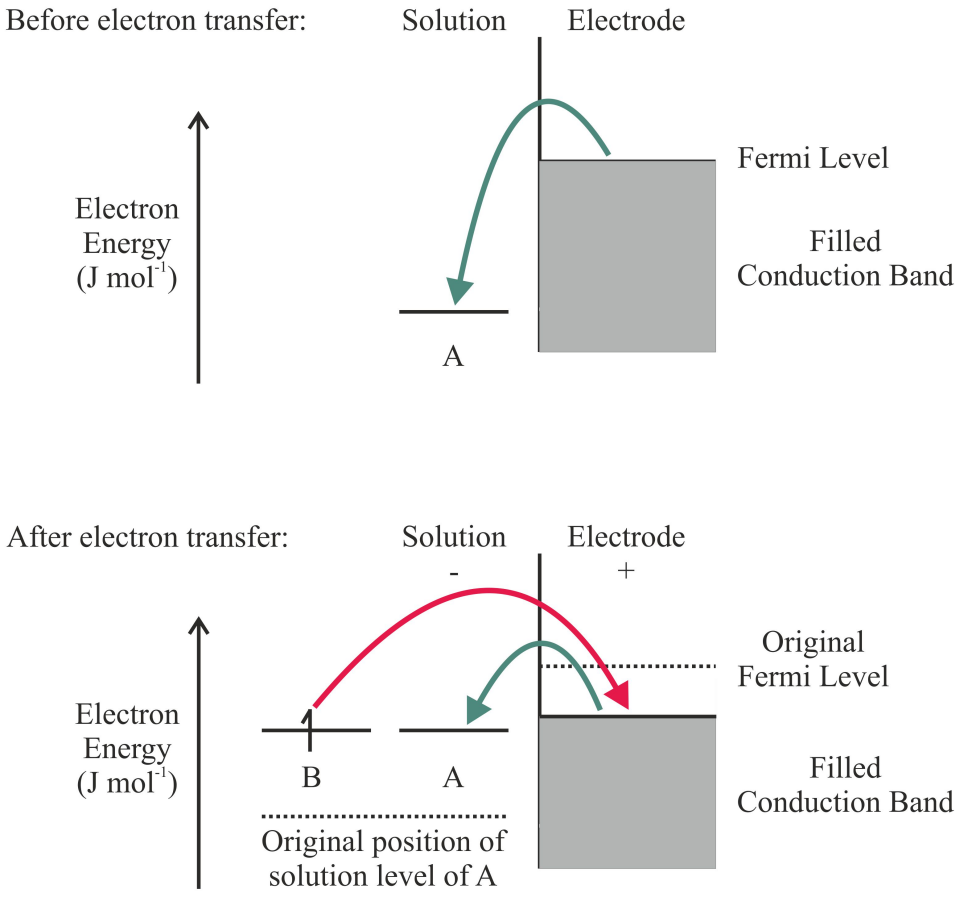

Figure 1.1: Illustration of energy levels of the ions in solution and the metallic electrode during the attainment of electrochemical equilibrium between A and B.

unoccupied molecular orbital (LUMO) of A in the solution phase. In this case, it provides a driving force for the delocalized electrons to jump from the metal Fermi level to the vacant orbital in A to generate B. As the electrons transit, positive charges start to build up on the electrode and negative charges on the species A. Therefore, the Fermi level of the metal drops progressively and the energy levels of the solution phase A increases. Based on these thermodynamic ideas, the Fermi level of the metal will finally match the LUMO of A and the highest occupied molecular orbital (HOMO) of B, making the electron transfer in both direction energetically favourable. When the reaction rates to reduce A and to oxidise B are exactly the same, no net changes are observed in terms of the components of the solution species or their electronic energy levels, a dynamic equilibrium is achieved. In this heterogeneous process, the charge separation introduced at the interface between the electrode and the solution gives rise to the origin of the electrode potential established on the metal.[1] Note that very little charge is needed to establish the equilibrium, therefore the bulk concentration of species A and B are unchanged.

1.1.2 The Nernst Equation

The position of an electrochemical equilibrium is balanced by both the chemical and electrical energies of all the involved entities. The electrochemical potential $\overline{\mu_i}$ (J mol^{-1}) of a specific species i is introduced:[2]

$$\overline{\mu_i} = \mu_i + z_i F \phi \tag{1.2}$$

where μ_i and z_i are the chemical potential (J mol^{-1}) and the charge of molecule i, respectively. F is the Faraday constant (96485 C mol^{-1}) corresponding to the charge of one mole of electrons, and ϕ is the potential (V) of the electrode or the solution of species i. For a reaction attained at electrochemical equilibrium, the electrochemical potentials of

the reactants equal to those of the products giving a constant temperature and pressure. Thus Equation 1.1 can be expressed as:

$$m\overline{\mu_{\mathrm{A}}} + n\overline{\mu_{e^-}} = q\overline{\mu_{\mathrm{B}}} \tag{1.3}$$

Substituting Equation 1.2 into Equation 1.3:

$$m\left(\mu_{\mathrm{A}} + z_{\mathrm{A}}F\phi_{\mathrm{s}}\right) + n\left(\mu_{e^-} - F\phi_{\mathrm{m}}\right) = q\left(\mu_{\mathrm{B}} + z_{\mathrm{B}}F\phi_{\mathrm{s}}\right) \tag{1.4}$$

According to the conservation of charge:

$$mz_{\mathrm{A}} - n = qz_{\mathrm{B}} \tag{1.5}$$

Thus rearranging Equation 1.4 gives:

$$nF\left(\phi_{\mathrm{m}} - \phi_{\mathrm{s}}\right) = m\mu_{\mathrm{A}} + n\mu_{e^-} - q\mu_{\mathrm{B}} \tag{1.6}$$

Expanding the chemical potential terms using:

$$\mu_i = \mu_i^{\ominus} + RT\ln\frac{c_i}{c^{\ominus}} \tag{1.7}$$

where $\mu_i^{\ominus}$ is the standard chemical potential (J mol^{-1}) of i, R is the universal gas constant (8.314 J K^{-1} mol^{-1}), T is the absolute temperature (K), c_i is the concentration (mol m^{-3}) of solution phase i, and $c^{\ominus}$ is the standard concentration of one molar (1 M). Therefore:

$$\mu_{\mathrm{A}} = \mu_{\mathrm{A}}^{\ominus} + RT\ln\frac{c_{\mathrm{A}}}{c^{\ominus}} \tag{1.8}$$

$$\mu_{\mathrm{B}} = \mu_{\mathrm{B}}^{\ominus} + RT\ln\frac{c_{\mathrm{B}}}{c^{\ominus}} \tag{1.9}$$

Equation 1.6 turns into:

$$\phi_{\mathrm{m}} - \phi_{\mathrm{s}} = \frac{\Delta\mu^{\ominus}}{nF} + \frac{RT}{nF} \ln \frac{c_{\mathrm{A}}^{m}}{c_{\mathrm{B}}^{q} c^{\ominus (m-q)}} \tag{1.10}$$

where

$$\Delta\mu^{\ominus} = m\mu_{\mathrm{A}}^{\ominus} + n\mu_{e^-} - q\mu_{\mathrm{B}}^{\ominus} \tag{1.11}$$

which is a constant at a given temperature and pressure.

Equation 1.10 is the *Nernst equation* for a single electrode/solution interface at the electrochemical equilibrium.[2] In accordance with the formula, the potential difference between the two phases is determined by the concentration of the ions in the solution. Alteration of the potentials is consistent with the *Le Chatelier's principle*. Increasing the amount of A or reducing B will push Equation 1.1 towards right. More electrons are taken from the metal, resulting a more positive electrode potential relative to the solution. Thus the potential difference will increase as expected from the Nernst equation, and *vice versa*. Note for reactions involving an ideal gas, the gaseous pressure p_i (Pa) replaces the concentration c_i, and the standard pressure $p^{\ominus}$ (1 atm) is used instead of the standard concentration $c^{\ominus}$. In the situation of pure solids or liquids, the chemical potential approximates to their standard chemical potential to give:

$$\mu_i \simeq \mu_i^{\ominus} \tag{1.12}$$

No concentration terms relating to pure solids or liquids therefore appear in the Nernst equation.

The Nernst equation (Equation 1.10) discussed above only applies to ideal solutions. However, most concentrated solutions encountered are not ideal due to the ion-ion and ion-solvent interactions in the electrolyte, as explained in part by *Debye–Hückel theory*.

In order to recognize non-ideality, the activity a_i (mol m^{-3}) of ions i is introduced:

$$a_i = \gamma_i c_i \tag{1.13}$$

where γ_i is the activity coefficient of species i. Equation 1.10 can be modified to give:

$$\phi_{\mathrm{m}} - \phi_{\mathrm{s}} = \frac{\Delta\mu^{\ominus}}{nF} + \frac{RT}{nF} \ln \frac{a_{\mathrm{A}}^{m}}{a_{\mathrm{B}}^{q} a^{\ominus (m-q)}} \tag{1.14}$$

where $a^{\ominus}$ is the standard molar activity (1 M).

In reality it is experimentally impossible to measure an absolute value of the potential difference at a single electrode/solution interface. Therefore a second electrode is introduced to make the measurement feasible. The electrode on which potentials are monitored is the working electrode (WE) and the electrode introduced to facilitate measurement is called the reference electrode (RE):[3]

$$E = (\phi_{\mathrm{m}} - \phi_{\mathrm{s}})_{\mathrm{WE}} - (\phi_{\mathrm{m}} - \phi_{\mathrm{s}})_{\mathrm{RE}} \tag{1.15}$$

where E is the measured potential difference (V) between two electrodes. Thus at a fixed temperature and pressure, for a reference electrode with a known concentration:

$$E = C + \frac{RT}{nF} \ln \frac{a_{\mathrm{A}}^{m}}{a_{\mathrm{B}}^{q} a^{\ominus (m-q)}} \tag{1.16}$$

where C is a constant.

Classically electrode potentials are measured relative to the standard hydrogen electrode (SHE):

$$\mathrm{H^+}_{(\mathrm{aq})} + \mathrm{e^-}_{(\mathrm{m})} \rightleftharpoons \frac{1}{2}\mathrm{H}_{2(\mathrm{aq})} \tag{1.17}$$

where the concentration of protons $c_{\mathrm{H^+}}$ must be 1 M for ideal solutions, at standard

temperature (298 K) and $p\mathrm{H}_2$ is 1 atm, to give a defined potential of 0.00 V. In particular, the standard electrode potentials $E^{\ominus}$ (V) of arbitrary redox couples are measured against the SHE under conditions where all the species involved in the potential determining equilibrium are at unit activity. Therefore Equation 1.16 can be modified as:

$$E = E^{\ominus} + \frac{RT}{nF} \ln \frac{a_{\mathrm{A}}^{m}}{a_{\mathrm{B}}^{q} a^{\ominus (m-q)}} \tag{1.18}$$

Although the standard electrode potential $E^{\ominus}$ has thermodynamic generality, it is restricted to rigorous experimental conditions. Equation 1.18 is also inconvenient to be applied as the activity or activity coefficient is usually unknown. Therefore, the formal potential $E_{\mathrm{f}}^{\ominus}$ (V) is introduced here:

$$E_{\mathrm{f}}^{\ominus} = E^{\ominus} + \frac{RT}{nF} \ln \frac{\gamma_{\mathrm{A}}^{m}}{\gamma_{\mathrm{B}}^{q}} \tag{1.19}$$

Thus the Nernst equation becomes:

$$E = E_{\mathrm{f}}^{\ominus} + \frac{RT}{nF} \ln \frac{c_{\mathrm{A}}^{m}}{c_{\mathrm{B}}^{q} c^{\ominus (m-q)}} \tag{1.20}$$

Note unlike the standard electrode potential $E^{\ominus}$, the formal potential $E_{\mathrm{f}}^{\ominus}$ is not only dependent on the temperature and pressure, but also related to the concentration of the redox species as well as their existing supporting medium, which in turn have an effect on the ion activities. When the solution is ideal, *viz* $\gamma_i = 1$ for all i, the formal potential is equal to the standard electrode potential.

To summarize, the Nernst equation describes the electrode potential for an electrochemical reaction at dynamic equilibrium. Rapid electron transfers are required. However, almost all the experiments in this thesis are performed under non-equilibrium situations. Potentials are usually applied to disturb the equilibrium and accordingly, two types of pro-

cesses may occur at the working electrode depending on whether electrons are transferred across the metal/solution interface (Faradaic currents) or not (non-Faradaic currents). This will be further explored in the following sections.

1.2 Faradaic Processes

The *Faradaic* reaction of an electroactive species is governed by *Faraday's law of electrolysis*, where electrons are transferred across the electrode/solution interface causing redox reactions to occur:[2]

$$m = \frac{QM}{nF} \tag{1.21}$$

where m is the mass (g) of the electroactive species, Q is the total electric charge (C) passed, M is the molar mass (g mol^{-1}) of the species, n is the number of electrons transferred per ion i, and F is the Faraday constant (96485 C mol^{-1}).

1.2.1 Electrode Kinetics

As discussed above, the Nernst equation only applies to a *true* electrochemical equilibrium under "fast electrode kinetics". Appreciation of the rates of electron transfer are therefore essential for understanding the Faradaic process at an electrode away from equilibrium.

The Butler-Volmer Equation

The *Butler-Volmer equation* is frequently applied to describe the relationship between the kinetics and the potential difference at an electrode/solution interface. Taking a one-electron transfer reaction with unity (1:1) stoichiometry as an example. As shown in Equation 1.1, in the case m, n and q all equal to 1:

$$\mathrm{A_{(aq)}} + \mathrm{e^-_{(m)}} \underset{k_{\mathrm{ox}}}{\overset{k_{\mathrm{red}}}{\rightleftharpoons}} \mathrm{B_{(aq)}} \tag{1.22}$$

The electrical current I (A) passing through the electrode can be quantified:

$$I = -FAj \tag{1.23}$$

where A is the geometric area (m^2) of the electrode, and j is the heterogeneous interfacial flux (mol m^{-2} s^{-1}) at the interface. The rest of the terms have been defined previously. According to the rate laws, the net process is:

$$j = k_{\mathrm{red}} c_{\mathrm{A}}(z = 0) - k_{\mathrm{ox}} c_{\mathrm{B}}(z = 0) \tag{1.24}$$

where k_{red} and k_{ox} are the rate constants (m s^{-1}) of the reduction and oxidation, receptively. They are sensitive to temperature, pressure as well as electrical potential difference across the two phases. $c_{\mathrm{A}}(z = 0)$ and $c_{\mathrm{B}}(z = 0)$ are the surface concentrations (mol m^{-3}) of the electroactive species A and B, which are usually deviated from the bulk, and z is the spatial coordinate perpendicular to the electrochemical interface. In accordance with the *transition state theory*,[4, 5] the redox rate constants k_{red} and k_{ox} can be defined assuming an Arrhenius behavior:[6]

$$k_{\mathrm{red}} = A_{\mathrm{red}} \exp\left(-\frac{\Delta G^{\ddagger}_{\mathrm{red}}}{RT}\right) \tag{1.25}$$

$$k_{\mathrm{ox}} = A_{\mathrm{ox}} \exp\left(-\frac{\Delta G^{\ddagger}_{\mathrm{ox}}}{RT}\right) \tag{1.26}$$

where A_{red} and A_{ox} are the pre-exponential factors, depending on the reaction frequency of these electroactive species. $\Delta G^{\ddagger}_{\mathrm{red}}$ and $\Delta G^{\ddagger}_{\mathrm{ox}}$ are the standard Gibbs energies of activation (J mol^{-1}), also known as the "energy barriers" to reaction. R is the universal gas constant (8.314 J K^{-1} mol^{-1}), and T is the absolute temperature (K). Figure 1.2 provides an energy profile of the redox process:

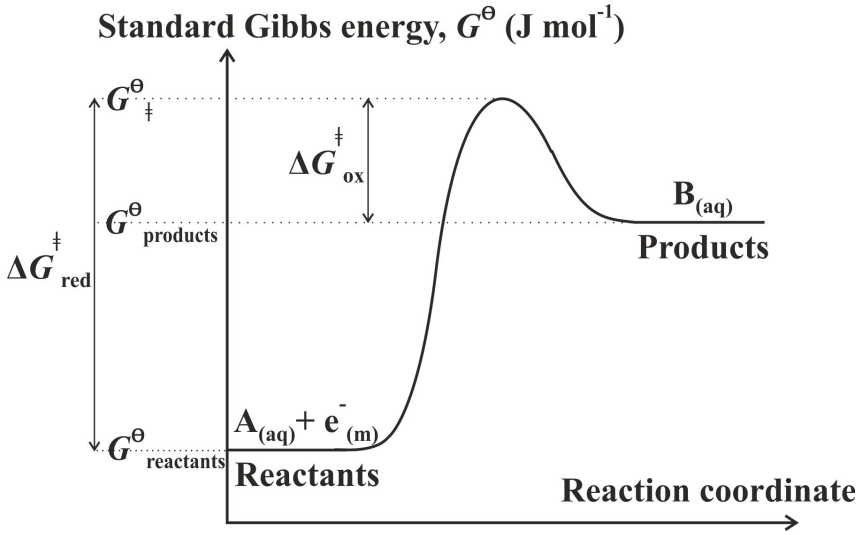

Figure 1.2: A reaction profile for a one-electron transfer process of unity stoichiometry, where ϕ_{m} is more positive relative to ϕ_{s}.

$$\Delta G^{\ddagger}_{\mathrm{red}} = G^{\ominus}_{\ddagger} - G^{\ominus}_{\mathrm{reactants}} \tag{1.27}$$

$$\Delta G^{\ddagger}_{\mathrm{ox}} = G^{\ominus}_{\ddagger} - G^{\ominus}_{\mathrm{products}} \tag{1.28}$$

where $G^{\ominus}_{\mathrm{reactants}}$, $G^{\ominus}_{\mathrm{products}}$ and $G^{\ominus}_{\ddagger}$ are the standard molar Gibbs energies of the reactants, products and transition state (J mol^{-1}), accordingly. Based on Section 1.1, these can be further expanded to give:

$$\begin{aligned} G^{\ominus}_{\mathrm{reactants}} &= G^{\ominus}_{\mathrm{A}} + G^{\ominus}_{\mathrm{e^-}} \\ &= (\mu^{\ominus}_{\mathrm{A}} + z_{\mathrm{A}} F\phi_{\mathrm{s}}) + (\mu^{\ominus}_{\mathrm{e^-}} - F\phi_{\mathrm{m}}) \\ &= (\mu^{\ominus}_{\mathrm{A}} + \mu^{\ominus}_{\mathrm{e^-}}) + (z_{\mathrm{A}} - 1)F\phi_{\mathrm{s}} - F(\phi_{\mathrm{m}} - \phi_{\mathrm{s}}) \\ &= C_1 + (z_{\mathrm{A}} - 1)F\phi_{\mathrm{s}} - F(\phi_{\mathrm{m}} - \phi_{\mathrm{s}}) \end{aligned} \tag{1.29}$$

$$\begin{aligned} \text{and} \quad G^{\ominus}_{\mathrm{products}} &= G^{\ominus}_{\mathrm{B}} = \mu^{\ominus}_{\mathrm{B}} + z_{\mathrm{B}} F\phi_{\mathrm{s}} \\ &= \mu^{\ominus}_{\mathrm{B}} + (z_{\mathrm{A}} - 1)F\phi_{\mathrm{s}} \\ &= C_2 + (z_{\mathrm{A}} - 1)F\phi_{\mathrm{s}} \end{aligned} \tag{1.30}$$

where $z_A - 1 = z_B$ according to conservation of charge. C_1 and C_2 are constants. Thus, the transition state (‡) can be assumed to lie in between the reactants and products:

$$\begin{aligned} G_{\ddagger}^{\ominus} &= C_3 + (z_A - 1)F\phi_s - (1-\alpha)F(\phi_m - \phi_s) \\ &= C_4 + (z_A - 1)F\phi_s - \beta F(\phi_m - \phi_s) \end{aligned} \tag{1.31}$$

where C_3 and C_4 are constants. α and β are the transfer coefficients ranging from zero to one with a sum of unity for a one-electron transfer process. The magnitudes of α and β define the position of the transition state (‡). If α is close to zero, the transition state is reactant (A) like, whilst if α is near one it is product (B) like. The situation is *vice versa* for β. In most cases, the transition state sits intermediate between the reactants and products to give:

$$\alpha \sim \beta \sim 0.5 \tag{1.32}$$

Equations 1.25 and 1.26 can thus be rewritten as:

$$k_{red} \propto \exp\left[-\frac{\alpha F}{RT}(\phi_m - \phi_s)\right] \tag{1.33}$$

$$k_{ox} \propto \exp\left[\frac{\beta F}{RT}(\phi_m - \phi_s)\right] \tag{1.34}$$

However, as discussed above, the potential difference $\phi_m - \phi_s$ cannot be measured at a single electrode/solution interface. Therefore, a reference electrode is introduced and Equations 1.33 and 1.34 can be modified to:

$$k_{red} = k_{red}^{\ominus} \exp\left[-\frac{\alpha F}{RT}(E - E_f^{\ominus})\right] \tag{1.35}$$

$$k_{ox} = k_{ox}^{\ominus} \exp\left[\frac{\beta F}{RT}(E - E_f^{\ominus})\right] \tag{1.36}$$

where $k^{\ominus}_{\mathrm{red}}$ and $k^{\ominus}_{\mathrm{ox}}$ are the standard reduction and oxidation rate constants (m s^{-1}), respectively. $\eta_0 = E - E^{\ominus}_{\mathrm{f}}$ is defined as the overpotential (V) that measures the potential difference between the potential applied to the working electrode and the formal potential of the A/B redox couple. Both potentials are conventionally measured against the SHE. Substituting Equations 1.35 and 1.36, the rate law shown in Equation 1.24 can be rearranged to give the Butler-Volmer equation.[7–9] For a heterogeneous reaction flux:

$$j = k^{\ominus}_{\mathrm{red}} \exp\left[-\frac{\alpha F}{RT}\left(E - E^{\ominus}_{\mathrm{f}}\right)\right] c_{\mathrm{A}}(z=0) - k^{\ominus}_{\mathrm{ox}} \exp\left[\frac{\beta F}{RT}\left(E - E^{\ominus}_{\mathrm{f}}\right)\right] c_{\mathrm{B}}(z=0) \tag{1.37}$$

Using the dimensionless potential:

$$\theta = \frac{F}{RT}\left(E - E^{\ominus}_{\mathrm{f}}\right) \tag{1.38}$$

a simplified notation is obtained:

$$j = k^{\ominus}_{\mathrm{red}} \exp\left(-\alpha\theta\right) c_{\mathrm{A}}(z=0) - k^{\ominus}_{\mathrm{ox}} \exp\left(\beta\theta\right) c_{\mathrm{B}}(z=0) \tag{1.39}$$

Note in the special case that the system is at the dynamic equilibrium, no net current flows across the interface, *viz* $j = 0$:

$$E = E^{\ominus}_{\mathrm{f}} + \frac{RT}{F} \ln \frac{c_{\mathrm{A}}(z=0)}{c_{\mathrm{B}}(z=0)} + \frac{RT}{F} \ln \frac{k^{\ominus}_{\mathrm{red}}}{k^{\ominus}_{\mathrm{ox}}} \tag{1.40}$$

since $\alpha + \beta = 1$. However, as discussed in Section 1.1.2, the Nernst equation at the electrochemical equilibrium is written as:

$$E = E^{\ominus}_{\mathrm{f}} + \frac{RT}{F} \ln \frac{c_{\mathrm{A}}(z=0)}{c_{\mathrm{B}}(z=0)} \tag{1.41}$$

Therefore it follows:

$$k_{\mathrm{red}}^{\ominus} = k_{\mathrm{ox}}^{\ominus} = k^{\ominus} \tag{1.42}$$

where $k^{\ominus}$ is the standard electrochemical rate constant (m s^{-1}).

The Tafel Law

The values of the transfer coefficients α and β can be derived by the *Tafel analysis* under irreversible limiting conditions. As shown in Equation 1.37, the net flux is balanced by both reduction and oxidation of the electroactive species A and B, with an arbitrary potential E imposing on the working electrode. Under extreme situations where the electron transfer in one redox direction is substantially faster than the other:

$$E \gg E_{\mathrm{f}}^{\ominus} \quad \text{or} \quad E \ll E_{\mathrm{f}}^{\ominus} \tag{1.43}$$

the reaction in the opposite direction are negligible to give:

$$j_{\mathrm{red}} = k_{\mathrm{red}}^{\ominus} \exp\left[-\frac{\alpha F}{RT}\left(E - E_{\mathrm{f}}^{\ominus}\right)\right] c_{\mathrm{A}}(z=0) \quad \text{for a reductive process} \tag{1.44}$$

$$j_{\mathrm{ox}} = -k_{\mathrm{ox}}^{\ominus} \exp\left[\frac{\beta F}{RT}\left(E - E_{\mathrm{f}}^{\ominus}\right)\right] c_{\mathrm{B}}(z=0) \quad \text{for a oxidative process} \tag{1.45}$$

Provided $c_{\mathrm{A}}(z=0)$ and $c_{\mathrm{B}}(z=0)$ do not change significantly over the range of potential study:

$$\ln|I_{\mathrm{red}}| = -\frac{\alpha F E}{RT} + C_1 \tag{1.46}$$

$$\ln|I_{\mathrm{ox}}| = \frac{\beta F E}{RT} + C_2 \tag{1.47}$$

where I_{red} and I_{ox} are the reduction and oxidation currents (A), receptively. C_1 and C_2 are constants. Thus, *Tafel plots* can be obtained by plotting either $\ln|I_{\mathrm{red}}|$ or $\ln|I_{\mathrm{ox}}|$ against the electrode potential E. The transfer coefficient α and β are determined from

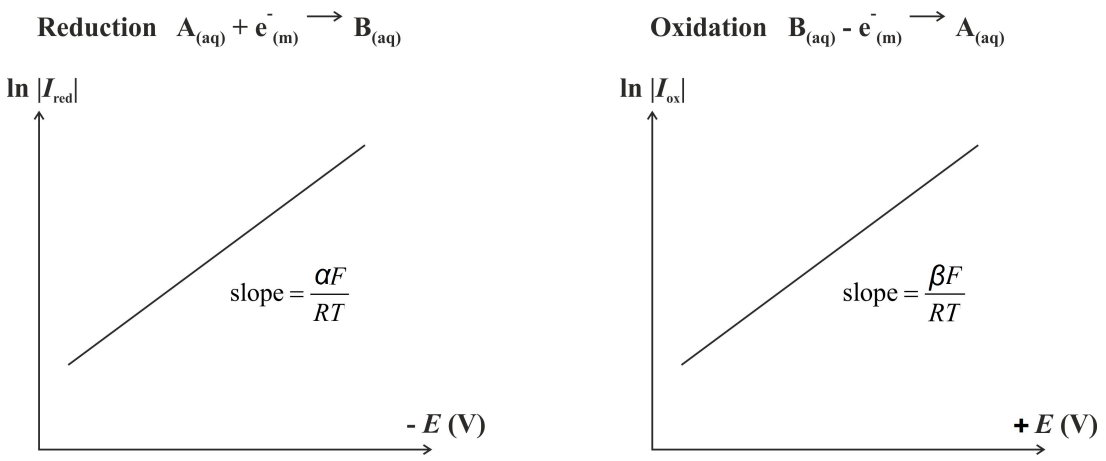

Figure 1.3: Tafel plots.

the gradients, as shown in Figure 1.3 where:

$$\alpha = -\frac{RT}{F}\frac{\partial \ln |I_{\text{red}}|}{\partial E} \tag{1.48}$$

$$\beta = \frac{RT}{F}\frac{\partial \ln |I_{\text{ox}}|}{\partial E} \tag{1.49}$$

The Volcano Plot

In multiple electron transfer processes, the transfer coefficients α and β provide information about the *rate-determining step* (RDS), and the underlying mechanisms are revealed.

For the proton/hydrogen redox couple reaction considered in Equation 1.17, different mechanisms are proposed as the reaction kinetics heavily depends on the extent and rate of formation and destruction of the intermediate adsorbed hydrogen H_{ads} on the electrode surface.[11, 12] Generally the chemical mechanism is considered in terms of three fundamental steps:

$$H^+ + e^- + M \rightleftharpoons H_{ads} \tag{1.50}$$

$$2\,H_{ads} \rightleftharpoons H_2 + 2\,M \tag{1.51}$$

$$\text{or} \quad H_{ads} + H^+ + e^- \rightleftharpoons H_2 + M \tag{1.52}$$

where M is an active adsorption site. Historically, these three reactions are referred to as the Volmer, Tafel and Heyrovský reactions, respectively.[13–15]. Thus a "volcano" curve can be plotted, as shown in Figure 1.4. This shows in effect the standard electrochemical rate constant $k^{\ominus}$ plotted against the estimated enthalpy of adsorption $-\Delta H_{\text{ads}}$ (J mol^{-1}) of hydrogen atom on various electrode materials.[10, 16] In Figure 1.4, j_0 is the exchange current density (A m^{-2}), which is defined as the current density at zero overpotential of the hydrogen evolution reaction. $\Delta H_{\text{M-H}}$ is the metal-hydrogen bond enthalpy (J mol^{-1}). From the diagram, as the enthalpy of hydrogen adsorption becomes more exothermic (negative), $k^{\ominus}$ first rises to a maximum followed by a steady decrease. Note that all of the metal electrodes on the ascending (left) part have transfer coefficients $\alpha \sim 0.5$, whereas those on the descending (right) side have $\alpha \sim 1.5$. This can be explained by considering the Volmer–Tafel mechanism, where the rate-determining step is the first (Volmer) or the second (Tafel) step, respectively.

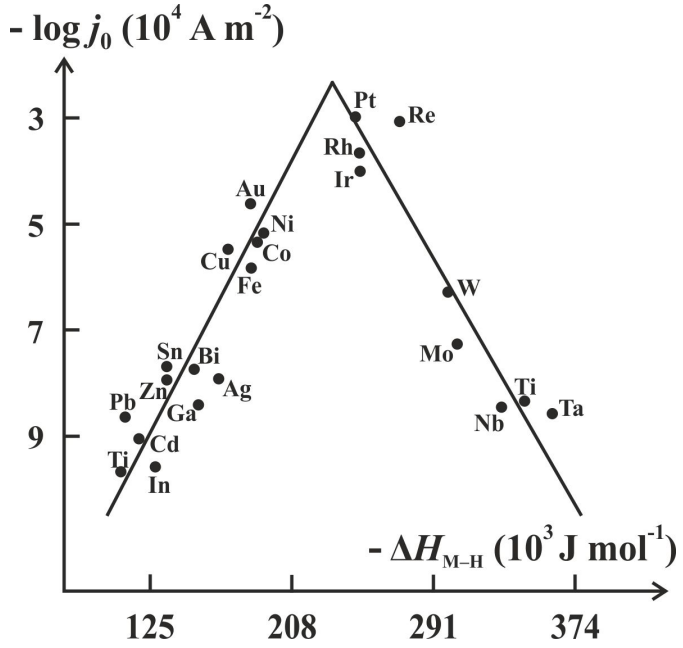

Figure 1.4: Exchange current density for the electrolytic hydrogen evolution reaction (HER) versus the strength of the intermediate metal–hydrogen bond formed in the electrochemical reaction.[10]

1.2.2 The Electrochemical Cell

A three-electrode system is widely employed in electrochemical experiments to study the electrode kinetics.[2, 17] Figure 1.5 is a schematic graph showing all three electrodes. The working electrode (WE) provides the electrochemical interface of interest. The reference electrode (RE) facilitates the measurement of potential difference at the working electrode/solution interface, as discussed in Section 1.1. The counter/auxiliary electrode (CE) connects the working electrode allowing Faradaic currents to flow.

A potentiostat is used to control all three electrodes, as shown in Figure 1.6. A fixed potential E is imposed between a working and a reference electrodes. The measured potential difference E can be realized, as illustrated by Equation 1.15 (Section 1.1.2), given the current passing through the latter electrode is infinitesimal. As the reference electrode provides a constant value of $(\phi_{\mathrm{m}} - \phi_{\mathrm{s}})_{\mathrm{RE}}$, any variation in E will give rise to a direct change in $(\phi_{\mathrm{m}} - \phi_{\mathrm{s}})_{\mathrm{WE}}$. However, the resulting $(\phi_{\mathrm{m}} - \phi_{\mathrm{s}})_{\mathrm{WE}}$ across the working electrode/solution

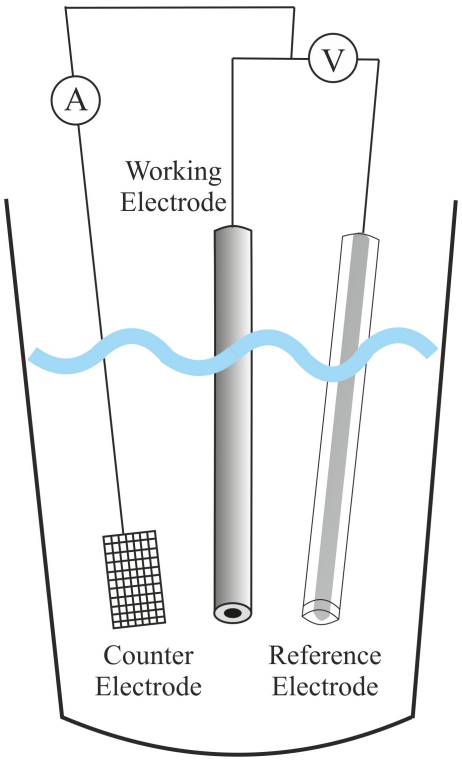

Figure 1.5: Schematic diagram of a three-electrode cell showing the working, reference and counter electrodes.

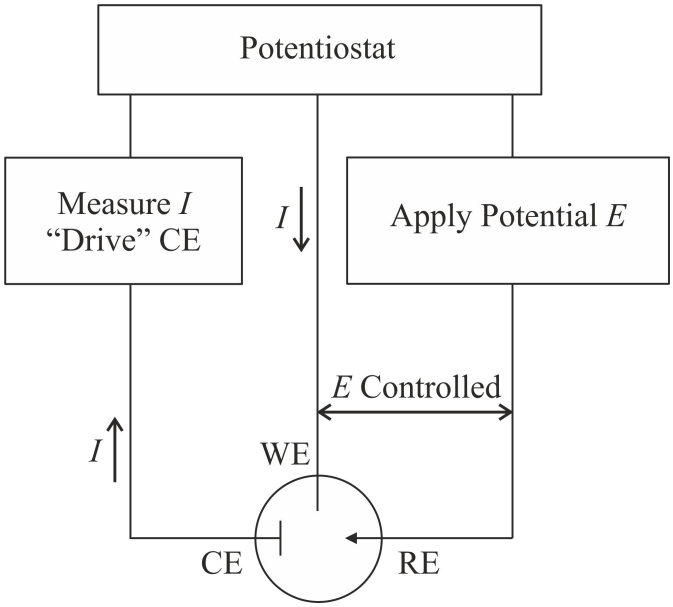

Figure 1.6: A potentiostat is required for preforming electrochemical experiments.

interface inevitably leads to a current flowing around the external circuit, which varies as a function of the applied potential. If only two electrodes are present in solution, appreciable current must pass through the reference electrode to complete the electric circuit. This leads to a chemical change within the reference electrode and gives an altered $(\phi_{\mathrm{m}} - \phi_{\mathrm{s}})_{\mathrm{RE}}$ according to the Nernst equation. The measured potential difference now becomes:

$$E = (\phi_{\mathrm{m}} - \phi_{\mathrm{s}})_{\mathrm{WE}} - (\phi_{\mathrm{m}} - \phi_{\mathrm{s}})_{\mathrm{RE}} + I\boldsymbol{R} \tag{1.53}$$

where $I\boldsymbol{R}$ is the contribution from the electrical resistance of the bulk solution between the working and the reference electrodes, also named as "ohmic drop". From Equation 1.53, a change on the applied potential will simultaneously vary $(\phi_{\mathrm{m}} - \phi_{\mathrm{s}})_{\mathrm{WE}}$ and $I\boldsymbol{R}$. As $I\boldsymbol{R}$ is an unknown factor, the potential difference across the working electrode/solution interface is no longer controlled. To avoid this situation, a counter electrode is therefore introduced as the third electrode to pass the same amount of current as the working electrode. Consequently, a voltage is assigned to the counter electrode by the potentiostat to fit the current flow.[2] Note that the choice of counter electrode material is important

as first, it should be inert in the electrolyte solution to avoid any interference with the target species. Second, it is required to be highly conductive with a sufficient surface area to guarantee an easy passage of electrons without restricting the electrochemical reaction. A large area carbon rod or a platinum wire/mesh is commonly used in the experiments.

In some large scale electroanalysis, the passage of current through the counter electrode may cause appreciable chemical consumption of the solution in its vicinity. To minimize the possible contamination of the solution around the working electrode, the counter electrode is usually separated behind a frit or located in a side arm of the cell.

The use of a two-electrode (working and reference) system is applicable in one important scenario where a microelectrode is employed as the working electrode.[18, 19] Since the electrode dimension is of micron scale, only a tiny amount of current ($\sim 10^{-9}$ A) passes through. Thus, the $\boldsymbol{IR}$ term can be ignored and negligible electrolytic change is induced within the reference electrode.

In this thesis, a three-electrode set-up is utilized for all conditions to avoid any potential shifts from any potential drops.

1.3 Non-Faradaic Processes

Non-Faradaic processes do not involve any charge transfers across the electrode/solution interface. However, reactions such as adsorption and desorption can take place, and the structure of the metal/electrolyte interface can be rearranged by changing potential or solution composition. Capacitative currents are generated and these can be described using a electrical double layer model. Particularly, the effects of non-Faradaic processes can be minimized by addition of supporting electrolyte to the solution. This is further illustrated in the following sections.

1.3.1 The Electrical Double Layer

The electrode/solution interface can experimentally behave like a capacitor if the potential across it is varied without any interfacial current flow. When a voltage is imposed across the phase boundary, charges build on the electrode surface and the electrostatic interactions occur as a driving force to redistribute electrolyte ions in solution, and to reorientate dipolar solvent molecules. A charging current results during this process. Eventually, a charge Q_{m} (C) is obtained on a very thin layer (< 0.1 Å) of the metal surface, because of an excess or deficiency of electrons, whilst a charge Q_{s} (C) is achieved on the solution, due to an excess of cations or anions adjacent to the electrode surface. The sign of the charge on the metal is dependent on the potential applied and the composition of the solution. To maintain overall electrical neutrality, equal but opposite charges are established on the metal and the solution to give $Q_{\mathrm{m}} = -Q_{\mathrm{s}}$. Note the charges Q_{m} and Q_{s} are often divided by the electrode area and expressed as the charge densities q_{m} and q_{s} (C m^{-2}). The entire array of the charged species and the oriented dipoles existing at the metal/solution interface is known as the *electrical double layer*.[6]

As revealed in Figure 1.7, the electrical double layer is actually composed of several parts. The *inner layer* (also called the *compact* or *Helmholtz layer*) is located closest to the metal. It contains mostly solvent molecules and sometimes desolvated ions that are directly in contact with the electrode surface. Such adsorption is strongly dependent on the chemical identity of the ions.[20] The *specifically adsorbed* ions have a total charge density q_{i} (C m^{-2}), and the position of their electrical centres forms the *Inner Helmholtz Plane* (IHP). Solvated ions are categorized as *non-specifically adsorbed* ions, as they can only approach the electrode to a certain distance, where the locus of their centres is called the *Outer Helmholtz Plane* (OHP). Because the interactions between these solvated ions and the charged electrode are long-range electrostatic forces, they are independent of the chemical properties of the ions. Due to thermal agitation, the non-specifically adsorbed

ions randomly diffuse from the OHP to the bulk, by virtue of Brownian motion, to give a three-dimensional region named the *diffuse layer*. The excess charge density in the diffuse layer is denoted as q_{d} (C m^{-2}). Thus, the total charge density of the solution side of the double layer can be written as:

$$q_{\mathrm{s}} = q_{\mathrm{i}} + q_{\mathrm{d}} = -q_{\mathrm{m}} \tag{1.54}$$

Also presented in Figure 1.7 is the potential variation across the double layer. Within the compact layer, the potential descends sharply and linearly with the distance away from the electrode surface. Whilst in the diffuse layer, it decays gradually to that of the

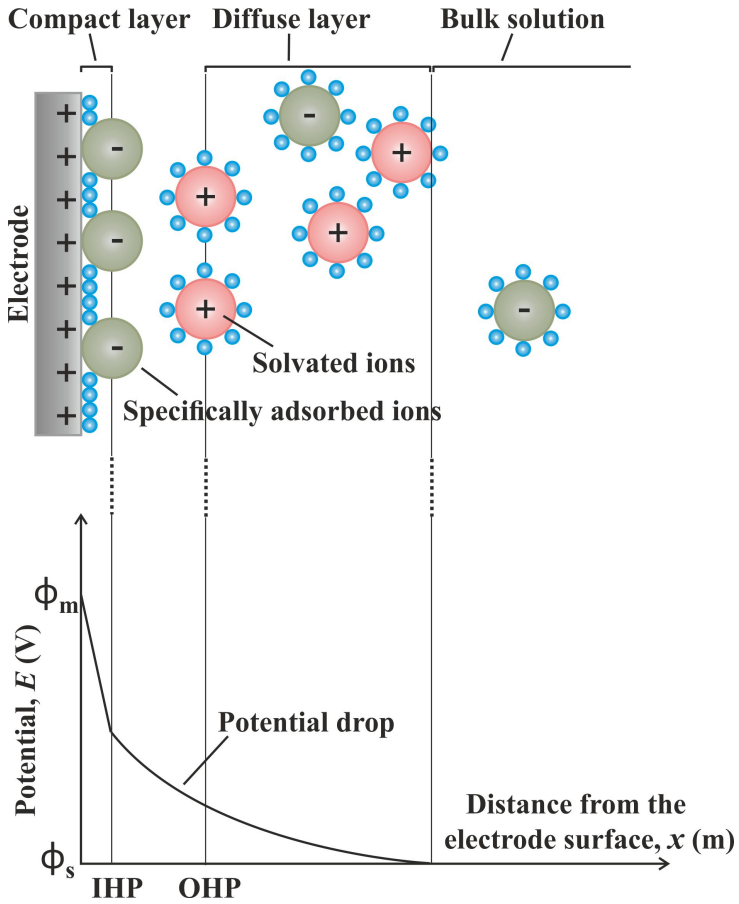

Figure 1.7: Model of the electrical double layer (top) and the potential drop $\phi_{\mathrm{m}} - \phi_{\mathrm{s}}$ across the double layer (bottom), where anions are specifically adsorbed at a more positive electrode. The green, red and blue spheres represent the anions, cations and solvent molecules, respectively, in the solution phase. ϕ_{m} and ϕ_{s} are the potentials on the metal and the solution in close proximity to the electrode surface.

electro-neutral bulk solution, providing a non-linear electric field gradient.

Different structures of the double layer leads to various potential drops across the electrode/solution interface, and this can influence the observed electrode kinetics. The thickness of the diffuse layer can be compressed by increase of the total ionic strength of the supporting electrolyte. Charging currents are found in electrochemical experiments due to the existence of the double-layer capacitance. Further discussion will be provided in the following sections.

1.3.2 Capacitative Current

When a voltage is changed across the double layer "capacitor", ions are induced to flow. This usually alters the electrode/solution interface and gives rise to a *capacitative* or *non-Faradaic current* I (A):

$$I = \frac{dQ}{dt} = C_{\mathrm{d}} A \frac{dE}{dt} = C_{\mathrm{d}} A \nu \tag{1.55}$$

where Q is the charge (C), t is the time (s), C_{d} is the capacitance of the double layer per unit area (F m^{-2}), E is the applied potential (V) across the electrode/solution interface, A is the electroactive layer area (m^2), and ν is the scan rate (V s^{-1}). At a given potential, C_{d} has a typical value in the range of 10–40 μF cm^{-2} in aqueous solution at 298 K. However, unlike real capacitors whose capacitances are independent of the voltage across them, C_{d} is often a function of the potential.

Non-Faradaic currents can be minimized to ease the analysis of Faradaic currents in the study of an electrochemical reaction. This is realized by using a microelectrode, applying a lower scan rate and/or adding excess supporting electrolyte.

1.3.3 Supporting Electrolyte

As discussed above, the thickness of the diffuse layer depends on the total ionic strength of the electrolyte. In the cases where concentration is greater than 10^{-2} M, it has a thickness of less than *ca.* 100 Å. In experimental practice, a *supporting* or *background electrolyte* is commonly added to solution to compress the electrolytic double layer. The added salt is usually associated with a high concentration of 10^{-1} M or above, and is chosen to be electrochemically inert at the potentials of interest. The addition of supporting electrolytes can be advantageous in several aspects. First, the double layer is compressed. Thus migration of the charged species is minimized, giving an easier model in terms of the diffusion only mass transport (see later in Section 1.4). Second, the potential drop $\phi_{\mathrm{m}} - \phi_{\mathrm{s}}$ between the electrode and the bulk solution is restricted within a distance of 10–20 Å. This is compatible with the quantum tunnelling of electrons, which provides a driving force for the Faradaic electron transfer processes. In the situation of a longer distance, only part of the potential drop is available at the sites of electron transfer, and the electrode kinetics are affected. Third, the solution conductivity is enhanced, thus the ohmic drop is reduced (see Section 1.2.2). Finally, a relatively constant ionic strength is maintained, therefore the activity coefficients are fixed in order to facilitate in the use of formal potentials (see Section 1.1.2).

Under fast electrode kinetics, electrochemical reactions are controlled by the mass transport of the electroactive species. In the next section, different categories of mass transport including diffusion, migration and convection will be introduced.

1.4 Mass Transport

Mass transport refers to the movement of materials from one location in solution to another. It can be generated either from an electrical or a chemical potential differ-

ence at two spots, or through a mechanical perturbation. The *Nernst-Plank equation* is used to describe the mass transport to an electrode, within one-dimensional Cartesian coordinates:[6]

$$j_i(x) = -D_i \frac{\partial c_i(x)}{\partial x} - \frac{z_i F}{RT} D_i c_i \frac{\partial \phi(x)}{\partial x} + c_i v(x) \tag{1.56}$$

where $j_i(x)$ is the total flux (mol m^{-2} s^{-1}) of an electroactive species i at distance x from the surface, D_i is the diffusion coefficient (m^2 s^{-1}), $c_i(x)$ is the concentration (mol m^{-3}), z_i is the ionic charge, $\phi(x)$ is the electric potential (V), and $v(x)$ is the local fluid velocity (m s^{-1}). The rest of the terms have been defined previously. The terms on the right-hand side contribute the three main modes of mass transport, which are diffusion, migration and convection, respectively.

In order to simplify the analysis of electrochemical systems, the migration and convection effects are usually eliminated to provide a diffusion only model. Full details will be elaborated in the following sections.

1.4.1 Diffusion

Diffusion is the spontaneous movement of a species down the concentration gradient, so as to maximize entropy. When a suitable potential is applied to a electrode in solution, electroactive species are consumed and depletion occurs at the electrode surface, resulting in a change of the concentration gradient from the bulk to the interface. This zone is called the *diffusion layer*, and it can be approximated using the Nernst model by extrapolating the *linear* region, as shown in Figure 1.8 in one dimension.

Fick's first and second laws are introduced in this section. The Cottrell equation is also mentioned as a solution of Fick's second law for a particular situation.

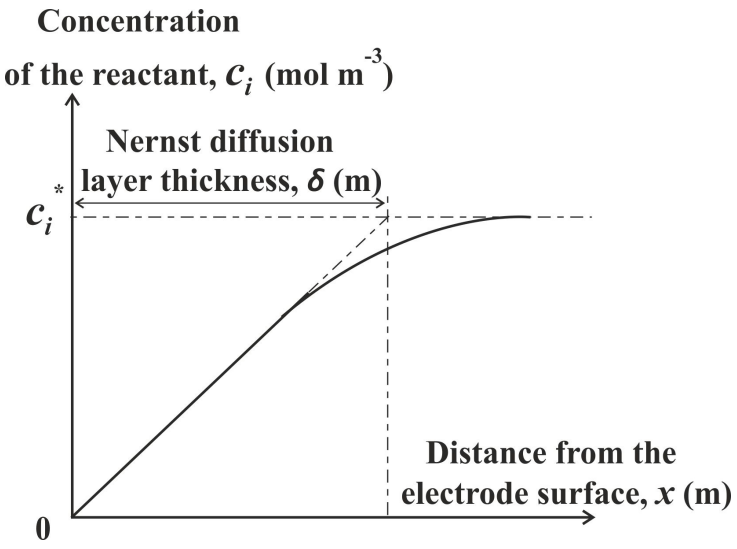

Figure 1.8: The one-dimensional Nernst diffusion layer.

Fick's First Law

Fick's first law quantifies the rate of diffusion using the diffusional flux at point x,[2] where its molecular basis can be illustrated by a one-dimensional cuboid model, as shown in Figure 1.9. The box has a width of $2\delta x$, and for an electrolyte i it can be evenly divided into two such that each compartment is on either side of the coordinate x, with concentrations $c_{i,1}$ and $c_{i,2}$ separated by a cross-sectional area A (m^2). Assumptions are made where molecules in each half have equal possibilities to move towards right or left, and a particle travels δx in time δt on average. Therefore, the number of moles transferred

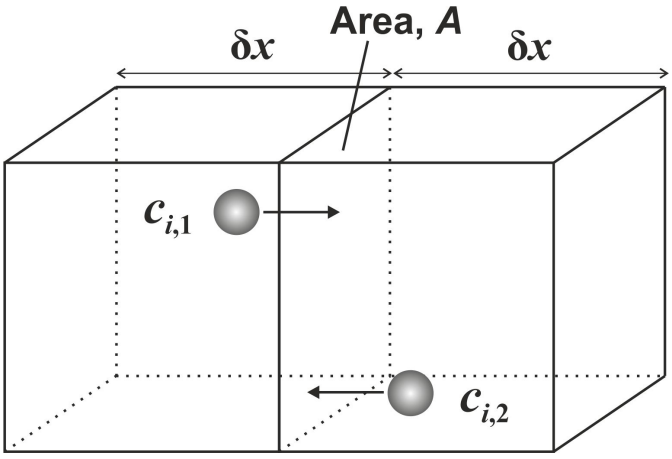

Figure 1.9: The molecular basis of Fick's first law in one dimension.

though a plane at x, during this time interval, is $\frac{1}{2}c_{i,1}A\delta x$ from left to right and $\frac{1}{2}c_{i,2}A\delta x$ from right to left, where a net rate is given by:

$$\text{Rate} = \frac{(c_{i,1} - c_{i,2})A\delta x}{2\delta t} \tag{1.57}$$

Accordingly, the diffusive flux $j_{\mathrm{d},i}(x)$ (mol m^{-2} s^{-1}) at point x can be written as:

$$j_{\mathrm{d},i}(x) = \frac{(c_{i,1} - c_{i,2})\delta x}{2\delta t} \tag{1.58}$$

As the local concentration gradient $\partial c_i(x)/\partial x$ (mol m^{-4}) at distance x is:

$$\frac{\partial c_i(x)}{\partial x} = -\frac{c_{i,1} - c_{i,2}}{\delta x} \tag{1.59}$$

Combining Equations 1.58 and 1.59 gives:

$$j_{\mathrm{d},i}(x) = -\frac{1}{2}\frac{\delta x^2}{\delta t}\frac{\partial c_i(x)}{\partial x} \tag{1.60}$$

Therefore, Fick's first law can be derived in terms of the diffusion coefficient D_i (m^2 s^{-1}):

$$j_{\mathrm{d},i}(x) = -D_i\frac{\partial c_i(x)}{\partial x} \qquad \text{with} \quad D_i = \frac{1}{2}\frac{\delta x^2}{\delta t} \tag{1.61}$$

Note that the negative sign in Equation 1.61 indicates the flux flows from high to low concentration. Importantly, the diffusion coefficient allows a measurement of how far the molecule travels in a certain time. The diffusion layer thickness δ (m) thus can be described by the *Einstein-Smoluchowski equation*:[21, 22]

$$\delta = \sqrt{\langle x^2 \rangle} = \sqrt{2D_i t} \tag{1.62}$$

where $\sqrt{\langle x^2 \rangle}$ is the root mean square displacement (m).

The diffusion coefficient is also highly temperature dependent following an Arrhenius relationship:

$$D_i = D_\infty \exp\left(-\frac{E_\mathrm{a}}{RT}\right) \tag{1.63}$$

where E_a is the activation energy for diffusion (J mol^{-1}), and D_∞ (m^2 s^{-1}) is the hypotetical value of D_i (m^2 s^{-1}) at infinite temperature. The rest of the terms have been defined previously. Therefore, it is essential to thermostatically control the experiments for all electrochemical measurements.

Furthermore, the value of D_i can be obtained from the *Stokes-Einstein equation*:

$$D_i = \frac{k_\mathrm{B} T}{6\pi\eta r_i} \tag{1.64}$$

considering a total contribution (both normal and tangential) from the frictional force of the solution. k_B is the Boltzmann constant (1.38×10^{-23} J K^{-1}), η is the dynamic viscosity (Pa s) of the medium, and r_i is the molecular radius (m), assuming a spherical molecule i. The rest of the terms have been defined previously. At room temperature, the diffusion coefficient has a typical value ranging from 10^{-6} to 10^{-5} cm^2 s^{-1} in aqueous solution. It is noted that the proton moves much more rapidly in aqueous solution, and has a much larger diffusion coefficient (D_{H^+}) compared to most other species of similar mobilities. This experimental fact is because of a synchronous proton movement, which can be interpreted in terms of the *Grotthuss mechanism*.[2]

Diffusion is further discussed with respect to the electrode size in Section 1.5.

Fick's Second Law

Given that Fick's first law is operative, *Fick's second law* states the rate of change in concentration by investigating how it varies against time t (s) at certain point x.[2] It

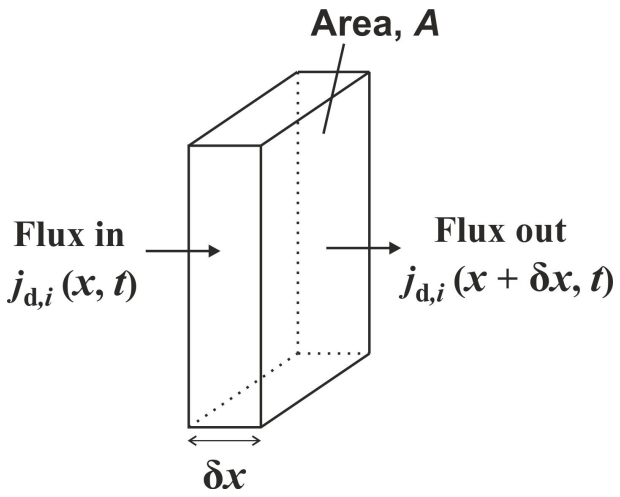

Figure 1.10: Flux in and out of a volume element $A\delta x$.

can be derived for a species i, by equating the concentration change at a point x to the flux difference in and out of a volume element $A\delta x$ over a time t. Considering a one-dimensional diffusion, as shown in Figure 1.10:

$$c_i(x, t+\delta t)A\delta x - c_i(x,t)A\delta x = j_{\mathrm{d},i}(x,t)A\delta t - j_{\mathrm{d},i}(x+\delta x, t)A\delta t \tag{1.65}$$

This can be rearranged to give:

$$\begin{aligned}
\left[c_i(x, t+\delta t) - c_i(x,t)\right]\delta x &= \left[j_{\mathrm{d},i}(x,t) - j_{\mathrm{d},i}(x+\delta x, t)\right]\delta t \\
\frac{c_i(x, t+\delta t) - c_i(x,t)}{\delta t} &= \frac{j_{\mathrm{d},i}(x,t) - j_{\mathrm{d},i}(x+\delta x, t)}{\delta x} \\
\frac{\partial c_i(x,t)}{\partial t} &= -\frac{\partial j_{\mathrm{d},i}(x,t)}{\partial x}
\end{aligned} \tag{1.66}$$

Substituting Fick's first law (Equation 1.61) into Equation 1.66 yields Fick's second law:

$$\frac{\partial c_i(x)}{\partial t} = D_i \frac{\partial^2 c_i(x)}{\partial x^2} \tag{1.67}$$

The Cottrell Equation

The *Cottrell equation* provides a solution of Fick's second law (Equation 1.67) for the case of a potential step to a macroelectrode. The electrode is located at $x = 0$ in a solution of a diffusing, electroactive species i with bulk concentration c_i^* (mol m^{-3}). It is initially ($t < 0$) passive as neither a potential is applied nor current drawn. At time $t = 0$, a large voltage is applied to the electrode. As the species reacts far more quickly at the interface compared to diffusion, this gives a zero concentration of i at the electrode surface. Boundary conditions can be formulated mathematically in one dimension to give:

$$\begin{aligned} &t \leqslant 0, \quad \text{all } x, \quad c_i = c_i^* \\ &t > 0, \quad x = 0, \quad c_i = 0 \\ &t > 0, \quad x \to \infty, \quad c_i = c_i^* \end{aligned} \tag{1.68}$$

and by introducing a new variable:

$$\Gamma = \frac{x}{2\sqrt{D_i t}} \tag{1.69}$$

where t is the time (s) during which the response is recorded. The rest of the terms have been defined previously. Equation 1.67 becomes:

$$\frac{d^2 c_i(x)}{d\Gamma^2} + 2\Gamma \frac{dc_i(x)}{d\Gamma} = 0 \tag{1.70}$$

Integration of this shows:

$$\frac{dc_i(x)}{d\Gamma} = C \exp(-\Gamma^2) \tag{1.71}$$

where C is a constant of integration. Thus it gives:

$$c_i^* - c_i = C\left[\int_0^\infty \exp(-\Gamma^2)\,d\Gamma - \int_0^\Gamma \exp(-\Gamma^2)\,d\Gamma\right] \tag{1.72}$$

It is also noted that:

$$\int_0^\infty \exp(-\Gamma^2)\,d\Gamma = \frac{\sqrt{\pi}}{2} \tag{1.73}$$

Therefore, the concentration evolved at point x in a given time t, subject to the boundary conditions above, can be deduced as:

$$c_i = c_i^* \frac{2}{\sqrt{\pi}} \int_0^\Gamma \exp(-\Gamma^2)\,d\Gamma \tag{1.74}$$

$$\text{or} \quad c_i = c_i^* erf\left(\frac{x}{2\sqrt{D_i t}}\right) \tag{1.75}$$

where *erf* is by definition the error function.

For a one-electron transfer process in Equation 1.22 (Section 1.2.1), the measured current at an electrode is directly proportional to the flux, as shown in Equation 1.23. The flux given by Fick's first law (Equation 1.61) can be written as:

$$j_{\mathrm{d},i}(x) = -D_i \frac{\partial c_i(x)}{\partial x}\bigg|_{x=0} = -\frac{D_i}{2\sqrt{D_i t}} \frac{\partial c_i(x)}{\partial \Gamma}\bigg|_{\Gamma=0} \tag{1.76}$$

which turns into:

$$I = \frac{FA\sqrt{D_i}c_i^*}{\sqrt{\pi t}} \tag{1.77}$$

where A is the electrode area (m). The rest of the terms have been defined previously. This result is known as the Cottrell equation. It shows that the current resulting from a potential step decays to zero with a dependence which is inversely proportional to the square root of time. The current response for a potential step chronoamperometry experiment can be predicted by the Cottrell equation, as will be discussed further in Section 1.6.2.

1.4.2 Migration

As elaborated in Section 1.3.1, the potential drop at the electrode/solution interface produces an electric field. This external field interacts with adjacent charged species electrostatically, thereby inducing ions to move to and from the electrode. This transport phenomenon is known as *migration*. For any species i, the migratory flux $j_{\mathrm{m},i}(x)$ (mol m^{-2} s^{-1}) at point x is not only proportional to its ionic charge z_i, diffusion coefficient D_i (m^2 s^{-1}) and concentration c_i (mol m^{-3}), but also the electric field, *viz* the gradient of the electric potential $\partial\phi(x)/\partial x$ (V m^{-1}) at that point. Within one-dimensional Cartesian coordinates:

$$j_{\mathrm{m},i}(x) = -\frac{z_i F}{RT} D_i c_i \frac{\partial \phi(x)}{\partial x} \tag{1.78}$$

where the terms have been defined previously.

The relative contributions of diffusion and migration to the flux of a species, and of the flux to the total current may vary at different locations in solution at a given time. For an electroactive substance, it is common that transport by both processes occurs at the vicinity to the electrode, unless supporting electrolyte is added to minimize migration (Section 1.3.3). As discussed above, under fast electrode kinetics the rate of reaction is controlled by the transport of the species at the interface, leading to a Faradaic current in the external circuit. Therefore, the total flux $j_i(x)$ (mol m^{-2} s^{-1}) can be split into its diffusive and migrational components where:

$$j_i(x) = j_{\mathrm{d},i}(x) + j_{\mathrm{m},i}(x) \tag{1.79}$$

Note that $j_{\mathrm{d},i}(x)$ and $j_{\mathrm{m},i}(x)$ can be in the same or opposite directions, depending on the orientation of the electric field or the charge on the electroactive species i. Figure 1.11 provides a schematic illustration of three reduction reactions of a positive, negative and uncharged species, respectively. $j_{\mathrm{m},i}(x)$ is always in the same direction as $j_{\mathrm{d},i}(x)$ for

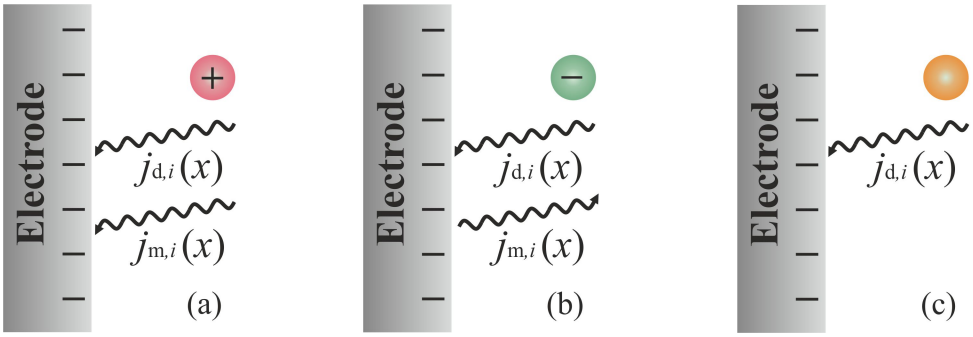

Figure 1.11: Reduction processes with different contributions of migratory flux: (a) a positively charged reactant, (b) a negatively charged reactant, and (c) a uncharged reactant.

cationic substance reacting at cathodes or anionic substance at anodes. It opposes $j_{d,i}(x)$ when anions are reduced at cathodes or cations oxidized at anodes.

However, migration can severely affect the current in electrochemical systems, thus it is often minimized to simplify the mathematical interpretation of the electrolysis process. As mentioned in Section 1.3.3, a supporting electrolyte with a much higher concentration than that of the electroactive species can be added to the solution. In this way, the interfacial potential drop is confined to a very close region to the electrode, making the double layer very thin with respect to the diffusion layer. Hence, the migratory flux of target ions is reduced to be negligible.

1.4.3 Convection

Convection is the movement of fluid species due to external forces. There are two forms of convection: natural and forced. *Natural convection* results from density and/or thermal gradients in solution. This is caused by chemical transformation when electrolysis takes place at the surface of working or counter electrodes, and/or *via* localized thermal variations such as imperfect thermostating or exo- or endothermicity of chemical processes. In general, natural convection is undesirable and irreproducible. It complicates the system and leads to a significant electrochemical perturbation at macrolectrodes, when the voltammetric measurement exceeds 10–20 seconds. This time window further provides

a lower limit to the scan rate when conducting voltammetry in current-potential experiments (see Section 1.6.1).

Forced convection arises from the stirring or agitation of solution *via* mechanical means. It can be deliberately introduced to dominate the mass transport in the system, allowing well-defined and easily interpreted analysis. Hence, mass transport can be enhanced and controlled convection achieved using a rotating disc electrode or a channel flow cell. By altering the rotation speed of the rotating disc, or the flow rate in the channel electrode, the kinetic and mechanistic information of the reaction can be probed.

The convective equivalent of Fick's first law can be readily derived in one dimension x:

$$j_{\mathrm{c},i}(x) = c_i v(x) \tag{1.80}$$

where $j_{\mathrm{c},i}(x)$ is the convective flux (mol m^{-2} s^{-1}) of species i at point x, and $v(x)$ is the local fluid velocity (m s^{-1}). The rest of the terms have been defined previously.

For the corresponding second law, one-dimensional transport is considered as shown in Figure 1.12. The temporal change in concentration of species i at point x is obtained by investigating the difference between the convective flux in and out at x and $x + \delta x$, respectively. According to the conservation of mass:

$$[c_i(x, t + \delta t) - c_i(x, t)]\, \delta x = [j_{\mathrm{c},i}(x, t) - j_{\mathrm{c},i}(x + \delta x, t)]\, \delta t \tag{1.81}$$

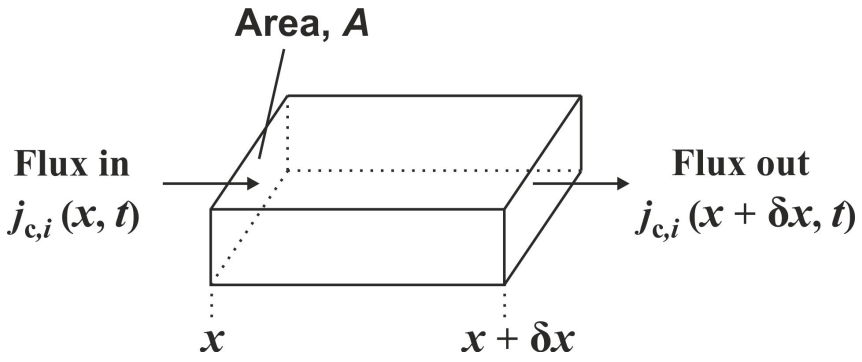

Figure 1.12: Convective transport in the x-direction.

Rearranging Equation 1.81 gives:

$$\frac{\partial c_i(x)}{\partial t} + \frac{\partial j_{c,i}(x)}{\partial x} = 0 \tag{1.82}$$

Substitution of the first law (Equation 1.80) yields the second law:

$$\frac{\partial c_i(x)}{\partial t} = -v(x)\frac{\partial c_i(x)}{\partial x} \tag{1.83}$$

Therefore, by combing Equations 1.67 and 1.83, the convective-diffusion equation for transport in one dimension x is acquired:

$$\frac{\partial c_i(x)}{\partial t} = D_i\frac{\partial^2 c_i(x)}{\partial x^2} - v(x)\frac{\partial c_i(x)}{\partial x} \tag{1.84}$$

Assuming fast electrode kinetics, the voltammogram is controlled by mass transport. However, it is hard to determine the influence of each individual component of all the three modes of mass transport. Thus, in this thesis, migration and convection are minimized whilst only diffusional response is considered.

1.5 Macroelectrodes vs Microelectrodes

Macroelectrodes and *microelectrodes* are divided according to their characteristic dimensions, with the former on a scale of millimetres or more and the latter of microns. This size difference gives them contrasting voltammatric behaviors, originating from two distinct diffusion models, as shown in Figure 1.13.

For macrodisc electrodes, *linear diffusion* prevails during electrolysis, where the flux of materials can be assumed exclusively normal to the electrode surface. This property is known as "uniform accessibility". The diffusion layer thickness is much smaller than the electrode radius, which is defined in Equation 1.62 (Section 1.4.1) for a one-dimensional

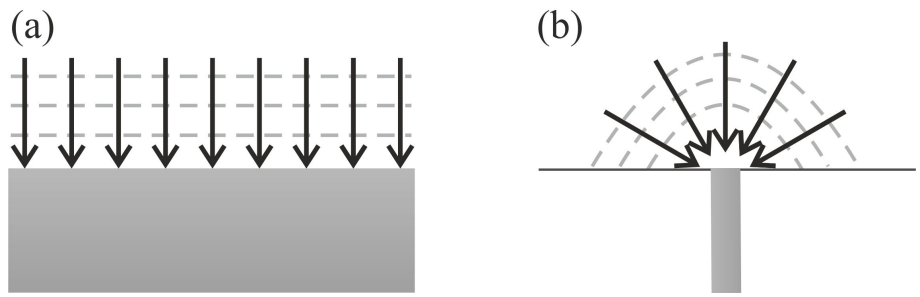

Figure 1.13: (a) Linear diffusion at a macroelectrode. (b) Convergent diffusion at a microelectrode. Arrow: diffusion of the electroactive species. Dashed line: the diffusion layer.

diffusive flux. When experiment proceeds, the diffusion layer progressively expands due to natural convection (see Section 1.4.3) since the bulk solution is well-mixed.

Conversely, microdisc electrodes are "non-uniformly accessible" at steady state, and the diffusion layer thickness is larger than the electrode radius. Within the experimental timescale, a hemispherical diffusion layer is well developed and the transport is radial. This *convergent diffusion* is much more efficient than the linear one, resulting a greater flux compared to its "macro" counterpart. The small dimension provides microelectrodes with several advantages, such as an enhanced Faradaic current density, as well as a reduced capacitive current (see Section 1.3.2) and a decreased ohmic drop (see Section 1.2.2). Due to the high rate of mass transport, measurement of "fast electrode kinetics" becomes achievable at microelectrodes.

Quantitative analysis of electrochemical reactions using macro- and microelectrodes is usually obtained by two popular methods: voltammetry and chronoamperometry. These two techniques will be introduced in the subsequent section.

1.6 Electrochemical Techniques

Voltammetry and *chronoamperometry* are introduced in this section as they are important methodologies that are widely employed in electrochemical analysis. The electrical current

is measured against voltage or over time at a set potential, respectively, and mechanistic information about the reaction is revealed.

1.6.1 Linear-Sweep and Cyclic Voltammetry

A *linear-sweep voltammogram* (LSV) is obtained when the potential at a working electrode is swept linearly from values E_1 to E_2. The applied potential $E(t)$ (V) varies as a function of the scan rate ν (V s^{-1}) at which the potential is swept and the time of the sweep t (s):

$$E(t) = E_1 + \nu t \tag{1.85}$$

A *cyclic voltammogram* (CV) can be extended from the LSV, where the direction of sweep is reversed at voltage E_2 and the electrode potential is scanned back to the original value E_1.[23–26] This forms a triangular potential cycle, and the potential can be expressed as:

$$\begin{aligned} 0 < t \leq t_{\text{switch}}, \quad & E(t) = E_1 + \nu t \\ t \geq t_{\text{switch}}, \quad & E(t) = E_1 + \nu t_{\text{switch}} - \nu\,(t - t_{\text{switch}}) \\ & \quad = E_1 + 2\nu t_{\text{switch}} - \nu t \end{aligned} \tag{1.86}$$

where t_{switch} is the switch time (s) of the sweep direction. Figure 1.14 shows the voltage ramps of the linear-sweep and cyclic voltammetry. Note that the scan rate can be determined by the slope of the potential-time plot:

$$\nu = \frac{\partial E(t)}{\partial t} \tag{1.87}$$

and it can be positive or negative in sign.

In next section, voltammetry of electrochemically reversible and irreversible processes are introduced. As explained in Section 1.5, electroactive species exhibits distinct diffu-

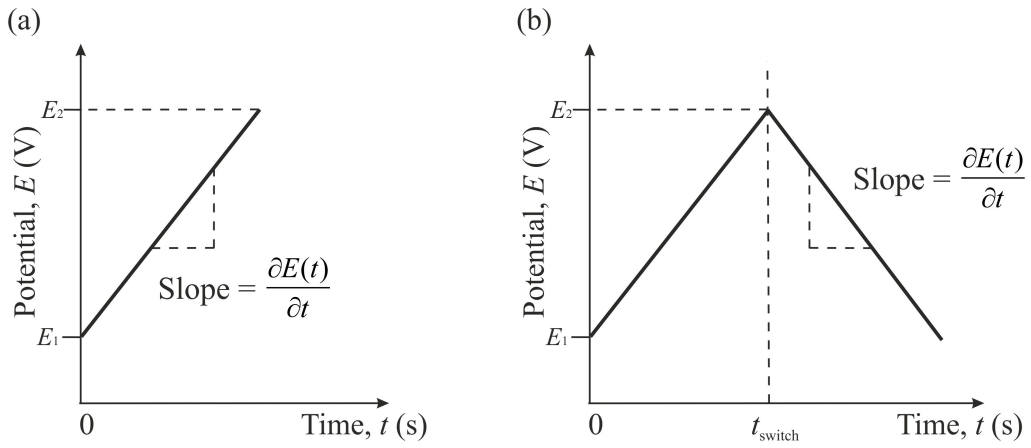

Figure 1.14: The potential-time profile of (a) a linear and (b) a cyclic voltammogram swept between potentials E_1 and E_2.

sional behaviors towards different size of electrodes, which leads to a profound influence on the shape of voltammograms. Therefore, voltammetric characteristics of both macro- and microelectrodes are considered in this context.

Reversible vs Irreversible Process

As discussed in Section 1.2.1, "fast" and "slow" electrode kinetics correspond to large and small values of the electron transfer rate constant. This in turn leads to the concept of two electrochemical limits: "reversible" and "irreversible", respectively.

Figure 1.15 illustrates voltammograms of a one-electron transfer process with unity stoichiometry at macro- and microelectrodes. For each electrode, simulations are conducted at all the same conditions other than a difference in the standard electrochemical rate constant $k^{\ominus}$ (m s^{-1}). The three curves in both situations refer to the electrochemical *reversibility*, *quasi-reversibility* and *irreversibility*. The distinction between fast and slow electrode kinetics can be classified by the rate of electron transfer, as shown in Section 1.2.1, and that of the mass transport, which is introduced below.

The rate of the mass transport is measured by the local mass transport coefficient m_{T}

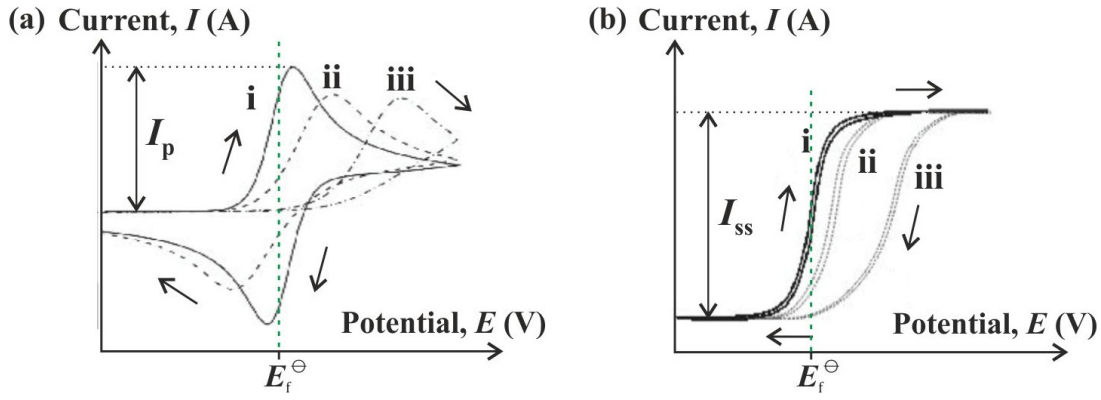

Figure 1.15: Voltammograms of diffusive species at (a) macrodisc electrodes: peak-shaped responses and (b) microdisc electrodes: sigmoidal responses. (i) Reversible, (ii) quasi-reversible, and (iii) irreversible systems. Arrow: scan direction of the voltammetry.

(m s^{-1}):

$$m_{\mathrm{T}} = \frac{D_i}{\delta} \tag{1.88}$$

where D_i is the diffusion coefficient (m^2 s^{-1}) of species i. δ is the diffusion layer thickness (m) with a dependence on time, as shown in Equation 1.62 (Section 1.4.1). The sweep time t (s) of the voltammetry can be expressed as:

$$t \propto \frac{RT}{F\nu} \tag{1.89}$$

where ν is the voltage scan rate (V s^{-1}). The rest of the terms have been defined previously. Thus for a cyclic voltammetric experiment:

$$m_{\mathrm{T}} \propto \sqrt{\frac{FD_i\nu}{RT}} \tag{1.90}$$

Therefore at the two kinetic extremes:

$$\text{Reversible,} \quad k^{\ominus} \gg m_{\mathrm{T}} \tag{1.91}$$

$$\text{Irreversible,} \quad k^{\ominus} \ll m_{\mathrm{T}} \tag{1.92}$$

For an electrochemically reversible system, as the electron transfer rate is fast enough relative to that of the mass transport, an equilibrium between the redox couple is achieved and the whole process is governed by the *Nernst equation*, shown in Equation 1.20 (Section 1.1.2). Whilst for an irreversible system, the electron transfer rate is smaller than the rate of mass transport. The current follows the *Butler–Volmer equation*, shown in Equation 1.37 (Section 1.2.1), which is a function of both the electrochemical rate constant and the concentration of species. In addition, by varying the scan rate both the electrode kinetics and the mechanism of electrode process can be investigated. In the limit of a fast scan rate, a minimum time is allowed for the diffusion layer to relax into the solution. Thus, by Fick's first law, shown in Equation 1.61, material flux is extremely quick. Therefore, all processes can, at least in principle, appear to be electrochemically irreversible. Voltammetric responses are elaborated below for macro- and microdisc electrodes, respectively.

Voltammetry at Macroelectrodes

For macrodisc electrodes, *peak-shaped* responses are typically observed in the current-voltage plot. This shape of voltammetry can be understood as initially no current is observed at the starting potential. When the experiment progresses, the potential applied becomes more favourable towards the electrolysis, leading to a current flow. A forward peak results when the electron transfer rate is balanced by the rate of diffusion of the electroactive species. As the voltammetry continues to sweep, the current falls off because the diffusion of material is not sufficient to replenish the species consumed at the electrode surface. When the voltammetric scan is reversed, similar principle applies and a backward peak is obtained. The measured forward peak current $I_{\mathrm{p,f}}$ (A) shows a square root dependence of the scan rate. This transport-controlled peak signal can be determined by the *Randles-Ševčík equations*, for a one-electron reduction with unity stoichiometry at 298 K:[2]

$$\text{Reversible,} \quad I_{\text{p,f}} = -0.446FAc_i^*\sqrt{\frac{FD_i\nu}{RT}}$$
$$= -2.69 \times 10^5 A\sqrt{D_i}c_i^*\sqrt{\nu} \tag{1.93}$$
$$\text{Irreversible,} \quad I_{\text{p,f}} = -0.496\sqrt{\alpha}FAc_i^*\sqrt{\frac{FD_i\nu}{RT}}$$
$$= -2.99 \times 10^5\sqrt{\alpha}A\sqrt{D_i}c_i^*\sqrt{\nu} \tag{1.94}$$

where α is the transfer coefficient, and A is the electrode area (m). The rest of the terms have been defined previously. Note that this square root relationship does not hold in the quasi-reversible situation, which is the intermediate state between the fully reversible and irreversible limits. Thus a parameter Λ, first introduced by Matsuda and Ayabe, is commonly employed to characterize this transition:[27]

$$\Lambda = \frac{k^{\ominus}}{\sqrt{\frac{FD_i\nu}{RT}}} \tag{1.95}$$

where the terms have been defined previously. The following ranges for the three classifications are suggested at macroelectrodes:

$$\text{Reversible,} \qquad \Lambda \geq 15, \quad k^{\ominus} \geq 0.3\sqrt{\nu} \quad \text{cm s}^{-1} \tag{1.96}$$
$$\text{Quasi-Reversible,} \quad 15 > \Lambda > 10^{-3}, \quad 0.3\sqrt{\nu} > k^{\ominus} > 2 \times 10^{-5}\sqrt{\nu} \quad \text{cm s}^{-1} \tag{1.97}$$
$$\text{Irreversible,} \qquad \Lambda \leq 10^{-3}, \quad k^{\ominus} \leq 2 \times 10^{-5}\sqrt{\nu} \quad \text{cm s}^{-1} \tag{1.98}$$

where at 298 K the transfer coefficient α and the diffusion coefficient D_i are assumed to be 0.5 and 1×10^{-5} cm^2 s^{-1}, respectively.

It is also noticed that the waveshapes and peak potentials of the forward and backward processes provide extra information about the reaction kinetics at macroelectrodes. As

disclosed in Figure 1.15, the major difference between a reversible and an irreversible voltammogram is the potential separation between the two peaks ΔE_p (V):

$$\Delta E_\mathrm{p} = |E_\mathrm{p,f} - E_\mathrm{p,b}| \tag{1.99}$$

where $E_\mathrm{p,f}$ and $E_\mathrm{p,b}$ are the forward and backward peak potentials (V), respectively. It follows that as the standard electrochemical rate constant decreases, the peak-to-peak separation increases with a small decrease in the peak current. At low scan rates, the reversible limit can be expressed as:

$$\begin{aligned} \Delta E_\mathrm{p} &= 2.218 \frac{RT}{F} \\ &= 57 \text{ mV} \quad \text{(at 298 K)} \end{aligned} \tag{1.100}$$

At high scan rates, the irreversible limit can be written as:

$$\begin{aligned} \Delta E_\mathrm{p} &= \frac{RT}{\alpha F} \ln \nu + C \\ &= \frac{59.4}{\alpha} \lg \nu + C \text{ mV} \quad \text{(at 298 K)} \end{aligned} \tag{1.101}$$

where C is a constant and $\lg \equiv \log_{10}$. The rest of the terms have been defined previously. In the reversible limit, the peak-to-peak separation is independent of the scan rate. Whilst under quasi- and irreversible conditions, the peak-to-peak separation becomes larger as the scan rate increases. In these two situations, a higher overpotential is required to overcome the kinetic barrier and drive the electrochemical reaction. The mid-point potential E_mid (V) of the forward and backward peaks is defined:[2]

$$E_\mathrm{mid} = \frac{1}{2} \left(E_\mathrm{p,f} + E_\mathrm{p,b} \right) \tag{1.102}$$

Thus, the mid-point potential can be expressed by the formal potential $E_{\mathrm{f}}^{\ominus}$ (V):

$$\text{Reversible,} \qquad E_{\mathrm{mid}} = E_{\mathrm{f}}^{\ominus} + \frac{RT}{2F} \ln\left(\frac{D_{\mathrm{B}}}{D_{\mathrm{A}}}\right) \tag{1.103}$$

$$\text{Irreversible,} \qquad E_{\mathrm{mid}} = E_{\mathrm{f}}^{\ominus} + \frac{RT}{F} \ln\left(\frac{D_{\mathrm{B}}}{D_{\mathrm{A}}}\right) \tag{1.104}$$

assuming the transfer coefficient is 0.5 under irreversible conditions. The rest of the terms have been defined previously. In the above equations, $E_{\mathrm{mid}} = E_{\mathrm{f}}^{\ominus}$ when $D_{\mathrm{A}} = D_{\mathrm{B}}$. Therefore no matter the reaction is reversible or not, the formal potential of the redox couple can be quantified by the mid-point potential, as shown in Figure 1.15.

Voltammetry at Microelectrodes

In the case of microdisc electrodes, *sigmoidal* responses are generated with an authentic *steady-state current* I_{ss} (A). For the same electrochemical process as above:

$$I_{\mathrm{ss}} = 4FD_i c_i^* r_{\mathrm{e}} \tag{1.105}$$

where r_{e} is the radius of the electrode (m). The rest of the terms have been defined previously. From the equation, the steady-state current correlates to the diffusion coefficient of the electroactive species. This is attributed to the contrasting diffusion models, as the convergent diffusion at microelectrodes is more efficient than the planar diffusion at macroelectrodes (see Section 1.5). In this situation, the diffusion of electroactive species is sufficient to compensate its depletion at the electrode surface. Note that at a very fast sweep rate, the diffusion may transit from radial to linear as a result of the short experimental timescale, leading to a wave-shaped voltammogram at microelectrodes.

From Figure 1.15, the voltammetric curves are increasingly broadened from reversible to irreversible limit. A shift is also shown at the half-wave potential $E_{1/2}$ (V), which is

the potential where the current is half of the steady-state current:

$$I = \frac{1}{2} I_{\mathrm{ss}} \tag{1.106}$$

Similarly, a parameter $\mathcal{K}$ is introduced to categorize the kinetic transition between the two extremes:[6]

$$\mathcal{K} = \frac{r_{\mathrm{e}} k^{\ominus}}{D_i} \tag{1.107}$$

where the terms have been defined previously. The boundaries of the three kinetic regimes at microelectrodes can be expressed as:

$$\text{Reversible,} \qquad \mathcal{K} > 10 \tag{1.108}$$

$$\text{Quasi-Reversible,} \qquad 10 \geq \mathcal{K} \geq 10^{-2\alpha} \tag{1.109}$$

$$\text{Irreversible,} \qquad \mathcal{K} < 10^{-2\alpha} \tag{1.110}$$

Therefore, the half-wave potential can be quantified *via* the formal potential $E_{\mathrm{f}}^{\ominus}$ (V):

$$\text{Reversible,} \qquad E_{1/2} = E_{\mathrm{f}}^{\ominus} + \frac{RT}{F} \ln\left(\frac{D_{\mathrm{B}}}{D_{\mathrm{A}}}\right) \tag{1.111}$$

$$\begin{aligned} \text{Irreversible,} \qquad E_{1/2} &= E_{\mathrm{f}}^{\ominus} + \frac{RT}{\alpha F} \ln \mathcal{K} \\ &= E_{\mathrm{f}}^{\ominus} + \frac{RT}{\alpha F} \ln\left(\frac{r_{\mathrm{e}} k^{\ominus}}{D_{\mathrm{A}}}\right) \end{aligned} \tag{1.112}$$

where the terms have been defined previously. For a reversible process, $E_{1/2} = E_{\mathrm{f}}^{\ominus}$ when $D_{\mathrm{A}} = D_{\mathrm{B}}$, as shown in Figure 1.15. While for an irreversible precess, the half-wave potential is dependent on the electrochemical rate constant.

Details about the voltammetry of surface-adsorbed species will be illustrated in the next section.

Voltammetry of Surface-Adsorbed Species

Hitherto in this thesis, all species participating in the electrochemical process have been assumed to be present in the solution phase. Nevertheless, it is possible that one or more species adsorb on the electrode surface, and voltammetry of the *surface-bound* species varies significantly from that of diffusive species in the solution phase.

Considering a stable, reversible electrochemical redox reaction undergoing a one-electron transfer process with unity stoichiometry:

$$\mathrm{A_{(ads)}} + \mathrm{e^-{}_{(m)}} \rightleftharpoons \mathrm{B_{(ads)}} \tag{1.113}$$

The surface coverage can be used to quantify the amount of A and B uniformly adsorbed on the electrode surface throughout the process. Assuming the maximum surface coverage $\Gamma_{\max}$ (mol m^{-2}) is fixed gives:

$$\Gamma_{\max} = \Gamma_{\mathrm{A}}(t) + \Gamma_{\mathrm{B}}(t) \tag{1.114}$$

where $\Gamma_{\mathrm{A}}(t)$ and $\Gamma_{\mathrm{B}}(t)$ are the surface coverage (mol m^{-2}) of A and B. With a hypothesis of fast electrode kinetics, Nernstian equilibrium is attained in response to an applied potential. Note that under the reversible condition, voltammetry shows an ideal behavior. The current response is *fully* symmetric about the formal potential of the redox couple, as there is no diffusional hysteresis.

For surface-adsorbed species, the current-potential waveshapes are controlled only by the rate of electron transfer. Therefore, in the case of slow electrode kinetics the voltammogram is distorted. As the reaction becomes increasingly irreversible, a larger overpotential is required to drive the reaction. Peak potentials of both forward and backward current signals deviate from the formal potential, leading to a large peak-to-peak separation. These two situations are delineated in Figure 1.16.

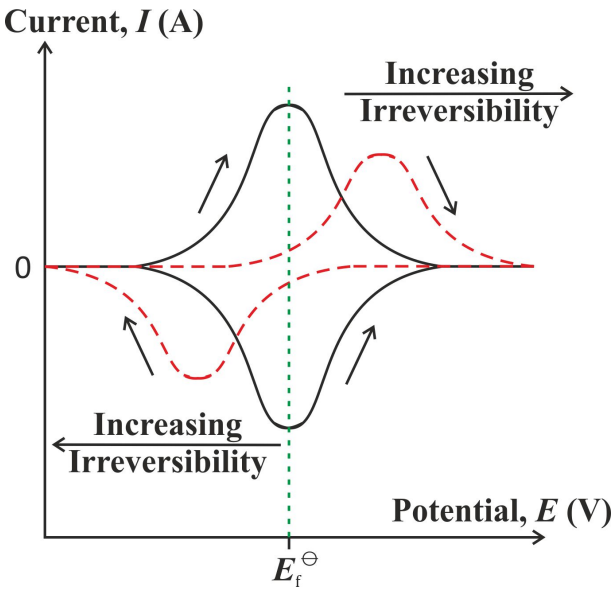

Figure 1.16: Typical cyclic voltammetric responses of surface-bound species A and B. Black solid line: a reversible process. Red dashed line: an irreversible process. Arrow: sweep direction of the voltammetry.

The quantities of the adsorbed materials A and B can be evaluated simply by measuring the charges under the voltammetric trace. This is possible as the current decays to zero towards both positive and negative potentials, due to a finite adsorption of A and B. The forward peak current is directly proportional to the scan rate, in contrast to the case of solution phase voltammetry where it scales with the square root of the scan rate:[28]

$$\text{Reversible,} \quad I_{\mathrm{p,f}} = \frac{F^2}{4RT} A\Gamma_{\mathrm{A}}\nu \tag{1.115}$$

$$\text{Irreversible,} \quad I_{\mathrm{p,f}} = \frac{\alpha F^2}{2.718RT} A\Gamma_{\mathrm{A}}\nu \tag{1.116}$$

where Γ_{A} is the surface coverage (mol m^{-2}) of reactant A at the electrode. The rest of the terms have been defined previously. This provides a diagnostic test to discover if the process is surface-limited or diffusion-controlled.

In this thesis, hydrogen adsorption is involved in most of the electrochemical experiments. This will be further discussed in Chapters 4–8. Chronoamperometry is introduced in the next section.

1.6.2 Chronoamperometry

A *chronoamperogram* (CA) can be measured when the potential applied to a working electrode is instantaneously stepped from a starting potential E_1 where usually no reaction takes place to a second potential E_2 at which electrolysis of interest occurs. A large current is observed, immediately following the step, that falls steadily with time. This arises because for suitably large applied potentials, the magnitude of current is controlled by the diffusion of electroactive materials to the electrode. The initial concentration gradients (see Fick's first law in Section 1.4.1) immediately after the potential step are extremely steep, as there is little time for any depletion of species to occur. As the the experiment proceeds, continuous consumption of reactants takes place in the vicinity of electrode, giving a spatially increasing diffusion layer. The shape of the chronoamperometric scan depends on the diffusion geometry, which will be illustrated separately in the following text for macro- and microelectrodes.

For macrodisc electrodes, the current decreases gradually, and ultimately approaches zero at long times. This is because inefficient diffusion cannot replenish the reactants in time, making that all the electroactive species near the electrode are consumed. Figure 1.17 shows the variation of the applied potential, and the corresponding current response in a potential step experiment. This current decay is described by the Cottrell equation as a function of time, shown in Equation 1.77 (Section 1.4.1) for a linear diffusion model.

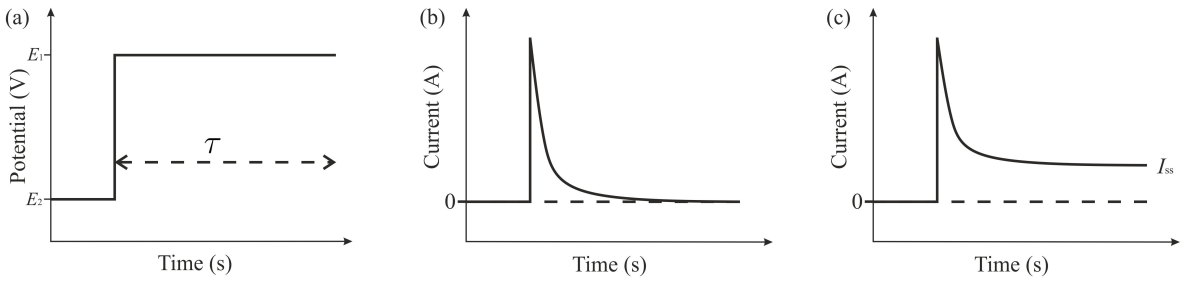

Figure 1.17: (a) The potential-time profile for a single-step chronoamperometry experiment. The resulting chronoamperometric responses at (b) macroelectrodes and (c) microelectrodes.

Note that the potential E_2 is assumed to be large enough that the concentration of materials at the electrode surface is zero.

As discussed in Section 1.5, for microdisc electrodes the flux is not constant over the electrode surface. The Fick's second law appropriate to cylindircal coordinates can be written as:

$$\frac{\partial c_i(x)}{\partial t} = D_i \frac{\partial^2 c_i(x)}{\partial r^2} + \frac{D_i}{r}\frac{\partial c_i(x)}{\partial r} + D_i \frac{\partial^2 c_i(x)}{\partial z^2} \tag{1.117}$$

where r is a radial coordinate from the centre of the disc, and z is the perpendicular distance from the electrode surface. The rest of the terms have been defined previously. A schematic diagram of the three-dimensional coordinates is shown in Figure 1.18. To solve the potential step problem of interest, boundary conditions are applied. Again, the potential E_2 is sufficient that the concentration of species at the electrode surface is zero:

$$\begin{aligned}
&t < 0, \quad \text{all } r,\ z && c_i = c_i^* \\
&t \geq 0, \quad z = 0,\ r < r_\mathrm{e} && c_i = 0 \\
&t \geq 0, \quad z \to \infty,\ \text{all } r && c_i = c_i^* \\
&t \geq 0, \quad r \to \infty,\ \text{all } z && c_i = c_i^*
\end{aligned} \tag{1.118}$$

where r_e is the electrode radius (m), and c_i^* is the bulk concentration (mol m^{-3}) of species i. Unlike macroelectrodes, in this situation a steady-state current is observed when time

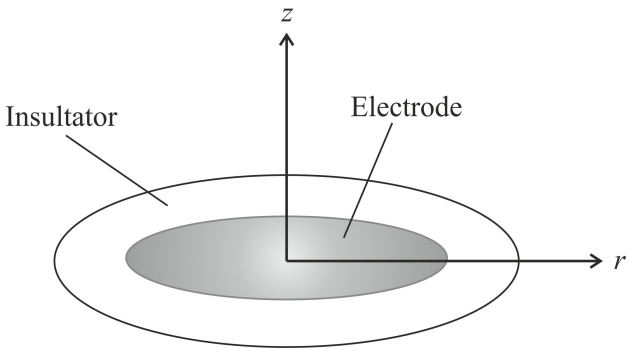

Figure 1.18: A microdisc electrode showing cylindrical coordinates r and z.

tends to infinity. As shown in Equation 1.105 (Section 1.6.1), the magnitude of the flux under steady-state conditions is proportional to the disc radius. It indicates that the smaller the electrode the greater the current density, and the faster material diffuses to and from the electrode surface. The full current-time transient is calculated as:

$$I = 4FD_i c_i^* r_e f(\tau) \tag{1.119}$$

where the dimensionless time τ is given by:

$$\tau = \frac{4D_i t}{{r_e}^2} \tag{1.120}$$

At short times when $\tau < 1$:

$$f(\tau) = \left(\frac{\pi}{4\tau}\right)^{\frac{1}{2}} + \frac{\pi}{4} + 0.094\tau^{\frac{1}{2}} + \cdots \tag{1.121}$$

Whilst at long times $\tau > 1$:

$$f(\tau) = 1 + 0.71835\tau^{-\frac{1}{2}} + 0.005626\tau^{-\frac{3}{2}} - 0.00646\tau^{-\frac{5}{2}} + \cdots \tag{1.122}$$

It follows that at very short times:

$$4D_i t \ll {r_e}^2 \tag{1.123}$$

the diffusion layer thickness is thin compared with the electrode radius, thus the diffusion to the electrode surface is effectively planar. Therefore, the current transient can be approximated *via* the Cottrell equation for linear diffusion (Equation 1.77) to give:

$$I = 4FD_i c_i^* r_e \left(\frac{\pi}{4\tau}\right)^{\frac{1}{2}} \tag{1.124}$$

where $A = \pi {r_e}^2$. However at longer times, the decay of current is less rapid than the Cottrellian $1/\sqrt{t}$ due to radial diffusion contributing to the current. As the current is a balance between a Cottrellian and a steady-state term, the timescale to reach steady-state is shorter if the electrode is smaller.

In particular, the *Shoup and Szabo equation* is widely employed to approximate both short and long time responses at microdisc electrodes:[29]

$$f(\tau) = 0.7854 + 0.8862\tau^{-\frac{1}{2}} + 0.2146 \exp\left(-0.7823\tau^{-\frac{1}{2}}\right) \tag{1.125}$$

The diffusion coefficient D_i and the bulk concentration c_i^* of analyte can be measured by the technique of chronoamperometry with the aid of a best-fit simulation since:

$$\text{at short times,} \quad I \propto \sqrt{D_i} c_i \quad \text{and} \tag{1.126}$$

$$\text{at long times,} \quad I \propto D_i c_i \tag{1.127}$$

In this thesis, a current-time transient is employed to study individual nanoparticles. This method is known as "nanoimpacts", which will be further elaborated in Chapter 2.

1.7 Aims of the Thesis

This thesis aims at developing a comprehensive understanding of the porosity of single particles and its influence on nanoparticle electrochemistry. This is realized first in Chapter 4 *via* thiol-tagged platinum nanoparticles (PtNPs). Upon impact, nitro groups are reduced and current transients observed. Charges are then measured from the spike transients, and the number of tag molecules is revealed. An alternative method is employed in Chapter 5 namely the surface platinum oxidation. From nanoimpacts and X-ray photoelectron spectroscopy (XPS), spike charge and the oxidation state of the platinum oxides

are determined, respectively. The number of platinum atoms oxized is thus calculated. Both methods reflect the internal structure of the particles. In particular, the results obtained from Chapters 4 and 5 are consistent, indicating an accuracy of the experimental measurements. Next, the electrocatalytic behavior of the PtNPs is explored in Chapter 6 *via* the hydrogen oxidation reaction (HOR) on both ensemble and individual particles. By comparing the kinetic parameters determined from these two techniques, the importance of nanoimpacts is emphasized to fully and correctly understand the reaction kinetics. Studies of the hydrogen oxidation on PtNPs are continued in Chapter 7 *via* random arrays and single particles. Voltammetric and current-time responses of these mesoporous PtNPs are obtained, which are highly sensitive to the morphology and interfacial structure of particles. Therefore, the catalytic ability of PtNPs is shown to relate to their porosity. Finally, Chapter 8 provides information about the structure-activity relationship of the nanoparticles. The electrochemically active surface area (ECSA) of the particles correlates to its catalytic activity, which can be measured simultaneously *via* hydrogen evolution reaction (HER). Therefore the total mesoporous nanoparticle surface area, both *internally* and *externally*, is active towards the evolution of hydrogen.

Bibliography

[1] Faulkner, L. R. *Journal of Chemical Education* **1983**, *60*, 262–264.

[2] Compton, R. G.; Banks, C. E. *Understanding Voltammetry*, 2nd ed.; Imperial College Press, 2011.

[3] Runo, J. R.; Peters, D. G. *Journal of Chemical Education* **1993**, *70*, 708–713.

[4] Truhlar, D. G.; Hase, W. L.; Hynes, J. T. *Journal of Physical Chemistry* **1983**, *87*, 2664–2682.

[5] Truhlar, D. G.; Garrett, B. C.; Klippenstein, S. J. *Journal of Physical Chemistry* **1996**, *100*, 12771–12800.

[6] Bard, A.; Faulkner, L. *Electrochemical Methods: Fundamentals and Applications*, 2nd ed.; John Wiley & Sons, 2000.

[7] Butler, J. A. V. *Transactions of the Faraday Society* **1924**, *19*, 659–665.

[8] Butler, J. A. V. *Transactions of the Faraday Society* **1924**, *19*, 729–733.

[9] Butler, J. A. V. *Transactions of the Faraday Society* **1924**, *19*, 734–739.

[10] Trasatti, S. *Journal of Electroanalytical Chemistry and Interfacial Electrochemistry* **1972**, *39*, 163–184.

[11] Santos, E.; Quaino, P.; Schmickler, W. *Physical Chemistry Chemical Physics* **2012**, *14*, 11224–11233.

[12] Parsons, R. *Transactions of the Faraday Society* **1958**, *54*, 1053–1063.

[13] Tafel, J. *Zeitschrift für Physikalische Chemie* **1905**, *50*, 641–712.

[14] Erdey-Grúz, T.; Volmer, M. *Zeitschrift für Physikalische Chemie* **1930**, *150*, 203–213.

[15] Heyrovský, J. *Recueil des Travaux Chimiques des Pays-Bas* **1927**, *46*, 582–585.

[16] Quaino, P.; Juarez, F.; Santos, E.; Schmickler, W. *Beilstein Journal of Nanotechnology* **2014**, *5*, 846–854.

[17] Ellis, W. D. *Journal of Chemical Education* **1973**, *50*, A131–A147.

[18] Rogers, E. I.; Silvester, D. S.; Poole, D. L.; Aldous, L.; Hardacre, C.; Compton, R. G. *Journal of Physical Chemistry C* **2008**, *112*, 2729–2735.

[19] Fleischmann, M.; Lasserre, F.; Robinson, J.; Swan, D. *Journal of Electroanalytical Chemistry and Interfacial Electrochemistry* **1984**, *177*, 97–114.

[20] Fisher, A. *Electrode Dynamics*; Oxford University Press, 1996.

[21] Einstein, A. *Annalen der Physik* **1905**, *17*, 549–560.

[22] von Smoluchowski, M. *Annalen der Physik* **1906**, *21*, 756–780.

[23] Mabbott, G. A. *Journal of Chemical Education* **1983**, *60*, 697–702.

[24] Van Benschoten, J. J.; Lewis, J. Y.; Heineman, W. R.; Roston, D. A.; Kissinger, P. T. *Journal of Chemical Education* **1983**, *60*, 772–776.

[25] Kissinger, P. T.; Heineman, W. R. *Journal of Chemical Education* **1983**, *60*, 702–.

[26] Chen, Y.; Ma, Q.; Jia, H.; Wang, Y. *Journal of Materials Science: Materials in Electronics* **2016**, *27*, 10237–10243.

[27] Matsuda, H.; Ayabe, Y. *Zeitschrift für Elektrochemie, Berichte der. Bunsengesellschaft für physikalische Chemie* **1955**, *59*, 494–503.

[28] Compton, R. G.; Batchelor-McAuley, C.; Dickinson, E. J. F. *Understanding Voltammetry: Problems and Solutions*, 2nd ed.; Imperial College Press, 2012.

[29] Shoup, D.; Szabo, A. *Journal of Electroanalytical Chemistry and Interfacial Electrochemistry* **1982**, *140*, 237–245.

Chapter 2

Single Nanoparticle Electrochemistry

The physical and chemical properties of a material can change dramatically when the size decreases from the macroscale to the nanoscale, leading to potential applications for nanoparticles in the fields of biotechnology, catalysis, and energy.[1–4] The fundamental concepts and theories of electrochemistry were introduced in the last chapter. However, most studies are based on macroscopic (ensemble) measurements that realize averaged results. This is not always straightforward and may incur errors when it comes to the microscopic (nano) level. It is therefore essential to develop a technique that can probe *individual* particle activities. One of these emerging methods is "nanoimpacts". In this chapter, a brief introduction is provided to both the nanomaterials and the nano-impact technique employed in the following chapters.

2.1 Nanomaterials

Nanoparticles (NPs) refer to a specific class of material of any shape with dimensions in the range of 1-100 nm.[5] They have received tremendous attention in recent decades because of their size/shape dependent properties which are significantly different from their corresponding bulk media. Changed characteristics such as optical, electronic and mechanical properties are observed as a result of the so-called *quantum confinement*. This effect is realized when the size of material becomes small enough. Once it approaches the

de Broglie wavelength of its electron wave function, bandgap increases and energy levels become discrete, leading for example to a blueshift in photon emission. Other examples are that for some metallic nanoparticles, fluorescent properties start to develop as the particle dimension drops below 2 nm.[6] In contrast, bulk metals do not fluoresce because the continuum of their energy spectra allow a free flow of electrons across the material. For other types of nanoparticles such as quantum dots, fluorescence may even arise at a size greater than 2 nm, due to the special electronic structure of the semiconductor materials. As these optoelectronic properties are highly tuneable and correlated to both size and shape of the particles, this makes quantum dots of wide interest.[7] Apart from the prominent field of nanoplasmonics, the physical properties of particles also alter tremendously at the nanoscale. Most notably, the reduced size of nanoparticles gives them a large percentage of surface atoms.[8] This in turn leads to a high surface-area-to-volume ratio and a likely high density of active sites that can significantly improve their catalytic efficiency. Details about the catalytic ability of nanomaterials are revealed in Chapters 6–8 in this thesis.

In addition, the properties of nanoparticles can be heavily influenced by the presence of capping agents. First, they reduce the extent or rate of the agglomeration/aggregation of particles *via* different mechanisms such as electrostatic or steric repulsions.[9] Second, they control the size or shape of materials through their synthesis, from which the position of the surface plasmon peak of metal particles can be fixed. These stabilisation and characterization effects of capping agents are further illustrated in Chapter 3, and monitored by UV-Vis spectroscopy and transmission electron microscopy in the rest of this thesis.

As mensioned earlier, metal nanoparticles find ever increased usages in vast fields such as biosensing, electrocatalysis and fundamental electrochemical studies due to their tiny size.[10] In particular, they have excellent performance in energy conversion and storage.

For example, platinum (Pt) is widely used in hydrogen fuel cells to catalyze the anodic hydrogen oxidation reaction (HOR).[11–13] This is feasible because of its outstanding electrocatalytic activity among other pure metals. An enhanced current density is allowed by the fast electrode kinetics, so that only a low overpotential is required in this process. In this thesis, the porosity of platinum nanoparticle (PtNP) aggregates is investigated in Chapters 4 and 5, and their catalytic performance explicated in Chapters 6–8. Essential reactions for energy applications are studied, notably hydrogen oxidation and evolution. In the next section, the technique employed to investigate individual nanoparticles is introduced.

2.2 Nanoimpacts

Many electrochemical studies have reported measurements using ensembles in which nanoparticles are drop-casted or adsorbed on an electrode surface before electrochemical experiments. However, the results are averaged over a large population of nanoparticles which make them difficult to interpret. This may also lead to inevitable errors as the particles may be poly-dispersed or orientated. Agglomeration or loss of materials are also likely to arise (see Chapter 6). Single particle techniques are highly desirable to correctly and fully understand nanoparticle reactions.

Electrode-particle impacts (or "nanoimpacts") has recently become a popular electroanalytical approach as it provides a simple but efficient way to characterize individual particles, and to probe their catalytic activities in the solution phase (see Chapters 4–8).[14–18] This technique is preformed by immersing an electrode into a nanoparticle suspension. By virtue of the Brownian motion, particles move diffusively and randomly collide with the potentiostated electrode. They can either stick or diffuse away, if the electrode is suitably potentiostatted. Charge can be transferred between the particles and the electrode, and a resulting Faradaic current may be observed in the current-time

response.

Early work in this field was carried out by Heyrovský *et al.* on metal oxide semiconductors, such as SnO_2, TiO_2 and mixed TiO_2/Fe_2O_3 colloids.[19–22] Voltammetric signals of these colloidal suspensions were realized in the presence of aqueous solutions, where proton reductions were mediated on the surface of particles upon their collision with a mercury electrode. This methodology was subsequently extended to metallic powders, such as Cu, Fe, Ni, Mo and W samples.[23] A set of current spikes were observed in the voltammograms, attributed to the catalysis of solution species on the particles, or the reduction of their surface oxides upon impacts. Although the current-time response of individual particles were not recorded, Heyrovský reported two routes *via* ensemble studies that are mainly applied in single particle impacts nowadays: *direct* and *indirect* detection of particles, respectively. Pertinent schematic diagrams are shown in Figure 2.1.

In so-called *direct* reactions, nanoparticles themselves are reduced or oxidized. Cur-

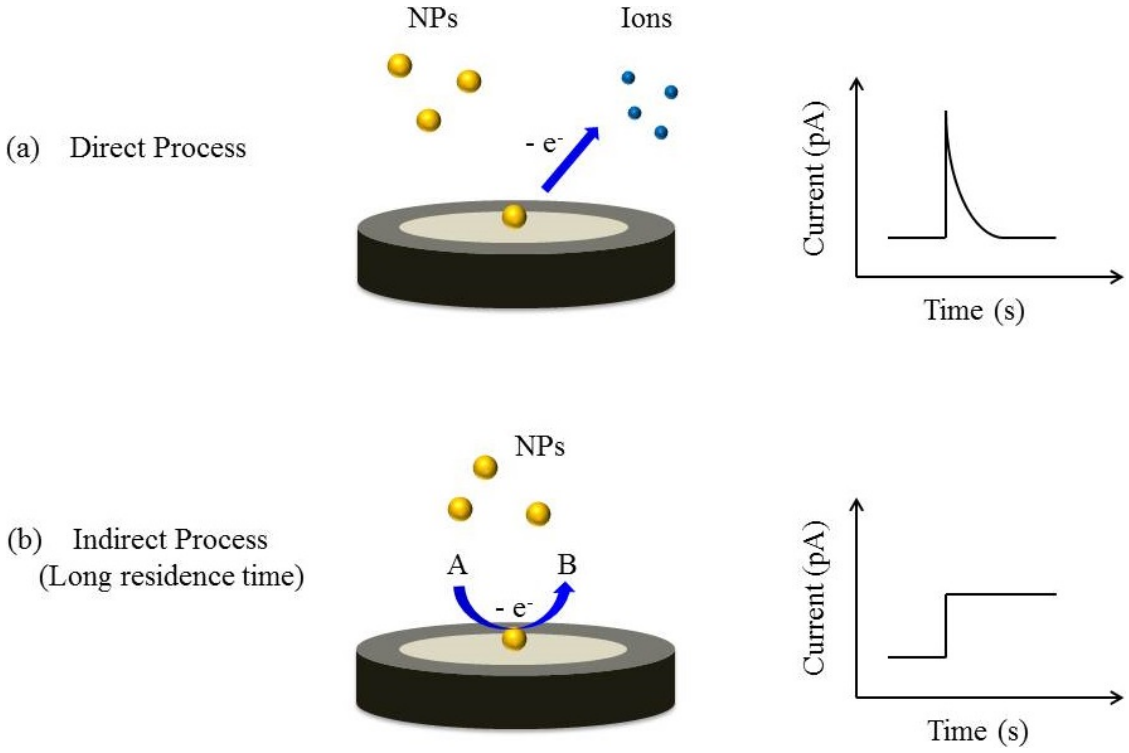

Figure 2.1: The two major scenarios of nanoimpacts: (a) direct process, and (b) indirect process with a long residence time of particles on the electrode. The current-time transient generated by each mechanism is present adjacent to the schematic diagram.

rent spikes are obtained due to the consumption of impacting materials through the measurement.[24–31] In contrast for *indirect* processes, redox reactions of solution phase species are mediated by the nanoparticles.[15, 32–36] As catalytically active particles stochastically collide with an inert electrode, transient currents are observed often due to the catalytic activity of the nanoparticles. A current step is obtained if the residence time of particles on the electrode is long enough. Note that in the former case nanoparticles are consumed or destroyed after impacts, while in the latter they remain unchanged as the electrochemical reaction only takes place on the surface of the particles. Examples and applications of each impact process are introduced separately below.

Note that the electrode adopted in nano-impact experiments is usually of size in microns in order to reduce the particle collision frequency and the background noise. In this way, individual impact events can be resolved.

Direct Process

Direct detection *via* impacts has many significant applications. First, it can be used to identify the nanoparticles.[37] According to the onset potential at which the impact signals arise, the type of particles involved can be confirmed. Stuart and co-workers reported the characterization of Ag and Ni nanoparticles *via* nano-impact experiments. The onset potentials of Ag oxidation appeared at 0.45 V vs Ag/AgCl (saturated KCl), whereas Ni oxidation only occurred at potentials beyond 1.55 V. Since these potentials matched the oxidation potentials of nanoparticles in voltammagrams, their chemical compositions could be inferred.

Second, the size of the nanoparticles can be quantified by integrating the area underneath each current transients. This corresponds to the charge transferred per single particle. Applying Faraday's law of electrolysis, shown in Equation 1.21 (Chapter 1), the amount of materials can be realized and converted to the radius of an individual par-

ticle if the latter is assumed to be spherical. Oxidative impacts have been extensively applied to a range of metal particles, such as Ag,[38] Au,[29] Ni[37] and Cu[39] for their size determination. The dimension of metal oxide particles, such as Fe_3O_4,[40] can be obtained from both anodic and cathodic particle coulometries. Most recently, electrochemical sizing has been developed for organic particles, such as indigo dye,[41] oil blue dye[25] and vitamin C encapsulated liposomes.[26] Typically, the sizes of various particles derived from nanoimpacts correlate with measurements from electron microscopy, and/or light scattering spectroscopy techniques such as nanoparticle tracking analysis (NTA) or dynamic light scattering (DLS).

In addition, the stability of particles can be revealed by monitoring their size variation over time. This is further discussed in Section 3.3 (Chapter 3).[42] Ellison and colleagues determined the size distribution of monomers, dimers, trimers, tetramers, pentamers and hexamers of Ag particles using nanoimpacts.[43] Lees *et al.* reported that the particle agglomeration/aggregation can be slowed down by adding a high concentration of trisodium citrate. The electrolyte was present as a capping agent due to its particle stabilising ability.[9]

Finally, nanoimpacts can determine the concentration of nanoparticles with the aid of the Shoup and Szabo equation, as shown in Equation 1.125 (Chapter 1). This is possible as the frequency of the spikes scales with the particle concentration in the suspension.[37]

Indirect Process

Indirect detection of impacts has been employed diversely. The frequency of the current transients again correlates to the particle concentration, whilst the amplitude of current steps provides information about the concentration of electroactive species. Most importantly, extra information such as the reaction kinetics and catalytic activities of the nanoparticles may also be apparent. This may lead to deeper insights into specific

structure-activity relationships.[44] Initial experiments were conducted by Xiao and Bard using a carbon electrode to study the reduction of proton on impacting Pt particles.[32] Many examples followed ranging from water oxidation mediated by IrO_x particles,[45] to hydrogen peroxide reduction catalyzed by Ag particles[46] and CeO_2[47] particles, and proton reduction on impacting Ni/NiO particles.[48]

Apart from the two main scenarios of nanoimpacts discussed above, an alternative non-destuctive approach named tag-redox process has also been proposed. This is further discussed in the following section.

Tag-Redox Process

Tag-redox coulometry (TRC) is employed where redox active molecules first adsorb on the surface of inert nanoparticles before any electrochemical reaction can take place. Upon impacts, the nanoparticles persist while the tag molecules undergo redox reactions. Figure 2.2 shows a schematic diagram of this process. The number of molecules attached to each nanoparticles can be determined from the transient charges. Assuming a self-assembled monolayer (SAM) is formed on the particle surface, the surface coverage and porosity of individual nanoparticles is revealed from the known molecular area of the tag. The radius of particles can thus be estimated if it is assumed spherical. In the work of Zhou *et al.*, Ag nanoparticles were tagged with 1,4-nitrothiophenol (NTP).[49, 50] The

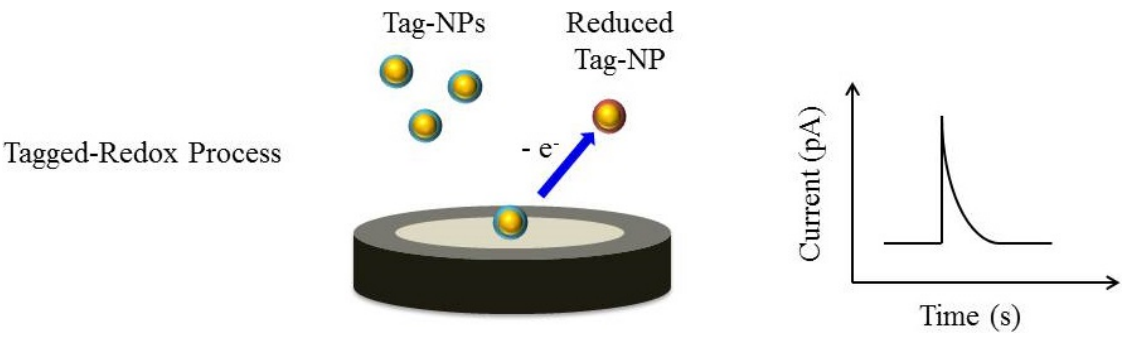

Figure 2.2: Tag-redox coulometry. The current-time transient generated by the mechanism is shown adjacent to the schematic diagram.

particle size obtained was consistent with those from direct oxidative impacts using bare Ag particles. Plowman *et al.* further applied this technique to Au nanorods.[51] The surface area of these nanorods were derived and their dimension inferred and found to be in agreement with non-electrochemical microscopic measurements. More recently, there is an increasing interest in applying this method to biological systems. Sepunaru *et al.* reported the detection of Escherichia coli bacteria[52] and influenza viruses[53] tagged with Ag particles. The frequency of the current spikes and their magnitude are linearly proportional to the concentration of the bacteria or virus and to the surface coverage of the nanoparticles, respectively.

The current transients discussed so far are all Faradaic impacts. Alternatively, non-Faradaic (capacitative) impacts can also be observed. This is further elaborated in the next section.

Capacitative Impacts

Capacitative impacts arise from the displacement of charge from the electrode/solution interface (double layer), resulting either an uncharged or charged particle during impact.[14] In order to maintain the electrical neutrality, electrons leave or enter the electrode in response to the alterations in the ionic charge distribution at the interface. Oxidative or reductive current spikes are observed if the applied potential is positive or negative to the potential of zero charge (PZC), respectively. No spikes are shown if the potential equals the PZC. Figure 2.3 shows a schematic diagram of possible mechanisms. In the first case, the double layer is disturbed and reforms upon impact of a particle with the electrode surface, generating an uncharged particle. Whereas in the second case, the impacting particle is charged as it collides with and leaves the electrode surface. Note that in neither situation electron transfer occurs *across* the interface. Scholz and co-workers used capacitive signals for the detection of liposomes[54, 55] and montmorillonite particles[56]

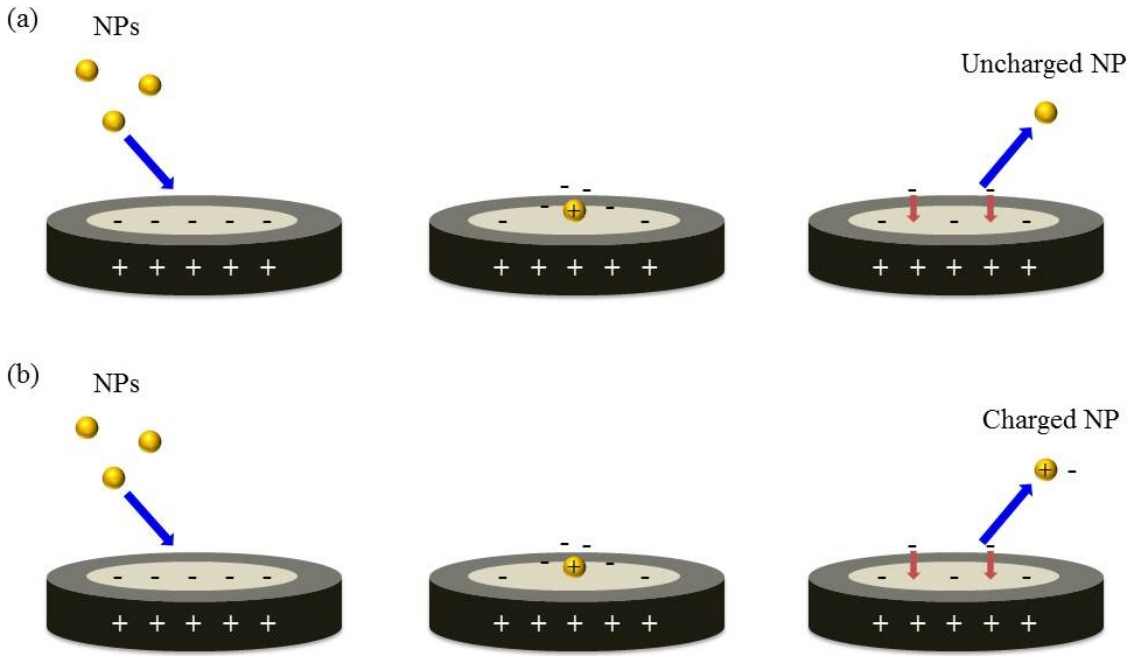

Figure 2.3: Two types of capacitative impacts. The electrode double layer is perturbed and restored by an impacting particle. Either (a) an uncharged or (b) a charged particle is formed after the collision.

at a mercury electrode. Similar experiments were carried out by Banks *et al.* to study liquid alkane droplets[57] and solid particles such as C, Al and Cu powders,[58] where capacitative impacts are obtained under sonication. Note that the charge passed per transient correlated to the size and conductivity of impacting particles, as well as to the applied potential.

In the next chapter, non-electrochemical characterization techniques for nanoparticles are summarized.

Bibliography

[1] Kim, T.; Hyeon, T. *Nanotechnology* **2014**, *25*, 012001.

[2] Bandaru, P.; Yamada, H.; Narayanan, R.; Hoefer, M. *Materials Science & Engineering, R: Reports* **2015**, *96*, 1–69.

[3] Raimondi, F.; Scherer, G. G.; Kötz, R.; Wokaun, A. *Angewandte Chemie, International Edition* **2005**, *44*, 2190–2209.

[4] Tong, R.; Hemmati, H. D.; Langer, R.; Kohane, D. S. *Journal of the American Chemical Society* **2012**, *134*, 8848–8855.

[5] Vert, M.; Doi, Y.; Hellwich, K.-H.; Hess, M.; Hodge, P.; Kubisa, P.; Rinaudo, M.; Schué, F. *Pure and Applied Chemistry* **2012**, *84*, 377–410.

[6] Rao, C. N. R.; Kulkarni, G. U.; Thomas, P. J.; Edwards, P. P. *Chemical Society Reviews* **2000**, *29*, 27–35.

[7] Li, J.; Zhu, J.-J. *Analyst* **2013**, *138*, 2506–2515.

[8] Nützenadel, C.; Züttel, A.; Chartouni, D.; Schmid, G.; Schlapbach, L. *European Physical Journal D* **2000**, *8*, 245–250.

[9] Lees, J. C.; Ellison, J.; Batchelor-McAuley, C.; Tschulik, K.; Damm, C.; Omanović, D.; Compton, R. G. *ChemPhysChem* **2013**, *14*, 3895–3897.

[10] Murray, R. W. *Chemical Reviews* **2008**, *108*, 2688–2720.

[11] Strmcnik, D.; Uchimura, M.; Wang, C.; Subbaraman, R.; Danilovic, N.; van der Vliet, D.; Paulikas, A. P.; Stamenkovic, V. R.; volume, N. M. M. N. C. *Nature Chemistry* **2013**, *5*, 300–306.

[12] Conway, B.; Tilak, B. *Electrochimica Acta* **2002**, *47*, 3571–3594.

[13] Shao, M., Ed. *Electrocatalysis in Fuel Cells: A Non- and Low- Platinum Approach*; Springer-Verlag London, 2013.

[14] Sokolov, S. V.; Eloul, S.; Kätelhön, E.; Batchelor-McAuley, C.; Compton, R. G. *Physical Chemistry Chemical Physics* **2017**, *19*, 28–43.

[15] Bard, A. J.; Zhou, H.; Kwon, S. J. *Israel Journal of Chemistry* **2010**, *50*, 267–276.

[16] Rees, N. V. *Electrochemistry Communications* **2014**, *43*, 83–86.

[17] Pumera, M. *ACS Nano* **2014**, *8*, 7555–7558.

[18] Cheng, W.; Compton, R. G. *TrAC, Trends in Analytical Chemistry* **2014**, *58*, 79–89.

[19] Heyrovský, M.; Jirkovsky, J. *Langmuir* **1995**, *11*, 4288–4292.

[20] Heyrovský, M.; Jirkovsky, J.; Mueller, B. R. *Langmuir* **1995**, *11*, 4293–4299.

[21] Heyrovský, M.; Jirkovsky, J.; Struplova-Bartackova, M. *Langmuir* **1995**, *11*, 4300–4308.

[22] Heyrovský, M.; Jirkovsky, J.; Struplova-Bartackova, M. *Langmuir* **1995**, *11*, 4309–4312.

[23] Korshunov, A.; Heyrovský, M. *Electroanalysis* **2006**, *18*, 423–426.

[24] Toh, H. S.; Jurkschat, K.; Compton, R. G. *Chemistry – A European Journal* **2015**, *21*, 2998–3004.

[25] Zhou, X.-F.; Cheng, W.; Compton, R. G. *Nanoscale* **2014**, *6*, 6873–6878.

[26] Cheng, W.; Compton, R. G. *Angewandte Chemie, International Edition* **2014**, *53*, 13928–13930.

[27] Zhou, X.-F.; Cheng, W.; Compton, R. G. *Angewandte Chemie, International Edition* **2014**, *53*, 12587–12589.

[28] Cheng, W.; Zhou, X.-F.; Compton, R. G. *Angewandte Chemie, International Edition* **2013**, *52*, 12980–12982.

[29] Zhou, Y.-G.; Rees, N. V.; Pillay, J.; Tshikhudo, R.; Vilakazi, S.; Compton, R. G. *Chemical Communications* **2012**, *48*, 224–226.

[30] Zhou, Y.-G.; Rees, N. V.; Compton, R. G. *Angewandte Chemie, International Edition* **2011**, *123*, 4305–4307.

[31] Stuart, E. J. E.; Tschulik, K.; Batchelor-McAuley, C.; Compton, R. G. *ACS Nano* **2014**, *8*, 7648–7654.

[32] Xiao, X.; Bard, A. J. *Journal of the American Chemical Society* **2007**, *129*, 9610–9612.

[33] Kahk, J. M.; Rees, N. V.; Pillay, J.; Tshikhudo, R.; Vilakazi, S.; Compton, R. G. *Nano Today* **2012**, *7*, 174–179.

[34] Guo, Z.; Percival, S. J.; Zhang, B. *Journal of the American Chemical Society* **2014**, *136*, 8879–8882.

[35] Ly, L. S. Y.; Batchelor-McAuley, C.; Tschulik, K.; Kätelhön, E.; Compton, R. G. *Journal of Physical Chemistry C* **2014**, *118*, 17756–17763.

[36] Jung, A. R.; Lee, S.; Joo, J. W.; Shin, C.; Bae, H.; Moon, S. G.; Kwon, S. J. *Journal of the American Chemical Society* **2015**, *137*, 1762–1765.

[37] Stuart, E. J. E.; Zhou, Y.-G.; Rees, N. V.; Compton, R. G. *RSC Advances* **2012**, *2*, 6879–6884.

[38] Zhou, Y.-G.; Rees, N. V.; Compton, R. G. *Angewandte Chemie, International Edition* **2011**, *50*, 4219–4221.

[39] Haddou, B.; Rees, N. V.; Compton, R. G. *Physical Chemistry Chemical Physics* **2012**, *14*, 13612–13617.

[40] Tschulik, K.; Haddou, B.; Omanović, D.; Rees, N. V.; Compton, R. G. *Nano Research* **2013**, *6*, 836–841.

[41] Cheng, W.; Zhou, X.-F.; Compton, R. G. *Angewandte Chemie, International Edition* **2013**, *125*, 13218–13220.

[42] Rees, N. V.; Zhou, Y.-G.; Compton, R. G. *ChemPhysChem* **2011**, *12*, 1645–1647.

[43] Ellison, J.; Tschulik, K.; Stuart, E. J. E.; Jurkschat, K.; Omanović, D.; Uhlemann, M.; Crossley, A.; Compton, R. G. *ChemistryOpen* **2013**, *2*, 69–75.

[44] Wustholz, K. L.; Henry, A.-I.; McMahon, J. M.; Freeman, R. G.; Valley, N.; Piotti, M. E.; Natan, M. J.; Schatz, G. C.; Van Duyne, R. P. *Journal of the American Chemical Society* **2010**, *132*, 10903–10910.

[45] Kwon, S. J.; Fan, F.-R. F.; Bard, A. J. *Journal of the American Chemical Society* **2010**, *132*, 13165–13167.

[46] Stuart, E. J.; Rees, N. V.; Compton, R. G. *Chemical Physics Letters* **2012**, *531*, 94–97.

[47] Sardesai, N. P.; Andreescu, D.; Andreescu, S. *Journal of the American Chemical Society* **2013**, *135*, 16770–16773.

[48] Zhou, Y.-G.; Rees, N. V.; Compton, R. G. *Physical Chemistry Chemical Physics* **2013**, *15*, 761–763.

[49] Zhou, Y.-G.; Rees, N. V.; Compton, R. G. *Chemical Communications* **2012**, *48*, 2510–2512.

[50] Rees, N. V.; Zhou, Y.-G.; Compton, R. G. *Chemical Physics Letters* **2012**, *525-526*, 69–71.

[51] Plowman, B. J.; Young, N. P.; Batchelor-McAuley, C.; Compton, R. G. *Angewandte Chemie, International Edition* **2016**, *55*, 7002–7005.

[52] Sepunaru, L.; Tschulik, K.; Batchelor-McAuley, C.; Gavish, R.; Compton, R. G. *Biomaterials Science* **2015**, *3*, 816–820.

[53] Sepunaru, L.; Plowman, B. J.; Sokolov, S. V.; Young, N. P.; Compton, R. G. *Chemical Science* **2016**, *7*, 3892–3899.

[54] Hellberg, D.; Scholz, F.; Schauer, F.; Weitschies, W. *Electrochemistry Communications* **2002**, *4*, 305–309.

[55] Hellberg, D.; Scholz, F.; Schubert, F.; Lovrić, M.; Omanović, D.; Hernández, V. A.; Thede, R. *Journal of Physical Chemistry B* **2005**, *109*, 14715–14726.

[56] Scholz, F.; Hellberg, D.; Harnisch, F.; Hummel, A.; Hasse, U. *Electrochemistry Communications* **2004**, *6*, 929–933.

[57] Banks, C. E.; Rees, N. V.; Compton, R. G. *Journal of Physical Chemistry B* **2002**, *106*, 5810–5813.

[58] Rees, N. V.; Banks, C. E.; Compton, R. G. *Journal of Physical Chemistry B* **2004**, *108*, 18391–18394.

Chapter 3

Characterization Methods

In this chapter, characterization methods for nanoparticles applied in this thesis are introduced namely transmission electron microscopy (TEM), ultraviolet-visible spectroscopy (UV–vis) and X-ray photoelectron spectroscopy (XPS). The full experimental information for each particular projects is described in the individual chapters.

3.1 Transmission Electron Microscopy (TEM)

Information about the size, morphology and interfacial structure of nanoparticles are essential to the work reported in this thesis as these properties have an effect on their catalytic activities (see Chapters 4–8). Transmission electron microscopy (TEM) is employed here for this purpose.

Figure 3.1 is a general layout of a TEM microscope. Unlike a conventional optical microscope, TEM uses a beam of electrons that is transmitted through the specimen to generate a image.[1] High energy electrons are first emitted from an electron gun at the top of the TEM and travelled through vacuum in the column of the microscope. They are then accelerated by an anode and focused by the use of condenser lens. A thin, coherent beam is generated and high-angle electrons are filtered by the condenser aperture. The resulting beam continues in the column until it interacts with an ultrathin specimen.[2] Only some of the electrons pass through the sample depending upon its thickness and composition. After that, objective lens are employed to focus the transmitted electrons into an image.

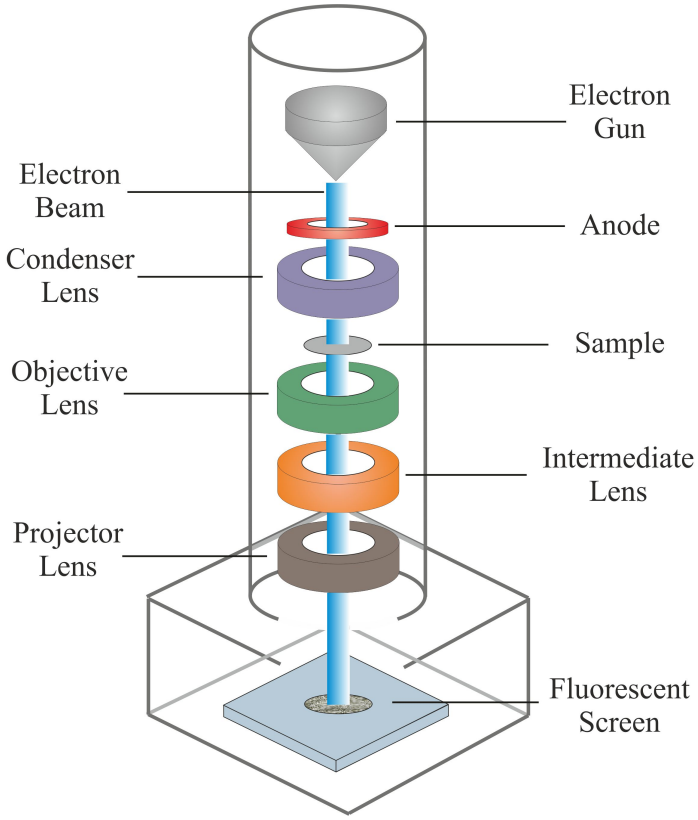

Figure 3.1: Schematic plot describing the main components of a TEM microscope.

The formed image is amplified by intermediate and projector lens, and finally projected on a fluorescent screen for the user to see. Note, uneven brightness is observed at various points of the image, since according to the density of the sample, different amounts of electrons are transmitted. Traditional bright field TEM shows a "shadow image" of the specimen. The more electrons transmitted, the brighter the image is seen, and *vice versa*. Details of the sample preparation of TEM are specified in Experimental Section in Chapters 4–8.

As the wavelength of the electrons is much smaller than that of light, the TEM provides much better (several orders of magnitude) resolution than the optical microscope. A high resolution TEM magnifies sample images with atomic resolution. In the present work, a suspension on a carbon grid is often used. Another prominent advantage of TEM is that it allows samples to be "visualized". However, several limitations need to be considered. First, TEM is very costly to build and maintain. Second, isolated rooms are

necessary since the electron microscopes are extremely sensitive to external vibrations and electromagnetic fields. Third, the specimen must be electron transparent and able to tolerate the vacuum environment.[1, 3, 4] It is therefore impossible to realize hydrated or live samples. Finally, the electron radiation is likely to destroy the particles.[5] Hence, to reduce the damage alternative ways are often adopted to prepare TEM samples. For example, the particles can be cooled with the liquid nitrogen, or pre-treated using an electrochemical procedure.[6, 7]

The TEM results presented in this thesis were carried out with a JEOL JEM-3000F FEGTEM (300 kV accelerating voltage) or a JEOL JEM-2100 (200 kV accelerating voltage) microscope. Dr. Neil P. Young (Department of Materials, University of Oxford) carried out the TEM analysis of the platinum nanoparticles (PtNPs) presented in Chapters 4–8.

3.2 X-Ray Photoelectron Spectroscopy (XPS)

TEM reveals information about the physical structure and surface morphology of nanoparticles. However, it is also important to analyze the elemental composition and/or the oxidation state of a material's surface (see Chapter 5).[8] X-ray photoelectron spectroscopy (XPS), which is also referred to as electron spectroscopy for chemical analysis (ESCA), is one of the standard techniques used for this.

Figure 3.2 shows a picture of a XPS spectrometer. Measurements are carried out under ultra-high vacuum conditions to avoid scattering of the electrons by gases. First a monochromatic X-ray is incident on a solid sample. Core level electrons are excited and emitted from the very top surface (1–10 nm) of the sample, as present in Figure 3.3. The ejected electrons are then collected by an electron collection lens and analyzed simultaneously by an electron energy analyzer and an electron detector. The kinetic energy (KE) of these escaped electrons depends on two factors: the photon energy (hf)

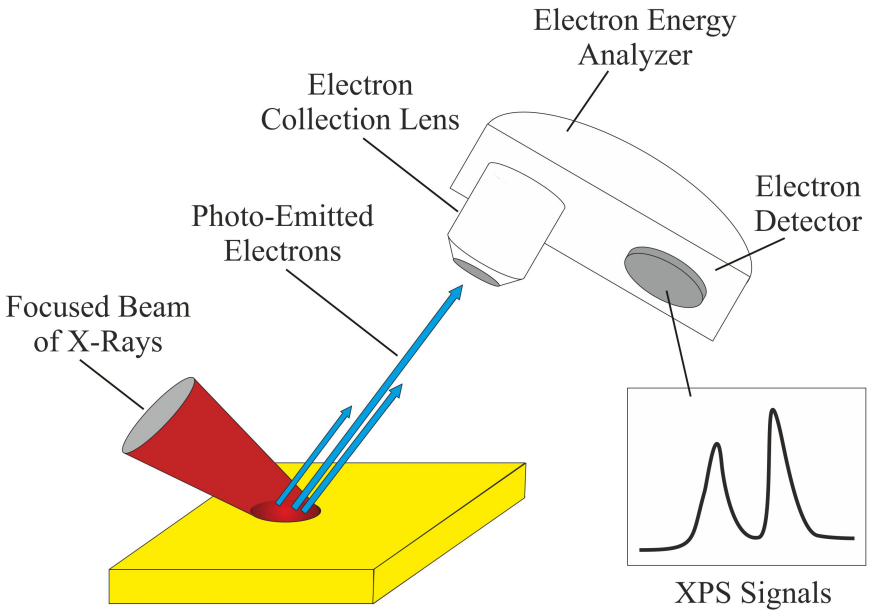

Figure 3.2: Schematic diagram of the major components of a X-ray photoelectron spectrometer.

and the binding energy (BE) of the electrons. The latter is the amount of energy required to remove an electron from the surface. According to the *Planck–Einstein relation*, the energy of a photon of all types of electromagnet radiation is given by:

$$E = hf \tag{3.1}$$

where h is the Planck constant (6.62×10^{-34} J s), and f is the frequency (Hz) of the radiation. Hence by the conservation of energy, this photonemission process can be described using an equation:

$$\mathrm{KE} = hf - (\mathrm{BE} + \Phi) \tag{3.2}$$

where Φ is the work function that is the energy required for the electron to release itself from the surface. The binding energy is influenced by a few parameters, such as the identity of the element and the orbital from which the electron is ejected. In particular, it can be affected by the oxidation state or the chemical environment of the atom, which is observed as a chemical shift in the spectrum. For a given core level, the binding energy

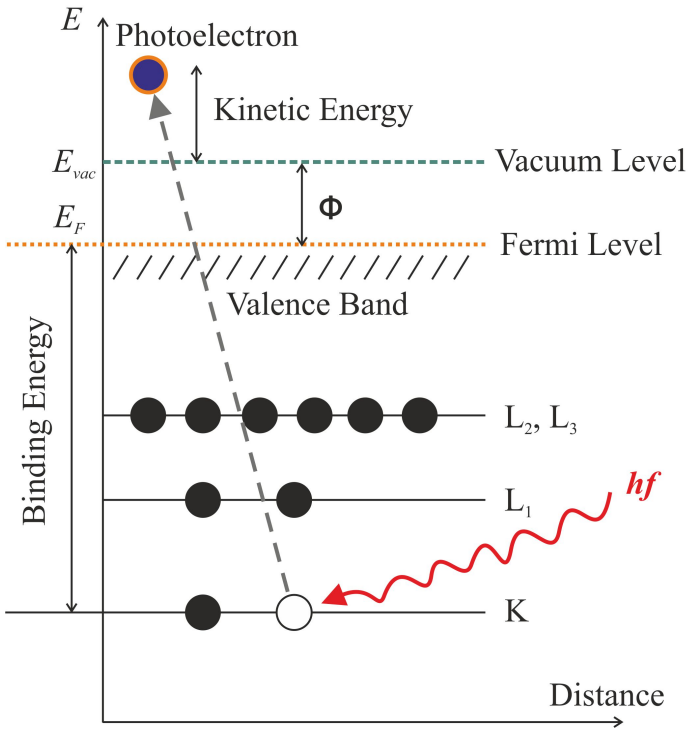

Figure 3.3: Energy level diagram of a metal showing electrons being photoemitted from a core level to a state above the vacuum level with a finite kinetic energy.

is constant. Thus by varying the photon energy, the kinetic energy of the photoelectron can be changed. Finally, a XPS spectrum is acquired by plotting the number of electrons measured (electron counts) against the binding energy of electrons detected. Peak splitting is also inspected for some elements to generate a multiplet with a different intensity ratio. This splitting is understood as a result of the spin-orbit interaction of the electrons in the atom, often approximated by one of the models of Russell-Saunders (LS) or j-j coupling. The relative intensities of the two signals indicate the degeneracies of the two final states, the probability to transition to a specific state. For each element, a characteristic set of spectral peaks forms at different binding energies corresponding to its electron configuration, and which gives a direct indication of its identity. The number of electrons within each XPS signals quantifies the amount of element in the sample.[9] Therefore the chemical composition of the material is achieved.

To summarize, XPS provides an accurate, sensitive and non-destructive method of

surface analysis. However, several restrictions arise. First, it is an expensive technique. Second, potential sample damage may be caused by the radiation. Third, a high vacuum environment is necessary, where liquid/volatile materials must be dried before any measurements taken. Fourth, hydrogen is hard to detect and finally, the data collection and analysis of XPS is slow (0.5 to 8 hours per sample).

The XPS data shown in Chapter 5 were conducted using a Thermo Scientific^{TM} K-Alpha^{TM} X-Ray Photoelectron Spectrometer. Dr. Robert G. Palgrave (Department of Chemistry, University College London) conducted the XPS of the platinum oxides described in Chapter 5.

3.3 Ultraviolet-Visible (UV–Vis) Spectroscopy

Ultraviolet-visible (UV–vis) spectroscopy is absorption spectroscopy in the visible (400–800 nm) and the ultraviolet (190–400 nm) spectral regions. In most cases, a deuterium lamp is employed to cover the 170–375 nm interval and a tungsten/halogen filament lamp for the 350–2500 nm range. Optical properties of materials can be determined as most molecules absorb light within these wavelength. In particular, UV–vis spectroscopy measures the concentrations of transition metal ions and conjugated organic compounds in their solution phase.

Figure 3.4 shows the fundamental structure of a single beam UV–vis spectrophotometer. A monochromator (typically a diffraction grating) is employed to restrict the light source into a specific wavelength beam. As shown in the diagram, a white light is first projected onto a prism before being dispersed into a spectrum. It is then filtered by an exit slit to form a monochomatic light. The homochromic beam is absorbed when transmitted through an optically transparent cuvette, in which a liquid sample is held. Finally, the intensity of the resulting light is measured and analyzed by a detector.

For atoms or molecules, the absorption of UV–vis radiation is correlated to the exci-

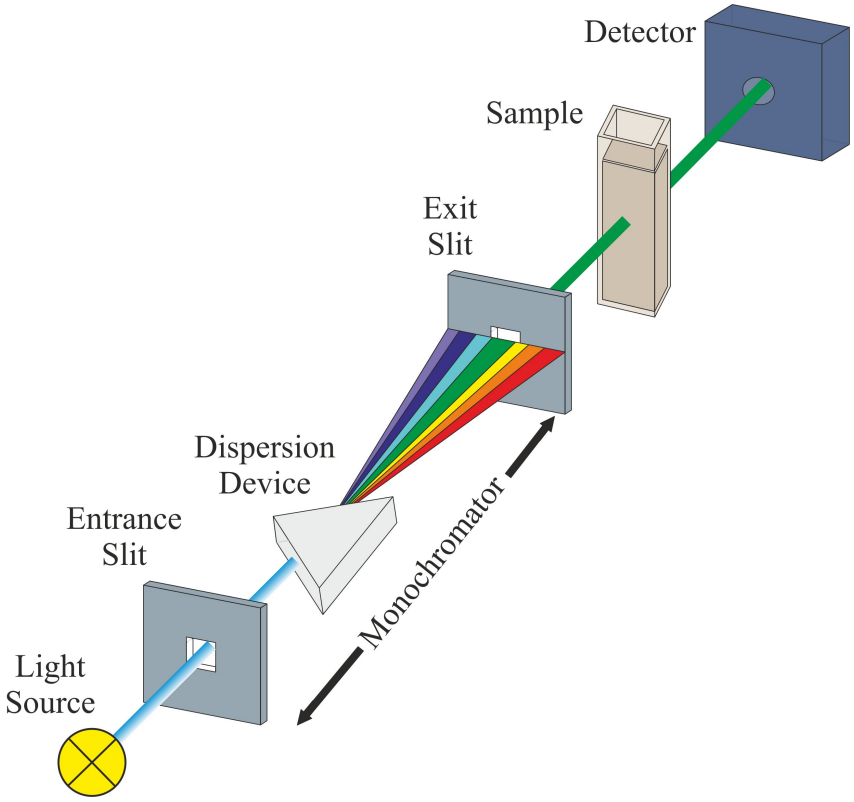

Figure 3.4: Schematic graph showing the major components of a UV–vis spectrophotometer.

tation of electrons from lower (HOMO) to higher (LUMO) energy levels. As their energy orbitals are discrete, only the light with the correct energy will trigger the electronic transitions and therefore be absorbed, as shown in Figure 3.5. In each possible situation, an electron is promoted from a full bonding or non-bonding orbital (ground state) to an empty anti-bonding orbital (excited state), following absorption of light. According to the Planck–Einstein relation (Equation 3.1), the energy required to excite the electron to different levels depends on the frequency of the beam. Since the wavelength λ (m) of radiation is inversely proportional to its frequency (f):

$$\lambda = \frac{\boldsymbol{c}}{f} \tag{3.3}$$

where $\boldsymbol{c}$ is the speed of light (m s^{-1}), radiation of higher frequency (thus shorter wavelength) will allow the transmissions between a larger gap or to a higher energy level.

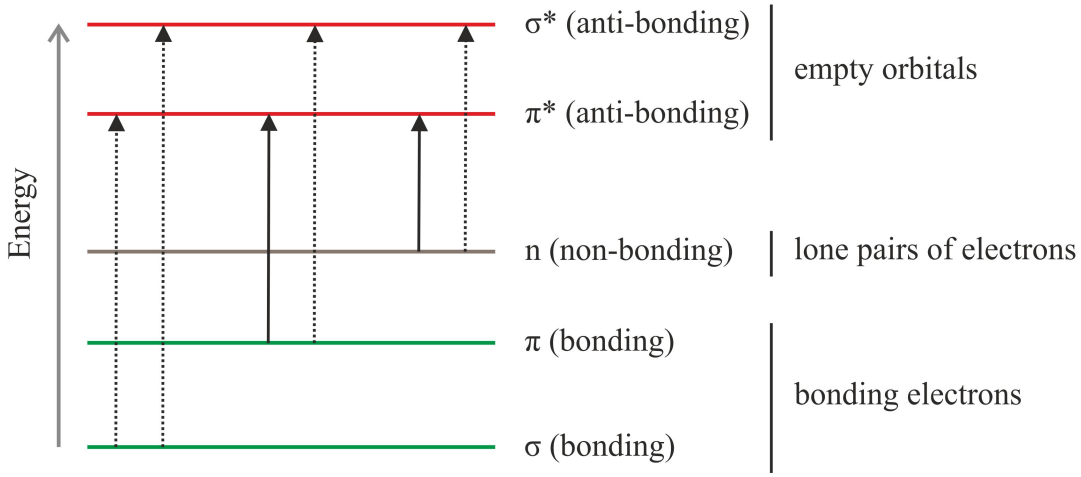

Figure 3.5: Graphic plot of all possible electron excitation in an atom or molecule following absorption of light. The black arrows indicate the possible electron promotions *via* UV–vis radiation ($\pi \rightarrow \pi^*$, $n \rightarrow \pi^*$). The dotted arrows depict energy jumps outside the spectrum range and therefore can not be detected. Relative energies are illustrated for each orbital of the matter.

The *Beer–Lambert law* can be applied to quantitatively detect the absorbance $\boldsymbol{A}$ of the nanoparticle suspension by measuring its transmittance, which equals to the ratio of the intensities of the incident light before, $\boldsymbol{I_0}$ (W m^{-2}), and after, $\boldsymbol{I}$ (W m^{-2}), it passes through the sample. This is, in turn, directly proportional to the concentration c (mol m^{-3}) of the absorbing species and the path length L (m) of the beam through the solution:[10]

$$\boldsymbol{A} = \log_{10}\left(\frac{\boldsymbol{I_0}}{\boldsymbol{I}}\right) = \varepsilon c L \tag{3.4}$$

where ε is the extinction coefficient (m^2 mol^{-1}) of the species. Thus by detecting the absorbance, with a fixed path length and a known extinction coefficient, the concentration of the solution phase absorber can be obtained. An absorbance spectrum can be achieved by plotting absorbance against wavelength. By mapping the acquired absorbance spectrum to literature data, the functional groups or identity of a compound is realized. Furthermore, the kinetics or mechanism of a reaction can often be studied by monitoring the absorbance of a reactant, intermediate or product over time.

In this thesis (Chapters 6–8), UV–vis spectroscopy is employed to investigate the ag-

glomeration state of PtNPs, where a localized surface plasmon resonance (LSPR) of the metal particles is produced and analyzed. The surface plasmon signal is caused by the resonance of the collective oscillation of electrons in its conduction band with a given wavelength of an incident light.[11] The LSPR of PtNPs exhibits a strong absorbance band in the visible region (200–300 nm) which can be detected by the UV–vis, although it may be influenced by the solution media and capping agents.[12] As the nanoparticle agglomerates, the surface plasmon peak broadens and red-shifts to higher wavelengths, and its intensity decreases. UV–vis can provide information of the stability of the nanoparticles by monitoring their absorbance over time.

In general, UV–vis reflects the characteristics of sample according to the amount of light absorbed by the liquid sample. It is notable for its quick analysis and easy to use. However, limitations such as deviation from the Beer–Lambert law gives a non-linear relationship between the absorption and concentration. The accuracy and sensitivity of measurements also depend on several factors, for example the linearity of the light beam and the noise level of the electronic circuit.

The UV–vis experiments described in Chapters 6–8 were performed with a Shimadzu UV-1800 UV–vis spectrophotometer.

In the following chapters, one or a combination of the techniques are used to fully characterise the nanoparticles. Details are provided in Experimental Section in each chapter.

Bibliography

[1] Williams, D.; Carter, C. *Transmission Electron Microscopy: A Textbook for Materials Science*, 2nd ed.; Springer US, 2009.

[2] Flegler, S.; Heckman, J.; Klomparens, K. *Scanning and Transmission Electron Microscopy: An Introduction*; Oxford University Press, 1993.

[3] Orloff, J., Ed. *Handbook of Charged Particle Optics, Second Edition*, 2nd ed.; CRC Press, 2017.

[4] Reimer, L.; Kohl, H. *Transmission Electron Microscopy: Physics of Image Formation*, 5th ed.; Springer-Verlag New York, 2008.

[5] Egerton, R.; Li, P.; Malac, M. *Micron* **2004**, *35*, 399–409, International Wuhan Symposium on Advanced Electron Microscopy.

[6] Egerton, R. *Ultramicroscopy* **1980**, *5*, 521–523.

[7] Mayrhofer, K. J.; Ashton, S. J.; Meier, J. C.; Wiberg, G. K.; Hanzlik, M.; Arenz, M. *Journal of Power Sources* **2008**, *185*, 734–739.

[8] van der Heide, P. *X-Ray Photoelectron Spectroscopy: An introduction to Principles and Practices*; John Wiley & Sons, 2011.

[9] Hüfner, S. *Photoelectron Spectroscopy: Principles and Applications*; Springer Series in Solid-State Sciences 82; Springer-Verlag Berlin Heidelberg, 2003.

[10] Clark, B., Frost, T., Russell, M., Eds. *UV Spectroscopy: Techniques, instrumentation and data handling*; Springer Netherlands, 1993.

[11] Kumar, C., Ed. *UV-VIS and Photoluminescence Spectroscopy for Nanomaterials Characterization*; Springer-Verlag Berlin Heidelberg, 2013.

[12] Creighton, J. A.; Eadon, D. G. *Journal of the Chemical Society, Faraday Transactions* **1991**, *87*, 3881–3891.

Chapter 4

Exploring Nanoparticle Porosity Using Nanoimpacts: Platinum Nanoparticle Aggregates

In this chapter, the porosity of platinum nanoparticles (PtNPs) is explored for the first time using tag-redox coulometry (TRC). This is achieved by monitoring the reduction of the 4-nitrothiophenol (NTP)-tagged PtNPs on carbon electrodes *via* both immobilisation and nanoimpacts. The average charge per impact is measured and attributed to the nitro group reduction of the NTP molecules adsorbed on individual PtNPs. The number of NTP molecules and thus the "active surface area" of the PtNPs is calculated and compared with two models: fully solid and mesoporous nanoparticles. The extent of the particle porosity is revealed. This allows a fuller understanding of the (electro-)catalytic behavior of nanoparticles by providing insight into their porosity and "true/active surface areas".

The work herein presented has been published in *Physical Chemistry Chemical Physics*[1] and was carried out in collaboration with Dr. Stanislav V. Sokolov, Dr. Eden E. L. Tanner and Dr. Neil P. Young (Department of Materials, University of Oxford). Dr. Eden E. L. Tanner helped with the interpretation of the experimental results. Dr. Stanislav V. Sokolov and Dr. Neil P. Young performed the transmission electron microscopy (TEM) for the mesoporous PtNPs.

4.1 Introduction

Nanoparticles find ever increasingly diverse applications embracing the catalysis of chemical and biochemical reactions, the electrocatalysis of electrode reactions, especially those important for energy transformation processes and environmental remediation.[2–8] Key to many uses, both fundamental and applied, is the availability of very high surface areas, in relation to mass, in comparison with conventional materials. This can significantly promote the adsorption of molecular species which often lies at heart of the physical and chemical process of interest. Whilst this is encouraged by the intrinsic nanoscale of the particles it can be further enhanced if the nanoparticles themselves show significant nanoporosity. This can be realized synthetically by the aggregation during formation of ultra-small nanoparticles clumping together to form porous larger nanoparticles[9] or by the initial formation of alloys followed by a dealloying protocol which selectively removes one of the alloy components.[10] Nanoporosity has been suggested variously to lead to improved adsorption in environmental applications,[11–15] catalyzed oxygen reduction kinetics,[16–19] changed optical properties[20, 21] and enhanced pseudocapacitor performance.[22]

Many of the applications of porous nanoparticles involve their being exposed to a solution phase where they might form a coating on an electrode, adsorb environmental targets or catalyze a desired reaction. It is therefore of interest to develop experiments to probe the extent to which the internal surfaces of a porous nanoparticle "see" the surrounding solution phase, or to put the issue in a different form, to find the extent to which the internal surfaces of a porous nanoparticle or nanoparticle aggregate are accessible to solution phase species. Traditionally such nanoporosity has been accessed *via ex-situ* gas phase adsorption isotherm approaches, such as the Brunauer–Emmett–Teller (BET) method. However the qualitative contrast between gas/solid and liquid/solid interfaces coupled with the very small size of the molecules (such as nitrogen) used in gas

adsorption measurements makes the development of *in-situ* approaches desirable.

This work reports on the use of the nano-impact method to measure the surface coverage of redox active molecules adsorbed on the surface of platinum nanoparticles (PtNPs) (*ca.* 24.3 nm radius) which are themselves composed of aggregates of much smaller particles and for which transmission electron microscopy (TEM) reveals significant nanoporosity. In the nano-impact method[23–26] single nanoparticles suspended in solution from time to time impact on the surface of a microelectrode by virtue of their Brownian motion. If the electrode is held at a suitable potential the nanoparticle itself may be oxidized or reduced[27, 28] or, in the case of the experiments reported below, surface layers of absorbate on the particles may be electrolyzed. Measurement of the charge then, in the latter case, shows the extent of the surface coverage which, when compared with TEM data, allows an assessment of the particle porosity and the scale to which the internal surfaces of the porous particles are accessible to the solution phase.

4.2 Experimental Section

4.2.1 Chemicals

4-nitrothiophenol (NTP) (80%, $O_2NC_6H_4SH$) (structure as shown in Figure 4.1), perchloric acid (70%, $HClO_4$) and sodium perchlorate monohydrate (98%, $NaClO_4 \cdot H_2O$) were

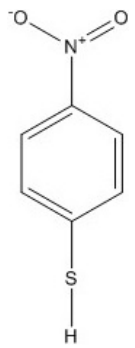

Figure 4.1: Structure of a NTP molecule.

obtained from Sigma-Aldrich, Dorset, U.K. Citrate-capped platinum nanoparticles (PtNPs) were provided by NanoComposix, San Diego, CA, U.S.A. with a reported diameter 50 nm and concentration of 3.3×10^{13} particles L^{-1}.[29] All solutions were prepared with ultrapure water from Millipore with a resistivity of not less than 18.2 MΩ cm at 298 K.

4.2.2 Characterization

Dr. Neil P. Young (Department of Materials, University of Oxford) conducted the transmission electron microscopy (TEM) analysis for the mesoporous PtNPs as described below.

TEM (JEOL JEM-3000F FEGTEM, 300 kV accelerating voltage) was performed to determine the size of PtNPs. Samples were prepared by depositing a drop of the stock PtNP sol (3.3×10^{13} particles L^{-1}) onto holey carbon grids (Agar Scientific, Stansted, U.K.), followed by drying in air prior to imaging. ImageJ software[30] (National Institutes of Health, U.S) was used to analyze the TEM images. The PtNPs used were found to be made up of an aggregation of smaller particles (around 2 nm radius from TEM), and typical images are shown in Figure 4.2 a and b. A total of 165 PtNP aggregates were sized and their radii calculated, as shown in Figure 4.2 c. A mean radius of 24.3 ± 1.6 nm was obtained, close to the value of 25 nm provided by the manufacturer.

To clarify, in this work, "PtNP" refers to the platinum nanoparticle aggregate (*ca.*

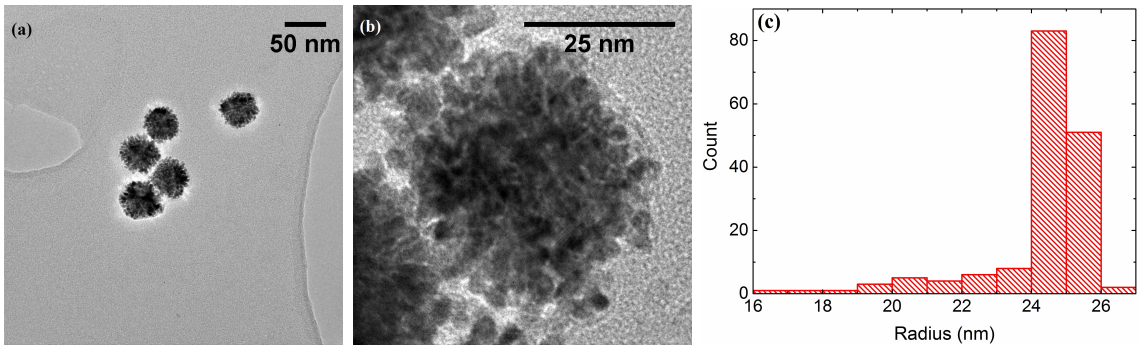

Figure 4.2: (a) TEM bright field image of PtNPs. (b) High-resolution TEM image of one PtNP. (c) Size distribution of the PtNPs with an average radius of 24.3 ± 1.6 nm.[31]

24.3 nm radius), and "small nanoparticle" is the component of a PtNP (*ca.* 2 nm radius).

4.2.3 Preparation of NTP-tagged PtNPs

PtNPs were tagged by NTP *via* mixing a PtNP sol (3.3×10^{13} particles L^{-1}, directly from the manufacturer) with 0.5 mM NTP aqueous solution with a volume ratio of 1:1 for 1 to 30 hr. The excess NTP molecules were removed by centrifuging and the tagged nanoparticles were washed three times with water.

4.2.4 Electrochemistry

A three electrode system in a Faraday cage was employed for all electrochemical experiments, with a μAutolab III (Metrohm Autolab B.V., Utrecht, The Netherlands) or an in-house potentiostat.[32] The working electrode was a glassy carbon (GC) macrodisk (3 mm diameter; BASi, West Lafayette, IN, U.S.A.) or a carbon fibre microdisc (33 μm diameter; BASi, West Lafayette, IN, U.S.A.) electrode. Both electrodes were polished with alumina powders (Buehler, Lake Bluff, IL, U.S.A.) in a size sequence: 1.0 μm, 0.3 μm and 0.05 μm. The reference electrode was a saturated calomel electrode (SCE) [Hg/Hg_2Cl_2, saturated KCl] (+0.241 V vs standard hydrogen electrode, SHE; BASi, West Lafayette, IN, U.S.A.) or a leakless silver/silver chloride electrode [Ag/AgCl, 1.0 M KCl] (+0.235 V vs SHE; Cypress Systems, Lawrence, KS, U.S.A.). The counter electrode was a graphite rod (6 mm diameter; Sigma-Aldrich, Dorset, U.K.) or a platinum foil (Goodfellow, Cambridge, U.K.). All experiments were conducted under a nitrogen atmosphere. All electrochemical measurements were thermostatted at 25 ± 0.5 °C.

In the experimental data reported in this chapter, potentials are quoted on the SCE or the Ag/AgCl (1.0 M KCl) scales.

Adsorption and Drop-Casting Experiments

The GC macroelectrode was modified first by adsorption of molecular NTP directly on the electrode surface, and second by drop casting NTP-tagged PtNPs onto the surface. For direct adsorption, the electrode was immersed in a NTP solution (0.5 mM) for 1 h, then rinsed with water and sonicated before experiments to remove the excess molecules from the electrode surface. For modification with previously modified PtNPs, a NTP-tagged PtNP sol (3 μL) was drop casted onto the electrode surface, which was subsequently allowed to dry under flowing nitrogen prior to experimentation.

Nano-Impact Experiments

Potentiostatic control and impact current measurement were achieved through an in-house built low noise potentiostat.[32] A NI USB-6003 data acquisition (DAQ) device (National Instruments, Austin, TX, U.S.A.) was connected to a computer interface *via* USB for analogue-digital conversion. Python 2.7 was employed to write a script to control the DAQ device, which was run through the IDE Canopy (Enthought, Austin, TX, U.S.A.). Currents were measured at the working electrode (running to ground) by a low-noise current amplifier LCA-4K-1G (FEMTO, Messtechnik GmbH, Germany), within a limited output bandwidth of two cascaded passive RC-filters (100 Hz). The DAQ device oversampled the outcoming signal and converted it from analogue to digital at a stream rate of 4 kHz. To allow potentiostatic control, a highly stabilized (1 kHz bandwidth) classic adder potentiostat[33] was used. Importantly, for the reference buffer a high quality operational amplifier, LMC6001 (Farnell, Leeds, U.K.) with an ultra-low-input bias (25 fA) was selected; and for potential control at the counter electrode a high quality low-noise operational amplifier, AD797 (Farnell, Leeds, U.K.) was adopted.

To note, in the context of nano-impact experiments the potentiostat conserves charge and therefore the integral of the current spikes is unaffected in their size analysis.[34]

4.3 Results and Discussion

The porosity of PtNPs was next established by tag-redox coulometry (TRC). This was achieved through the electrochemical analysis of nitro group reduction of 4-nitrothiophenol (NTP) molecules using both cyclic voltammetric and nano-impact techniques. First, a glassy carbon (GC) macroelectrode was modified either by immersion into an NTP solution or drop casting a NTP-tagged PtNP sol and recording cyclic voltammograms (CVs). Second, an overpotential was carefully selected from voltammetric measurements in order to sufficiently reduce the NTP-tagged nanoparticles. Applying the chosen potential to the TRC, reductive transients were observed. From this, the number of NTP molecules was calculated and compared with two theoretical models: a solid sphere, and a completely mesoporous nanoparticle formed by aggregation of a large number of smaller particles. This therefore allows an estimation of the PtNP porosities, which can be further confirmed by the TEM images (Figure 4.2 a and b).

4.3.1 Voltammetric and Nano-Impact Measurements

Initial experiments were conducted to explore the redox properties of molecular NTP adsorbed on both GC electrode and PtNP surfaces. First, a GC electrode was modified by NTP molecules (as shown in Section 4.2.4) before being transferred to an aqueous solution of 10.0 mM $HClO_4$ and 30.0 mM $NaClO_4$. CVs were recorded and a reductive peak was obtained at *ca.* -0.4 V (vs SCE), as shown in Figure 4.3 a. In the absence of NTP, no signal was observed (red line in Figure 4.3 a), indicating the peak was due to the presence of NTP. This response likely corresponds to a four-electron, four-proton reduction of the nitro group to the hydroxylamine (Figure 4.4). Evidence for this can be found in literature.[35–37]

Next, a GC electrode was modified with NTP-tagged PtNPs (see Section 4.2.4) and analogous experiments were performed. A reductive wave was observed at *ca.* -0.2 V (vs

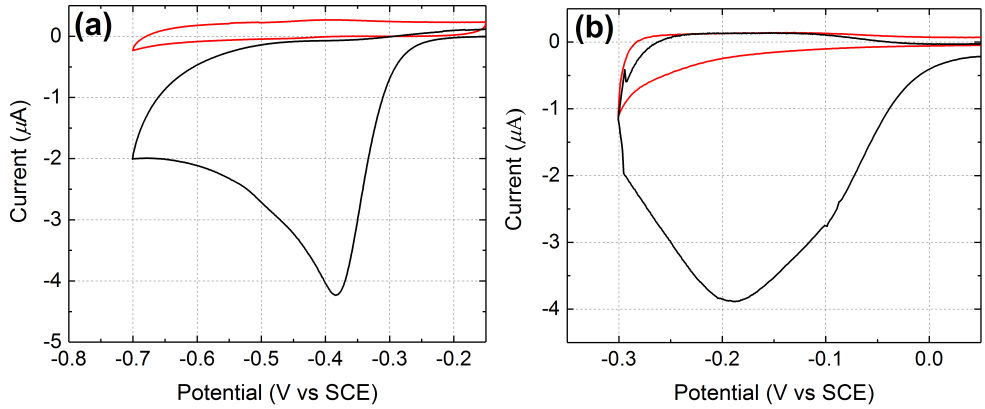

Figure 4.3: CVs for a GC macroelectrode with (black) or without (red) modification of (a) NTP and (b) NTP-tagged PtNPs. All scans were performed in a nitrogen saturated solution of 10.0 mM $HClO_4$ and 30.0 mM $NaClO_4$ at a scan rate of 25 mV s^{-1}.

SCE) and again attributed to the nitro group reduction, as shown in Figure 4.3 b.[38] No peak was seen when drop casting stock PtNPs (red line in Figure 4.3 b). The peak potentials of the nitro group reduction varied between GC to PtNP surfaces, representing the different environments influencing possibly both the thermodynamics and kinetics of the process. Therefore, based on the voltammetric response of NTP adsorbed on PtNPs, an applied potential of -0.25 V (vs SCE) was chosen for the nano-impact experiments such that measurements were recorded at sufficiently negative potentials in order to maximize the obtained reductive current by ensuring full reduction of the surface layers.

Finally, nano-impact measurements were conducted to investigate the reductive charge of nitro group per nanoparticle. Chronoamperograms (CAs) were recorded in an aqueous electrolyte of 10.0 mM $HClO_4$ and 30.0 mM $NaClO_4$ at -0.25 V (vs Ag/AgCl in 1.0 M

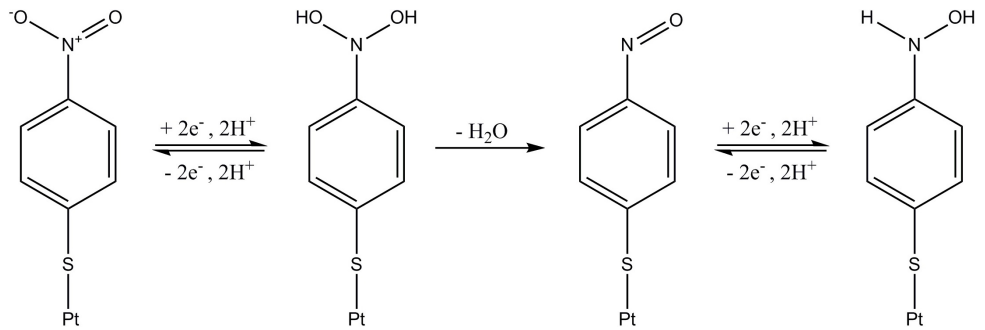

Figure 4.4: The likely four-electron reduction of adsorbed NTP.

KCl). This potential was carefully selected from the drop-casting experiment (Figure 4.3 b) and was sufficient for a complete reduction of the nitro group of the adsorbed NTP. In the experiments, 60 pM NTP-tagged PtNPs were added and spikes were clearly observed with an approximately millisecond duration, as shown in Figure 4.5 (black line). These are attributed to the reduction of the nitro group taking place when the NTP-tagged PtNPs make contact with the carbon fibre substrate. No impact spikes were observed in the case of untagged PtNP or electrolyte only, confirming that the nitro group reduction of NTP molecules on the surface of the nanoparticles is the source of the transients (red lines in Figure 4.3 a and b).

The average charge passed per transient Q (C) was found to vary with the NTP modification time of the nanoparticles: it increased up to 5 h and then leveled off as shown in Figure 4.6. The reason for this is probably because the tag molecule continually adsorbs onto the PtNP surface until a complete self-assembled monolayer (SAM) forms.[39, 40] The surface was saturated after 5 h and thus no additional NTP can be inserted at a longer modification time t (h).

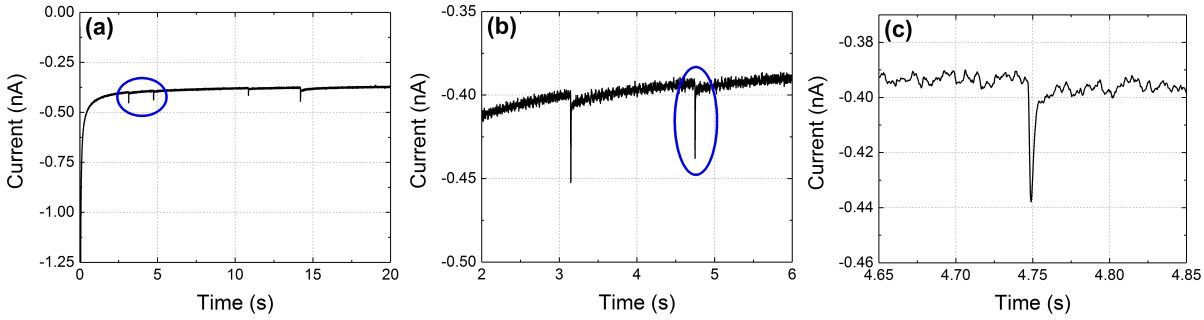

Figure 4.5: (a) Chronoamperometric profiles with NTP-tagged PtNPs. (b) A zoom of circled reductive transients in (a). (c) Further amplification of the circled spike in (b). All scans were recorded in a nitrogen saturated solution of 10.0 mM $HClO_4$ and 30.0 mM $NaClO_4$ and potentiostatted at -0.25 V vs Ag/AgCl (1.0 M KCl).

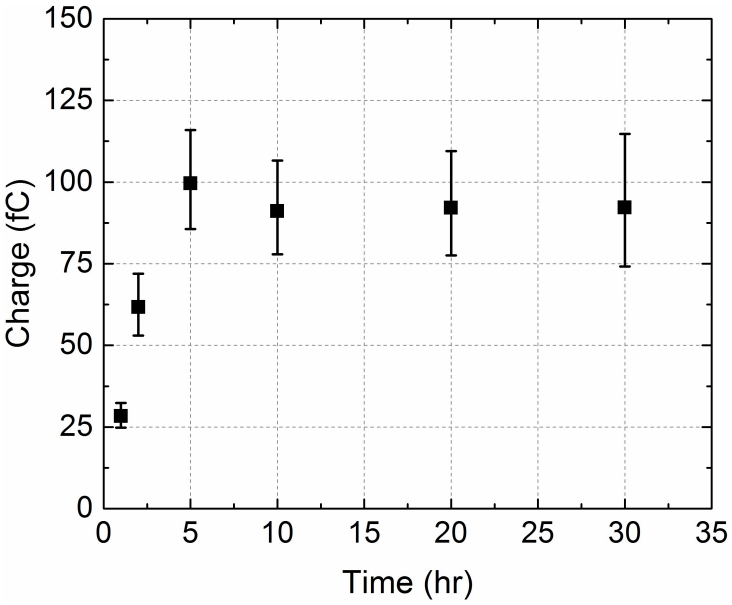

Figure 4.6: The variation of the average charge per impact transient, from overall 251 measurements, as a function of time allowed for NTP molecules to adsorb onto PtNPs.

4.3.2 Calculation of the Number of NTP Molecules Adsorbed per PtNP

A total of 160 spikes obtained at 5, 10, 20 and 30 h modification times were analyzed, corresponding to impacts of particles with a full NTP monolayer coverage. Charges were

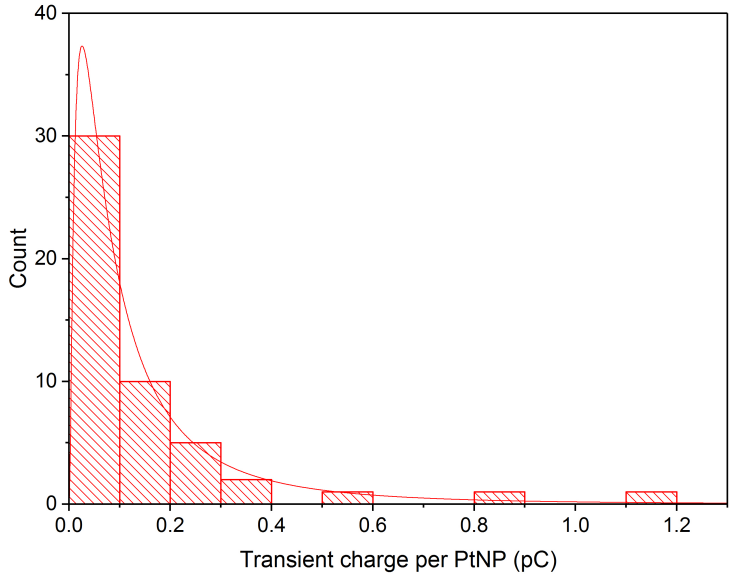

Figure 4.7: Example of transient charges measured at 10 h modification time fitted with a lognormal distribution curve.

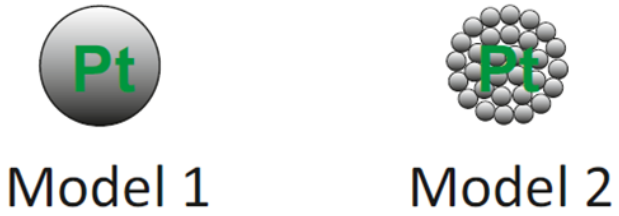

Figure 4.8: Two theoretical models of PtNPs.

measured and fitted with a lognormal distribution curve, as presented in Figure 4.7.[41] A mean charge of 0.094 ×/ 1.1 pC passed per impact transient was calculated,[42] which is related to the number of tag molecules N_{NTP}, *via* the electronic charge e (C) according to:

$$Q = 4eN_{\mathrm{NTP}} \tag{4.1}$$

Hence, the average number of NTP molecules attached to the surface of a single PtNP can be calculated as (1.5 ×/ 1.1) $\times 10^5$ molecules, from the experimental measurement of the transients. This can be further discussed and compared with the results from two simple geometric models: solid vs mesoporous spheres, as shown in Figure 4.8. In the former a single non-porous solid particle is considered; in the latter the particle is mesoporous and made of numerous smaller particles.

For Model 1, the assumption was made that the PtNP is a solid, smooth sphere of radius 24.3 nm and its surface area $S_{\text{solid PtNP}}$ (m^2) is:

$$S_{\text{solid PtNP}} = 4\pi R^2 \tag{4.2}$$

where R is the radius of the non-porous, solid spherical PtNP.

Assuming optimal close-packing was adopted by the NTP molecules on a two-dimensio -nal surface plane, the fractional filling efficiency f_1 is 0.91 for spheres or ellipses[43] and

the surface area of a PtNP can be written as:

$$S_{\text{solid PtNP}} = \frac{A_{\text{NTP}} \times N_{\text{NTP}}}{f_1} \tag{4.3}$$

where A_{NTP} is the adsorption area (m^2) occupied per NTP, as reported by literature (48.3 Å^2).[39] Combining Equations 4.2 and 4.3 gives:

$$N_{\text{NTP}} = \frac{(4\pi R^2) \times f_1}{A_{\text{NTP}}} \tag{4.4}$$

Therefore, the number of NTP adsorbed per nanoparticle can be determined as 0.14×10^5 molecules due to the formation of a SAM, or less when the modification was incomplete.

In Model 2, each PtNP (*ca.* 24.3 nm radius) was an aggregate of identical small nanoparticles (*ca.* 2 nm radius, estimated from Figure 4.2 b). As it is difficult to know the inner configuration of the aggregates from the TEM images, these small solid spheres were assumed to arrange in a densest close-packing in space and the fractional filling efficiency f_2 is 0.74.[43]

As the volume of a spherical PtNP V_{PtNP} (m^3) is:

$$V_{\text{solid PtNP}} = \frac{4}{3}\pi R^3 \tag{4.5}$$

the space occupied by the small nanoparticles is $V_{\text{solid PtNP}} \times f_2$. This can be written as:

$$\begin{aligned} V_{\text{mesoporous PtNP}} &= V_{\text{solid PtNP}} \times f_2 \\ &= V_{\text{small particles}} \times N_{\text{small particles}} \end{aligned} \tag{4.6}$$

Combining Equations 4.5 and 4.6:

$$\left(\frac{4}{3}\pi R^3\right) \times 0.74 = \left(\frac{4}{3}\pi r^3\right) \times N_{\text{small particles}} \tag{4.7}$$

where r is the small nanoparticle radius (*ca.* 2 nm) and $N_{\text{small particles}}$ is the number of small nanoparticles per PtNP. Therefore, a number of *ca.* 1327 small nanoparticles were determined to be present in one PtNP. The surface area of a mesoporous PtNP $S_{\text{mesoporous PtNP}}$ (m^2) is:

$$\begin{aligned} S_{\text{mesoporous PtNP}} &= S_{\text{small particles}} \times N_{\text{small particles}} \\ &= \frac{A_{\text{NTP}} \times N_{\text{NTP}}}{f_1} \end{aligned} \tag{4.8}$$

Rearranging Equation 4.8 yields:

$$\begin{aligned} N_{\text{NTP}} &= \frac{S_{\text{mesoporous PtNP}} \times f_1}{A_{\text{NTP}}} \\ &= \frac{[(4\pi r^2) \times N_{\text{small particles}}] \times f_1}{A_{\text{NTP}}} \end{aligned} \tag{4.9}$$

The number of tag molecules per PtNP is then 1.3×10^5 for full NTP adsorption, or fewer at an insufficient modification time.

Comparing the number of NTP obtained from experiments (1.5×10^5 molecules) with the ones from solid (0.14×10^5 molecules) and mesoporous (1.3×10^5 molecules) PtNP models, the experimental result is closer to the fully mesoporous case, suggesting a significant degree of porosity in the PtNPs used. TEM images also reveal clusters of small nanoparticles (Figure 4.2 a and b), but the knowledge of their internal packing was limited. It is concluded that the NTP molecules can partially insert into the PtNP aggregates, and undergo adsorption at their inner surface.

This result is significant as first, it extends the method of TRC to investigation of the porosity of nanoparticles. Electrons are transferred *via* either direct electron transfer or a "hopping" mechanism,[44, 45] enabling an *in-situ* quantification of inner structures for porous nanoparticle. In addition to this, electroactive tag molecules can be suitably selected and reduced or oxidized without destroying the underlying core. Second and most

importantly, it can be realized that the electrocatalytic ability and other properties of the nanomaterials cannot be correctly understood without realizing their porosities.[9, 17, 46–48] In particular, the extent to which "catalytic" properties can be attributed to a change of effective area or to altered intrinsic activity resulting from either quantum confinement or surface morphology effects, requires a realistic estimation of the "active surface area" of the particle in solution. The assumption that the internal surfaces do not contribute to any (electro-)catalysis may lead to incorrect inferences.

4.3.3 Conclusions

In summary, mesoporous PtNPs in this chapter are formed of an aggregate of many $(10^2 - 10^3)$ much smaller nanoparticles. Most of their internal surfaces are shown to be available for electrocatalytic reaction and hence can be inferred to be accessible to the solution phase in which the particles are suspended. The nano-impacts method provides a methodology for the *in-situ* measurement of the "active surface area" of the nanoparticles which is essential in understanding the origin of any catalytic behavior shown by the nanoparticles. The next chapter will elaborate an alternative method to explore the porosity of nanoparticles using surface platinum oxidation.

Bibliography

[1] Jiao, X.; Sokolov, S. V.; Tanner, E. E. L.; Young, N. P.; Compton, R. G. *Physical Chemistry Chemical Physics* **2017**, *19*, 64–68.

[2] Kim, T.; Hyeon, T. *Nanotechnology* **2014**, *25*, 012001.

[3] Bandaru, P.; Yamada, H.; Narayanan, R.; Hoefer, M. *Materials Science & Engineering, R: Reports* **2015**, *96*, 1–69.

[4] Raimondi, F.; Scherer, G. G.; Kötz, R.; Wokaun, A. *Angewandte Chemie, International Edition* **2005**, *44*, 2190–2209.

[5] Tong, R.; Hemmati, H. D.; Langer, R.; Kohane, D. S. *Journal of the American Chemical Society* **2012**, *134*, 8848–8855.

[6] Chen, A.; Holt-Hindle, P. *Chemical Reviews* **2010**, *110*, 3767–3804.

[7] Chen, A.; La Russa, D. J.; Miller, B. *Langmuir* **2004**, *20*, 9695–9702.

[8] Thearle, R. A.; Sofer, Z.; Bouša, D.; Pumera, M. *ChemPhysChem* **2016**, *17*, 2096–2099.

[9] Bigall, N. C.; Härtling, T.; Klose, M.; Simon, P.; Eng, L. M.; Eychmüller, A. *Nano Letters* **2008**, *8*, 4588–4592.

[10] Mani, P.; Srivastava, R.; Strasser, P. *Journal of Power Sources* **2011**, *196*, 666–673.

[11] Jung, H. B.; Xu, H.; Konishi, H.; Roden, E. E. *Journal of Geochemical Exploration* **2016**, *169*, 80–88.

[12] Chen, Y.; Ma, Q.; Jia, H.; Wang, Y. *Journal of Materials Science: Materials in Electronics* **2016**, *27*, 10237–10243.

[13] Liu, J.; Wang, Z.; Sheng, A.; Liu, F.; Qin, F.; Wang, Z. L. *Environmental Science & Technology* **2016**, *50*, 5606–5613.

[14] Sokolov, S. V.; Tschulik, K.; Batchelor-McAuley, C.; Jurkschat, K.; Compton, R. G. *Analytical Chemistry* **2015**, *87*, 10033–10039.

[15] Ni, B.; Wang, X. *CrystEngComm* **2015**, *17*, 6796–6808.

[16] Snyder, J.; McCue, I.; Livi, K.; Erlebacher, J. *Journal of the American Chemical Society* **2012**, *134*, 8633–8645.

[17] Guo, H.; Liu, X.; Bai, C.; Chen, Y.; Wang, L.; Zheng, M.; Dong, Q.; Peng, D. *ChemSusChem* **2015**, *8*, 486–494.

[18] Han, B.; Carlton, C. E.; Kongkanand, A.; Kukreja, R. S.; Theobald, B. R.; Gan, L.; O'Malley, R.; Strasser, P.; Wagner, F. T.; Shao-Horn, Y. *Energy & Environmental Science* **2015**, *8*, 258–266.

[19] Li, J.; Wang, A.; Yang, Y. China Patent, CN 104003404. 2014.

[20] Chang, E. P.; Evans, J. S. *Biochemistry* **2015**, *54*, 5348–5355.

[21] Wang, D.; Schaaf, P. Germany Patent, DE 102014003993. 2015.

[22] Lang, X.; Hirata, A.; Fujita, T.; Chen, M. *Advanced Energy Materials* **2014**, *4*, 1301809.

[23] Cheng, W.; Compton, R. G. *TrAC, Trends in Analytical Chemistry* **2014**, *58*, 79–89.

[24] Pumera, M. *ACS Nano* **2014**, *8*, 7555–7558.

[25] Rees, N. V. *Electrochemistry Communications* **2014**, *43*, 83–86.

[26] Robbs, P. H.; Rees, N. V. *Physical Chemistry Chemical Physics* **2016**, *18*, 24812–24819.

[27] Zhou, Y.-G.; Haddou, B.; Rees, N. V.; Compton, R. G. *Physical Chemistry Chemical Physics* **2012**, *14*, 14354–14357.

[28] Giovanni, M.; Ambrosi, A.; Sofer, Z.; Pumera, M. *Electrochemistry Communications* **2015**, *56*, 16–19.

[29] NanoComposix, 50 nm Citrate NanoXact^{TM} Platinum Nanoparticles (Certificate of Analysis Examples): http://50.87.149.212/_Specification%20Sheets/Platinum%20Spec%20Sheets/PT50-NX-CIT-MGM1553.pdf?2581746.

[30] Pérez, J.; Pascau, J. *Image Processing with ImageJ*; Packt Publishing, 2013.

[31] To measure the nanoparticle size each PtNP aggregate was assumed to be a sphere, and a circle was drawn to include all the fuzzy small nanoparticles at the aggregate surface.

[32] Batchelor-McAuley, C.; Ellison, J.; Tschulik, K.; Hurst, P. L.; Boldt, R.; Compton, R. G. *Analyst* **2015**, *140*, 5048–5054.

[33] Souto, R. M. *Electroanalysis* **1994**, *6*, 531–542.

[34] Sokolov, S. V.; Eloul, S.; Kätelhön, E.; Batchelor-McAuley, C.; Compton, R. G. *Physical Chemistry Chemical Physics* **2017**, *19*, 28–43.

[35] Rubinstein, I. *Journal of Electroanalytical Chemistry and Interfacial Electrochemistry* **1985**, *183*, 379–386.

[36] Zhou, Y.-G.; Rees, N. V.; Compton, R. G. *Chemical Communications* **2012**, *48*, 2510–2512.

[37] Plowman, B. J.; Young, N. P.; Batchelor-McAuley, C.; Compton, R. G. *Angewandte Chemie, International Edition* **2016**, *55*, 7002–7005.

[38] A background subtraction was performed to reduce the capacitative contribution to the signal.

[39] Nielsen, J. U.; Esplandiu, M. J.; Kolb, D. M. *Langmuir* **2001**, *17*, 3454–3459.

[40] Cecchet, F.; Lis, D.; Guthmuller, J.; Champagne, B.; Caudano, Y.; Silien, C.; Addin Mani, A.; Thiry, P. A.; Peremans, A. *ChemPhysChem* **2010**, *11*, 607–615.

[41] The transient charges from each modification time were dispersed in a lognormal distribution, with the mean μ and the standard error of mean $\sigma/\sqrt{n}$, as measurements of the minimum current restricted by the potentiostat. To clarify, the "back-transformed" values in terms of charge Q (C) can be written in a mathematical expression according to the lognormal law, with the median $\mu^* = e^{\mu}$ and the multiplicative standard error of mean $(\sigma/\sqrt{n})^* = e^{\sigma/\sqrt{n}}$. Therefore the sign $\times/$ (times/divide) was employed to denote the error, analogous to the $\pm$ notation used in a Gaussian distribution.

[42] Limpert, E.; Stahel, W. A.; Abbt, M. *BioScience* **2001**, *51*, 341–352.

[43] Matsumoto, T.; Nowacki, W. *Zeitschrift für Kristallographie – Crystalline Materials* **1966**, *123*, 401–421.

[44] Amatore, C.; Bouret, Y.; Maisonhaute, E.; Goldsmith, J. I.; Abruña, H. D. *ChemPhysChem* **2001**, *2*, 130–134.

[45] Amatore, C.; Bouret, Y.; Maisonhaute, E.; Goldsmith, J. I.; Abruña, H. D. *Chemistry – A European Journal* **2001**, *7*, 2206–2226.

[46] Guo, Z.; Percival, S. J.; Zhang, B. *Journal of the American Chemical Society* **2014**, *136*, 8879–8882.

[47] Ahn, H. S.; Bard, A. J. *Angewandte Chemie, International Edition* **2015**, *54*, 13753–13757.

[48] Kim, J.; Kim, B.-K.; Cho, S. K.; Bard, A. J. *Journal of the American Chemical Society* **2014**, *136*, 8173–8176.

Chapter 5

Understanding Nanoparticle Porosity *via* Nanoimpacts and XPS: Electro-Oxidation of Platinum Nanoparticle Aggregates

The porosity of platinum nanoparticle (PtNP) aggregates is investigated electrochemically *via* particle-electrode impacts and by X-ray photoelectron spectroscopy (XPS). The mean charge per oxidative transient is measured from nanoimpacts; XPS shows the formation of PtO and PtO_2 in relative amounts defined by the electrode potential, and an average oxidation state is deduced as a function of potential. Analogous to Chapter 4, the number of platinum atoms oxidized per PtNP is calculated and compared with the same two models: solid and mesoporous spheres. In the present experiment there are two limiting cases: oxidation of the full particle, or oxidation of the surface only of the particles or their constituent particles. This allows insight into extent to which the internal surface of the aggregate is "seen" by the solution and is electrochemically active. Furthermore, results in this chapter are consistent with the conclusions in Chapter 4, indicating accuracy of the measurements in both studies.

The work has been published in *Physical Chemistry Chemical Physics*[1] and was performed in collaboration with Dr. Eden E. L. Tanner, Dr. Stanislav V. Sokolov, Dr. Robert G. Palgrave (Department of Chemistry, University College London) and Dr. Neil

P. Young (Department of Materials, University of Oxford). Dr. Eden E. L. Tanner helped with the interpretation of the experimental results. Dr. Stanislav V. Sokolov and Dr. Neil P. Young carried out the transmission electron microscopy (TEM) for the mesoporous PtNPs. Dr. Robert G. Palgrave conducted the X-ray photoelectron spectroscopy (XPS) analysis.

5.1 Introduction

In the previous chapter, the platinum nanoparticles (PtNPs) were modified with 4-nitrothi-ophenol (NTP) molecules. Results obtained from nanoimpacts were compared with calculations from two theoretical models and the porosity of PtNPs was successfully revealed. Nevertheless several assumptions were made in the analysis, for example the NTP molecules was assumed to formed a monolayer on the surface of the PtNPs and the size of the NTP molecule quoted was originally detected on a gold surface. Therefore in this chapter, it is important to design another experiment to further verify the results in Chapter 4.

The nano-impact method was applied here again but now to study the electrochemical oxidation of platinum nanoparticles which are themselves aggregates of much smaller particles. The porosities can be seen but not quantified *via* transmission electron microscopy (TEM), as shown in Figure 4.2 (Chapter 4). In the nano-impact method[2–5] individual particles, in this case platinum nano-aggregates, suspended in aqueous solution from time to time collide with a microelectrode under potentiostatic control resulting in their oxidation (or reduction).[6, 7] In the work reported below for the case of platinum particles if a suitably positive potential is applied the formation of surface oxides results. The charge produced reflects the extent of the surface oxidation so revealing the extent to which internal surfaces are electroactive. In the case of platinum, the electro-oxidation is likely to produce both PtO and PtO_2 so complementary XPS measurements are performed to

allow the interpretation of the impact data as a function of potential. Finally a comparison is made with similar nanoparticles "tagged" with a redox active probe (Chapter 4)[8] but of a relatively large size compared to the species involved in platinum oxides.

5.2 Experimental Section

5.2.1 Chemicals

Perchloric acid (70%, $HClO_4$) and sodium perchlorate monohydrate (98%, $NaClO_4 \cdot H_2O$) were obtained from Sigma-Aldrich, Dorset, U.K. Citrate-capped platinum nanoparticles (PtNPs) were provided by NanoComposix, San Diego, CA, U.S.A. with a reported diameter 50 nm and concentration of 3.3×10^{13} particles L^{-1}.[9] All solutions were prepared with ultrapure water from Millipore with a resistivity of not less than 18.2 MΩ cm at 298 K.

5.2.2 Characterization

Both stock PtNPs and PtNP oxides were characterized *via* transmission electron microscopy (TEM) and X-ray photoelectron spectroscopy (XPS).

TEM

Dr. Neil P. Young (Department of Materials, University of Oxford) conducted the TEM analysis for the mesoporous PtNPs as described below.

The size of PtNPs was determined by TEM (JEOL JEM-3000F FEGTEM, 300 kV accelerating voltage). Details of the sample preparation and analysis were given in Section 4.2.2 (Chapter 4). Each PtNP was found to be an aggregate of much smaller nanoparticles (about 2 nm radius from TEM), with a mean radius of 24.3 ± 1.6 nm. Example images of the particles and the corresponding size distributions were shown in Figure 4.2 (Chapter

4). Note that this size of PtNP aggregates (24.3 nm radius) was selected in order to guarantee a favourable signal-noise ratio.

XPS

Dr. Robert G. Palgrave (Department of Chemistry, University College London) carried out the XPS for the platinum oxides as described below.

XPS (Thermo K-alpha spectrometer) was carried out to measure the elemental composition of both PtNPs and PtNP oxides. Samples were prepared by depositing a drop of the stock PtNP sol (3.3×10^{13} particles L^{-1}) onto GC plates (SPI Supplies, West Chester, PA, U.S.A.), followed by drying in air prior to cyclic voltammograms (CVs) and imaging. The CVs were conducted in an aqueous solution of 10.0 mM $HClO_4$ and 30.0 mM $NaClO_4$, and scanned from 0 to various stopping potentials (from 1.5 to 2.0 V vs SCE) at a rate of 25 mV s^{-1}. The XPS instrument utilized a 72 W monochromated Al Kα X-ray source ($E = 1486.6$ eV) focused to a spot of 400 microns diameter at the sample surface. Charging was compensated for by use of a dual beam (electron and Ar^+ ion) flood gun. The electron energy analyzer consists of a double focusing 180 degree hemisphere with mean radius of 125 mm, operated in constant analyzer energy (CAE) mode, and a 128 channel position sensitive detector. The pass energy was set to 200 eV for survey scans and 50 eV for high resolution regions. The binding energy scale of the instrument is regularly calibrated using three points (Ag, Au, Cu). Spectra were analyzed using the Thermo Avantage software.

To clarify, in this work, "PtNP" refers to the platinum nanoparticle aggregate (*ca.* 24.3 nm radius), and "small nanoparticle" is the component of a PtNP (*ca.* 2 nm radius).

5.2.3 Electrochemistry

A three electrode system in a Faraday cage was employed for all electrochemical experiments, with a μAutolab III (Metrohm Autolab B.V., Utrecht, The Netherlands) or an in-house potentiostat.[10] The working electrode was a glassy carbon (GC) macrodisk (3 mm diameter; BASi, West Lafayette, IN, U.S.A.) or a carbon fibre microdisc (33 μm diameter; BASi, West Lafayette, IN, U.S.A.) electrode. Both electrodes were polished with alumina powders (Buehler, Lake Bluff, IL, U.S.A.) in a size sequence: 1.0 μm, 0.3 μm and 0.05 μm. The reference electrode was a saturated calomel electrode (SCE) [Hg/Hg_2Cl_2, saturated KCl] (+0.241 V vs standard hydrogen electrode, SHE; BASi, West Lafayette, IN, U.S.A.) or a leakless silver/silver chloride electrode [Ag/AgCl, 1.0 M KCl] (+0.235 V vs SHE; Cypress Systems, Lawrence, KS, U.S.A.) (this is used in the nano-impact experiments to avoid leakage). The counter electrode was a graphite rod (6 mm diameter; Sigma-Aldrich, Dorset, U.K.) or a platinum foil (Goodfellow, Cambridge, U.K.). All experiments were conducted under a nitrogen atmosphere. All electrochemical measurements were thermostatted at 25 ± 0.5 °C.

In the experimental data reported below, potentials are quoted on the SCE or the Ag/AgCl (1.0 M KCl) scales.

Drop-Casting Experiments

The GC macroelectrode was modified by drop casting of a stock PtNP sol (3 μL) onto the surface, which was subsequently allowed to dry under flowing nitrogen prior to experimentation.

Nano-Impact Experiments

Details of the in-house potentiostat can be found in Section 4.2.4 (Chapter 4).[8] To note again, in the context of nano-impact experiments the potentiostat conserves charge and

therefore the integral of the current spikes is unaffected in their size analysis.[11]

5.3 Results and Discussion

The porosity of PtNPs was established by analysing platinum oxidation using both electrochemical (cyclic voltammetry and nanoimpacts) and X-ray photoelectron spectroscopy (XPS) techniques. First, cyclic voltammograms (CVs) were conducted; a glassy carbon (GC) macroelectrode was modified by drop casting a PtNP sol and recording CVs. PtNPs were oxidized at different potentials, and XPS was used to detect different platinum oxides. Second, nano-impact methodology was employed whereby overpotentials were applied to oxidize the PtNP aggregates and oxidative transients were observed. From these, the number of platinum atoms oxidized was calculated and again, compared with two theoretical models: a solid sphere, and a completely mesoporous nanoparticle formed by aggregation of a large number of smaller particles, as shown in Figure 4.7 (Chapter 4). This therefore allows an estimation of the PtNP porosities.

5.3.1 Voltammetry, XPS and Nano-Impact Measurements

Experiments were conducted to explore the redox properties of PtNPs. First, a GC electrode was modified with stock PtNPs (see Section 5.2.3) before being transferred to an aqueous solution of 10.0 mM $HClO_4$ and 30.0 mM $NaClO_4$. CVs were recorded and a oxidative peak was obtained at *ca.* 1.8 V vs SCE, as shown in Figure 5.1. In the absence of PtNPs, no signal was observed (blue dash line in Figure 5.1), indicating the peak was due to the PtNP oxidation. To clarify, this solution combination is selected to allow comparison with the work in Chapter 4.[8]

XPS was then performed to measure the elemental composition of platinum oxides. Note that surface oxides or hydroxides of PtNPs may exist in the commercial PtNP sam-

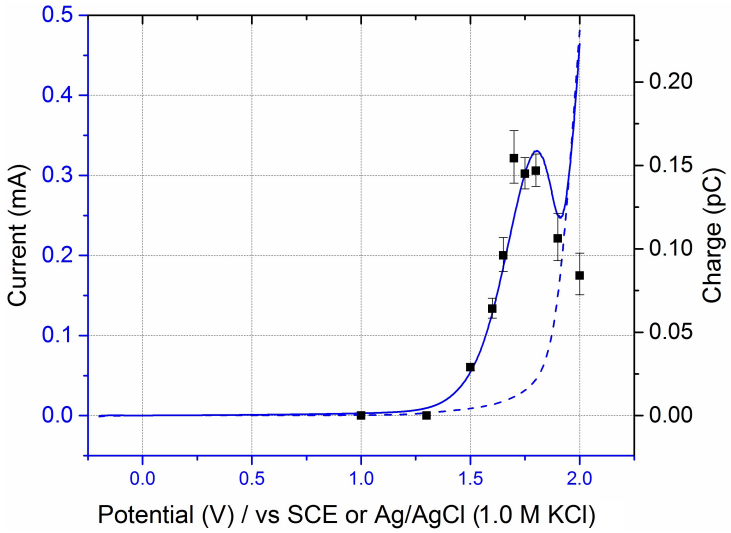

Figure 5.1: CVs for a GC macroelectrode with (blue solid line) or without (blue dash line) PtNP modification. The average charge per impact transient, from overall 482 measurements, varies as a function of the potential applied in the process of oxidation (black squares). All scans were performed in a nitrogen saturated solution of 10.0 mM $HClO_4$ and 30.0 mM $NaClO_4$, either at a scan rate of 25 mV s^{-1} or potentiostated at various potentials.

ple and contribute a source of error. 7 samples were prepared by drop casting PtNPs on GC plate substrates; CVs were swept and stopped at different potentials from 1.50 to 2.00 V. XPS spectra were recorded in the 64–87 eV region corresponding to elemental platinum. The Pt 4f spectrum was fitted with up to three doublets. The Pt(0) peak was modelled with an asymmetric peak shape to account for the plasmon energy tailing in the metal, as has been observed previously for Pt(0) nanoparticles,[12] while higher oxidation states were modelled with symmetrical Gaussian–Lorentzian convolutions. Pt $4f_{7/2}$ components were found at binding energies of around 71.1 eV corresponding to Pt(0), and 74.0 eV corresponding to Pt(IV).[12–14] An additional doublet was required with Pt $4f_{7/2}$ at around 71.8 eV binding energy, lower than expected for PtO[14] but similar to that reported for partially oxidized PtNPs.[12, 13] These environments cannot be unambiguously assigned to specific chemical species, for example they may be oxides or hydroxides, but are labelled here as Pt(0), Pt(II) and Pt(IV) in order of increasing binding energy. Table 5.1 and Figure 5.2 show that as the stopping potential increases, the amount of Pt(0)

CV Stopping Potential (V)	Criteria	Pt(0)	Pt(II)	Pt(IV)	Average Platinum Oxidation State
1.50	Amount	81.2	9.5	9.3	0.6
	BE (eV)	71.1	71.7	74.0	
1.60	Amount	76.4	6.0	17.6	0.8
	BE (eV)	71.2	71.9	74.1	
1.70	Amount	64.5	15.0	20.6	1.1
	BE (eV)	71.1	71.7	74.0	
1.80	Amount	55.0	15.0	30.0	1.5
	BE (eV)	71.1	71.7	74.0	
1.85	Amount	57.5	22.1	20.4	1.3
	BE (eV)	71.0	71.8	74.0	
1.90	Amount	54.5	12.9	32.6	1.6
	BE (eV)	71.0	71.6	74.2	
2.00	Amount	49.0	21.0	30.0	1.6
	BE (eV)	71.0	71.7	74.0	

Table 5.1: XPS analysis of PtNP oxidation. The average platinum oxidation state was calculated at various potentials.

decreases and both Pt(II) and Pt(IV) increase. This gave an overall increasing average platinum oxidation state, suggesting that, as expected, greater oxidation of the PtNPs occurs at higher overpotentials. Note that the average platinum oxidation states obtained at variable potentials here are similar to those predicted in the Pourbaix diagram.[15]

Next, nano-impact measurements were conducted to investigate the oxidative charge per PtNP. Chronoamperograms (CAs) were recorded in an aqueous electrolyte of 10.0 mM $HClO_4$ and 30.0 mM $NaClO_4$ at various potentials (vs Ag/AgCl in 1.0 M KCl). In the experiments, 60 pM PtNPs were added and spikes were clearly observed of an approximate tens of millisecond duration, as shown in Figure 5.3 (black line). These are attributed to the platinum oxidation taking place when the nanoparticles make contact with the carbon fibre substrate. No impact spikes were observed in the case of electrolyte

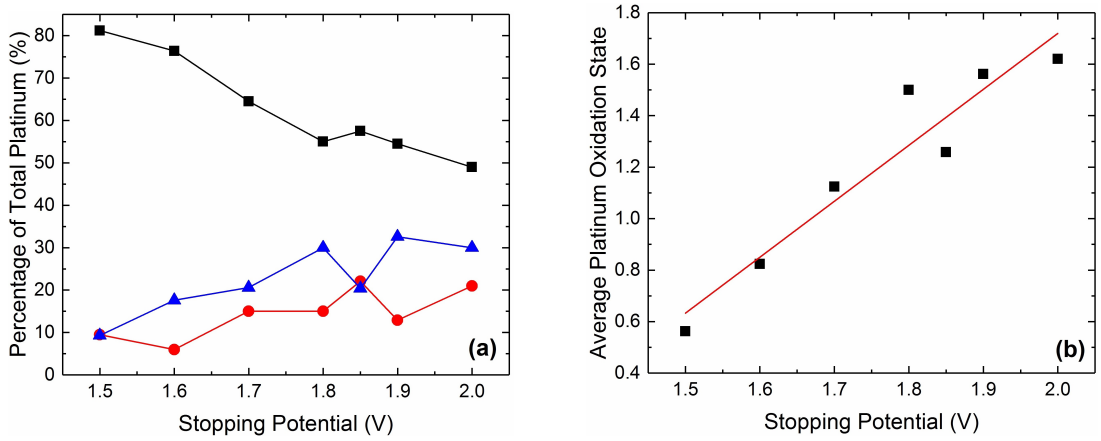

Figure 5.2: (a) Elemental composition of platinum oxides at different stopping potentials: Pt(0) (black), Pt(II) (red) and Pt(IV) (blue). (b) Linear fit of average platinum oxidation state against stopping potentials with a reported coefficient of determination R^2 of 0.89.

only, confirming that the oxidation of the PtNPs is the source of the transients.

The charge passed per transient Q (C) was found to vary with the overpotential applied and reach a maximum at *ca.* 1.8 V as shown in Figure 5.1 (black squares). This is because the PtNPs were increasingly oxidized as the potential increased; at high potentials nonconductive oxide layers were formed on the surface of the nanoparticles, reducing any further reaction. This gave a peak at potential at *ca.* 1.8 V (vs Ag/AgCl in 1.0 M KCl). The XPS measurements showed the average platinum oxidation state

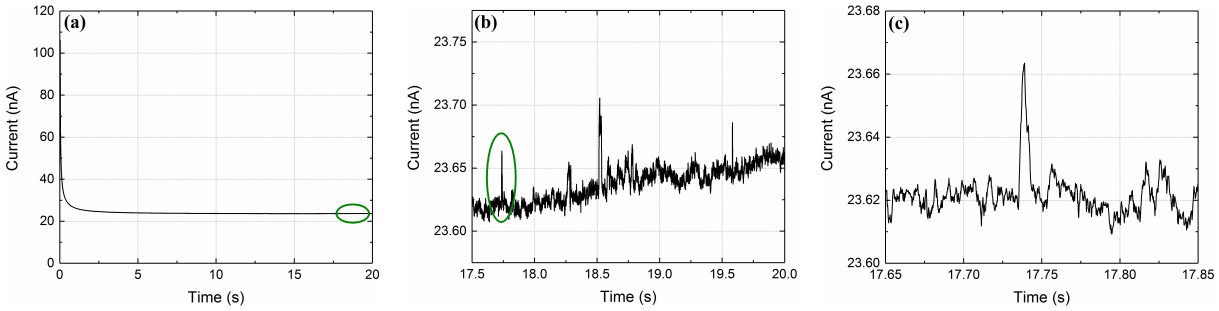

Figure 5.3: (a) CA with 60 pM PtNPs. (b) Zoom in of the circled reductive transients in (a). (c) Further amplification of the circled spike in (b). All scans were recorded in a nitrogen saturated solution of 10.0 mM $HClO_4$ and 30.0 mM $NaClO_4$ and potentiostated at various potentials (vs leakless Ag/AgCl in 1.0 M KCl).

increased consistently as the stopping potential increased to allow a further oxidation, so the reduced activity at high potentials may be related to the formation of PtO_2.

5.3.2 Calculation of the Number of Platinum Atoms Oxidized per PNP

A total of 482 spikes obtained at various potentials were analyzed. Charges were measured and fitted with a lognormal distribution curve, as presented in Figure 5.4.[16] A mean charge passed per impact transient Q (C) was therefore calculated at various overpotentials, as shown in Table 5.2.[17] The charge is related to the number of platinum atoms oxidized N_{Pt} per PtNP aggregate *via* the electronic charge e (C) according to:

$$Q = neN_{\mathrm{Pt}} \tag{5.1}$$

where n is the number of electron transferred during the process.

Hence, the average number of platinum atoms oxidized per PtNP aggregate can be calculated at various potentials using the average platinum oxidation state from XPS.

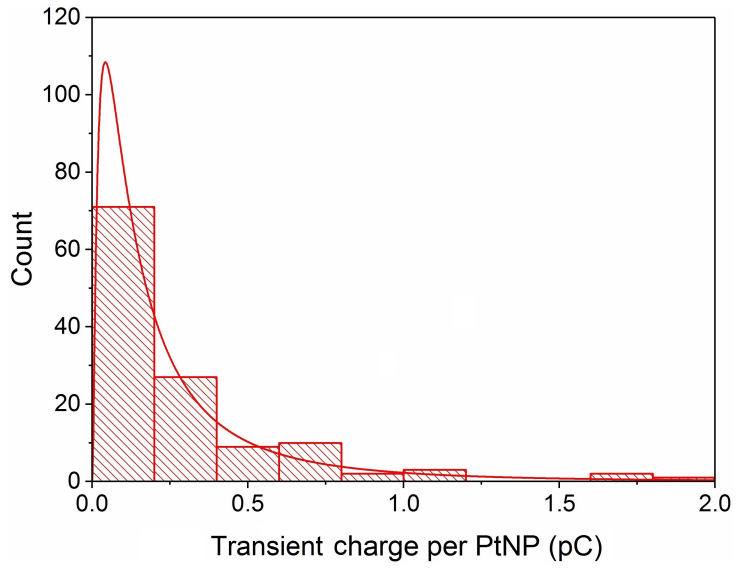

Figure 5.4: Example of transient charges measured at 1.70 V fitted with a lognormal distribution curve.

Potential (V)	Average Charge per PtNP from Nanoimpact (pC)	Average Platinum Oxidation State from XPS	Number of Platinum Atoms Oxidised per PtNP
1.50	0.03 ×/ 1.07	0.6	3.1×10^5
1.60	0.06 ×/ 1.10	0.8	4.7×10^5
1.65	0.10 ×/ 1.11	-	-
1.70	0.15 ×/ 1.11	1.1	8.5×10^5
1.75	0.15 ×/ 1.07	-	-
1.80	0.15 ×/ 1.07	1.5	6.2×10^5
1.85	-	1.3	-
1.90	0.11 ×/ 1.14	1.6	4.3×10^5
2.00	0.08 ×/ 1.16	1.6	3.1×10^5

Table 5.2: Average charge per PtNP aggregate from nano-impact measurements.[16] Number of platinum atoms oxidized per PtNP was calculated at various potentials using the average platinum oxidation state from XPS.

These can be further discussed and again, compared with the results from two simple geometric models (solid or mesoporous spheres), as shown in Figure 4.7 (Chapter 4). Within each model, two limiting extreme cases will be considered – full and surface oxidation. For full oxidation, all platinum atoms in the PtNP aggregates are oxidized; while for surface oxidation, only those platinum atoms on the surface are oxidized.

Calculations were conducted for the following two geometric models where a close-packing arrangement was assumed for the platinum atoms or the small nanoparticles in the PtNP aggregates. In Model 1, each PtNP was a solid, smooth sphere of radius 24.3 nm; in Model 2, each PtNP (*ca.* 24.3 nm radius) was an aggregate of identical small nanoparticles (*ca.* 2 nm radius, estimated from Figure 4.2 b in Chapter 4). The number of platinum atoms oxidized can be obtained from both models for full and surface oxidation, and summarised in Table 5.3 (for details see below). To note, Model 1 was only calculated

Number of Platinum Atoms Oxidised per PtNP	Full Oxidation	Surface Oxidation
Solid Sphere (Model 1)	4.0×10^6	0.11×10^6
Porous Sphere (Model 2)	2.9×10^6	1.0×10^6

Table 5.3: Number of platinum atoms oxidized per PtNP from two models (solid and mesoporous), in the cases of full or surface oxidation.

as a possible bound and in the experiments the particle was not fully oxidized.

For Model 1, the assumption was made that the PtNP is a solid, smooth sphere of radius 24.3 nm. This was calculated as a limiting case. The volume $V_{\text{solid,full}}$ (m^3) is:

$$V_{\text{solid,full}} = \frac{4}{3}\pi R^3 \tag{5.2}$$

where R is the radius of the non-porous, solid spherical PtNP.

The mass $m_{\text{solid,full}}$ (g) can be written as:

$$\begin{aligned} m_{\text{solid,full}} &= \rho V_{\text{solid,full}} \\ &= \left(21.46 \times 10^6\right) \times \left[\frac{4}{3}\pi \left(24.3 \times 10^{-9}\right)^3\right] \\ &= 1.3 \times 10^{-15} \text{ g} \end{aligned} \tag{5.3}$$

where ρ is the density (g m^{-3}) of platinum.[18]

Therefore, the total number of platinum atoms per PtNP is:

$$\begin{aligned} N_{\text{Pt}} = \frac{1.3 \times 10^{-15}}{195.084} &= 6.7 \times 10^{-18} \text{ mol} \\ &= 4.0 \times 10^6 \text{ atoms} \end{aligned} \tag{5.4}$$

The surface area $S_{\text{solid,surface}}$ (m^2) can be written as:

$$S_{\text{solid,surface}} = 4\pi R^2 \tag{5.5}$$

Assuming optimal close-packing was adopted by the platinum atoms on a two-dimensional surface plane, the fractional filling efficiency f_1 is 0.91 for spheres or ellipses[19] and the total surface area of all platinum atoms on the surface $S'_{\text{solid,surface}}$ (m^2) is:

$$\begin{aligned} S'_{\text{solid,surface}} &= S_{\text{solid,surface}} \times f_1 \\ &= A_{\text{Pt}} \times N_{\text{Pt}} \end{aligned} \tag{5.6}$$

The cross-sectional area A_{Pt} (m^2) of a platinum atom is:

$$A_{\text{Pt}} = \pi r_{\text{Pt}}^2 \tag{5.7}$$

where r_{Pt} is the radius of a platinum atom.

Rearranging Equation 5.6, the number of platinum atoms on the surface of each PtNP can be determined as:

$$\begin{aligned} N_{\text{Pt}} &= \frac{(4\pi R^2) \times f_1}{\pi r_{\text{Pt}}^2} \\ &= \frac{\left[4\pi \left(24.3 \times 10^{-9}\right)^2\right] \times 0.91}{\pi \left(138.5 \times 10^{-12}\right)^2} \\ &= 0.11 \times 10^6 \text{ atoms} \end{aligned} \tag{5.8}$$

For Model 2, each PtNP (*ca.* 24.3 nm radius) was considered to an aggregate of identical small nanoparticles (*ca.* 2 nm radius, estimated from Figure 4.2 b in Chapter 4). Again, as it is difficult to know the inner configuration of the aggregates from the TEM images, these small solid spheres were assumed to arrange in a densest close-packing in space and the fractional filling efficiency f_2 is 0.74.[19] The volume of a spherical PtNP $V_{\text{mesoporous,full}}$ (m^3) is:

$$\begin{aligned} V_{\text{mesoporous,full}} &= V_{\text{solid,full}} \times f_2 \\ &= \left(\frac{4}{3}\pi R^3\right) \times 0.74 \end{aligned} \tag{5.9}$$

The mass can be written as:

$$\begin{aligned} m_{\text{mesoporous,full}} &= \rho V_{\text{mesoporous,full}} \\ &= \left(21.46 \times 10^{6}\right) \times \left[\frac{4}{3}\pi \left(24.3 \times 10^{-9}\right)^{3}\right] \times 0.74 \\ &= 9.5 \times 10^{-16} \text{ g} \end{aligned} \tag{5.10}$$

where ρ is the density of platinum.[18]

Hence the total number of platinum atoms per PtNP aggregate is:

$$\begin{aligned} N_{\text{Pt}} &= \frac{m_{\text{mesoporous,full}}}{m_{\text{Pt}}} = \frac{9.5 \times 10^{-16}}{195.084} \\ &= 4.9 \times 10^{-18} \text{ mol} = 2.9 \times 10^{6} \text{ atoms} \end{aligned} \tag{5.11}$$

The surface area $S_{\text{mesoporous,surface}}$ (m^2) is:

$$\begin{aligned} S_{\text{mesoporous,surface}} &= S_{\text{small particles}} \times N_{\text{small particles}} \\ &= \frac{A_{\text{Pt}} \times N_{\text{Pt}}}{f_1} \end{aligned} \tag{5.12}$$

Rearranging Equation 5.12, the number of platinum atoms on the surface of each PtNP aggregate is:

$$\begin{aligned} N_{\text{Pt}} &= \frac{(4\pi r^2) \times N_{\text{small particles}} \times f_1}{\pi r_{\text{Pt}}^2} \\ &= \frac{\left[4\pi \left(2 \times 10^{-9}\right)^2\right] \times 1327 \times 0.91}{\pi \left(138.5 \times 10^{-12}\right)^2} \\ &= 1.0 \times 10^{6} \text{ atoms} \end{aligned} \tag{5.13}$$

At each potential, nanoimpacts were applied to determine the mean oxidative charge per PtNP; whilst XPS was used to deduce the number of electrons transferred *via* measurements of the mean platinum oxidation state. The number of platinum atoms oxidized was calculated and compared with the ones from solid (4.0×10^6 or 0.11×10^6 atoms for full

and surface oxidation) and mesoporous (2.9×10^6 or 1.0×10^6 atoms for full and surface oxidation) PtNP models (Table 5.3). There is a good estimation between the maximum experimental result at 1.70 V (0.85×10^6) and the predicted value of the mesoporous, surface model (1.0×10^6), suggesting a significant degree of porosity in the PtNPs used. The small difference may be because that in the process of oxidation, some of the platinum atoms on the surface of small nanoparticles were accessible whilst some were not. This is further confirmed by the TEM images, as clusters of small nanoparticles can be seen in Figure 4.2 a and b (Chapter 4), but the knowledge of their internal packing was limited. Finally, the results from the oxidation of the mesoporous platinum nano-aggregates can be compared with data obtained by the "tagging" of the platinum surface with the redox active species 4-nitrothiophenol (NTP) which irreversibly adsorbs at platinum. As shown in Chapter 4, nanoimpacts using the same NTP-tagged platinum particles indicated that *ca.* 1.5×10^5 NTP molecules were adsorbed.[8] As the area occupied by one NTP molecule on the platinum surface is 48.3 $Å^2$ per adsorbate,[20] this suggests that each NTP molecule is associated with 7.3 platinum atoms (assuming a two-dimensional close-packing of Pt atoms on the surface) leading to an estimate of the number of surface platinum atoms "seen" as being 1.1×10^6. This value is surprisingly consistent with the number 1.0×10^6 determined from the platinum surface oxidation presented in this chapter. Whilst the level of agreement is possibly to some extent fortuitous (approximations include a monolayer of platinum oxides only being formed) the methods both indicate a high level of particle porosity.

This result is significant as it investigates the porosity of nanoparticles using an easy, accessible direct redox process. The *in-situ* methodology can be extended to other electrocatalytic reactions on any other nanomaterials, where the internal structure is essential to understand the full process.[8, 21–25]

5.4 Conclusions

In summary, PtNP aggregates with an internal structure of many (10^2–10^3) small nanoparticles can be investigated *via* direct electrochemical redox reactions. Nanoimpacts were applied, together with XPS, to explore the number of actively oxidized platinum atoms. This provides information about the porosity of nanoparticles and the results are consistent with the findings in Chapter 4, indicating accuracy of the experimental measurements in both cases. Furthermore, the internal structure of nanoparticles is essential in understanding the origin of their redox and catalytic properties. Therefore in the next chapter, the kinetics of the hydrogen oxidation reaction (HOR) will be studied and explained using the knowledge of the porosity of the particles derived in this and the last chapters.

Bibliography

[1] Jiao, X.; Tanner, E. E. L.; Sokolov, S. V.; Palgrave, R. G.; Young, N. P.; Compton, R. G. *Physical Chemistry Chemical Physics* **2017**, *19*, 13547–13552.

[2] Cheng, W.; Compton, R. G. *TrAC, Trends in Analytical Chemistry* **2014**, *58*, 79–89.

[3] Pumera, M. *ACS Nano* **2014**, *8*, 7555–7558.

[4] Rees, N. V. *Electrochemistry Communications* **2014**, *43*, 83–86.

[5] Robbs, P. H.; Rees, N. V. *Physical Chemistry Chemical Physics* **2016**, *18*, 24812–24819.

[6] Zhou, Y.-G.; Haddou, B.; Rees, N. V.; Compton, R. G. *Physical Chemistry Chemical Physics* **2012**, *14*, 14354–14357.

[7] Giovanni, M.; Ambrosi, A.; Sofer, Z.; Pumera, M. *Electrochemistry Communications* **2015**, *56*, 16–19.

[8] Jiao, X.; Sokolov, S. V.; Tanner, E. E. L.; Young, N. P.; Compton, R. G. *Physical Chemistry Chemical Physics* **2017**, *19*, 64–68.

[9] NanoComposix, 50 nm Citrate NanoXact™ Platinum Nanoparticles (Certificate of Analysis Examples): http://50.87.149.212/_Specification%20Sheets/Platinum%20Spec%20Sheets/PT50-NX-CIT-MGM1553.pdf?2581746.

[10] Batchelor-McAuley, C.; Ellison, J.; Tschulik, K.; Hurst, P. L.; Boldt, R.; Compton, R. G. *Analyst* **2015**, *140*, 5048–5054.

[11] Sokolov, S. V.; Eloul, S.; Kätelhön, E.; Batchelor-McAuley, C.; Compton, R. G. *Physical Chemistry Chemical Physics* **2017**, *19*, 28–43.

[12] Dablemont, C.; Lang, P.; Mangeney, C.; Piquemal, J.-Y.; Petkov, V.; Herbst, F.; Viau, G. *Langmuir* **2008**, *24*, 5832–5841.

[13] Şen, F.; Gökağaç, G. *Journal of Physical Chemistry C* **2007**, *111*, 5715–5720.

[14] Bancroft, G. M.; Adams, I.; Coatsworth, L. L.; Bennewitz, C. D.; Brown, J. D.; Westwood, W. D. *Analytical Chemistry* **1975**, *47*, 586–588.

[15] Pourbaix, M. J. N.; Van Muylder, J.; de Zoubov, N. *Platinum Metals Review* **1959**, *3*, 47–53.

[16] The transient charges from each potential were dispersed in a lognormal distribution (evidence shown in Fig. 5.4), with the mean μ and the standard error of mean $\sigma/\sqrt{n}$, as measurements of the minimum current restricted by the potentiostat. To clarify, the "back-transformed" values in terms of charge Q (C) can be written in a mathematical expression according to the lognormal law, with the median $\mu^* = e^{\mu}$ and the multiplicative standard error of mean $(\sigma/\sqrt{n})^* = e^{\sigma/\sqrt{n}}$. Therefore the sign $\times/$ (times/divide) was employed to denote the error, analogous to the $\pm$ notation used in a Gaussian distribution.

[17] Limpert, E.; Stahel, W. A.; Abbt, M. *BioScience* **2001**, *51*, 341–352.

[18] Haynes, W. *CRC Handbook of Chemistry and Physics*, 97th ed.; CRC Press, 2016.

[19] Matsumoto, T.; Nowacki, W. *Zeitschrift für Kristallographie – Crystalline Materials* **1966**, *123*, 401–421.

[20] Nielsen, J. U.; Esplandiu, M. J.; Kolb, D. M. *Langmuir* **2001**, *17*, 3454–3459.

[21] Guo, Z.; Percival, S. J.; Zhang, B. *Journal of the American Chemical Society* **2014**, *136*, 8879–8882.

[22] Ahn, H. S.; Bard, A. J. *Angewandte Chemie, International Edition* **2015**, *54*, 13753–13757.

[23] Kim, J.; Kim, B.-K.; Cho, S. K.; Bard, A. J. *Journal of the American Chemical Society* **2014**, *136*, 8173–8176.

[24] Bigall, N. C.; Härtling, T.; Klose, M.; Simon, P.; Eng, L. M.; Eychmüller, A. *Nano Letters* **2008**, *8*, 4588–4592.

[25] Guo, H.; Liu, X.; Bai, C.; Chen, Y.; Wang, L.; Zheng, M.; Dong, Q.; Peng, D. *ChemSusChem* **2015**, *8*, 486–494.

Chapter 6

Hydrogen Oxidation Reaction on Platinum Nanoparticles: Understanding the Kinetics of Electrocatalytic Reactions *via* Nanoimpacts

The kinetics of the hydrogen oxidation reaction (HOR) on platinum nanoparticles (PtNPs) is explored in this chapter. The steady-state current for HOR on individual PtNPs is measured *via* the nano-impact approach. Adopting the Tafel-Volmer mechanism, the adsorption rate constant for HOR on PtNPs is calculated as 0.020 ± 0.008 m s^{-1}. The HOR is also studied on electrodes where PtNPs are immobilized *via* drop casting on the supporting substrate prior to experimentation and the kinetic parameters contrasted with those from the nano-impact experiments. The distinction in the kinetic parameters between the nano-impact and the drop-casting approaches reveals that the measurement on an individual nanoparticle is required in order to correctly understand the electrochemical reaction catalyzed by nanoparticles, because the aggregation or loss of the nanoparticles drop-casted on the electrode leads to unavoidable errors in the measurement.

The work presented here has been published in *Journal of Physical Chemistry C*[1] and was performed in collaboration with Dr. Chuhong Lin, Dr. Christopher Batchelor-McAuley and Dr. Neil P. Young (Department of Materials, University of Oxford). Dr.

Chuhong Lin developed the theory and carried out all the simulations. Dr. Christopher Batchelor-McAuley helped with the interpretation of the experimental results. Dr. Neil P. Young performed the characterization of the nanoparticles.

6.1 Introduction

In the area of catalysis, the small size provides large surface-to-volume ratio and often a high density of defects, which may alter the catalytic properties of nanoscale materials.[2] Furthermore, the investigations of nanoparticles lead to new insights into the structure–activity relationship of catalysts[3, 4] and help to understand the principles of the catalysis and heterogeneous reactions. In the previous two chapters (Chapters 4 and 5) the porosity of nanoparticles were studied using two different methods and the conclusions are consistent. As the internal structure of nanoparticles is necessary in understanding the catalytic reactions, in this chapter the kinetics of hydrogen oxidation reaction (HOR) will be explored on the same platinum nanoparticles (PtNPs) and the results will be explained based on the knowledge of the porosity of PtNPs.

The electrocatalytic activity of nanoparticles is commonly studied as an ensemble effect by immobilizing a large number of nanoparticles on an inert, conductive substrate.[5] Inherent in such work is the assumption that the structure and the morphology of the nanoparticles on the surface are well-known. However, the coverage of the nanoparticles may change in the experiment due to the aggregation or loss of the nanoparticles, misleading the analysis of experimental phenomena observed on the nanoparticle ensemble.[6–8]

In recent years, the electrochemical characterization of nanoparticles has developed rapidly.[9–11] On dispersing nanoparticles into solution, an individual nanoparticle can collide with an electrode due to its Brownian motion. Impacts are revealed by current spikes or steps at the electrode. As illustrated in Chapter 2, the current can be generated from two main processes: *direct* and *mediated*. The so-called "nano-impact" or "single

nanoparticle collision" approach using individual nanoparticles allows the characterization of the properties and components of nanomaterials,[12–14] as well as the detection of target species in the solution.[15, 16] This electroanalytical approach also provides information about the electrolyte–electrode interface and reaction kinetics, as shown in Chapter 1.[17–19]

In this work, the kinetics of the HOR on PtNPs is investigated. This reaction system is selected because it is a paradigmatic example of an inner sphere reaction and is of both fundamental and commercial interest.[20] Study of the HOR is implemented both on ensembles of PtNPs and at individual PtNPs. The adsorption rate constant for the HOR on individual PtNPs is measured to be 0.020 ± 0.008 m s^{-1}. It is further found that the kinetics for HOR on PtNPs detected from an ensemble of PtNPs is significantly underestimated, emphasizing the importance of applying the nano-impact technique to correctly understand electrocatalytic reactions on nanoparticles. Physical insights into the differences between single nanoparticle and ensemble behavior are drawn.

6.2 Experimental Section

6.2.1 Chemicals

Hydrogen ($\geq$ 99.98% H_2) was supplied from BOC, Surrey, U.K. Potassium nitrate ($\geq$ 99.0%, KNO_3) was obtained from Sigma-Aldrich, Dorset, U.K. Citrate-capped platinum nanoparticles (PtNPs) were provided by nanoComposix, San Diego, CA, U.S.A., with a reported size 25 nm and concentration 3.5×10^{13} particles L^{-1}. All solutions were prepared with ultrapure water from Millipore, with a resistivity of not less than 18.2 MΩ cm at 298 K.

Note that solution are saturated with hydrogen prior to experiments to minimize mass transport limitations. Bubbling time was varied to obtain the optimum length to saturate

the aqueous solution with hydrogen.

6.2.2 Characterization

The stock PtNP samples were characterized *via* transmission electron microscopy (TEM) and ultraviolet–visible (UV–vis) spectroscopy.

TEM

Dr. Neil P. Young (Department of Materials, University of Oxford) conducted the TEM analysis for the mesoporous PtNPs as described below.

TEM (JEOL JEM-3000F FEGTEM, 300 kV accelerating voltage) was performed to determine the size of nanoparticles. Details of the sample preparation and analysis were given in Section 4.2.2 (Chapter 4). The particles were found to be made up of an aggregation of smaller particles (radius about 2 nm), with a mean radius of 24.3 ± 1.6 nm. Example images of the particles and the corresponding size distributions were shown in Figure 4.2 (Chapter 4).

To clarify, in this work, "PtNP" refers to the platinum nanoparticle aggregate (*ca.* 24.3 nm radius), and "small nanoparticle" is the component of a PtNP (*ca.* 2 nm radius). The "PtNP modified electrode" is an inert, conductive electrode (gold) modified by electroactive PtNPs *via* either drop-casting or the nano-impact approach, where the electrochemical reaction only occurs on the PtNPs.

UV–Vis Spectroscopy

For UV–vis (Shimadzu UV-1800 UV–vis spectrophotometer) measurements, the stock PtNP suspension was diluted by a factor of 2 with ultrapure water to obtain absorbance in an analytically meaningful range. Both deuterium and halogen light sources were used, with the sample being scanned from 900 to 200 nm. A broad surface plasmon peak around

295 nm was recorded indicating the presence of PtNPs.[21]

6.2.3 Electrochemistry

Drop-Casting Experiments

A three-electrode system in a Faraday cage was used for all drop cast electrochemical experiments. A μAutolab III from Metrohm Autolab B.V., Utrecht, The Netherlands, was employed as a potentiostat. The working electrode was a gold macrodisk electrode of radius 1.01 mm from BASi, West Lafayette, IN, U.S.A., and the electrode was polished with alumina powders from Buehler, Lake Bluff, IL, U.S.A., in a size sequence of 1.0, 0.3, and 0.05 μm. The reference electrode was a standard mercury/mercurous sulfate electrode (MSE) [Hg/Hg_2SO_4, K_2SO_4 (saturated; +0.64 V vs standard hydrogen electrode, SHE)] from BASi, West Lafayette, IN, U.S.A. The counter electrode was a graphite rod of diameter 6 mm from Sigma-Aldrich, Dorset, U.K. All experiments were conducted under a hydrogen atmosphere. All electrochemical and UV–vis spectroscopy measurements were thermostated at 25 ± 0.5 °C.

Nanoparticle modification of the gold macroelectrode was achieved through drop casting 1 μL of the stock PtNP suspension, directly from the manufacturer, onto the electrode surface. The electrode was subsequently allowed to dry under flowing nitrogen prior to experimentation.

Nano-Impact Experiments

All nano-impact electrochemical experiments were performed on a three electrode system in a Faraday cage. The working electrode was a gold microdisc electrode of diameter 10.0 μm from ALS, Tokyo, Japan, and the electrode was polished with alumina powders from Buehler, Lake Bluff, IL, U.S.A., of decreasing sizes: 1.0, 0.3, and 0.05 μm. A leakless silver/silver chloride electrode [Ag/AgCl, 1.0 M KCl] from Cypress Systems, Lawrence,

KS, U.S.A., functioned as a reference electrode (measured as -0.006 V vs saturated calomel electrode, SCE, [Hg/Hg_2Cl_2, KCl (saturated)], which is equivalent to +0.235 V vs SHE). A platinum foil from Goodfellow, Cambridge, U.K., acted as a counter electrode. All solutions were thoroughly saturated with hydrogen prior to both electrochemical and UV–vis spectroscopy experiments. All measurements were made under thermostated conditions at 25.0 ± 0.5 °C.

Details of the in-house potentiostat can be found in Section 4.2.4 (Chapter 4).[22] To note again, in the context of nano-impact experiments the potentiostat conserves charge and therefore the integral of the current spikes is unaffected in their size analysis.[23]

In the experimental data report below, all potentials are converted to the SHE scale.

6.3 Theory and Simulation

Dr. Chuhong Lin developed the theory and carried out all the simulations as described below.

The simulation model for the platinum nanoparticles (PtNPs) modified electrode and the mechanism of the hydrogen oxidation reaction (HOR) on Pt are discussed in this section. Different geometries of the PtNP are compared in order to explore a suitable and simple simulation model for the HOR on PtNPs.

6.3.1 Simulation for PtNP Modified Electrode

As shown in the TEM images in Figure 4.2 (Chapter 4), a PtNP can be regarded as a sphere with an average radius of 24.3 nm. For the PtNP modified electrode, the PtNPs are assumed to be regularly dispersed on a supporting substrate. Although a regular distribution of the PtNPs is an idealized model, it has been previously applied successfully in the simulation for the drop-casting experiments, especially at low nanoparticle

coverages.[24–28] Therefore, the PtNP modified electrode is treated as a regular array in this work. For a nanoparticle array, the geometry of the nanoparticle also plays a crucial role. There is previous work discussing the influence of the particle geometry in the simulation for nanoparticle modified electrodes.[29] Here two geometries are discussed in the study of HOR on PtNPs: a "sphere model" and a "disc model".

Figure 6.1 illustrates the "sphere model" for the PtNP modified electrode. Figure 6.1 a shows the regular distribution of the spherical PtNPs dispersed on the supporting substrate. The simulation space for each individual PtNP is estimated on the basis of the diffusion domain approximation.[28, 30, 31] It has been shown that the diffusion domain approximation turns the three-dimensional problem into a simpler two-dimensional

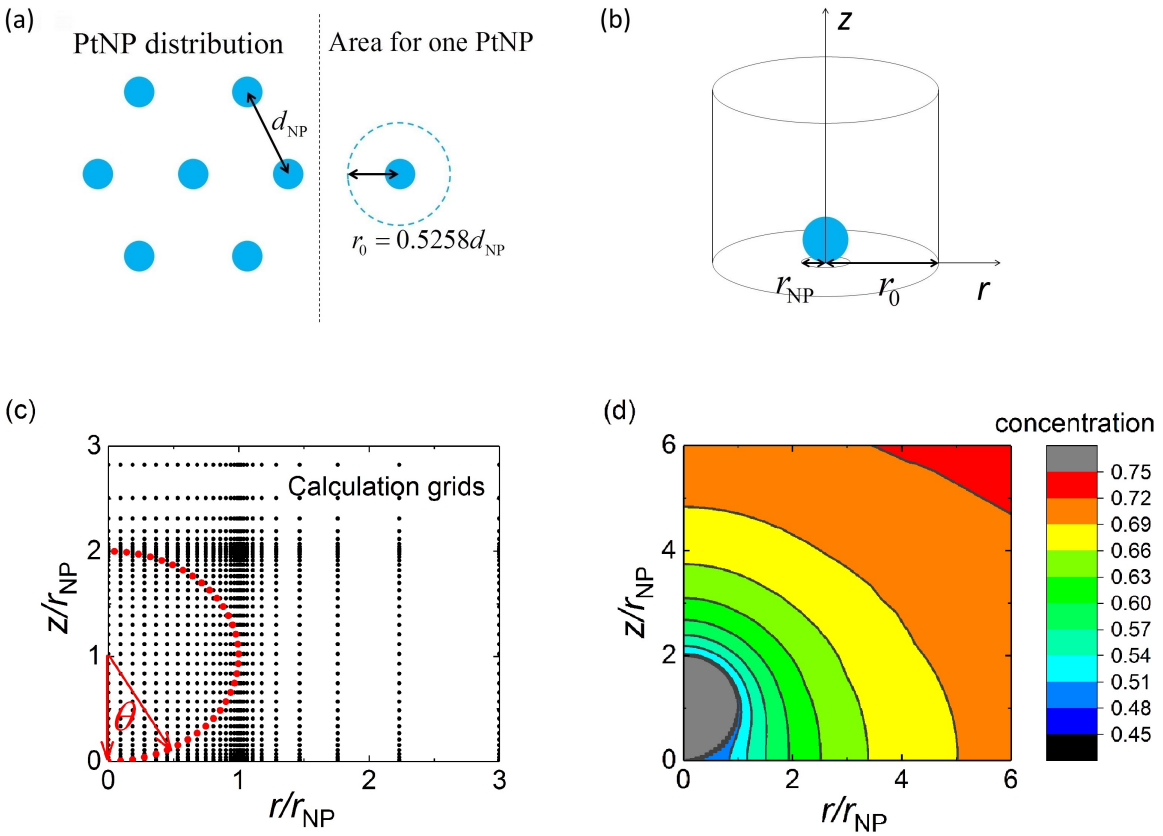

Figure 6.1: Simulation for the PtNP modified electrode with the sphere model. (a) Distribution of the PtNPs on the supporting electrode, where the blue circles are PtNPs and the dashed line shows the simulation area for each PtNP. (b) Simulation space for one PtNP, where the blue sphere is the PtNP. (c) Calculation grids applied in a simulation cell, where the red points are the boundary of a PtNP. (d) An example concentration profile of the reactant.

problem while attaining similar accuracy.[24, 28, 30, 31] Figure 6.1 b shows the simulation space under a two-dimensional cylindrical coordinate for a spherical PtNP. In the cylindrical coordinate system, r is the coordinate parallel to the supporting electrode surface and z is that perpendicular to the supporting electrode. d_{NP} is the average center-to-center distance between two adjacent PtNPs, which can be inferred from the particle coverages used in the experiment. The distribution of the particles is approximated by a hexagonal packing arrangement and the simulating area for an individual PtNP on the supporting substrate is considered as a circular cell with a radius of $0.5258 d_{\mathrm{NP}}$.[32] The radius of the particle is r_{NP} and the radius of the simulation cell is r_0. Thus, the d_{NP} and the coverage of PtNPs have the following relationship:

$$\text{Coverage} = \frac{{r_{\mathrm{NP}}}^2}{\left(0.5258 d_{\mathrm{NP}}\right)^2} \tag{6.1}$$

As the simulation area for one PtNP is symmetric, only half of the space needs to be calculated and the three-dimensional space in Figure 6.1 b can be converted to a two-dimensional cell, as shown in Figure 6.1 c.[33] Figure 6.1 c displays the simulation geometry and the calculation grids for a PtNP based on the approach in the literature.[34–36] Within the area where $r < r_{\mathrm{NP}}$ and $z < 2r_{\mathrm{NP}}$, the grids are given by:

$$\begin{aligned} r_m &= r_{\mathrm{NP}} \sin\left(\theta_m\right),\ \theta_m = 0,\ \frac{\pi}{200},\ \cdots,\ \frac{99\pi}{200},\ \frac{\pi}{2} \\ z_n &= r_{\mathrm{NP}} \left[1 - \cos\left(\theta_n\right)\right],\ \theta_n = 0,\ \frac{\pi}{200},\ \cdots,\ \frac{199\pi}{200},\ \pi \end{aligned} \tag{6.2}$$

where m and n are the indexes of r and z directions. θ is the angle shown in Figure 6.1 c. In the simulation, the angle from 0 to π in the sphere is evenly separated into 200 parts. For the rest, general expanding grids are applied.[37] Figure 6.1 d is an example of the concentration profile for an individual spherical PtNP, showing how the concentration of the reactant gradually changes from the bulk solution to the electroactive surface.

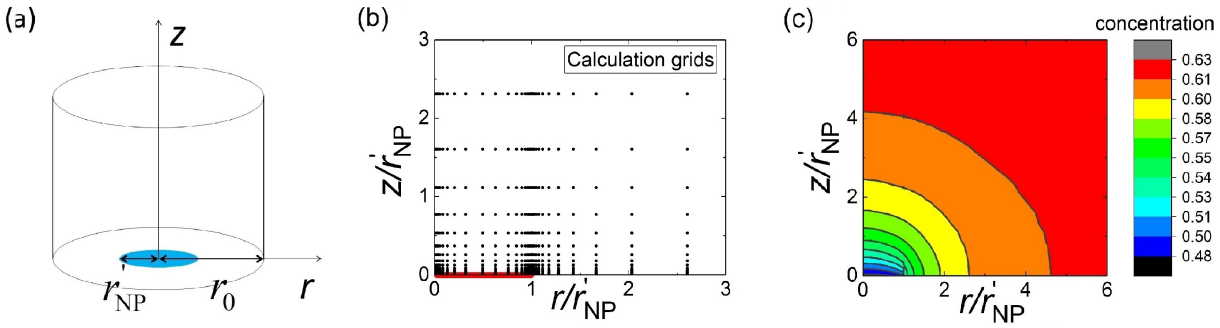

Figure 6.2: Simulation for the PtNP modified electrode with the disc model. (a) Simulation space for one PtNP disc, where the blue sphere is the electroactive area for the PtNP. (b) Calculation grids applied in the simulation cell, where the red line shows the position of the electroactive area. (c) An example concentration profile of the reactant.

An alternative but more approximate approach to simulate the PtNP modified electrode is to apply a disc geometry for the PtNP and keep the equivalent electroactive surface area to the PtNP sphere.[29] For the sphere model, the radius of the PtNP sphere r_{NP} is the average radius for real PtNPs, 25 nm. But as the PtNP disc should have the same surface area with the spherical one, the radius of the PtNP disc r'_{NP} is taken as equal to $2r_{\mathrm{NP}}$, 50 nm. The simulation space and the calculation grids are shown in Figure 6.2, also with an example of the concentration profile for the reactant on an individual disc PtNP. As the geometry is relatively simple in the disc model, general expanding grids are applied in the (r, z) space. In the r direction, as the boundaries are located at $r = 0$ and $r = r'_{\mathrm{NP}}$, the grids symmetrically expand from both 0 and r'_{NP} to the middle point $0.5r'_{\mathrm{NP}}$.

6.3.2 Mechanism of the HOR

The HOR on Pt electrodes is widely thought to follow the Tafel-Volmer mechanism, where the hydrogen molecule first adsorbs and dissociates to two adsorbed H atoms before electron transfer:[4, 38–41]

$$\mathrm{H_2} + 2\,\mathrm{Pt} \underset{k_{\mathrm{d}}}{\overset{k_{\mathrm{a}}}{\rightleftharpoons}} 2\,\mathrm{H_{ads}} \tag{6.3}$$

$$\mathrm{H_{ads}} \underset{k_{\mathrm{red}}}{\overset{k_{\mathrm{ox}}}{\rightleftharpoons}} \mathrm{H^+} + \mathrm{Pt} + \mathrm{e^-} \tag{6.4}$$

where H_{ads} is the hydrogen atom adsorbed on the Pt, k_a and k_b are the adsorption and desorption rate constants, and k_{ox} and k_{red} are the oxidative and reductive electron transfer rate constants. In the above electron transfer step (Equation 6.4), k_{ox} and k_{red} are assumed to follow the Butler–Volmer equation:

$$k_{ox} = k^{\ominus} \exp\left[\frac{\beta F}{RT}\left(E - E_{f,H^+/H_{ads}}\right)\right] \tag{6.5}$$

$$k_{red} = k^{\ominus} \exp\left[-\frac{\alpha F}{RT}\left(E - E_{f,H^+/H_{ads}}\right)\right] \tag{6.6}$$

where α and β are the cathodic and anodic transfer coefficients and $\alpha + \beta = 1$.[42, 43] For the HOR, the values of both transfer coefficients are assumed to be 0.5. $E_{f,H^+/H_{ads}}$ is the formal potential for H^+/H_{ads} redox couple, which can be derived from the Gibbs energy balance in HOR:

$$E_{f,H^+/H_{ads}} = E_{f,H^+/H_2} + \frac{RT}{2F} \ln\left(\frac{k_a c^{\ominus}}{k_d}\right) \tag{6.7}$$

where $c^{\ominus}$ is the standard concentration, equal to 1 mol dm^{-3}. $E_{f,H^+/H_2}$ is the formal potential for the HOR with the H^+/H_2 redox couple. Under the experimental conditions, $E_{f,H^+/H_2}$ is -0.0991 V.[44]

The reaction rate equations for the HOR at a PtNP are:

$$j_{H_2}(\vec{r}_{surf}, t) = -k_a c_{H_2}(\vec{r}_{surf}, t)\left[\frac{\Gamma_M(\vec{r}_{surf}, t)}{\Gamma_{max}}\right]^2 + k_d\left[\frac{\Gamma_{H_{ads}}(\vec{r}_{surf}, t)}{\Gamma_{max}}\right]^2 \tag{6.8}$$

$$\begin{aligned}\frac{\partial \Gamma_{H_{ads}}(\vec{r}_{surf}, t)}{\partial t} = {} & 2k_a c_{H_2}(\vec{r}_{surf}, t)\left[\frac{\Gamma_M(\vec{r}_{surf}, t)}{\Gamma_{max}}\right]^2 - 2k_d\left[\frac{\Gamma_{H_{ads}}(\vec{r}_{surf}, t)}{\Gamma_{max}}\right]^2 \\ & - k_{ox}\left[\frac{\Gamma_{H_{ads}}(\vec{r}_{surf}, t)}{\Gamma_{max}}\right] + k_{red} c_{H^+}(\vec{r}_{surf}, t)\left[\frac{\Gamma_M(\vec{r}_{surf}, t)}{\Gamma_{max}}\right]\end{aligned} \tag{6.9}$$

$$j_{H^+}(\vec{r}_{surf}, t) = k_{ox}\left[\frac{\Gamma_{H_{ads}}(\vec{r}_{surf}, t)}{\Gamma_{max}}\right] - k_{red} c_{H^+}(\vec{r}_{surf}, t)\left[\frac{\Gamma_M(\vec{r}_{surf}, t)}{\Gamma_{max}}\right] \tag{6.10}$$

where $\vec{r}_{\text{surf}}$ refers to the surface of the PtNP:

$$\vec{r}_{\text{surf}} = \begin{cases} r^2 + (z - r_{\text{NP}})^2 = {r_{\text{NP}}}^2 & \text{PtNP sphere} \\ r \leq r'_{\text{NP}},\ z = 0 & \text{PtNP disc} \end{cases} \tag{6.11}$$

The parameters r and z are the cylindrical coordinates used in Section 6.3.1, t is time (t), Γ_i is the surface coverage (mol m^{-2}), $\Gamma_i/\Gamma_{\text{max}}$ is the fractional surface coverage (unitless), Γ_{max} is the maximum surface coverage (mol m^{-2}) at the electrode surface, and $\Gamma_{\text{max}} = \Gamma_{\text{H}_{\text{ads}}}(\vec{r}_{\text{surf}}, t) + \Gamma_{\text{M}}(\vec{r}_{\text{surf}}, t)$. The maximum surface coverage reported in the literature for a monolayer hydrogen adsorption is about 2.2×10^{-5} mol m^{-2} on polycrystalline Pt.[39] The same maximum surface coverage value is applied below in the simulations for PtNP clusters. Considering the rough surface of the PtNPs, the kinetic parameters defined in Equations 6.8–6.10 are "combined" parameters in which the variation of Γ_{max} is taken into consideration.[41, 45]

On the surface of the inert supporting substrate and the edge of the simulation cell, a reflective boundary condition is applied:

$$\left.\frac{\partial c_i(\vec{r}, t)}{\partial \vec{r}}\right|_{\vec{r}_{\text{sub}}, \vec{r}_{\text{edge}}} = 0 \tag{6.12}$$

$\vec{r}_{\text{sub}}$ is the supporting substrate:

$$\vec{r}_{\text{sub}} = \begin{cases} z = 0 & \text{PtNP sphere} \\ r > r'_{\text{NP}},\ z = 0 & \text{PtNP disc} \end{cases} \tag{6.13}$$

$\vec{r}_{\text{edge}}$ is the edge of the simulation cell where $r = r_0$ in both sphere and disc simulation models.

As the electrolyte applied in the experiment to ensure the electrochemical reaction is fully supported, and hence, the mass transport can be taken to be exclusively "diffusional".[46]

The mass transport of the redox species H_2 and H^+ in the solution is described by Fick's second law:

$$\frac{\partial c_i\left(\vec{r},t\right)}{\partial t} = D_i \nabla^2 c_i\left(\vec{r},t\right) \tag{6.14}$$

where i refers to H_2 or H^+, and D_i is the diffusion coefficient. The diffusion coefficients of H_2 and H^+ applied in this work are the values measured in KNO_3 electrolyte,[44, 47] which are 5.0×10^{-9} and 8.1×10^{-9} m^2 s^{-1}, respectively.

Before the electrochemical reaction ($t = 0$), the chemisorption of H_2 on Pt is assumed to follow the Langmuir isotherm:

$$\frac{\left[\Gamma_{H_{ads}}\left(\vec{r}_{surf}, t=0\right)/\Gamma_{max}\right]^2}{\left[1-\Gamma_{H_{ads}}\left(\vec{r}_{surf}, t=0\right)/\Gamma_{max}\right]^2} = \frac{k_a c_{H_2}\left(\vec{r}_{surf}, t=0\right)}{k_d} \tag{6.15}$$

The initial concentrations of H_2 and H^+ are:

$$\begin{aligned} c_{H_2}\left(\vec{r}, t=0\right) &= 0.77 \text{ mM} \\ c_{H^+}\left(\vec{r}, t=0\right) &= 0 \end{aligned} \tag{6.16}$$

The electrolyte solution in the experiment is saturated with H_2 and the hydrogen solubility at standard pressure as given by the Henry's law constant is 0.77 mM.[44]

During the cyclic voltammetry scanning, the electrode potential E and the time t are linked by:

$$\begin{aligned} t < t_{switch},\ E &= E_{ini} + \nu t \\ t > t_{switch},\ E &= E_{switch} - \nu\left(t - t_{switch}\right) \end{aligned} \tag{6.17}$$

where E_{ini} and E_{switch} are the initial and the switching potentials, t_{switch} is the time at which the direction of sweep is switched, and ν is the scan rate.

By solving the diffusion Equation 6.14 with the known initial conditions (Equations 6.15 and 6.16) and boundary conditions (Equations 6.8–6.13), the flux densities j of the

redox species H_2 and H^+ can be calculated from:

$$j_i = -D_i \frac{\partial c_i\left(\vec{r}, t\right)}{\partial \vec{r}}\bigg|_{\vec{r}_{\mathrm{surf}}} \tag{6.18}$$

where i refers to H_2 or H^+. Hence, the cyclic voltammogram (CV) can be simulated:

$$I(E) = F \int_{\mathrm{surf}} j_{\mathrm{H}^+}(E)\ \mathrm{d}A \tag{6.19}$$

where A is the surface area of the PtNP.

The resulting problem was solved numerically by means of the Newton–Raphson method and the alternating direction implicit (ADI) method, the details of which can be found in the literature.[37] In this work, CVs are simulated for the HOR on PtNP modified electrodes. The differences between the sphere model and the disk model will be discussed in next subsections. The simulation was written in C++ with OpenMP for multithreading and simulations were performed using an Intel(R) Xeon(R) 3.60G CPU. The run time varied between approximately 20 min to 20 h per voltammogram, depending on the mesh and the simulation parameters applied to reach convergence.[48]

6.3.3 HOR on PtNP Arrays for Different Geometry Models

Generally the diffusion conditions experienced by PtNPs arrays are determined by the experimental time scale and the coverages of the nanoparticles, and can be divided into four limiting categories, defined as "cases 1–4" in the literature.[29, 32] In cases 1 and 2, the diffusion zones for each particle are separated. But the diffusion zone is perpendicular to the surface of each individual particle for case 4, while it is radial from the surface for case 2. In case 3, the radial diffusion zones for each individual particle overlap somewhat. In case 4, the diffusion zones for each particle fully overlap such that the overall diffusion region becomes planar and linear to the whole electrode. However, as in the experiments

the size of the PtNP (25 nm) and the scan rate for HOR in the cyclic voltammetry (0.1 V s^{-1}) is fixed, the diffusion condition is determined by the coverage of the PtNPs on the supporting substrate and the reaction kinetics. Thus, case 1, which only occurs under an ultrashort experimental time scale, will not be discussed in this work, while cases 2–4 are shown in Figure 6.3.

Apart from the diffusion conditions, different reaction kinetics are considered in addition: one case is where the reaction rate of HOR is fast and the limiting factor for the reaction rate is diffusion, another is where that the reaction rate of the HOR is limited

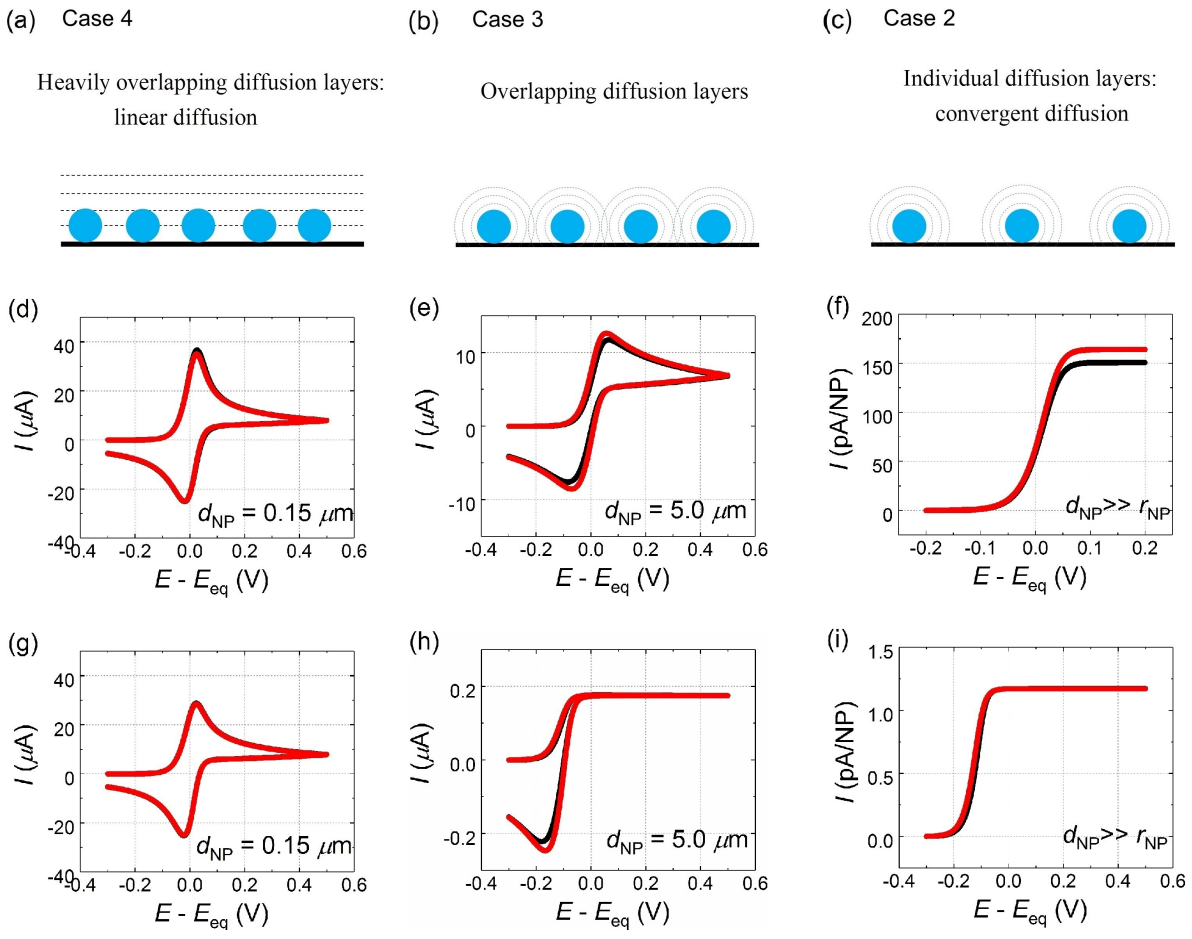

Figure 6.3: Comparison between the voltammograms with the sphere model (black lines) and the disc model (red lines). The reaction rates in (d), (e) and (f) are limited only by the diffusion process and $k_a = 1$ m s^{-1}. The reaction rates in (g), (h) and (i) are limited by the adsorption of H_2 and $k_a = 0.001$ m s^{-1}. k_d is 1.0 mol m^{-2} s^{-1} and $k^{\ominus}$ is 1.0 m s^{-1}. r_{NP} in the nanosphere model is 25 nm and r'_{NP} in the nanodisk model is 50 nm. $c^*_{H_2}$ is 0.78 mM. D_{H_2} is 5.0×10^{-9} m^2 s^{-1} and D_{H^+} is 8.1×10^{-9} m^2 s^{-1}.

by slow adsorption. From a previous study of HOR on Pt, it is known that on microsize electrodes, the reaction rate of HOR is limited by the slow dissociative adsorption of H_2, and the electron transfer rate is relatively fast.[45] Therefore, only the adsorption kinetics and the diffusion of the reactant are taken into consideration as possible limiting factors for the HOR on the PtNP array.

Figure 6.3 a, b and c illustrate the diffusion conditions for three different coverages of PtNPs, that is, cases 4, 3 and 2, respectively. The diffusional cases for the three situations are distinct and thus lead to various voltammetric features. Figure 6.3 d–f and g–i are simulated with different kinetics: the reaction rate is "fast" in Figure 6.3 d–f, and the reaction is limited by the slow adsorption process in Figure 6.3 g–i. When the reaction is fast and the reaction rate is only limited by the diffusion of the reactant, these diffusion-controlled voltammograms change with different PtNP coverages, as shown in Figure 6.3 d–f. The "case 4" voltammetry of Figure 6.3 d, corresponding to linear diffusion in Figure 6.3 a, appears when the center-to-center distance between two adjacent PtNPs is small (compared to the diffusion layer thickness) and the diffusion layers for each PtNP overlap. In contrast, the fully steady-state ("case 2") voltammetry of Figure 6.3 f, corresponding to the convergent diffusion in Figure 6.3 c, can be observed when the distance between particles is large (compared to the diffusion layer thickness) and the diffusion regions for each particle are separated. In the diffusion condition of Figure 6.3 b, the "case 3" voltammetric waveshape is between the "case 4" voltammetry and the "case 2" one, as shown in Figure 6.3 e.

Figure 6.3 g, h and i show the "case 4", "case 3" and "case 2" voltammograms under the adsorption-limited reactions. Although the diffusion-controlled voltammograms and the adsorption-limited ones have similar voltammetric features under the same PtNP coverage, the formation of the waveshapes and the steady-state currents are distinct. In the voltammograms of Figure 6.3 d–f, the diffusion process is the limiting factor for the

reaction, while in Figure 6.3 g–i, the slow adsorption process of H_2 prevents the increase of the current with the overpotential. Compared to the diffusion-controlled situation for one-electron transfer reaction on nanoparticle arrays, which has been well-established in the literature,[29, 36] the HOR has a more complex CE mechanism (C: chemical step; E: electrochemical step). As can be seen from Figure 6.3, the voltammetric responses for the CE reaction on nanoparticle arrays are strongly dependent on the reaction kinetics.

In Figure 6.3, the two simulation geometries, the spherical model of Figure 6.1 and the disc model of Figure 6.2, are also compared with respect to various distribution densities of the nanoparticles and different reaction kinetics. The simulated voltammograms based on the sphere model are shown in black lines while those from the disc are in red. The electroactive areas for HOR on spherical and disc PtNPs are the same in the two simulation models. The voltammograms of the HOR in Figure 6.3 d–f are simulated with fast and reversible reaction kinetics. In this case, the waveshapes for PtNP spheres and discs are very similar in "case 4" (Figure 6.3 d) and "case 3" (Figure 6.3 e) voltammograms. But the diffusion-controlled steady-state currents ("case 2", Figure 6.3 f) for an isolated nanosphere and an isolated nanodisk are different. In the steady state, the analytical diffusion-controlled steady-state currents for HOR on the isolated sphere and the isolated disk of equivalent surface areas can be expressed by:[32, 49]

$$I_{\text{diff,disk}} = 4nFD_{\text{H}_2}c^*_{\text{H}_2}r'_{\text{NP}} \tag{6.20}$$

$$I_{\text{diff,sphere}} = 4\pi nFD_{\text{H}_2}c^*_{\text{H}_2}r_{\text{NP}}\ln(2) \tag{6.21}$$

where r_{NP} in Equation 6.21 is the average radius of the PtNP sphere and r'_{NP} is the radius of the nanodisk, equal to $2r_{\text{NP}}$.

The "case 4", "case 3" and "case 2" voltammetries, for cases where the reaction rate is limited by the adsorption kinetics, are shown in Figure 6.3 g–i. When the coverage

density of the particles is high on the supporting substrate, the forward peaks of the two simulated geometries overlap and the backward peaks have similar waveshapes and peak currents, as shown in Figure 6.3 g and h. For the steady-state voltammetry in Figure 6.3 i, in contrast to the results of Figure 6.3 f, the kinetics-limited steady-state current is insensitive to the change of the geometry of the electroactive PtNP. Therefore, the alternative of the sphere model by the disc one is suitable for the kinetics-limited steady-state voltammetry. In steady state, when the adsorption process is a limiting factor, the adsorption-limited current I_{ad} on a disc microelectrode or nanoelectrode can be expressed as a function of k_{a}:[45]

$$I_{\mathrm{ad}} = I_{\mathrm{diff}} \frac{\frac{k_{\mathrm{a}} r_{\mathrm{NP}}}{D_{\mathrm{H_2}}}}{\frac{4}{\pi} + \frac{k_{\mathrm{a}} r_{\mathrm{NP}}}{D_{\mathrm{H_2}}}} \tag{6.22}$$

which is also valid for an isolated PtNP sphere, but when applying to an isolated PtNP sphere, it needs to be noted that I_{diff} used in Equation 6.22 is the diffusion current in the planar geometry model, calculated from Equation 6.20.

6.4 Results and Discussions

In this section, the drop-casting and the nano-impact techniques are applied to study the hydrogen oxidation reaction (HOR) on platinum nanoparticles (PtNPs). By combining the experimental results with the numerical simulations, kinetic information is collected from both experiments and then analyzed, contrasted, and discussed.

6.4.1 Aggregation Study of PtNPs

UV–vis analysis was performed prior to electrochemical measurements, in the presence of electrolyte (20 mM KNO_3) and gas (air, nitrogen, or hydrogen) to monitor any aggregation of the PtNPs.[21] In particular, hydrogen, H_2, dissociatively adsorbs strongly on platinum and so may displace the capping agent (citrate in the case of interest). It has been

reported[50] that in the presence of hydrogen PtNPs are more susceptible to aggregation: the lower surface charge is thought to decrease the stability of the PtNPs in solution and promote aggregation. Changes in the surface plasmon signals were measured *via* UV–vis spectroscopy at a wavelength of 295 nm. Note that the aggregation can be affected by size, shape of the nanoparticles, and the experimental environment (capping agent, solvent).[51–54]

As shown in Figure 6.4, in both cases of air and saturated nitrogen, no significant variations of the surface plasmon peak were observed during the experimental time scale, indicating stability of PtNPs. With a long exposure time in the presence of hydrogen, the recorded surface plasmon signal attenuated and red-shifted, indicating the aggregation of the nanoparticles. However, over a period of 30 min, the difference between the signals in the presence of hydrogen, nitrogen, or air were tiny and peak heights were closely similar, suggesting little, if any, aggregation happened. Hence in the following, the PtNPs were

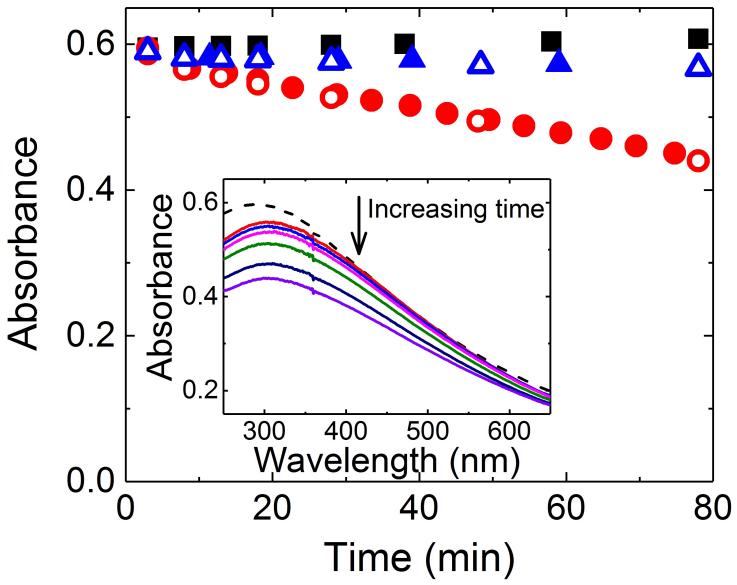

Figure 6.4: Plot of the absorbance against the experimental time measured at a wavelength of 295 nm. Black squares, blue triangles, and red circles represent PtNPs in 20 mM KNO_3 with air, nitrogen, and hydrogen, respectively. Inlay: UV–vis spectrum of PtNPs in 20 mM KNO_3 with hydrogen. The very first absorbance in all three situations and the dotted UV–vis curve in inlay were PtNPs data collected in 20 mM KNO_3 with air, before bubbling any nitrogen or hydrogen. All five points overlaid to give a reproducible UV–vis measurement.

concluded to be stable over this time scale. Consequently, electrochemical measurements were conducted within 30 min in the presence of hydrogen to avoid aggregation.

6.4.2 HOR on Individual PtNPs

The nano-impact technique enables the study of electrochemical reactions at an individual nanoparticle.[9–11] In this work, the HOR on individual PtNPs is explored *via* the nano-impact approach, as described in Section 6.2.3. A gold microdisc electrode (radius of 5.0 μm) was employed and immersed in a 20 mM KNO_3 solution saturated with hydrogen gas. PtNPs were added into the electrolyte solution; when a PtNP strikes and sticks on the supporting Au electrode, current "spikes" and "steps" are observed in the chronoamperograms (CAs).

Figure 6.5 shows a typical current–time profile corresponding to the HOR on individual PtNPs. Figure 6.5 a provides the CAs of 50 s duration at an overpotential of 0.44 V vs the standard hydrogen electrode (SHE). The black line is the CA measured in the presence of 20 pM PtNPs, while the red line shown for comparison is the "blank" CA, where no PtNP was added to the electrolyte. As shown in the inner panel of Figure 6.5 a, current "steps" are recorded in the CA in the presence of PtNPs. In the "blank" CA, no signal steps are visible. In the CA with PtNPs added, current "steps" are only observed in the presence of H_2, indicating that steps are related to the oxidation of hydrogen on the

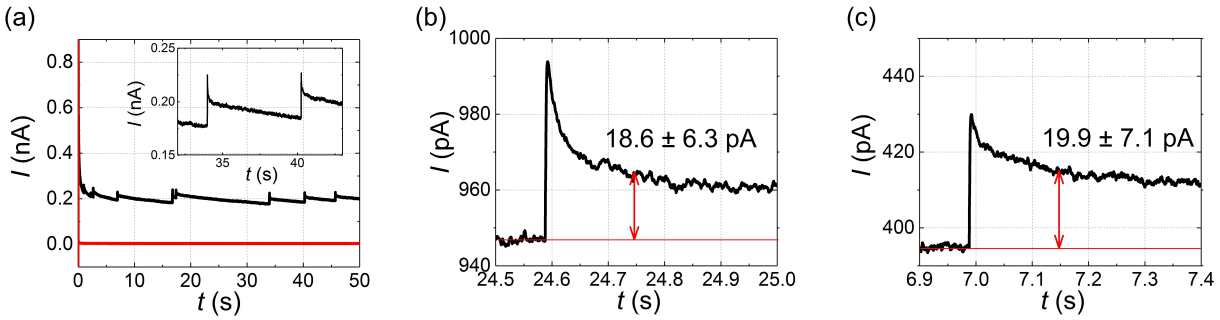

Figure 6.5: (a) CAs for a 5.0 μm Au microelectrode in 20 mM KNO_3 saturated with H_2. (b) and (c) Typical individual PtNP signals seen at (b) 0.34 and (c) 0.44 V (vs SHE).

PtNPs. For the case where both H_2 and PtNPs are present, the stepped nature of the responses suggests that the PtNPs are irreversibly adsorbed on the Au electrode.

Figure 6.5 b and c show two representative current steps for HOR on individual PtNPs recorded at 0.34 and 0.44 V (vs SHE), respectively. The current difference between the point at 150 ms from the starting point and the background (illustrated by the red lines in Figure 6.5 b and c) is regarded as the steady-state current for HOR to an individual PtNP at a certain potential. By averaging the currents measured from several steps, the influence of the noise level on the signals caused by potentiosat is minimized. The average steady-state current is thus measured as 18.6 ± 6.3 pA at 0.34 V and 19.9 ± 7.1 pA at 0.44 V, where the standard deviation somewhat reflects not only the possible experimental noise/error but also the distribution of nanoparticle sizes. As the reacting current does not increase with the potential from 0.34 to 0.44 V, the assumption that the current is indeed at steady state is reasonable and the steady-state current can be taken about 20 ± 7 pA. According to Equation 6.21, if the HOR on an individual PtNP is diffusion-controlled, the diffusional steady-state current I_{diff} would be expected to be 164 pA. The measured steady-state current on isolated PtNPs is clearly smaller than the diffusion-controlled value, showing that even on nanosize Pt, the reaction rate of the HOR is kinetically limited, probably by the slow adsorption kinetics. Equation 6.22 describes the relationship between the adsorption rate constant k_a and the adsorption-limited steady-state current I_{ad}. The adsorption rate constant for HOR on an individual PtNP can be therefore calculated as 0.020 ± 0.008 m s^{-1}.

The adsorption rate constant k_a for HOR measured on polycrystalline Pt microdisc electrodes is reported as 5×10^{-4} m s^{-1}.[41] As estimated, the steady-state current in Figure 6.5 implies an approximate k_a value of 0.02 m s^{-1} for HOR on the nanosize platinum. k_a thus approximately increases by $40\times$ from the polycrystalline Pt electrodes to the PtNPs. This may be because that compared to bulk Pt, the PtNP has much higher

effective surface area. The k_a defined in the Tafel-Volmer mechanism is a "combined" adsorption rate constant,[45] which is not only dependent on the property of the catalyst, but also related to the maximum surface coverage Γ_{max}. For the same material, when Γ_{max} increases, the value of the "combined" k_a increases as a function of the square of Γ_{max}. Thus, the enhancement of k_a from 5×10^{-4} m $^{-1}$ to 0.02 m $^{-1}$ may suggest an increase of Γ_{max}. The simulation constant $\Gamma_{max} = 2.2 \times 10^{-5}$ mol m^{-2} is only valid if the surface of the PtNP can be regarded as smooth as the polycrystalline surface. However, as can be seen from the TEM images (Figure 4.2 in Chapter 4), the surface of the PtNP is composed of many smaller nanoparticles and is likely much "rougher" than a polished polycrystalline Pt surface. Therefore, a PtNP with a rough surface likely has a larger surface density of active sites for HOR than the smooth Pt electrode, indicating why the combined adsorption rate constant changes by about 40× from the polycrystalline Pt to the PtNP.

6.4.3 HOR on Drop-Casted PtNPs

To further explore the kinetics of the HOR on nanosized Pt, the HOR was next studied using PtNPs drop-casted on a gold electrode with various coverages *via* both experiment and numerical simulation. In contrast to the nano-impact experiments, the PtNPs were first immobilized on the supporting Au macroelectrode (radius of 1.01 mm) prior to experimentation. Eight drop-casted electrodes with different coverages of PtNPs were employed in this work. The coverage is the percentage of the area occupied by all the PtNPs in the overall area of the substrate:

$$\text{Coverage of PtNPs (\%)} = \frac{(\pi {r_{NP}}^2) \times N_{NP}}{\pi {r_{Au}}^2} \times 100 \tag{6.23}$$

where N_{NP} is the number of PtNPs and r_{Au} is the radius of the substrate Au electrode. The kinetic study of the HOR on the drop-casted electrodes is more complicated than on individual PtNPs, as the voltammetric features (for instance, the peak current) cannot be described by a simple equation but have to be modeled by numerical simulation. The simulation for the HOR on drop-casted PtNP electrodes has been introduced in Section 6.3. Since the HOR on PtNPs is known to be adsorption-limited, the disc model is applied in the simulation of the PtNP ensemble for convenience.

As mentioned above, the aggregation or loss of the drop-casted nanoparticles can affect the experimental results measured from the drop-casted electrodes.[6] For this reason, the reproducibility of the HOR on various drop-casted PtNPs was tested and two of them are taken as examples: one is the electrode with a relatively high coverage of PtNPs (*ca.* 4.0%) and the other has a low coverage (*ca.* 0.06%). Figure 6.6 shows the reproducibility of the cyclic voltammograms (CVs) for the HOR on the two electrodes. For both coverages, three voltammograms were recorded independently. Reasonable reproducibility is observed, especially for high coverage. The variability likely arises from some loss of the material. Therefore, the CVs with the highest signals were taken as represented of the coverages expected.

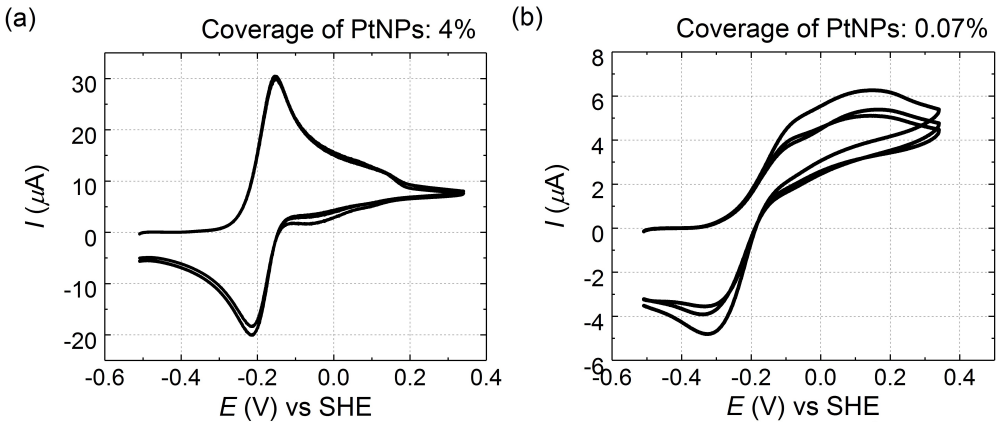

Figure 6.6: CVs of the HOR on two drop-casted electrodes with different coverages of PtNPs: (a) 4.0% and (b) 0.06%. The electrolyte is 0.2 M KNO_3, the bulk concentration of hydrogen is 0.78 mM and the scan rate is 0.1 V s^{-1}. The substrate Au electrode has a 1.01 mm radius.

The experimental CVs for the HOR on various drop-casted electrodes are shown in Figure 6.7 a. The coverage of PtNPs varies from 0.03 to 4.0%. From Figure 6.7 a, for large PtNP coverages, the CV shows an apparent peaked waveshape. When the coverage of the PtNP decreases, the peak becomes less observable. Figure 6.7 b shows the dependence of the forward peak current on the coverage of PtNP. The black line represents the experimental peak currents of Figure 6.7 a, while the blue, red, and yellow lines are the peak currents obtained *via* the numerical simulation with different adsorption rate constants k_a, 0.06, 0.02, and 0.007 m s^{-1}. In the simulation, when the value of k_a changed, the desorption rate constant k_d (mol m^{-2} s^{-1}) and the standard heterogeneous rate constant $k^{\ominus}$ (m s^{-1}) are assigned the same number as k_a (m s^{-1}). The detailed discussion about the choice of k_d and $k^{\ominus}$ for the cyclic voltammetry simulation can be found below in Section A.2 (Appendices). Among the simulated results shown in Figure 6.7 b, those shown for the 0.02 m s^{-1} k_a are the peak currents simulated with the adsorption rate constant measured in the nano-impact experiments. However, in Figure 6.7 b, the experimental peak currents for HOR on the drop-casted PtNPs clearly fit better with the simulated results of 0.007 than 0.02 m s^{-1}, indicating the adsorption rate constant measured on the

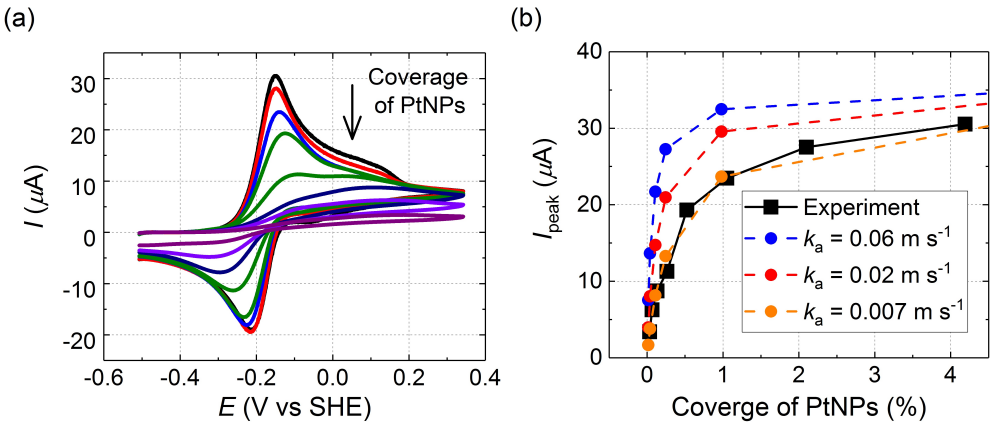

Figure 6.7: (a) CVs for HOR on PtNPs drop-casted electrodes. The coverages of PtNPs from high to low are 4.0, 2.0, 1.0, 0.50, 0.25, 0.12, 0.06, and 0.03%. Detailed calculation of the experimental coverages can be found below in Section A.1 (Appendices). (b) Experimental and simulated forward peak currents varying as a function of the coverage of PtNPs. The black square points are from (a). The blue, red, and yellow circle points are from numerical simulations with k_a equal to 0.06, 0.02, and 0.007 m s^{-1}.

drop-casted PtNPs appears significantly less than that on the individual PtNPs.

It is now recognized[6, 7, 55] that the drop-casting method leads to aggregation on surfaces and also that electrical contact between the nanoparticles and the substrate electrode cannot be guaranteed. The disagreement between the kinetic data inferred from the two techniques likely, again, points to the limitation of the drop-casting approach. Applying the idealized nanoparticle coverages will thus lead to an underestimation for the kinetics of the electrochemical reaction. On the contrary, the nano-impact technique provides the opportunity to measure the reacting current occurring on an individual, active nanoparticle and thus the kinetic parameters determined from the nano-impact experiment are more likely to reflect the physical reality.

6.5 Conclusions

Two different electrochemical approaches, cyclic voltammetry on drop-casted electrodes and nanoimpacts are used to determine the kinetics of the hydrogen oxidation reaction (HOR) on platinum nanoparticles (PtNPs). The adsorption rate constant for HOR on PtNPs can be quantified *via* the steady-state current measured on individual PtNPs in the nano-impact chronoamperometry or the voltammetric responses on the drop-casted PtNP ensembles with various PtNP coverages. In comparison with the adsorption rate constant measured on the bulk platinum electrodes,[41] the adsorption rate for the HOR is larger on the PtNPs. This is likely a consequence of the high effective surface area of the nanoparticle as evidenced by the TEM data. At the same time, the kinetic parameter obtained from the drop-casted PtNP ensembles (*ca.* 0.007 m s^{-1}) differs from the value on the individual PtNPs (*ca.* 0.02 m s^{-1}), reflecting that the kinetics of the electrocatalytic reaction can be misinterpreted and underestimated if the measurement is implemented on an ensemble of nanoparticles rather than at individual nanoparticles. The underestimation is attributed to aggregation or loss of the nanoparticle on the electrode surface in the drop-

casting experiments. The nano-impact technique which allows the detection of individual nanoparticles has merits in the study of kinetics for electrocatalytic reactions. In the next chapter, the activity studies on the HOR will be continued using the same mesoporous PtNPs as in this chapter and in addition another fully solid PtNPs. Clear comparison will be made and dramatic difference of the nano-impact signals will be shown in the results.

Appendices

A.1 Calculation of Coverage of PtNPs

The surface coverage of platinum nanoparticles (PtNPs) can be calculated using the area occupied by all the PtNPs on the substrate electrode divided by that of the electrode and dilution of the stock sample was taken into account. The PtNP suspension was reported, by the manufacturer (nanoComposix, San Diego, CA, U.S.A.), to have a particle concentration of 3.5×10^{13} particles L^{-1} with a 25 nm PtNP radius. The gold macroelectrode was measured to have a radius of 1.01 mm and the volume of each drop cast was 1 μL. DF is the dilution factor of the stock PtNP suspension. Herein:

$$\text{Coverage of PtNPs (\%)} = \frac{\left[\pi \times (25 \times 10^{-9})^2\right] \times (3.5 \times 10^{13}) \times (1 \times 10^{-6})}{\left[\pi \times (1.01 \times 10^{-3})^2\right] \times \text{DF}} \times 100 \quad \text{(A.1)}$$

In the drop-casting experiments discussed in Figure 6.7 (main text), the amount of PtNPs added to the supporting substrate can be converted to the coverage of PtNPs according to Equation A.1 and the values are shown in Table A.1.

Dilute factor	Idealized coverages of PtNPs (%)
0.5	4.0
1	2.0
2	1.0
4	0.50
8	0.25
16	0.12
32	0.06
64	0.03

Table A.1: The idealized coverages of PtNPs for the variety of drop-casted electrodes applied in the experiment of Figure 6.7 a (main text).

A.2 Kinetic Parameters Applied in Simulation of Figure 6.7

For the hydrogen oxidation reaction (HOR) on the drop-casted PtNP clusters, there are four variables determining a voltammogarm: the centre-to-centre distance d_{NP}, the adsorption rate constant k_{a}, the desorption rate constant k_{d}, and the standard heterogeneous rate constant $k^{\ominus}$. The parameter d_{NP} can be inferred from the experimental data as discussed in Section A.1 and for the HOR where the reaction rates are limited by the slow adsorption process, the parameter k_{a} can be calculated from the steady-state current. Therefore, only the voltammetric responses of the parameters k_{d} and $k^{\ominus}$ are unclear for HOR on the PtNPs.

Figure A.1 shows example voltammograms with various kinetic parameters. The influences of k_{d} and $k^{\ominus}$ are studied with two PtNP coverages (the large PtNP coverage

where $d_{\mathrm{NP}} = 0.15$ μm and the small PtNP coverage where $d_{\mathrm{NP}} = 5.0$ μm) and two various adsorption rate constants (the fast adsorption process where $k_{\mathrm{a}} = 1$ m s^{-1} and the slow adsorption one where $k_{\mathrm{a}} = 0.001$ m s^{-1}). From Figure A.1 a, c, e and g, it is found that a slow desorption rate constant k_{d}, corresponding to the process from $\mathrm{H_{ads}}$ to $\mathrm{H_2}$, can apparently decrease the backward peak current, especially under a small particle coverage or a slow adsorption process. From Figure A.1 b, d, f and h, the decrease of the standard heterogeneous rate constant $k^{\ominus}$, can lead to an observable potential shift in the voltammogram and the peak-to-peak separation increases due to the irreversibility of the electron transfer step. Similarly to the influences caused by k_{d}, the voltammogram is affected more by $k^{\ominus}$ when the PtNP coverage is small or the adsorption process is slow.

As for the drop-casting experiments shown in Figure 6.7 (main text), the voltammogram is nearly reversible when the PtNP coverage is high while it shows a quasi-reversible feature especially under a small PtNP coverage, which indicates the value of $k^{\ominus}$ cannot be either too small or too large. The back peaks are observed in all the experimental voltammograms, indicating that the desorption process cannot be ignored in the simulation. As the range of possible k_{d} and $k^{\ominus}$ is found and the value of k_{a} is determined by the experimental results, for convenience, the same desorption rate constant and standard heterogeneous rate constant are selected in the simulation of Figure 6.7 b (main text).

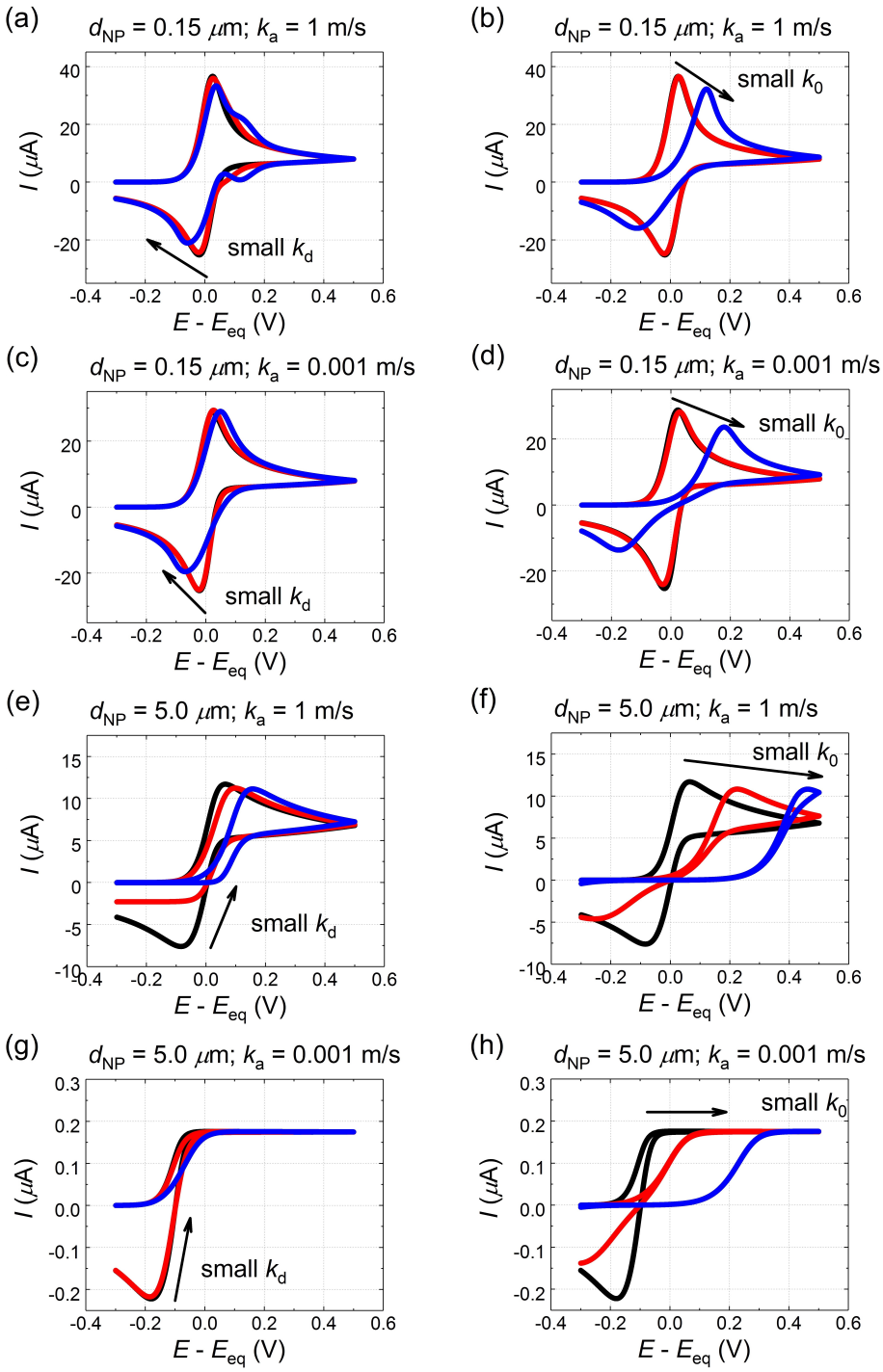

Figure A.1: Voltammetric responses to the kinetic parameters k_d and $k^{\ominus}$ with different particle coverages on the supporting substrate. In panels (a), (c), (e) and (g), $k^{\ominus}$ = 1 m s^{-1} and k_d = 1 (black), 0.01 (red) and 0.0001 (blue) mol m^{-2} s^{-1}. In panels (b), (d), (f) and (h), k_d = 1 m s^{-1} and $k^{\ominus}$ = 1 (black), 0.01 (red) and 0.0001 (blue) mol m^{-2} s^{-1}. E–E_{eq} is the overpotential applied in the simulation.

Bibliography

[1] Jiao, X.; Lin, C.; Young, N. P.; Batchelor-McAuley, C.; Compton, R. G. *Journal of Physical Chemistry C* **2016**, *120*, 13148–13158.

[2] Perez, J.; Gonzalez, E.; Ticianelli, E. *Electrochimica Acta* **1998**, *44*, 1329–1339.

[3] Mukerjee, S. *Journal of Applied Electrochemistry* **1990**, *20*, 537–548.

[4] Chen, S.; Kucernak, A. *Journal of Physical Chemistry B* **2004**, *108*, 13984–13994.

[5] Batchelor-McAuley, C.; Kätelhön, E.; Barnes, E. O.; Compton, R. G.; Laborda, E.; Molina, A. *ChemistryOpen* **2015**, *4*, 224–260.

[6] Toh, H. S.; Batchelor-McAuley, C.; Tschulik, K.; Uhlemann, M.; Crossley, A.; Compton, R. G. *Nanoscale* **2013**, *5*, 4884–4893.

[7] Toh, H. S.; Jurkschat, K.; Compton, R. G. *Chemistry – A European Journal* **2015**, *21*, 2998–3004.

[8] Toh, H. S.; Compton, R. G. *ChemistryOpen* **2015**, *4*, 261–263.

[9] Cheng, W.; Compton, R. G. *TrAC, Trends in Analytical Chemistry* **2014**, *58*, 79–89.

[10] Pumera, M. *ACS Nano* **2014**, *8*, 7555–7558.

[11] Rees, N. V. *Electrochemistry Communications* **2014**, *43*, 83–86.

[12] Sokolov, S. V.; Tschulik, K.; Batchelor-McAuley, C.; Jurkschat, K.; Compton, R. G. *Analytical Chemistry* **2015**, *87*, 10033–10039.

[13] Holt, L. R.; Plowman, B. J.; Young, N. P.; Tschulik, K.; Compton, R. G. *Angewandte Chemie, International Edition* **2016**, *55*, 397–400.

[14] Batchelor-McAuley, C.; Ellison, J.; Tschulik, K.; Hurst, P. L.; Boldt, R.; Compton, R. G. *Analyst* **2015**, *140*, 5048–5054.

[15] Kwon, S. J.; Bard, A. J. *Journal of the American Chemical Society* **2012**, *134*, 10777–10779.

[16] Alligrant, T. M.; Nettleton, E. G.; Crooks, R. M. *Lab on a Chip* **2013**, *13*, 349–354.

[17] Kätelhön, E.; Compton, R. G. *ChemElectroChem* **2015**, *2*, 64–67.

[18] Lin, Q.; Compton, R. G. *Journal of Physical Chemistry C* **2015**, *119*, 23463–23469.

[19] Li, X.; Batchelor-McAuley, C.; Whitby, S. A. I.; Tschulik, K.; Shao, L.; Compton, R. G. *Angewandte Chemie, International Edition* **2016**, *55*, 4296–4299.

[20] Gu, S.; Xu, B.; Yan, Y. *Annual Review of Chemical and Biomolecular Engineering* **2014**, *5*, 429–454.

[21] Creighton, J. A.; Eadon, D. G. *Journal of the Chemical Society, Faraday Transactions* **1991**, *87*, 3881–3891.

[22] Jiao, X.; Sokolov, S. V.; Tanner, E. E. L.; Young, N. P.; Compton, R. G. *Physical Chemistry Chemical Physics* **2017**, *19*, 64–68.

[23] Sokolov, S. V.; Eloul, S.; Kätelhön, E.; Batchelor-McAuley, C.; Compton, R. G. *Physical Chemistry Chemical Physics* **2017**, *19*, 28–43.

[24] Davies, T. J.; Compton, R. G. *Journal of Electroanalytical Chemistry* **2005**, *585*, 63–82.

[25] Davies, T. J.; Lowe, E. R.; Wilkins, S. J.; Compton, R. G. *ChemPhysChem* **2005**, *6*, 1340–1347.

[26] Wang, Y.; Ward, K. R.; Laborda, E.; Salter, C.; Crossley, A.; Jacobs, R. M. J.; Compton, R. G. *Small* **2013**, *9*, 478–486.

[27] Wang, Y.; Laborda, E.; Plowman, B. J.; Tschulik, K.; Ward, K. R.; Palgrave, R. G.; Damm, C.; Compton, R. G. *Physical Chemistry Chemical Physics* **2014**, *16*, 3200–3208.

[28] Brookes, B. A.; Davies, T. J.; Fisher, A. C.; Evans, R. G.; Wilkins, S. J.; Yunus, K.; Wadhawan, J. D.; Compton, R. G. *Journal of Physical Chemistry B* **2003**, *107*, 1616–1627.

[29] Ward, K. R.; Gara, M.; Lawrence, N. S.; Hartshorne, R. S.; Compton, R. G. *Journal of Electroanalytical Chemistry* **2013**, *695*, 1–9.

[30] Amatore, C.; Savéant, J.; Tessier, D. *Journal of Electroanalytical Chemistry and Interfacial Electrochemistry* **1983**, *147*, 39–51.

[31] Sliusarenko, O.; Oleinick, A.; Svir, I.; Amatore, C. *Electroanalysis* **2015**, *27*, 980–991.

[32] Compton, R. G.; Banks, C. E. *Understanding Voltammetry*, 2nd ed.; Imperial College Press, 2011.

[33] Davies, T. J.; Banks, C. E.; Compton, R. G. *Journal of Solid State Electrochemistry* **2005**, *9*, 797–808.

[34] Ward, K. R.; Lawrence, N. S.; Hartshorne, R. S.; Compton, R. G. *Journal of Physical Chemistry C* **2011**, *115*, 11204–11215.

[35] Kätelhön, E.; Barnes, E. O.; Krause, K. J.; Wolfrum, B.; Compton, R. G. *Chemical Physics Letters* **2014**, *595-596*, 31–34.

[36] Ward, K. R.; Lawrence, N. S.; Hartshorne, R. S.; Compton, R. G. *Journal of Electroanalytical Chemistry* **2012**, *683*, 37–42.

[37] Compton, R. G.; Laborda, E.; Ward, K. R. *Understanding Voltammetry: Simulation of Electrode Processes*; Imperial College Press, 2013.

[38] Frumkin, A. N.; Aikazyan, É. A. *Bulletin of the Academy of Sciences of the USSR, Division of Chemical Science* **1959**, *8*, 188–197.

[39] Conway, B.; Tilak, B. *Electrochimica Acta* **2002**, *47*, 3571–3594.

[40] Mann, R.; Thurgood, C. *Journal of Power Sources* **2011**, *196*, 4705–4713.

[41] Lin, C.; Jiao, X.; Tschulik, K.; Batchelor-McAuley, C.; Compton, R. G. *Journal of Physical Chemistry C* **2015**, *119*, 16121–16130.

[42] Guidelli, R.; Compton, R. G.; Feliu, J. M.; Gileadi, E.; Lipkowski, J.; Schmickler, W.; Trasatti, S. *Pure and Applied Chemistry* **2014**, *86*, 259–262.

[43] Guidelli, R.; Compton, R. G.; Feliu, J. M.; Gileadi, E.; Lipkowski, J.; Schmickler, W.; Trasatti, S. *Pure and Applied Chemistry* **2014**, *86*, 245–258.

[44] Jiao, X.; Batchelor-McAuley, C.; Kätelhön, E.; Ellison, J.; Tschulik, K.; Compton, R. G. *Journal of Physical Chemistry C* **2015**, *119*, 9402–9410.

[45] Lin, C.; Batchelor-McAuley, C.; Laborda, E.; Compton, R. G. *Journal of Physical Chemistry C* **2015**, *119*, 22415–22424.

[46] Dickinson, E. J. F.; Limon-Petersen, J. G.; Rees, N. V.; Compton, R. G. *Journal of Physical Chemistry C* **2009**, *113*, 11157–11171.

[47] Macpherson, J. V.; Unwin, P. R. *Analytical Chemistry* **1997**, *69*, 2063–2069.

[48] Kätelhön, E.; Compton, R. G. *Analyst* **2015**, *140*, 2592–2598.

[49] Streeter, I.; Compton, R. G. *Journal of Physical Chemistry C* **2007**, *111*, 18049–18054.

[50] Furlong, D. N.; Launikonis, A.; Sasse, W. H. F.; Sanders, J. V. *Journal of the Chemical Society, Faraday Transactions 1: Physical Chemistry in Condensed Phases* **1984**, *80*, 571–588.

[51] Kelly, K. L.; Coronado, E.; Zhao, L. L.; Schatz, G. C. *Journal of Physical Chemistry B* **2003**, *107*, 668–677.

[52] Evanoff, D. D.; Chumanov, G. *Journal of Physical Chemistry B* **2004**, *108*, 13957–13962.

[53] Mock, J. J.; Barbic, M.; Smith, D. R.; Schultz, D. A.; Schultz, S. *Journal of Chemical Physics* **2002**, *116*, 6755–6759.

[54] Stevenson, A. P.; Blanco Bea, D.; Civit, S.; Antoranz Contera, S.; Iglesias Cerveto, A.; Trigueros, S. *Nanoscale Research Letters* **2012**, *7*, 151.

[55] Cloake, S. J.; Toh, H. S.; Lee, P. T.; Salter, C.; Johnston, C.; Compton, R. G. *ChemistryOpen* **2015**, *4*, 22–26.

Chapter 7

Role of Nanomorphology and Interfacial Structure of Platinum Nanoparticles in Catalyzing the Hydrogen Oxidation Reaction

This chapter studies the hydrogen oxidation reaction (HOR) using both single mesoporous platinum nanoparticles (PtNPs; $r_{NP} = 23.1 \pm 2.1$ nm) and low density random arrays of the same particles. The activity of the platinum catalyst, towards the oxidation of hydrogen, is shown to be potential dependent and exhibits two peaks in activity. These peaks are measured at both random arrays of PtNPs and at the single entity scale. This alteration in the particle activity is directly reflected in the variation of the electrochemical current. These peaks in current do *not* relate to a mass-transport limitation of the reaction, and at high overpotentials the oxidation reaction becomes fully inhibited. This potential dependency is revealed at high current densities and arises due to the sensitivity of the reaction rate to the platinum interfacial structure; the decrease in activity [at *ca.* -0.2 V vs Ag/AgCl (1.0 M KCl) in 20 mM KNO_3] directly correlates with the potential at which underpotential deposited hydrogen (H_{upd}) is removed from the catalytic interface. The contribution of the internal mesoporous nanoparticle structure toward the total particle catalytic activity is further evidenced through comparison of the time-current transients recorded for individual mesoporous particles with authentically solid particles,

and by evidencing the sensitivity of the single particle catalytic activity to the supporting electrolyte concentration.

The work herein presented has been published in *ACS Catalysis*[1] and was carried out in collaboration with Dr. Christopher Batchelor-McAuley, Dr. Chuhong Lin, Dr. Enno Kätelhön, Dr. Eden E. L. Tanner and Dr. Neil P. Young (Department of Materials, University of Oxford). Dr. Christopher Batchelor-McAuley and Dr. Eden E. L. Tanner helped with the interpretation of the experimental results. Dr. Chuhong Lin and Dr. Enno Kätelhön carried out all the simulations. Dr. Neil P. Young performed the characterization of the mesoporous and solid PtNPs.

7.1 Introduction

The previous chapters (Chapter 4, 5 and 6) have discussed the porosity of the platinum nanoparticles (PtNPs) and how the internal structure of the particles can affect its catalytic activity. In this chapter, the role of interfacial structure will be studied on the same mesoporous PtNPs, and the function of nanomorphology will be investigated by comparing the reaction of the mesoporous PtNPs with authentically and fully solid PtNPs.

With the advent of energy conversion technologies such as fuel cells, redox flow batteries, and solar cells, the development of advanced electrocatalytic materials has been a significant focus. However, for a heterogeneous process at a solid–liquid interface, quantifying the efficiency of a given catalytic material is often complicated by the difficulty in clearly delineating the contributions from the chemical and physical aspects of the material; altering a surface's architecture[2] and morphology may vary the number and/or nature of the active sites, change the local mass transport, or in the case of a redox reaction cause the local solution potential profile to be altered. Development of new materials beyond recourse to empiricism requires the study of archetypal reactions under well-defined conditions to enable the development of greater theoretical insight. Over the preceding

century, the understanding of outer-sphere redox reactions has advanced massively with seminal contributions from Marcus,[3] Hush,[4, 5] and in relation to electrochemical interfaces, Chidsey.[6] In contrast, plausibly partially hindered by a lack of experimental information, the theoretical understanding of so-called inner-sphere reactions, proceeding *via* surface adsorbed intermediates, is arguably still relatively limited.

For a heterogeneous redox reaction, the electrochemical "reversibility" of the process is controlled by the interfacial rate constant relative to the local mass transport. Consequently, studying the kinetics of fast interfacial processes necessitates the use of high mass-transport conditions. One route by which such high rates of mass transport may be attained is through the study of interfacial reactions at individual nanoparticles.[7, 8] For many conventional experiments, the influence of the double layer upon the mass transport of solution phase material can (to a reasonable approximation due to the differing length scales involved) be ignored.[9] However, as experiments move from studying electrochemical reactions at the micro- to the nanoscopic scale, the diffusional depletion zone contracts and the two processes cannot be considered fully independent.[10] As a further complicating factor, interfacial redox processes proceed *via* surface intermediates; these species are necessarily situated within the so-called Inner Helmholtz Plane (IHP), and at such length scales the double layer structure, although considered at great length, remains essentially experimentally unvalidated.[11]

The proton/hydrogen redox couple is a paradigmatic example of an inner-sphere interfacial process, and it is upon this reaction that much of the insight into this reaction class is gained. At a platinum surface, the kinetics of the hydrogen/proton redox couple are "fast" with the electron transfer being near "reversible" in acid[12] and slower in alkaline media with the reaction rate exhibiting sensitivity to the surface crystallinity.[13] This reaction still holds information regarding the processes occurring at the ångström length scale with recent work by Koper *et al.* demonstrating the likely importance of the local

interfacial water structure in controlling the reaction rate.[14] Under alkaline conditions, the addition of a submonolayer coverage of $Ni(OH)_2$ was found to appreciably alter and increase the kinetics of this process. The influence of the nickel was interpreted as due to a change in the potential of zero free charge, hence influencing the "rigidity" of the water situated at the interface. At higher overpotentials and under high mass-transport conditions, it was recognized as early as the 1950's by Frumkin[15] that, even on platinum, the hydrogen oxidation reaction (HOR) becomes limited by the rate of chemisorption of hydrogen onto platinum surfaces. Recent work has demonstrated that in this adsorption limited regime, the current is not constant and exhibits two peaks in the activity of the catalyst as a function of potential. The origin of this so-called "fine structure" is debatable but has been previously described using a two-site model.[16] A significant focus of this chapter will be to further elucidate the physical origins of this variation in activity and evidence that this variability can be observed at the single particle scale.

Apart from being of fundamental importance, the hydrogen/proton redox couple is key to the possible realization of the hydrogen economy. Advances in fuel cells have led to a dramatic lowering of the required platinum loading, with the present state of the art requiring $\sim$0.25 g of platinum group metal per kilo Watt of power.[17] As a consequence of this decrease in the platinum loading and the operation of these devices at high currents, in part to afford greater power, large turnover rates occur at the surface of the catalyst, with current densities on the order of 1 A cm^{-2}.[18] Consequently, there is a distinct need to study well-characterized catalyst materials under conditions of high current density.[19] Single particle studies represent an extreme limit for the investigation of low particle loadings and ensure high rates of mass transport to the catalytic interface, ideal for the investigation of fast electrochemical processes. Traditionally electrocatalytic materials are characterized through the use of a rotating disc electrode, and it is by this methodology that all new fuel cell catalysts are benchmarked.[20–22] For commercial

rotating disc electrode (RDE) devices, the maximum rotation rate is commonly on the order of 10^4 rpm.[23] At these speeds, the diffusion-limited current for a molecular species in millimolar concentration is limited to a few mA cm^{-2} and corresponds to a diffusional mass-transport rate of $\sim 1 \times 10^{-3}$ m s^{-1}. The reporting of higher "kinetic" current densities is often achieved through the use of the Koutecký–Levich equation allowing, under optimal conditions, for the mass-transport limitation to be accounted for. For heterogeneous surfaces, the validity of such an approach may be questioned.[24–26] Importantly, the low current electrocatalyst characteristics as derived from RDE-type experiments do not necessarily correlate in a simple manner with whole device performance,[19] where in real applications the catalytic material is utilized under extreme current densities to ensure efficient and optimal use of the platinum group metals. Decreased catalyst loading at an RDE is one route by which higher specific current densities may be experimentally attained; however, with low catalyst loadings, complications arise in the production of reproducible and relatively homogeneous nanoparticle surface coverages.[20] Alternately, fabrication of macroscopic gas diffusion electrodes allows material to be studied under high current densities;[27] however, the mass-transport profile of such systems is poorly defined due to the need to account rigorously for the structure and tortuosity of the porous gas membrane. Single nanoparticle studies provide a complementary route for the fundamental investigation of interfacial reactions under high mass-transport conditions.

Previous work looking at the response of individual mesoporous PtNPs have emphasized electrochemical accessibility of the internal interfaces toward the formation of surface oxides[28] and have demonstrated the ability of hydrogen oxidation and evolution to be studied on the single particle scale.[29–31] This work studies the HOR at individual mesoporous nanoparticles revealing how the nanoparticle structure contributes to the catalytic performance of the material. The study of single nanoparticle reactions has been partially hampered by colloidal stability in the presence of electrolytes.[32, 33] However, since the

1980's it has been recognized that use of a microelectrode enables redox reactions to be driven at an electrochemical interface in the absence of high electrolyte concentrations and without significant ohmic distortion.[34, 35] This, as will be demonstrated, holds true at the nanoscale where due to the small currents involved (picoampere), redox reactions can be performed at individual nanoparticles in resistive media and importantly allow insight into the activity of the mesoscale nanoparticle structure.

This chapter investigates the influence of both the chemical (interfacial structure) and physical (nanoparticle mesoporous structure) factors contributing and controlling the activity of a platinum catalyst toward the oxidation of hydrogen. Both random arrays of particles and individual platinum entities show potential dependent variability in the catalytic activity of the material. However, studying the HOR on a single particle basis enables the reaction to be studied under conditions of very high mass transport (approaching 0.15 m s^{-1} for a completely isolated 23.1 nm radius particle). Under these high current density conditions, it is revealed that even at the single particle scale there are peaks in the catalytic activity, as reflected in the measured electrochemical current of the platinum catalyst, varying as a function of the applied potential. These peaks relate not to a mass-transport limitation but reflect the change and decrease of the interfacial reaction rate at high overpotentials. Moreover, by studying single catalytic nanoparticles one at a time the influence of the nanoparticles internal mesoporous structure upon the overall reaction rate is exemplified.

7.2 Experimental Section

7.2.1 Chemicals

Hydrogen ($\leq$ 99.98% H_2) was supplied from BOC, Surrey, U.K. Potassium nitrate ($\leq$ 99.0%, KNO_3), potassium perchlorate ($\leq$ 99%), and perchloric acid (70%) were obtained

from Sigma-Aldrich, Dorset, U.K. Potassium hydroxide was obtained from Fisher Scientific, Loughborough, U.K. Citrate-capped mesoporous platinum nanoparticles (mesoporous PtNPs) were provided by nanoComposix, San Diego, CA, U.S.A. with a reported diameter 50 nm and concentration 3.3×10^{13} particles L^{-1}. Solid platinum nanoparticles (solid PtNPs) were provided by Particular GmbH, Burgdorf, Germany, with a reported diameter 50 nm and concentration 100 mg L^{-1}. All solutions were prepared with ultrapure water from Millipore, with a resistivity of not less than 18.2 MΩ cm at 298 K.

7.2.2 Characterization

The stock mesoporous and solid PtNP samples were characterized *via* transmission electron microscopy (TEM) and ultraviolet–visible (UV–vis) spectroscopy.

TEM

Dr. Neil P. Young (Department of Materials, University of Oxford) conducted the TEM analysis for both the mesoporous and the solid PtNPs as described below.

TEM (JEOL JEM-3000F FEGTEM, 300 kV accelerating voltage or JEOL JEM-2100, 200 kV accelerating voltage) was performed using conventional bright field imaging to determine the size of mesoporous or solid PtNPs. Details of the sample preparation and analysis were given in Section 4.2.2 (Chapter 4). A total count of 86 mesoporous PtNPs gave a mean radius of 23.1 ± 2.1 nm, close to the value of 25 nm provided by the manufacturer; 49 small particles were averaged to give a mean radius of 2.0 ± 0.3 nm. Figure 7.1 shows two TEM images of mesoporous PtNPs. The size distributions of the mesoporous PtNPs and the component small nanoparticles are shown in Figure 7.2. A total count of 118 solid PtNPs gave a mean radius of 26.7 ± 9.5 nm, close to the value of 25 nm provided by the manufacturer. Figures 7.3 and 7.4 present the TEM images of solid PtNPs and the corresponding size distribution.

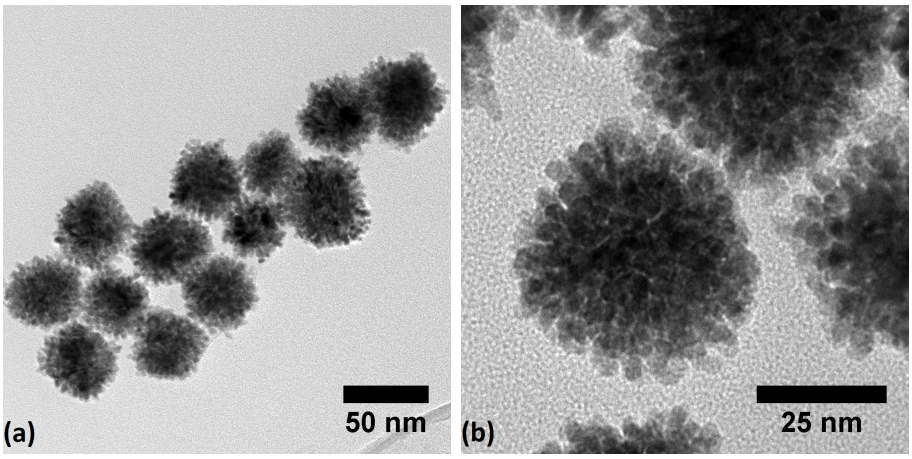

Figure 7.1: (a) and (b) are TEM images of mesoporous PtNPs.

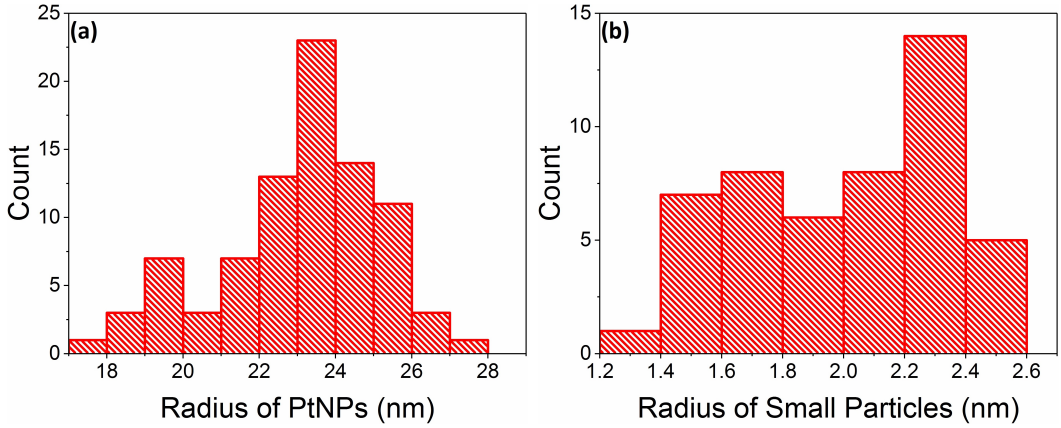

Figure 7.2: Size distributions of (a) mesoporous PtNPs and (b) small particles contained in the aggregate PtNP structure with average radii of 23.1 ± 2.1 nm and 2.0 ± 0.3 nm, respectively.

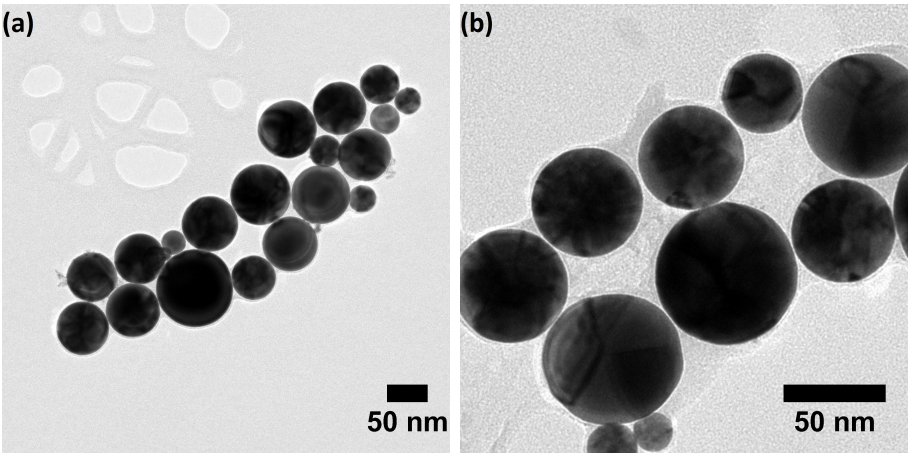

Figure 7.3: (a) and (b) are TEM images of solid PtNPs.

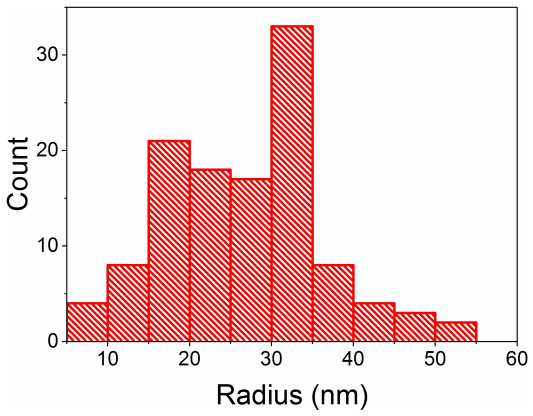

Figure 7.4: Size distribution of solid PtNPs with an average radius of 26.7 ± 9.5 nm.

To clarify, in this chapter, the "mesoporous PtNP" refers to the mesoporous 23.1 nm particle, and the "small particles" are the 2.0 nm components of a mesoporous PtNP.

UV–Vis Spectroscopy

For UV–vis (Shimadzu UV-1800 UV–vis spectrophotometer) measurements, the stock mesoporous or solid PtNP sol was diluted by a factor of 2 with ultrapure water to obtain absorbance in an analytically meaningful range. Both deuterium and halogen light sources were used, with the sample being scanned from 900 to 200 or 236 nm. A broad surface plasmon peak around 295 or 285 nm was recorded, indicating the presence of mesoporous or solid PtNPs.[36]

7.2.3 Electrochemistry

Macroelectrode and Drop-Casting Experiments

A three-electrode system in a Faraday cage was used for all ensemble electrochemical experiments. A μAutolab III from Metrohm Autolab B.V., Utrecht, The Netherlands, was employed as a potentiostat. The working electrode was a platinum or gold macrodisk electrode of radius 830 ± 5 μm or 1 mm from BASi, West Lafayette, IN, U.S.A. and the electrode was polished with alumina powders from Buehler, Lake Bluff, IL, U.S.A.

in a size sequence of 1.0, 0.3, and 0.05 μm. The reference electrode was a standard mercury/mercurous sulfate electrode (MSE) [Hg/Hg_2SO_4, K_2SO_4 (saturated; +0.64 V vs standard hydrogen electrode, SHE)] from BASi, West Lafayette, IN, U.S.A. or a leakless silver/silver chloride electrode [Ag/AgCl, 1.0 M KCl] from Cypress Systems, Lawrence, KS, U.S.A. (measured as -0.006 V vs saturated calomel electrode, SCE, [Hg/Hg_2Cl_2, KCl (saturated)], which is equivalent to +0.235 V vs SHE). The counter electrode was a graphite rod of diameter 6 mm from Sigma-Aldrich, Dorset, U.K., or a platinum foil from Goodfellow, Cambridge, U.K. All solutions were thoroughly saturated with hydrogen prior to both electrochemical experiments. All measurements were made under thermostated conditions at 25.0 ± 0.5 °C.

Ensemble and Nano-Impact Experiments

All ensemble and nano-impact electrochemical experiments were performed on a three electrode system in a Faraday cage. The working electrode was a gold microdisc electrode of diameter 10.0 μm from ALS, Tokyo, Japan, and the electrode was polished with alumina powders from Buehler, Lake Bluff, IL, U.S.A. of decreasing sizes: 1.0, 0.3, and 0.05 μm. Note that the gold electrode was employed in the experiments as it is inert at the potential of interest towards hydrogen evolution. A leakless silver/silver chloride electrode [Ag/AgCl, 1.0 M KCl] from Cypress Systems, Lawrence, KS, U.S.A. functioned as a reference electrode (measured as -0.006 V vs saturated calomel electrode, SCE, [Hg/Hg_2Cl_2, KCl (saturated)], which is equivalent to +0.235 V vs SHE). A platinum foil from Goodfellow, Cambridge, U.K., acted as a counter electrode. All experiments were conducted under a hydrogen atmosphere. All electrochemical measurements were thermostated at 25 ± 0.5 °C.

Details of the in-house potentiostat can be found in Section 4.2.4 (Chapter 4).[37] Python 3.5 (Canopy from Enthought, Austin, TX, U.S.A.) was employed to control the

data acquisition (DAQ). The DAQ device oversampled and digitized the incoming analogue signal at a stream rate of 100 kHz, and the digitized signal was subsequently filtered at a bandwidth of 100 Hz. To note again, in the context of nano-impact experiments the potentiostat conserves charge and therefore the integral of the current spikes is unaffected in their size analysis.[38]

7.3 Results and Discussion

This work commences by outlining the behavior of individual mesoporous platinum nanoparticles (PtNPs), a macroscopic platinum electrode, and random arrays of PtNPs toward the oxidation of hydrogen. Analysis methods enabling the rigorous characterization of the single particle response are employed, enabling direct comparisons to be drawn between the hydrogen oxidation behavior of the differing platinum structures (macro, micro array and nanoparticulate). Under high mass-transport conditions (*ca.* 0.15 m s^{-1}), the oxidation of hydrogen exhibits two voltammetric peaks at high overpotentials, in the region where the rate of reaction is limited by the adsorption kinetics of hydrogen to the catalytic interface. Through the study of the dependency of the platinum response, under high mass-transport conditions, to the solution phase pH, the sensitivity of the adsorption rate to the interfacial platinum surface structure is demonstrated. Finally, the chapter turns to consider the time-current response of individual nanoparticles, highlighting, first, the contribution of underpotential deposited hydrogen (H_{upd}) toward the oxidative current at the short time scale and, second, through comparison with the response of particles of a different morphology (solid vs mesoporous), the catalytic activity and contribution of the internal structure is evidenced.

7.3.1 HOR at Individual Nanoparticles

The nanoparticles predominantly used in this chapter are 23.1 ± 2.1 nm in radius, and each particle is formed from an aggregate of smaller particles with radii 2.0 ± 0.3 nm that leads to the particles having a mesoporous structure. In the final section of this chapter, the individual nanoparticle response will be contrasted with that of a sample of solid particles. Representative TEM images of the mesoporous particles are shown in Figure 7.5; further sizing information is provided in Section 7.2.2. As can be seen, the particles have an open structure and have a relatively large surface area; assuming the constituent 2.0 nm particles form a closed packed structure, the nanoparticles surface area can be calculated as being ~8.5 times greater than that of the equivalent solid circumscribed sphere.

First, a potentiostated gold microelectrode was immersed into a colloidal sol of mesoporous nanoparticles (20 pM), saturated with hydrogen (0.73 mM; shown later, calculated from Henry's law), and containing 20 mM KNO_3. At potentials positive of approximately -0.4 V vs Ag/AgCl (1.0 M KCl), small steps were observed in the measured current; an

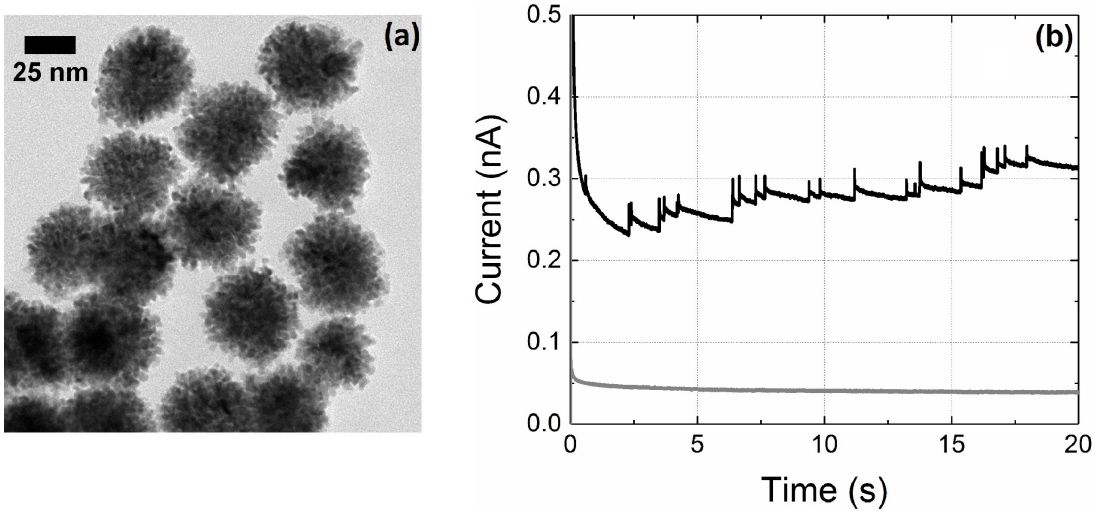

Figure 7.5: (a) TEM image of the mesoporous PtNPs. (b) CA of 20 pM mesoporous PtNPs in 20 mM KNO_3 at a gold microelectrode with an applied potential of 0.2 V (black line); the average step in current is 11.1 pA, as measured 200 ms after the individual feature onsets. Overlaid is a CA in the absence of impacting nanoparticles (gray line).

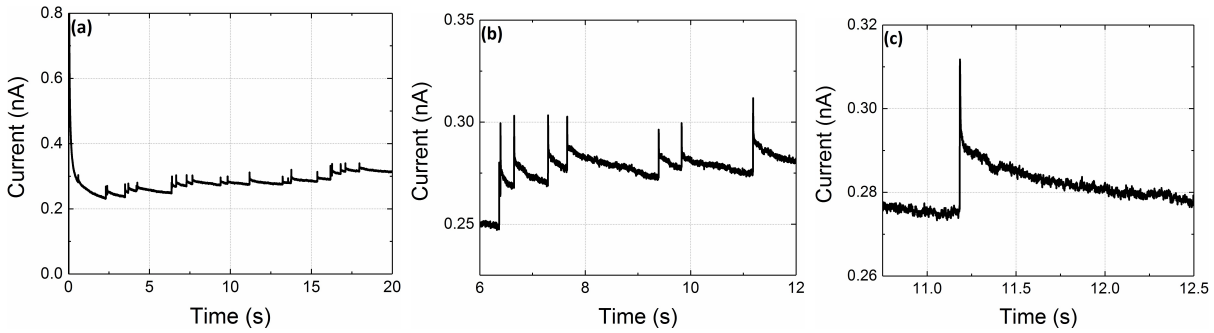

Figure 7.6: (a) CAs of 20 pM mesoporous PtNPs in 20 mM KNO_3 at a gold microelectrode with an applied potential of 0.2 V. (b) and (c) are zoomed in plots of (a).

example chronoamperogram (CA) recorded at +0.2 V is depicted in Figure 7.5 b, further zoomed in examples are shown in Figure 7.6. These small steps in current are associated with the arrival of individual platinum catalytic entities to the electrode surface. Upon impact and electrical contact of the particles to the electrode surface, the HOR is electrochemically driven to occur at the newly arrived nanoparticulate material, and this leads to a measurable increase in the current. These small (pA) steps in current are superimposed upon a monotonically changing background associated with the capacitative charging of the gold electrode substrate. Notably, within the available electrochemical window and in the absence of nanoparticles, no "steps" in current are observed; moreover, the gold electrode substrate itself is unable to catalyze the oxidation of hydrogen to any appreciable extent. Each new step represents the arrival of more new material to the interface, and the steady increase in the catalytic current over the course of the reaction strongly indicates that the nanoparticles are irreversibly adsorbing to the electrode surface. In this experiment, only 20 mM KNO_3 electrolyte is used to ensure the agglomeration of the nanoparticles in solution is minimized. The associated UV–vis spectra show below evidencing the metastability of the sol in this millimolar ionic strength solution.

UV-Vis Experiments Evidencing the Colloid Stability in Millimolar Electrolyte Concentrations

UV-vis experiments were conducted to evidence the stability of mesoporous and solid

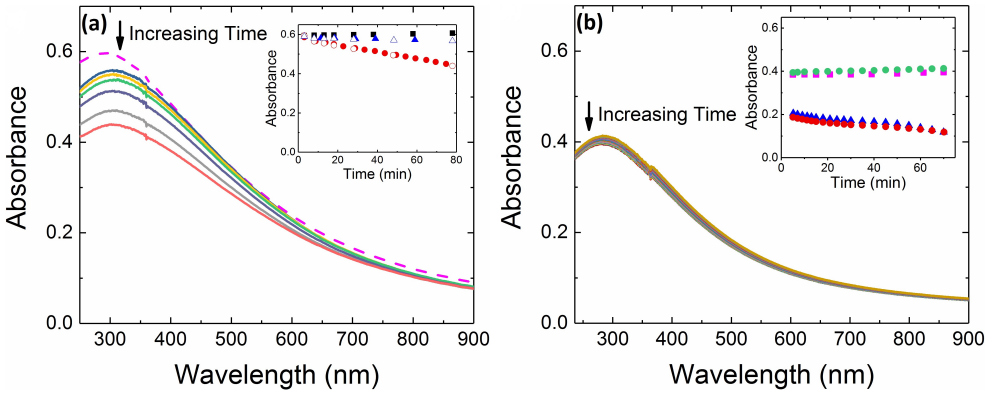

Figure 7.7: (a) UV-vis spectrum of the mesoporous PtNPs in 20 mM KNO_3 with H_2. Inlay: plot of the absorbance against the experimental time measured at a wavelength of 295 nm. Black squares, blue triangles and red circles represent PtNPs in 20 mM KNO_3 with air, N_2 and H_2, respectively. The dotted UV-vis curve and the very first absorbance in all three situations in inlay were PtNPs data collected in 20 mM KNO_3 with air, before bubbling any N_2 or H_2. All five points overlaid to give a reproducible UV-vis measurement. (b) UV-vis spectrum of solid PtNPs in water with H_2. Inlay: plot of the absorbance against the experimental time measured at a wavelength of 285 nm. Pink squares and green circles represent PtNPs in water with air and H_2; Blue triangles and red circles represent PtNPs in 20 mM KNO_3 with N_2 and H_2.

PtNP colloids. Both types of nanomaterials exhibit a broad but clearly defined plasmon adsorption peak at ∼300 nm. Mesoporous PtNPs were stable in 20 mM KNO_3 in the presence of H_2 within 30 minutes, as shown in Figure 7.7 a. The UV-vis plasmon adsorption peak decreased after 30 minutes, suggesting an agglomeration of the nanoparticles. In order to minimize the influence of agglomeration upon the results, all experiments were restricted to being performed in the first 30 minutes after any electrolyte was added to the nanoparticle sol. In contrast, the solid PtNPs were only stable in absence of electrolyte, as shown in Figure 7.7 b. This differing sensitivity towards the presence of salt reflects the fact that the solid nanoparticles have been produced using laser ablation in the absence of a capping agent.

The arrival of a nanoparticle at the gold surface and the corresponding recorded steps "up" in current yield a direct measure of the rate of reaction at an individual nano entity. These steps in current, examples of which are shown in Figure 7.5 b, are only a few tens

of picoamperes (11.1 pA on average, 200 ms after the onset of the event and at a potential of +0.2 V vs Ag/AgCl in 1.0 M KCl) in magnitude, and, as will be discussed below, the steps vary both in their shape and height as a function of potential but also vary between each stochastic event. First, however, it is possible to calculate the expected current per particle if the reaction was limited by the rate of mass transport of hydrogen to the nanoparticle. For a sphere on a flat surface, the diffusional mass-transport limit to the particle is equal to $4\pi nFDc^*_{H_2} r_{NP} \ln(2)$,[39] where r_{NP} is the radius of the nanoparticle and $c^*_{H_2}$ is the bulk concentration of hydrogen. From this the diffusional mass-transport limited flux to an isolated particle at the electrode surface is theoretically predicted to be ~142 pA. Relatedly, the diffusional mass-transport coefficient for material to/from such an isolated single particle on an electrode surface is equal to $\ln(2)D/r$, and for the present case of hydrogen oxidation at a 23.1 nm particle, this corresponds to a rate of ~0.15 m s^{-1}. Given the steps in current for the individual nanoparticles are only a few picoamperes in magnitude as compared to more than 100 pA, it is concluded that the nanoparticle response is limited at this single particle scale not by the mass transport of hydrogen to the catalytic surface, but due to the reaction being kinetically limited by the rate of the surface reaction. Consequently, the variability in the response of individual nanoparticles for a given set of conditions reflects the heterogeneity of the nanoparticle sample both in terms of the nanoparticle dimensions and also the individual particle's inherent activity toward catalysis of the HOR.

7.3.2 HOR at a Macroelectrode and Random Nanoparticle Arrays

To enable comparison of the nanocatalytic response to be made with that of the bulk material, the oxidation of hydrogen was studied at a polycrystalline Pt macroelectrode (radius of 0.83 mm), the response of which is shown in Figure 7.8 a (blue line). Under

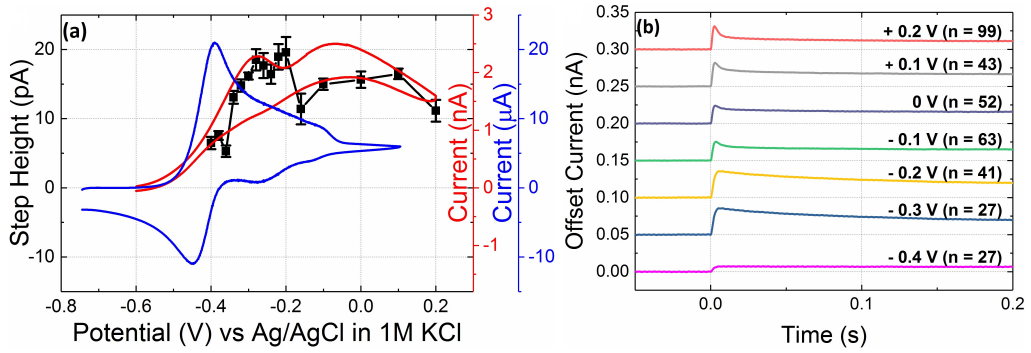

Figure 7.8: (a) CVs for HOR on a Pt macroelectrode (blue; CV of scan rate 100 mV s^{-1}, electrode of radius 831.5 μm) and an Au microelectrode with a random array of ~140 adsorbed PtNPs (red; CV of scan rate 200 mV s^{-1}, nanoparticle of radius 23.1 nm, electrode of radius 5 μm, ~5 min nanoparticle accumulation time). The electrolyte is 0.2 M KNO_3 for the Pt macroelectrodes and 20 mM for the Au microlectrode, both solutions are saturated with H_2. Overlaid is the variation in the magnitude of the current response of individual PtNPs as a function of the applied potential (black squares: measured from the time current transients, 200 ms after the nanoparticle arrival). (b) The averaged HOR response of individual PtNPs upon arrival, and electrical contact with, a potentiostated Au microelectrode as a function of the applied potential (vs Ag/AgCl in 1.0 M KCl). Current responses given as a function of time where $t = 0$ is taken as the nanoparticle arrival and is associated with the step in current, the number n of individual features recorded at each potential is reported in the image.

these low mass-transport conditions (*ca.* 5×10^{-4} m s^{-1}), the oxidation of hydrogen at the macroelectrode is fully reversible with an associated midpoint potential of -0.42 V vs Ag/AgCl in 1.0 M KCl (i.e. -0.185 V vs SHE); this is in excellent agreement with the thermodynamically predicted value of -0.43 V, the calculation of which is outlined below. It should be commented that although the present experiment is not performed under standard conditions and hence the oxidation does not occur at 0.0 V vs SHE, the redox potential is still thermodynamically well-defined in this system. The following text provides further information on the calculation of the characteristic oxidation potential for hydrogen in 20 mM KNO_3. The use of 20 mM KNO_3 as a supporting electrolyte is important in relation to the latter half of this chapter in which the experimental work is undertaken in the absence of added electrolyte. Finally, also observable in the voltammetric response of the macroelectrode, as shown in Figure 7.8 a (blue line), is the H_{upd} signal at approximately -0.2 V that is situated in the diffusional tail of the hydrogen oxidation

response.

The Formal Potential for Hydrogen Oxidation under Non-Standard Conditions

The analysis outlined below follows that previously reported.[40] For a hydrogen electrode, the electrode potential E (V) is:

$$E = E^{\ominus}_{\mathrm{H^+/H_2}} + \frac{RT}{F} \ln \left(\frac{a_{\mathrm{H^+}}/a^{\ominus}}{{p_{\mathrm{H_2}}}^{1/2}/p^{\ominus 1/2}} \right) \tag{7.1}$$

where $E^{\ominus}_{\mathrm{H^+/H_2}}$ is the standard hydrogen electrode (SHE) potential and is defined as 0.00 V, $a_{\mathrm{H^+}}$ is the proton activity (mol dm^{-3}), $a^{\ominus}$ is the standard activity (1 mol dm^{-3}), $p_{\mathrm{H_2}}$ is the hydrogen pressure (bar), and $p^{\ominus}$ is the standard pressure (1 bar).

For the ith species in solution, its activity a_i (mol dm^{-3}) is:

$$a_i = \gamma_i c_i \tag{7.2}$$

where γ_i is the activity coefficient, and c_i is the molar concentration (mol dm^{-3}). The activity of H_2 is fixed as for H_2 the solution phase is in equilibrium with the gas phase. The concentration of H_2 is calculated from Henry's law:

$$p_{\mathrm{H_2}} 10^{-k_s c_S} = K_{\mathrm{H_2}} c_{\mathrm{H_2}} \tag{7.3}$$

where $p_{\mathrm{H_2}}$ is the partial pressure (bar) and $K_{\mathrm{H_2}}$ is the corresponding Henry's law constant (dm^3 bar mol^{-1}), k_s is the salt parameter (dm^3 mol^{-1}), and c_S is the electrolyte concentration (mol dm^{-3}).

Therefore, the formal potential is:

$$E_{\mathrm{f}}^{\ominus} = E_{\mathrm{H^+/H_2}}^{\ominus} + \frac{RT}{F} \ln \left(\frac{\gamma_{\mathrm{H^+}} p^{\ominus 1/2}}{{K_{\mathrm{H_2}}}^{1/2} 10^{k_s c_S/2} a^{\ominus 1/2}} \right) \tag{7.4}$$

Using the appropriate literature values for the above expression, the formal potential (at unit concentration) for the hydrogen/proton redox couple is -0.0991 V vs SHE.[40]

Due to the non-unity stoichiometry of the proton/hydrogen redox couple the position of a voltammetric wave, as defined by its characteristic potential, will vary as a function of the concentration of the analyte. Under steady-state conditions it is possible to analytically define a half-wave potential, this half-wave potential is approximately equal to the midpoint potential for a voltammetric wave as given by:

$$\exp \theta_{1/2} = \left(\frac{D_{\mathrm{H_2}}}{D_{\mathrm{H^+}}} \frac{2 c^*_{\mathrm{H_2}}}{c^{\ominus}} \right)^{1/2} \tag{7.5}$$

where $\theta_{1/2}$ is the dimensionless half-wave potential,[41] $c^*_{\mathrm{H_2}}$ is the bulk hydrogen concentration, and $c^{\ominus}$ is the standard concentration (1 M). $D_{\mathrm{H_2}}$ and $D_{\mathrm{H^+}}$ are the proton and hydrogen diffusion coefficients, respectively. In this expression, the diffusion layer thickness has been assumed to be proportional to the inverse square root of the diffusion coefficient, i.e. $\delta_i \propto {D_i}^{0.5}$. The dimensionless potential is defined as:

$$\theta = \frac{F}{RT} \left(E - E_{\mathrm{f}}^{\ominus} \right) \tag{7.6}$$

From the above equations the midpoint potential for the oxidation of hydrogen is predicted to be -0.191 V vs SHE. In the experimental work the reference used is a Ag/AgCl (1.0 M KCl) electrode and the potential of this electrode is +0.235 V vs SHE. Consequently, the predicted midpoint potential for the oxidation of hydrogen under these conditions (0.2 M KNO_3) is -0.426 V vs Ag/AgCl (1.0 M KCl).

Due to the apparently fully irreversible accumulation of the PtNPs at the gold microelectrode surface (as evidenced in Section 7.3.1), the electrochemical response of a random array of adsorbed nanoparticles can be readily experimentally measured. For a gold electrode immersed in a PtNP sol, the cyclic voltammetric response of the electrode changes as a function of the electrode immersion time. The bare gold surface is unable to catalyze the HOR; consequently, due to the adsorption of the nanoparticles on to the gold interface and by the particles providing an increasingly large surface available to catalyze the HOR, the cyclic voltammetric current increases as a function of the time the electrode is exposed to the nanoparticle sol. Figure 7.9 provides example data showing the increase of the hydrogen oxidation response of a gold microelectrode as the individual nanoparticle becomes attached to the electrode surface. A gold microelectrode was immersed in a sol of 20 pM mesoporous PtNPs (20 mM KNO_3) before 30 continuous cyclic voltammograms (CVs) were performed. The current increases as a function of time as showing the accumulation of PtNPs at the electrode surface within 4 min from the 1^{st} to the 30^{th} CVs. Figure 7.8 a (red line) depicts a voltammogram of a gold microelectrode with mesoporous nanoparticles adsorbed to the interface, where the electrode has been in

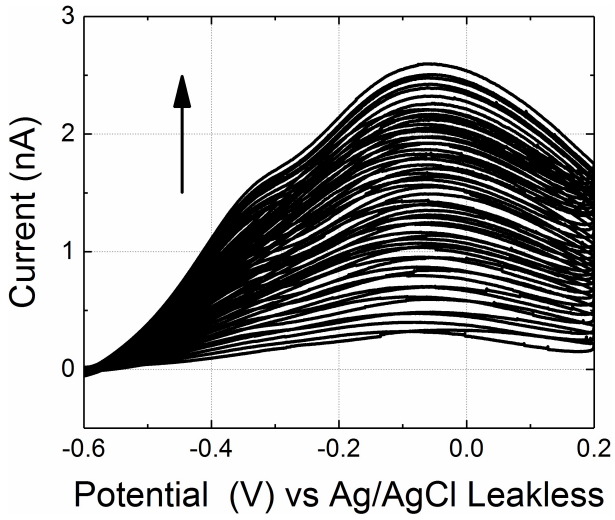

Figure 7.9: 30 continuous voltammograms of 20 pM mesoporous PtNPs in 20 mM KNO_3 with H_2 (CV of scan rate 200 mV s^{-1}). Arrows indicate the accumulation of particles on the electrode surface.

the sol for ∼5 min. Here, a well-defined wave corresponding to the catalytic oxidation of hydrogen at the nanoparticle array is observed and is seen to onset at the same potential as found for the platinum macroelectrode.

For this random array of PtNPs at the gold microelectrode, an important consideration is the maximum current attainable across the entire nanoparticle array. In the limit of large numbers of particles accumulating at the interface then the nanoparticle array will comprise of enough catalytic sites that the HOR will hypothetically become limited, not by the surface reaction, but by the mass transport of the hydrogen to the entire array. In this limit, the current will be sensitive to the geometry and size of the substrate electrode. The diffusional mass-transport limited flux to the entire gold microelectrode (radius = 5 μm) is calculated to be 14.1 nA. For the data shown in Figure 7.8 a at high overpotentials (> -0.3 V), the current is approximately 2.5 nA; consequently, this current is less than 20% of the maximum net current. Hence, to a reasonable approximation, the cyclic voltammetry of the nanoparticle array can be considered simply as a linear addition of the response of the individual nanoparticles (i.e. the current per particle is taken to be effectively independent of the nanoparticle surface coverage). From the nano-impact data at +0.2 V, the average step size of an individual event (Section 7.3.1) is found to have a magnitude of 11.1 pA; similarly at +0.2 V, the cyclic voltammetric response of the nanoparticle array, as depicted in Figure 7.8 a, has a current of 1.59 nA. Hence, the number of nanoparticles adsorbed on the gold electrode after 5 min of accumulation can be estimated for this voltammogram to be ∼140.

The cyclic voltammetric response of the nanoparticle array evidence the presence of two peaks (at -0.3 and -0.1 V) in the electrochemical response at anodic potentials. These peaks are directly associated with the change in the catalytic activity of the nanoplatinum surface as a function of the applied potential. The physical origin of these peaks at higher over potentials will be returned to later in the text.

7.3.3 Quantifying the Single Nanoparticle Behavior

The single nanoparticle toward the oxidation of hydrogen, as measured *via* chronoamperometry (Section 7.3.1), was investigated as a function of the applied electrode potential. To aid analysis of the nanoparticle impact results, the average nanoparticle response for a given set of conditions is calculated. Further details on this analysis procedure are provided in Section B.1 (Appendices). Figure 7.8 b depicts the averaged response of individual particles from a sample of mesoporous PtNPs ($r_{NP} = 23.1$ nm) toward the oxidation of hydrogen at a range of applied electrode potentials, each averaged current transient has been offset by 50 pA for clarity. Also shown in Figure 7.10 is the variation of the average nano-impact response (in total 128 spikes) at a potential of +0.2 V to a variation of the solution phase hydrogen concentration, evidencing the change in the magnitude of the single particle response but not the shape. Hydrogen concentration has been varied from 100, 70, 50 to 30%. Impacts of mesoporous PtNPs at 0.2 V were collected and averaged to show any trend, as shown in Figure 7.10 a. The normalized averaged CAs at different hydrogen concentrations show a close value of step heights, as depicted in Figure 7.10 b. The small discrepancy for the data at 30% hydrogen is most likely due to errors made in the gas mixing at this low hydrogen concentration end. As can be seen from Figure 7.8 b,

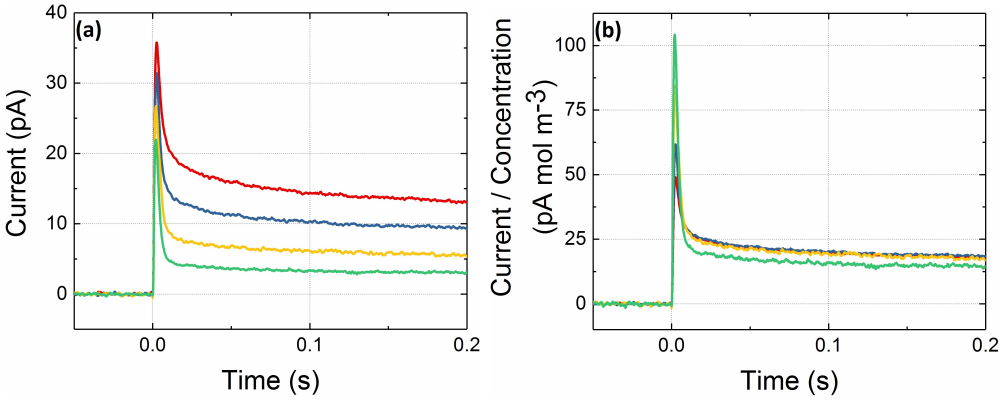

Figure 7.10: Averaged CAs with porous PtNPs for a 5 μm Au microelectrode in 20 mM KNO_3 with H_2 at a concentration of 30% (green), 50% (yellow), 70% (blue) and 100% (red) from bottom to top. (b) Normalized plots to show overlay of CAs at different hydrogen concentrations.

for all potentials more anodic than -0.4 V, the arrival of the nanoparticle to the electrode surface results in an abrupt increase in the catalytic current. Moreover, for all potentials above (and including) -0.3 V, a peak in the step response of the individual particles is observed at short times, the duration of this peak feature varies from 121 ms at -0.3 V to 49 ms at +0.2 V (as measured as a 90–10% drop, taking the current at 200 ms after the spike onset as a reference). Furthermore, both the magnitude (in terms of charge) of the peak and the current in the long time limit (*ca.* 200 ms after the recorded particle arrival) also vary as a function of the applied potential.

The variation in the single nanoparticle step size as measured 200 ms after the onset of the nano-impact feature has been quantified and is shown in Figure 7.8 a (black squares). The long time (200 ms) current response of the individual nanoparticles closely mirrors the response measured using cyclic voltammetry for the PtNP array; the single nanoparticle response toward the oxidation of hydrogen also shows two peaks in the activity of the platinum nanomaterial at -0.3 and -0.1 V vs Ag/AgCl (1.0 M KCl). These peaks, as will be outlined below, cannot be readily accounted for using the conventionally applied Tafel–Volmer reaction mechanism.

7.3.4 Oxidative Mechanism: Tafel–Volmer

At high overpotentials (i.e. at potentials anodic of -0.3 V vs Ag/AgCl in 1.0 M KCl), if the reaction rate at both the individual nanoparticles and the nanoparticle arrays are not limited by the mass transport of the hydrogen to the catalytic surface, what is the rate-determining step? The relative invariance of the oxidation rate as a function of mass transport in this regime has conventionally been understood in terms of relating to the rate-determining chemisorption of hydrogen to the electrode surface.[15] The Tafel–Volmer reaction mechanism is commonly employed to describe the kinetics of the HOR[41] and is given by:

$$\mathrm{H_2} + 2\,\mathrm{M} \underset{k_\mathrm{d}}{\overset{k_\mathrm{a}}{\rightleftharpoons}} 2\,\mathrm{H_{ads}} \tag{7.7}$$

$$\mathrm{H_{ads}} \overset{k_\mathrm{el}}{\rightleftharpoons} \mathrm{H^+} + \mathrm{e^-} + \mathrm{M} \tag{7.8}$$

where M and $\mathrm{H_{ads}}$ represent unoccupied and occupied surface adsorption sites, respectively. The rate constants of hydrogen, $\mathrm{H_2}$, adsorption and desorption are given by k_a ($\mathrm{m^5\ mol^{-2}\ s^{-1}}$) and k_d ($\mathrm{m^2\ mol^{-1}\ s^{-1}}$), respectively. The definition of the kinetic rate constants can be found in Section B.2 (Appendices). The rate of electron transfer is commonly assumed to be well-described using the Butler–Volmer formalism and hence the rate is defined by a rate constant k_el ($\mathrm{m^3\ mol^{-1}\ s^{-1}}$). It is on the basis of the involvement of an electron transfer in the Volmer reaction (and the similarly related Heyrovský reaction) that it is concluded that at higher overpotentials, this process is not the rate-determining step; were it to be controlling the electrochemical oxidation rate should exhibit a strong (exponential) dependency on the applied potential.

Through application of the Tafel–Volmer mechanism and solving the diffusion equation for the system's geometry, the expected voltammetric response for an array of diffusionally isolated spherical nanoparticles supported on an inert electrode surface can be simulated. The results of which are presented in Figure 7.11 a, where the simulated and experimental results (20 mM $\mathrm{KNO_3}$) have been overlaid. Full information on this simulation is provided in Section B.2 (Appendices). For this mechanism, the rate of electron transfer k_el, adsorption k_a, and desorption k_d rate constants are unknowns. However, the magnitude of the adsorption rate constant k_a can be estimated from the individual nanoparticle impacts at high overpotential to be 4.3×10^7 $\mathrm{m^5\ mol^{-2}\ s^{-1}}$. Under conditions where the rate of reaction is limited by the chemisorption of hydrogen then the electrochemical oxidative flux j reduces to the simplified expression:

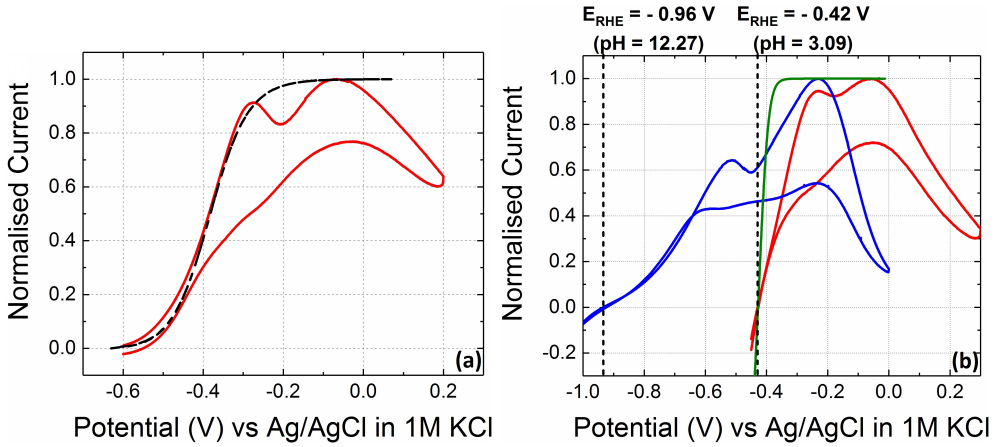

Figure 7.11: (a) Depicts the simulated response for the oxidation of hydrogen *via* the Tafel–Volmer mechanism at an isolated spherical PtNP in 20 mM KNO_3 (dash line). Kinetic parameters used in the simulation are $k_a = 4.3 \times 10^7$ m^5 mol^{-2} s^{-1}, $k_d = 4.3 \times 10^7$ m^2 mol^{-1} s^{-1}, and $k_{el} = 9.2 \times 10^2$ m^3 mol^{-1} s^{-1}. Overlaid for comparison is the experimental response (CV of scan rate 200 mV s^{-1}) of a PtNP array at a gold microelectrode in 20 mM KNO_3 (red line). (b) Voltammetric response (CV of scan rate 200 mV s^{-1}) of a gold microelectrode (radius = 5 μm) supporting a random array of PtNPs (radius = 23.1 nm) under both acidic (red, 1 mM $HClO_4$ and 19 mM $KClO_4$) and alkaline conditions (blue, 20 mM KOH); for clarity the calculated potentials for the RHE have been labeled for each pH. Also shown is the theoretically predicted fully reversible response for a microelectrode toward the oxidation of hydrogen in the presence of 1 mM protons (green line).

$$j = 2k_a c_{H_2} {\Gamma_M}^2 \tag{7.9}$$

where c_{H_2} is the surface concentration (mol m^{-3}) of hydrogen and Γ_M is the surface coverage (mol m^{-2}) of free active sites on the electrode surface. In the present simulation, the values of k_d and k_{el} only serve to shift the position of the overall voltammetric wave.

As can be seen from Figure 7.11 a, although the Tafel–Volmer mechanism is capable of giving an accurate prediction of the experimental current at low overpotentials (cathodic of -0.3 V), this mechanism is unable to describe the voltammetric variation in the current at higher overpotentials in the "adsorption limited regime". For both the single particle impacts and the voltammetric response of the array of nanoparticles at the gold electrode, so-called "fine structure" is observed in the hydrogen oxidation signal as shown in Figure 7.8 a). This fine structure in 20 mM KNO_3 is comprised of two peaks in the reaction-

limited current situated at approximately -0.3 and -0.1 V vs Ag/AgCl (1.0 M KCl). The magnitude of these peaks in the reaction-limited current and the fact that they are observable from analysis of the steady-state response (as measured after 200 ms) of the individual nanoparticle means that these peaks are not directly related to the oxidation of adsorbed hydrogen (i.e. H_{upd}); the feature is not simply related to the superposition of a surface process with the catalytic oxidation of hydrogen. Consequently, it is concluded that this variation in the oxidation rate in the adsorption limited regime must reflect a sensitivity and change in the adsorption rate constant k_a, or the surface coverage of the active sites on the catalytic interface Γ_M with the applied potential. For the peak at -0.1 V, the peak likely arises from anion specific adsorption leading to a decrease in the surface coverage of active sites at high overpotentials.[16] However, it is the origin of the peak at -0.3 V that is the focus of the following section.

7.3.5 Oxidative Mechanism: Dependence on pH

The oxidation of hydrogen at the mesoporous nanoparticles was further studied under both alkaline and acidic conditions. A gold microelectrode was immersed into a PtNP sol containing either 20 mM KOH or 1 mM $HClO_4$ and 19 mM $KClO_4$. Under acidic conditions, the nanoparticle sol is found to be far less stable as has been recently reported in the literature,[31] hence concentration of only 1 mM $HClO_4$ under acidic conditions was used. Under both acidic and alkaline conditions, steps in the chronoamperometric response were observed corresponding to the arrival of individual particles to the electrode surface. However, although the rate of hydrogen oxidation under acidic conditions is comparable to the situation found for the individual nanoparticle response in 20 mM KNO_3, the rate of hydrogen adsorption is found to be almost an order of magnitude lower under alkaline conditions (see below).

Mesoporous Platinum Nanoparticle (PtNP) Impacts under Acidic and Alkaline Conditions

Mesoporous PtNP impacts were conducted under acidic (1 mM $HClO_4$ and 19 mM $KClO_4$) and alkaline (20 mM KOH) conditions. Impacts from CA at the potential where the second peak appeared (-0.23 and -0.06 V respectively) were collected to give the average, as shown in Figure 7.12. From the average current responses at high overpotentials, the adsorption rate constants of HOR in the acidic and alkaline conditions can be estimated.

As shown in Equations 7.7 and 7.8 (Section 7.3.4), the mechanism of HOR on platinum is assumed to follow the Tafel–Volmer reaction.[41] As reported before,[42] the adsorption rate constant k_a in the Tafel–Volmer mechanism can be calculated from the high-overpotential steady-state current value I_{ss}. A simple equation to estimate the value of k_a is derived in the model of a microdisc electrode:

$$\frac{I_{ss}}{I_{diff}} = \frac{\frac{\pi r_{el}^{disc}\left(k_a {\Gamma_{max}}^2\right)}{4D_{H_2}}}{1 + \frac{\pi r_{el}^{disc}\left(k_a {\Gamma_{max}}^2\right)}{4D_{H_2}}} \tag{7.10}$$

where I_{diff} is the theoretical diffusion-limited current at the microdisc electrode. r_{el}^{disc} is

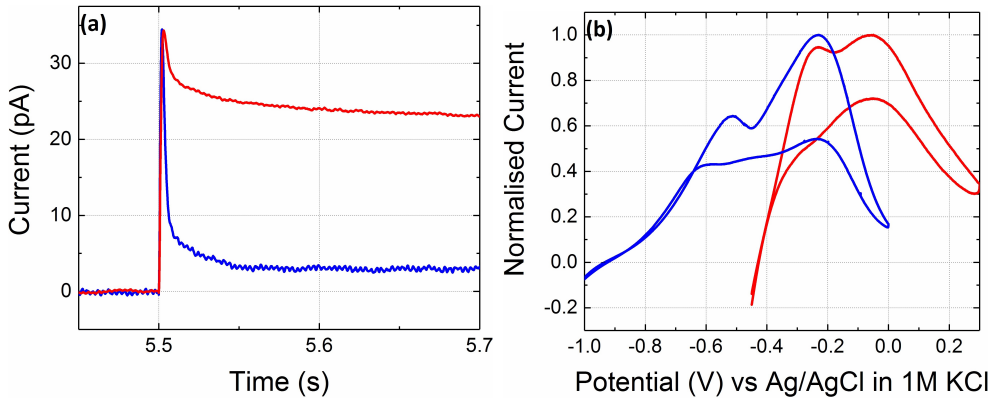

Figure 7.12: (a) Averaged impact signals of porous PtNPs in solution of 20 mM KOH (blue; at -0.23 V) and 1 mM $HClO_4$ and 19 mM $KClO_4$ (red; at -0.06 V). (b) Voltammetric responses (CV of scan rate 200 mV s^{-1}) of a gold microelectrode in solution of 20 mM KOH (blue) and 1 mM $HClO_4$ and 19 mM $KClO_4$ (red).

the radius of the microdisc electrode, D_{H_2} is the diffusion coefficient of H_2, and Γ_{max} is the maximum surface coverage of active sites. In the nano-impact experiment, the nanoparticle can be regarded as a microsphere electrode attached at a planar substrate. As discussed earlier in this thesis, under the limitation of adsorption, the current-voltage response of a microsphere electrode is equal to the case of a microdisc electrode with identical surface area, which means $r_{el}^{disc} = 2r_{el}^{sphere}$. The radius of the PtNP r_{el}^{sphere} is *ca.* 25 nm and the corresponding $r_{el}^{disc} = 50$ nm. The theoretical diffusion-limited current at high overpotentials can be calculated from:[43]

$$I_{diff} = 4nFD_{H_2}c^*_{H_2}r_{el}^{disc} \tag{7.11}$$

where $n = 2$ is the number of electrons transferred in HOR, $F = 96485$ C mol^{-1} is the Faraday constant, $c^*_{H_2} = 0.73$ mM is the bulk concentration of the hydrogen gas in solution, and $D_{H_2} = 5.0 \times 10^{-9}$ m^2 s^{-1}.[44] I_{diff} of a 50 nm microdisc electrode is calculated to be 141 pA.

Figure 7.12 a shows the average nano-impact currents of porous PtNPs in solution of 20 mM KOH (blue), and 1 mM $HClO_4$ and 19 mM $KClO_4$ (red) at high overpotentials of -0.23 and -0.06 V, respectively. In the acidic solution, I_{ss} is approximately 23 pA; in the alkaline solution, I_{ss} is approximately 3 pA. From Equation 7.10, when $\Gamma_{max} = 2.2 \times 10^{-5}$ mol m^{-2}, the adsorption rate constants in the acidic and alkaline solutions are calculated to be 5.3×10^7 m^5 mol^{-2} s^{-1} and 5.9×10^6 m^5 mol^{-2} s^{-1}. Figure 7.12 b shows CVs of a gold microelectrode in solution of 20 mM KOH (blue) and 1 mM $HClO_4$ and 19 mM $KClO_4$ (red). Currents are normalized in the plot.

Figure 7.11 b depicts the voltammetric response of a PtNP array at a gold microelectrode in 20 mM KOH (blue) and 1 mM $HClO_4$ and 19 mM $KClO_4$ (red). The nanoparticle arrays were formed, as before, by allowing nanoparticles in the solution phase to randomly

adsorb to the gold interface. The voltammograms were recorded after at least 2 min of electrode immersion. As evidenced by the reductive current at cathodic potentials, both voltammograms presented in Figure 7.11 b show significant hydrogen evolution in the voltammetric window of study; this is in contrast to the 20 mM KNO_3 case presented above, where the lack of pH buffering inhibits this process from occurring. Figure 7.11 b demonstrates that the position of the voltammetric wave, as defined by the potential at which it crosses the x-axis, shifts in a Nernstian manner with pH, as indicated by the calculated potential of the reversible hydrogen electrode (RHE) in Figure 7.11 b (dotted vertical lines). Moreover, the electron transfer kinetics are appreciably faster under acidic as compared to alkaline conditions, as evidenced by the voltammetric wave shape. However, although faster, the voltammetric response under acidic (pH 3.1) conditions is not at the reversible limit, as can be seen from deviation of the response away from that analytically predicted for a Nernstian reaction occurring at a diffusionally isolated particle (derivation of the reversible Nernstian response is given below).

Nernstian Response of a Microelectrode towards Proton/Hydrogen Redox Couple

This section provides an approximate solution, to describe the steady-state voltammetric response for a diffusionally isolated particle on a flat surface, where hydrogen oxidation and proton reduction can occur at the particle surface but not on the underlying flat electrode. The primary approximation is that the surface is uniformly accessible and that the concentration profile can be suitably approximated as linear.

The redox reaction of interest is:

$$H^+ + e^- \rightleftharpoons \frac{1}{2}H_2 \tag{7.12}$$

Moreover, the proton/hydrogen concentrations at the particle surface are assumed to be

fully described by the Nernst equation and hence the reaction is at the "reversible" limit. In contrast to previous work, this derivation accounts for the presence of both protons and hydrogen being present in the bulk solution. The Nernst equation for the above reaction is:

$$E = E_{\mathrm{f}}^{\ominus} + \frac{RT}{F} \ln \left(\frac{c_{\mathrm{H}^+}}{{c_{\mathrm{H}_2}}^{1/2} c^{\ominus 1/2}} \right) \tag{7.13}$$

where $c^{\ominus}$ is the standard concentration (1 mol dm^{-3}) and the formal potential has been defined earlier in Equation 7.4. The dimensionless potential is defined in Equation 7.6. This allows the Nernst equation to be written in the form:

$$\exp\left(2\theta\right) c^{\ominus} = \frac{{c_{\mathrm{H}^+}}^2}{c_{\mathrm{H}_2}} \tag{7.14}$$

At the nanoparticle surface, conservation of mass requires that the flux of electrons j (mol m^{-2} s^{-1}) is related to the flux of protons and hydrogen, accounting for the stoichiometry of the reaction:

$$j = -j_{\mathrm{H}^+} = 2j_{\mathrm{H}_2} \tag{7.15}$$

As mentioned earlier in this thesis, the electrochemical flux j is directly correlated to the net current I (A) by the following expression:

$$I = -nFAj \tag{7.16}$$

Under the assumption of a linear concentration profile and the mass tranport of the species to be a diffusion only process, then from Fick's first law the flux of species i is given by:

$$j_i = -\frac{D_i c_i^*}{\delta_i} + \frac{D_i c_i(z=0)}{\delta_i} \tag{7.17}$$

In the above expression δ_i is the diffusion layer thickness (m) associated with species

i. Under a steady-state diffusion regime at a microelectrode (i.e. an electrode with dimensions $< \sqrt{2Dt}$), the diffusion layer thickness is independent of the species' diffusion coefficient. For a sphere on a surface the mass-transport limited current is equal to:

$$I_{\mathrm{ss}} = 4\pi n F D_i c_i^* r \ln(2) \tag{7.18}$$

Hence, using the above approximations the diffusion layer thickness can be defined as:

$$\delta_i = \frac{r}{\ln(2)} \tag{7.19}$$

The limiting cathodic and anodic flux is given by the following expressions:

$$j_{c,\mathrm{lim}} = \frac{D_{\mathrm{H^+}} c^*_{\mathrm{H^+}}}{\delta_{\mathrm{H^+}}} \tag{7.20}$$

$$j_{a,\mathrm{lim}} = -\frac{2D_{\mathrm{H_2}} c^*_{\mathrm{H_2}}}{\delta_{\mathrm{H_2}}} \tag{7.21}$$

The combination of the above to analytical approximations with the Nernst equation allows with minimal rearrangement for the electrode flux j to be defined:

$$c_{\mathrm{H^+}}(z=0) = \frac{\delta_{\mathrm{H^+}} \left(j_{c,\mathrm{lim}} - j\right)}{D_{\mathrm{H^+}}} \tag{7.22}$$

$$c_{\mathrm{H_2}}(z=0) = \frac{\delta_{\mathrm{H_2}} \left(j - j_{a,\mathrm{lim}}\right)}{2D_{\mathrm{H_2}}} \tag{7.23}$$

$$j - j_{a,\mathrm{lim}} = \frac{\left(j_{c,\mathrm{lim}} - j\right)^2}{\boldsymbol{c}} \tag{7.24}$$

$$\text{where} \quad \boldsymbol{c} = \frac{\delta_{\mathrm{H_2}} {D_{\mathrm{H^+}}}^2 \exp(2\theta) c^{\ominus}}{2{\delta_{\mathrm{H^+}}}^2 D_{\mathrm{H_2}}} \tag{7.25}$$

This quadratic equation can be solved to find a general expression for the reversible flux

for the proton/hydrogen redox couple:

$$0 = \frac{j^2 + j_{c,\mathrm{lim}}^2 - 2jj_{c,\mathrm{lim}}}{\boldsymbol{c}} - j + j_{a,\mathrm{lim}} \tag{7.26}$$

$$j = \left(j_{c,\mathrm{lim}} + \frac{\boldsymbol{c}}{2}\right) \pm \sqrt{\left(j_{c,\mathrm{lim}} + \frac{\boldsymbol{c}}{2}\right)^2 - {j_{c,\mathrm{lim}}}^2 - \boldsymbol{c}j_{a,\mathrm{lim}}} \tag{7.27}$$

Importantly, only the expression with the negative term is of physical significance as other root does not tend to zero at low overpotentials. The expression defines the reversible limit plotted in Figure 7.11 b above (green line).

Figure 7.11 b also evidences that, although the pH has been altered dramatically (∼9.2 pH units), the minimum in the adsorption limited regime has only shifted a comparatively small amount. At pH 3.1, the local minimum in the reaction-limited current occurs at -0.18 V; however, at pH 12.3, this has only been shifted by approximately 0.27 to -0.45 V. As demonstrated in the following, the H_{upd} signal for the platinum surface occurs at approximately -0.2 V vs Ag/AgCl in 1.0 M KCl at pH 3.1 (1 mM $HClO_4$ and 19 mM $KClO_4$) and at -0.45 V at pH 12.3 (20 mM KOH, in the presence of citrate). Although the H_{upd} voltammetric signal is associated with the stoichiometric transfer of one proton per electron, the position of the wave is known to be sensitive to specific anion adsorption, and for polycrystalline platinum and for a number of crystal facets (most notably Pt 100 and Pt 110), the position of the wave varies with 40–50 mV pH^{-1} at pH values above 3.[45, 46] Moreover, conventionally, the position of the H_{upd} signal relative to the RHE has been used as a descriptor of the rate of electron transfer as a function of pH.[45]

Underpotential Deposited Hydrogen (H_{upd}) on Polycrystalline and Nanoparticulate Surfaces

The H_{upd} signal on a polycrystalline platinum electrode is shown in Figure 7.13 under both alkaline and acidic conditions (20 mM KOH, and 1 mM $HClO_4$ and 19 mM $KClO_4$). The H_{upd} signal is comparatively broad however it occurs under these conditions at approximately -0.6 and -0.2 V vs Ag/AgCl (1.0 M KCl).

For the mesoporous PtNPs the H_{upd} region was studied by accumulating the PtNPs at a gold microelectrode in the absence of H_2, with the electrode immersed in either a 20 mM KOH, or 1 mM $HClO_4$ and 19 mM $KClO_4$ solution in the presence of mesoporous PtNPs; control experiments were also conducted in the absence of mesoporous PtNPs, as shown in Figure 7.14 a. Under acidic conditions the H_{upd} signal is found to occur at comparable potentials to that found for the polycrystalline surface. However, under alkaline conditions the position of the wave is notably shifted to approximately -0.45 V. This positon of the H_{upd} wave is in excellent agreement with the hydrogen oxidation response which shows a minima in the oxidation rate at very comparable potentials. It is

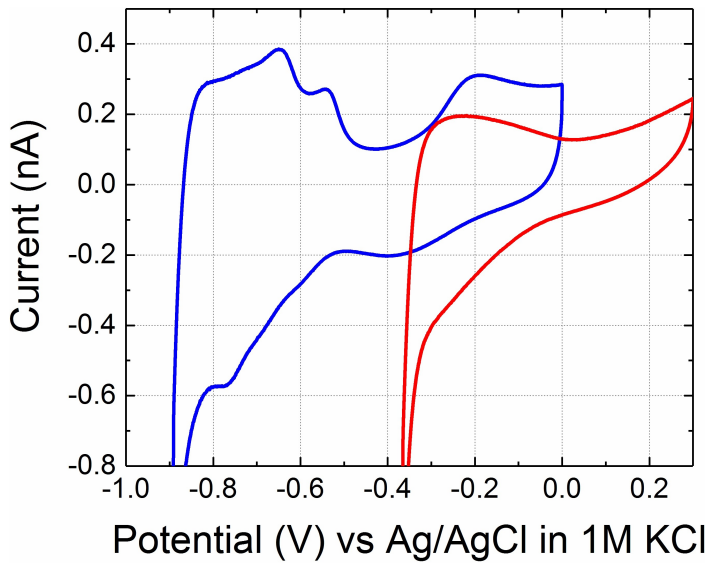

Figure 7.13: Voltammetric responses of platinum microelectrode in (a) 20 mM KOH (blue) and 1 mM $HClO_4$ and 19 mM $KClO_4$ (red) with mesoporous PtNPs.

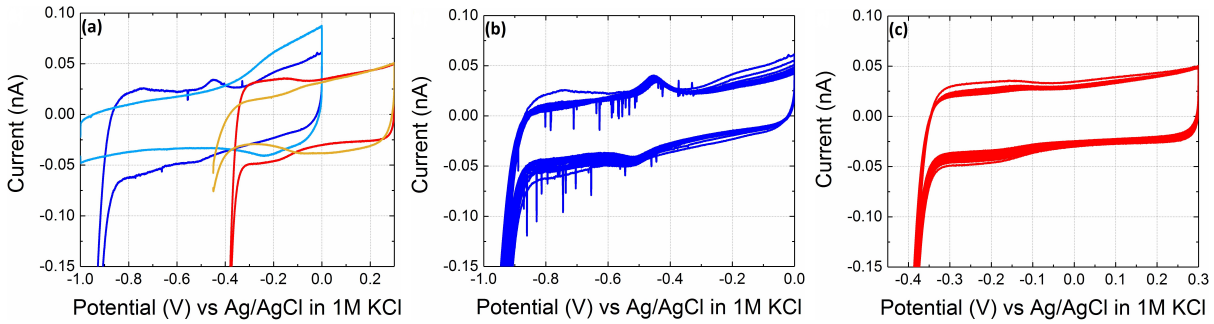

Figure 7.14: Voltammetric responses (CV of scan rate 200 mV s^{-1}) of gold microelectrode in (a) 20 mM KOH (blue) and 1 mM $HClO_4$ and 19 mM $KClO_4$ (red) with porous PtNPs. Blanks are shown to compare in cyan and yellow with no porous PtNPs in the solution. 30 ensemble voltammetric scans of gold electrode PtNPs were performed in (b) 20 mM KOH and (c) 1 mM $HClO_4$ and 19 mM $KClO_4$ respectively, in the presence of 20 pM mesoporous PtNPs.

concluded that the differing positions of the wave likely reflects the presence of citrate on the nanoparticle surface.

Figure 7.14 b and c depict 30 continuous CVs of a gold electrode immersed in 20 mM KOH, and 1 mM $HClO_4$ and 19 mM $KClO_4$ respectively, in the presence of 20 pM mesoporous PtNPs.

One interpretation for the "fine structure" in the activity of the HOR at higher overpotentials previously provided in the recent literature is that these two peaks in the adsorption limited regime correspond to two different adsorption sites and that at higher overpotentials both sites become blocked, plausibly due to competitive anion adsorption.[16] Alternatively, it is highlighted that this local minimum in activity, as evidenced by the drop in catalytic current, occurs at potentials comparable to those at which the H_{upd} occurs on the underlying platinum surface. In 20 mM KNO_3 this can clearly be seen from Figure 7.8 a where the local minima in the hydrogen adsorption rate occurs at potentials comparable to the H_{upd} signal as observed on the macroscopic platinum electrode.

This conclusion that the particle activity initially decreases with the removal of H_{upd} from the surface is, at first sight, difficult to reconcile with the Tafel–Volmer mechanism.

the total surface coverage of the active sites can be expressed as $\Gamma_{max} = \Gamma_M + \Gamma_{H_{ads}}$, where $\Gamma_{H_{ads}}$ is the surface coverage (mol m^{-2}) of adsorbed hydrogen H_{ads}. The value of Γ_{max} is often assumed to be a constant and for a clean Pt electrode given the value of $\Gamma_{max} = 2.2 \times 10^{-5}$ mol m^{-2},[47] where it is assumed that H_{upd} is the same as H_{ads}. Whether H_{upd} represents the primary intermediate in the HOR and is hence the same as H_{ads} in the Tafel–Volmer mechanism is debatable.[16] If H_{ads} was the same as H_{upd}, one would expect in accordance with the Tafel–Volmer mechanism that the oxidative removal of the H_{upd} would lead to an increase and not a decrease (as observed experimentally) in the surface reaction limited current. It is, however, on the basis of the presented experimental data, reasonable to conclude that the first peak in the HOR adsorption limited region relates directly to a change in the interfacial structure as a function of the applied potential; as the surface coverage of adsorbed hydrogen H_{upd} decreases, so too does the apparent hydrogen adsorption rate. Certainly due to lateral interaction between adsorbed hydrogens, the enthalpy of adsorption would not be anticipated to be a constant as a function of the surface coverage of hydrogen. Ultimately, it is concluded that either the adsorption rate k_a or the number of available active sites must decrease at higher overpotential. This decrease in the catalytic rate reflects a change in the interfacial structure either associated with the desorption of H_{upd} or due to specific anion adsorption.

7.3.6 Shape of Individual Nanoimpacts

Having explored the operative mechanism, the chapter now returns to consider the shape of the "step" response of individual nanoparticles, as exemplified in the data shown in Figure 7.8 b, and importantly explores the origin of the initial "spike" in current at times less than 200 ms after the impact of a nanoparticle. This spike in current when integrated is experimentally found to vary in magnitude in the range of 0.1–1 pC. The onset of the spike in the single nanoparticle time-current transient correlates closely with

the potential at which the H_{upd} signal is observed; this indicates that this process (H_{upd} removal) provides at least a partial charge contribution to the observed spike in current. For the impact response of the PtNPs at +0.2 V, the integral of the charge under the initial spike gives a charge of 0.22 pC. However, at -0.3 V, the charge associated with this initially non-steady-state oxidation event is found to be 1.1 pC. Assuming the total nanoparticle surface area is covered in hydrogen then this charge is equivalent to surface coverages of 384 μC cm^{-2} and 1.9 mC cm^{-2}, respectively.[48] In contrast on polycrystalline platinum, a monolayer of hydrogen has a surface coverage of 210 μC cm^{-2}. Consequently, at high overpotential (+0.2 V vs Ag/AgCl in 1.0 M KCl), it is reasonable to conclude that within the experimental uncertainty, the charge passed during this spike in current is associated simply with the removal of H_{upd} hydrogen from an individual PtNP.

However, at lower potentials, the far greater magnitude of the charge passed and its sensitivity to the applied potential indicates that at least one other process is occurring during the course of this spike in current. As highlighted in Sections 7.3.4 and 7.3.5, the interplay between H_{upd} surface coverage and the particle's activity toward the HOR is not simple. However, the "excess" charge passed during the spike in current at low overpotentials most likely reflects the higher activity of the nanoparticle toward the oxidation of hydrogen at the initial onset of the reaction where the surface coverage of H_{upd} is higher. During the course of the spike in current, and as the surface coverage of H_{upd} decreases, the activity of the particle toward the catalytic oxidation of hydrogen is concomitantly lowered. Hence, this result again evidences the important role of the surface coverage of the H_{upd} on the platinum surface and that the rate of the HOR is not simply directly controlled by the applied potential. In summary, the charge passed during the initial spike in current for an individual impacting nanoparticle at electrode potentials between -0.3 and +0.1 V (vs Ag/AgCl in 1.0 M KCl), as shown in Figure 7.8 b, is larger than anticipated simply for the removal of a monolayer of H_{upd} hydrogen for the platinum

nanosurface. The extra charge is consistent with arising due to the activity of the particle toward the catalytic oxidation of hydrogen decreasing as H_{upd} hydrogen is removed from the particle's surface; the two processes are not independent.

In light of the above discussion, models of the single nanoparticle catalytic oxidation event are developed in which the transfer function and hence the bandwidth of the measurement electronics are also accounted for. Further details are provided in Section B.3 (Appendices). These models focus on describing the single particle current transients at +0.2 V where the charge passed during the spike in current is consistent with arising predominantly from the removal of a monolayer of H_{upd} from the impacting particle surface. It is further noted that, upon arrival of the nanoparticle to the electrode surface and the formation of an electrical contact, the nanoparticle will become charged. This nanoparticle charging will lead to the occurrence of a small capacitative current. Assuming the double layer capacitance associated with the platinum surface is 20 μF cm^{-2}, then if the nanoparticle changes its potential by one volt the maximum expected capacitative charge per individual nanoparticle charging event is only anticipated to be on the order of 0.01 pC; this value is at least an order of magnitude less than what is found experimentally for the charge passed during the spike (*cf.* 0.2 pC). Consequently, in the following discussion only the Faradaic single nanoparticle response is considered.

Upon application of a potential to a nanoparticle, the time scale for a reaction to reach the steady state for a diffusionally limited process is given approximately by $r_{NP}{}^2/D$ ($\sim$125 ns in the present case), given the near reversible nature of HOR on platinum, other surface reaction processes may be anticipated to reach steady state on a similarly rapid time scale; consequently, in the absence of other contributing factors, a simple step in the current-time profile should be anticipated to occur after the arrival of a single nanoparticle entity at the electrode surface. Figure 7.15 a (red) presents the expected current transient for a single impacting nanoparticle where the rate at which the measured current increases is

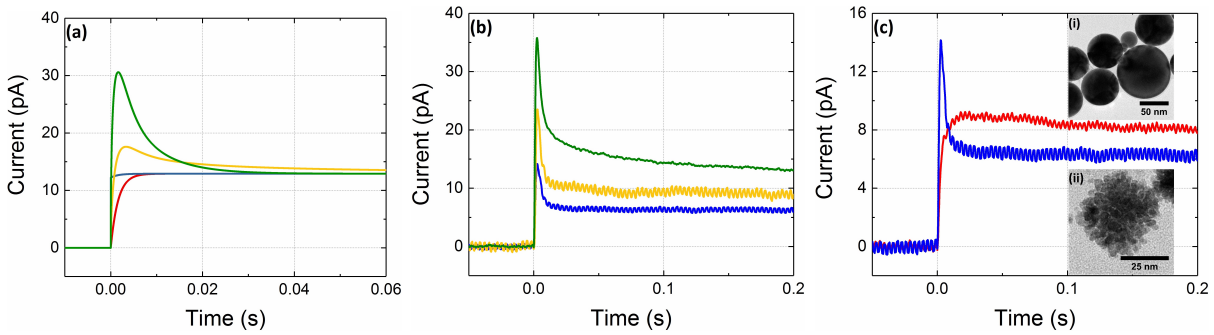

Figure 7.15: (a) Theoretically predicted impact response for the oxidation of hydrogen at individual nanoparticles accounting for the transfer function of the measurement device: reaction-limited process only (red); reaction-limited response plus the oxidation of hydrogen adsorbed on the external nanoparticle surface (blue); reaction-limited current and a contribution at short times from both the oxidation of hydrogen adsorbed on the external and internal surface (yellow and green) where the mass transport through the particle has been modeled using an "effective" diffusion coefficient (see text) of 1×10^{-15} and 1×10^{-14} m^2 s^{-1}, respectively. Note that these values are much smaller than the proton diffusion coefficient (5×10^{-9} m s^{-2}) in bulk aqueous phase, possibly due to the porosity of the nanoparticles. (b) Experimentally determined average response of mesoporous PtNPs toward the oxidation of hydrogen at +0.2 V vs Ag/AgCl (1.0 M KCl) in the presence of 20, 2, and 0 mM (green, yellow, and blue, respectively) additional KNO_3 electrolyte. (c) Averaged CAs for the oxidation of hydrogen with mesoporous (blue) and solid (red) PtNPs in the absence of additional electrolyte.

determined by the bandwidth of the measurement electronics, then, for the device used in this work, the steady-state response should be reached within approximately 10 ms of the onset of the nanoparticle impact. As shown in Figure 7.8 b, at cathodic potentials less than -0.3 V (vs Ag/AgCl in 1.0 M KCl, 20 mM KNO_3), the single nanoparticle responses are found to be of a simple "step" form and are well-described by this simple catalytic reaction only model. But this first model is incapable of explaining the initial peak in the time current transients as observed experimentally at +0.2 V.

The second model, Figure 7.15 a (blue) looks to account for the oxidation of surface-adsorbed hydrogen H_{upd} at only the outer surface of the particle. The oxidation of the H_{upd} on the external particle surface is assumed to occur very rapidly; consequently, the resulting step shape is that of a superposition of a step and an impulse response as depicted in Figure 7.15 a (blue). Here the current rises rapidly, but the response of the system is

not predicted to result in an appreciable peak at short times. Consequently, this clearly demonstrates that the internal structure of the mesoporous nanoparticle contributes to the peak observed experimentally for the individual nanoparticles.

In the third model, shown in Figure 7.15 a (green and yellow), the reaction-limited current, the near instantaneous oxidation of H_{upd} on the external surface, and a slower oxidation of the H_{upd} contained on the internal nanoparticle surface are all accounted for. Due to the mesoporous structure of the nanoparticle, their surface area is approximately 8.5 times greater than that of a sphere of an equivalent (circumscribed) size. Moreover, to provide a simplified model of the oxidation of the internal H_{upd}, it is assumed that the reaction is limited by the diffusion of the species out of the sphere. Consequently, the rate at which the internal hydrogen is oxidized is sensitive to an applied effective rate constant and the geometry of the system. The results of this model are presented in Figure 7.15 a, where the green and yellow lines have associated effective diffusion coefficients of 1×10^{-14} and 1×10^{-15} m^2 s^{-1}, respectively. This model successfully reflects the experimental shape of the nano-impact response and provides a clear parametrization of the observed spike shape, evidencing the likely relatively slow mass transport through the internal particle structure. The direct comparison between this rather simple model and the experimental data reveals an excellent qualitative agreement of theory and experiment. Owing to the simplicity of the theoretical model, there are, though, notable difference between the modeled and the measured spike shapes. Primarily, the rate at which the current profile tends to steady state and the magnitude of the peak response are both sensitive to the applied potential in the experimental work, potentially indicating the importance of migratory forces on material transport through the particle's internal structure.

7.3.7 Impacts in the Absence of Added Electrolyte and the Response of Solid Nanoparticles

In the previous section for the provided theoretically models, it was demonstrated that the initial spike in current at +0.2 V is consistent with arising from the removal of H_{upd} from the nanoparticle's mesoporous surface. The magnitude of the initial spike is, on this basis, anticipated to be sensitive to the nanoparticle structure. This final section of the chapter looks to explore experimental evidence for this conclusion. This will be achieved first by investigating the sensitivity of the nano-impact response to the presence of added electrolyte. Second, the influence of changing the nanoparticle morphology on the response of a single particle will be reported.

Figure 7.15 b depicts the average hydrogen oxidation transients for a series of individual particles studied with variable concentrations of added electrolyte. A gold microelectrode was immersed into a mesoporous PtNP sol and the electrode potential held at +0.2 V vs Ag/AgCl (1.0 M KCl). The nanoparticle sol was saturated with hydrogen and had a variable concentration of added supporting electrolyte (20, 2, and 0 mM KNO_3). The nanoparticle sol used within this work contains citrate as a stabilizing capping agent; consequently, even in the absence of additional electrolyte, a solution phase concentration of ∼0.2 mM citrate will be present in the nanoparticle sol. As shown in Figure 7.15 b, even in the absence of the addition of electrolyte, oxidative events associated with the arrival of PtNPs to the electrode surface are observed. Most notably, the magnitude of the individual nanoparticle impact events decreases as a function of the electrolyte concentration; however, the spike shape is relatively conserved. Figure 7.16 depicts the normalized impact responses allowing direct comparison of the oxidative spike shapes. The current has been normalized by dividing the measured response through by the current measured at 200 ms after the impact event.

If the reaction is limited by the rate of the surface reaction, why is the magnitude of

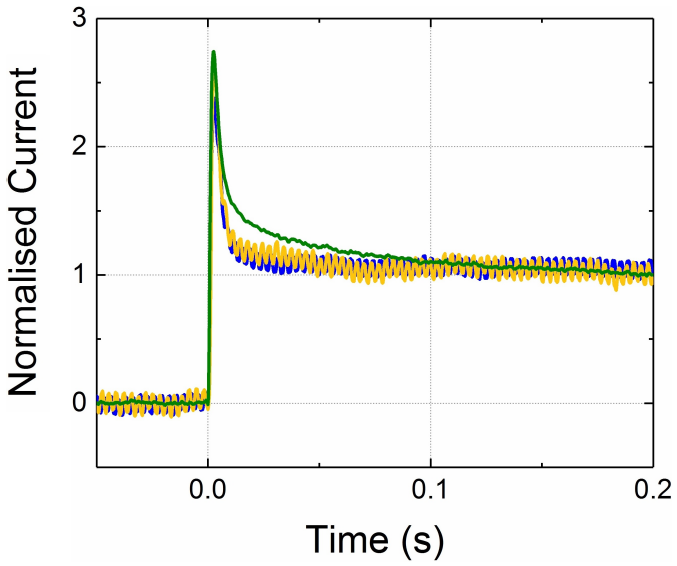

Figure 7.16: Normalized plots of experimentally determined average response of mesoporous PtNPs towards the oxidation of hydrogen at +0.2 V vs Ag/AgCl (1.0 M KCl) in the presence of 20 mM, 2 mM and 0 mM (green, yellow and blue respectively) additional KNO_3 electrolyte.

the single nanoparticle response (as evidenced in Figure 7.15 b) sensitive to the supporting electrolyte concentration? For the internal surfaces, it is reasonable that the HOR at this interface may be limited by a number of factors, including, the solution phase potential drop through the particle structure and/or the transport of either the reactant (hydrogen) or product (protons) in or out of the internal structure. Due to hydrogen being neutral, the mass transport of this material is not influenced to any appreciable extent by the local electric field; however, the product (protons) will be. It has previously been found that the oxidation of hydrogen at a platinum microelectrode can be studied under aqueous conditions in the absence of additional electrolyte; this occurs without significant distortion of the voltammetric response.[35] For the mesoporous nanoparticles in the absence of additional electrolyte, the solution phase conductivity will be approximately 29 μS cm^{-1} as based upon the known experimental citrate concentration (0.24 mM) and its estimated molar conductivity of 120 S cm^2 mol^{-1}.[49] Hence, on the nanoscale, very significant potential drops may occur through the solution phase of the internal nanoparticle structure.[50] Consequently, it is concluded that the used electrolyte concentration serves

to control the ohmic drop through the nanoparticle internal structure; under conditions of lower ionic strength, the HOR is likely restricted to occurring at a thinner layer near the external surface of the particle. For the nano-impact experiments performed using 20 mM KNO_3 in the near steady-state regime ($>$ 200 ms), the HOR on the internal particle surface contributes at least 40% of the catalytic current of the individual particle. However, the primary conclusion of this result is that at the nanoscale electrochemical reactions can be driven without the addition of excess supporting electrolyte. As will be discussed below, this has important consequence for the range of materials that can be studied using this technique.

Figure 7.15 c shows a comparison of an average spike event measured for the mesoporous nanoparticle and the same experiment performed using solid PtNPs (Section 7.2.2 provides further TEM characterization of these different materials) both recorded in the absence of additional electrolyte. Inlayed in Figure 7.15 c are representative TEM images of the material showing the differing internal structure of the nanoparticles. These solid nanoparticles are formed *via* laser ablation and consequently have a relatively large size distribution; moreover, the material is found to be comparatively highly sensitive to the addition of the supporting electrolyte. Consequently, the impact response of these solid PtNPs cannot be readily studied in the presence of additional electrolyte due to their lack of stability toward agglomeration. However, the averaged impact response of the solid nanoparticles (Figure 7.15 c) as recorded in the absence of addition electrolyte does not exhibit a significant peak in the current transients at short times, thus providing strong evidence that the peak in the nanoparticle response of the individual mesoporous PtNPs is directly related to the morphology of the nanostructure.

Both the alteration of the magnitude of the nanoparticle impact response as a function of the electrolyte concentration and the changed shape of the impact response between the mesoporous and solid particles serve to evidence the activity of the internal meso-

porous nanoparticle structure toward the oxidation of hydrogen. The observation of the variability in the HOR at high overpotentials, such that the reaction rate decreases at high overpotentials, yields insight into the origin of the observed sensitivity of the magnitude of the transient spike as a function of potential; at lower overpotentials, the internal structure is more active toward hydrogen oxidation and likely varies in activity not directly with the applied potential but is sensitive to the internal H_{upd} coverage, where equilibration of the internal H_{upd} surface coverage is slowed by the transport through the particles internal structure.

7.4 Conclusions

This chapter has demonstrated that, even at the single particle scale, the material's catalytic activity towards the oxidation of hydrogen is sensitive to the applied potential and exhibits two maxima in activity. These peaks in activity are directly reflected in the electrochemical current measured at both individual particles and sparse arrays of material. In contrast to the literature, the presence of the two peaks in activity are not ascribed as relating to the presence of two different catalytic sites, but by studying this reaction under different proton concentrations, the position of the first minima is shown to directly correlate with the potential of H_{upd} oxidation. The rate of adsorption of hydrogen to the interface is consequently highly sensitive to the interfacial structure, where at higher potentials the HOR is likely inhibited by specific anion adsorption. This conclusion is corroborated by the shape of the individual nanoparticle impact transients, where at low potentials the activity of the platinum particles dynamically decreases with time as H_{upd} is removed from the particle's interface.

Having provided greater insight into the HOR at these high current densities, the shape of the resulting single particle time-current transients is also shown to be sensitive to the structure of the nanomaterial. For the mesoporous particles used in this work, the

activity of the internal structure toward the oxidation of hydrogen is directly evidenced *via* comparison with solid particles.

In the following chapter, the single particle activity and surface area will be investigated simultaneously on the same mesoporous PtNPs using nanoimpacts.

Appendices

B.1 Procedure for Averaging Nano-Impact Step Responses

Dr. Chuhong Lin carried out all the simulations as described below.

The experimental time-current transients associated with the arrival and catalysis of hydrogen at a mesoporous particle results in nano-impact signals that commonly contain a sharp spike and a following step, as experimentally shown in Figure 7.6 (main text) and schematically outlined in Figure B.1. Both the background electrical noise and the nano-impact signal can be treated as a valley-peak pattern, which is a local minimal point followed by a local maximum point. Figure B.1 a shows three valley-peak examples.

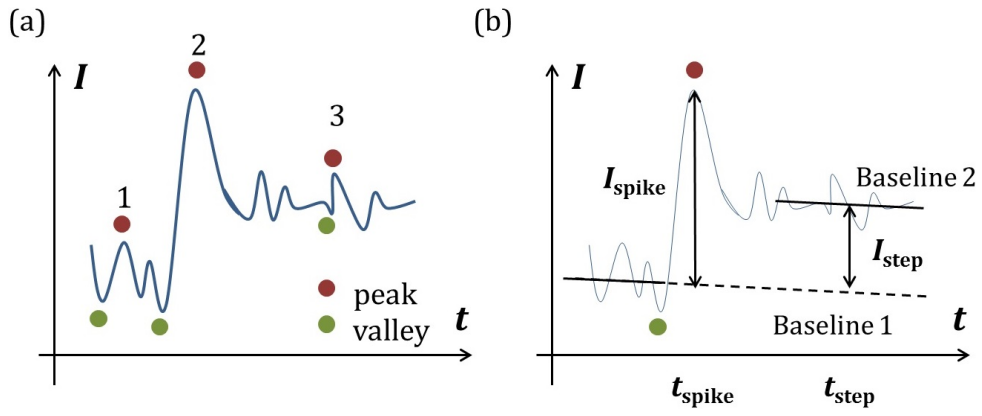

Figure B.1: (a) Schematic examples of individual nanoparticle time-current transients and the associated analysis procedure, highlighting three "valley-peak" pairs. (b) Illustration of the calculation of the spike height I_{spike} and the step height I_{step}.

The difference between the peak current I_{p} and the valley current I_{v} is the feature used to distinguish the signal from the noisy background. Only when $I_{\mathrm{p}} - I_{\mathrm{v}}$ is larger than the threshold value (which is determined by the user), the valley-peak pair is regarded as a signal. In Figure B.1 a, by choosing a reasonable threshold value, the valley-peak pair number 2 is identified as a signal and the other valley-peak pairs are regarded as background noises. Therefore in this way the signal can be realized.

Figure B.1 b illustrates the calculation of some signal features, the spike height I_{spike} and the step height I_{step}. The position of the spike of one nano-impact signal is represented by its time coordinate t_{spike}. Taken the influence of the background noise into consideration, the spike height is calculated as the difference between the peak current and the baseline current at t_{spike}. The baseline for spike height calculation is a linear fitting of the background current in a certain time period $[t_{\mathrm{v}} - \Delta t_{\mathrm{bl}},\ t_{\mathrm{v}}]$ (Δt_{bl} is the time interval determined by the user and t_{v} is the time coordinate of the valley), as illustrated by the solid part of Baseline 1 in Figure B.1 b. The dashed part of Baseline 1 is its extrapolation. The step corresponds to the condition where the reaction is at steady state. The time needed for the reaction to reach the steady state at a nanoparticle Δt_{s} is defined by the user. The time coordinate of the step $t_{\mathrm{step}} = t_{\mathrm{spike}} + \Delta t_{\mathrm{s}}$. But as the current near t_{step} is also noisy, it is necessary to simulate another baseline near t_{step} ($[t_{\mathrm{step}} - \Delta t_{\mathrm{bl}},\ t_{\mathrm{step}} + \Delta t_{\mathrm{bl}}]$), as the Baseline 2 shown in Figure B.1 b. The step height is calculated as the current difference between Baselines 1 and 2 at time t_{step}.

The average response of the nano-impact signals as shown in Figure 7.8 (main text) is found by averaging individual current features recorded under the same experimental conditions.

B.2 Tafel–Volmer Mechanism at an Isolated Nanoparticle Supported on a Plane

Dr. Chuhong Lin developed the theory and carried out all the simulations as described below.

The influence of adsorption and desorption on the Tafel–Volmer mechanism reaction on isolated microscale electrodes (which is analogous to the case of isolated nanoparticles in this chapter) with different electron-transfer models has been studied in the previous work.[42] The reaction rate equations of H_2, H^+ and the adsorbed hydrogen H_{ads} in the Tafel–Volmer reaction can be expressed as:

$$-D_{\mathrm{H_2}}\nabla c_{\mathrm{H_2}} = -k_{\mathrm{a}} c_{\mathrm{H_2}} {\Gamma_{\mathrm{M}}}^2 + k_{\mathrm{d}} {\Gamma_{\mathrm{H_{ads}}}}^2 \tag{B.1}$$

$$-D_{\mathrm{H^+}}\nabla c_{\mathrm{H^+}} = k_{\mathrm{el}} c^{\ominus} \exp\left(\frac{\beta F\eta}{RT}\right)\Gamma_{\mathrm{H_{ads}}} - k_{\mathrm{el}} c_{\mathrm{H^+}} \exp\left(-\frac{\alpha F\eta}{RT}\right)\Gamma_{\mathrm{M}} \tag{B.2}$$

$$\frac{\partial \Gamma_{\mathrm{H_{ads}}}}{\partial t} = 2k_{\mathrm{a}} c_{\mathrm{H_2}} {\Gamma_{\mathrm{M}}}^2 - 2k_{\mathrm{d}} {\Gamma_{\mathrm{H_{ads}}}}^2 - k_{\mathrm{el}} c^{\ominus} \exp\left(\frac{\beta F\eta}{RT}\right)\Gamma_{\mathrm{H_{ads}}} + k_{\mathrm{el}} c_{\mathrm{H^+}} \exp\left(-\frac{\alpha F\eta}{RT}\right)\Gamma_{\mathrm{M}} \tag{B.3}$$

where M is the unoccupied active site at the electrode surface, and the concentrations in the above equations refer to the surface concentrations. $\Gamma_{\max}$ is the maximum active site density (mol m^{-2}) at the electrode and in this work $\Gamma_{\max}$ is always assumed to be constant, 2.2×10^{-5} mol m^{-2}.[47] k_{a} and k_{d} are the adsorption and desorption rate constants, of which the units are m^5 mol^{-2} s^{-1} and m^2 mol^{-1} s^{-1}. k_{el} is the electron transfer rate constant (m^3 mol^{-1} s^{-1}) for the Volmer step. The oxidative and reductive reaction rate constants for the redox reaction are described by the Butler-Volmer equation. α and β are the transfer coefficients and $\alpha + \beta = 1$.[51, 52] Considering the different stoichiometry of the oxidative and reductive direction of the Volmer step, the oxidative reaction rate constant is expressed as $k_{\mathrm{el}}c^{\ominus}$ ($c^{\ominus} = 1$ mol m^{-3}) to keep the unit balanced in the reaction rate equation.

In short, a slow preceding adsorption (small adsorption rate constant k_a) leads to a steady-state current smaller than the diffusion-limited value. The adsorption-limited steady-state current can be expressed as a function of k_a and is independent of the desorption rate constant k_d and the electron-transfer rate constant k_{el}. The influence of k_d and k_{el} is reflected only on the potential shift of the overall voltammetric wave but not on the value of the steady-state current.

For HOR in media with different pHs, the values of the kinetic parameters may be different. The voltammograms recorded are simulated from neutral, acidic and alkaline cases below. Assuming that the PtNPs on the PtNP arrays are sparsely distributed, the voltammogram of a PtNP array = the number of PtNPs $\times$ the voltammogram of one PtNP.

B.2.1 Neutral Case (20 mM KNO_3 Electrolyte)

In this case, the adsorption rate constant k_a on one PtNP may be determined directly from the magnitude of a single nanoparticle impact and has a value of 4.3×10^7 m^5 mol^{-2}

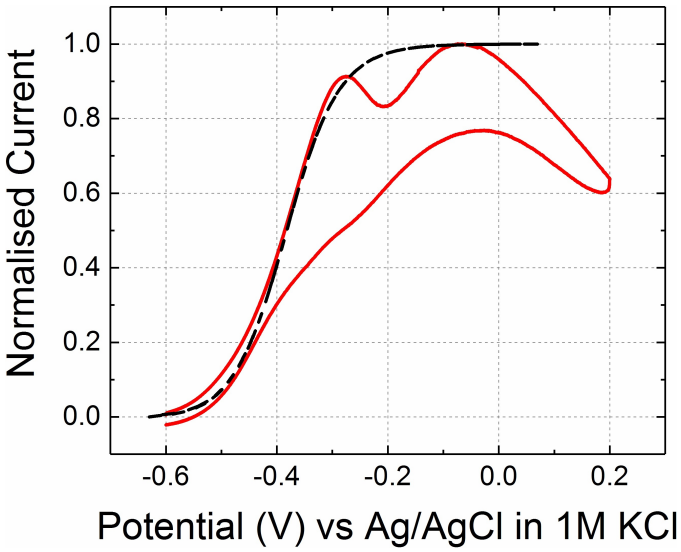

Figure B.2: Simulated response (black dash line) for the oxidation of hydrogen *via* the Tafel–Volmer mechanism at an isolated spherical PtNP in 20 mM KNO_3. Kinetic parameters used in the simulation are k_a, k_d and $k_{el} = 4.3 \times 10^7$ m^5 mol^{-2} s^{-1}, 4.3×10^7 m^2 mol^{-1} s^{-1} and 9.2×10^2 m^3 mol^{-1} s^{-1} respectively. Overlaid for comparison is the experimental response (CV of scan rate 200 mV s^{-1}) of a PtNP array at a gold microelectrode in 20 mM KNO_3 (red line).

s^{-1} under $\Gamma_{max} = 2.2 \times 10^{-5}$ mol m^{-2}. However, k_{el} and k_d are unknown. The waveshape of this voltammogram indicates that the oxidation is electrically irreversible (relative to the local mass transport); the position of the wave (near -0.43 V) indicates that the value of k_{el} and k_d cannot be too small. Figure B.2 with consistent parameters of $k_{el} = 9.2 \times 10^2$ m^3 mol^{-1} s^{-1} and $k_d = 4.3 \times 10^7$ m^2 mol^{-1} s^{-1} shows a good fit with experiment but these values are not unique.

B.2.2 Acidic Case (1 mM $HClO_4$ and 19 mM $KClO_4$ Electrolyte)

The adsorption rate constant k_a is about 5.3×10^7 m^5 mol^{-2} s^{-1} as estimated from the nano-impact step current at high overpotentials. In the acidic case, the waveshape is strongly dependent on k_{el}, so the value of k_{el} can be more precisely determined to be 1.2×10^4 m^3 mol^{-1} s^{-1}. As decreasing k_d shift the wave position, it is also found that k_d cannot be smaller than 5.3×10^7 m^2 mol^{-1} s^{-1}. Figure B.3 shows a simulation with kinetic parameters $k_a = 5.3 \times 10^7$ m^5 mol^{-2} s^{-1}, $k_d = 5.3 \times 10^7$ m^2 mol^{-1} s^{-1},

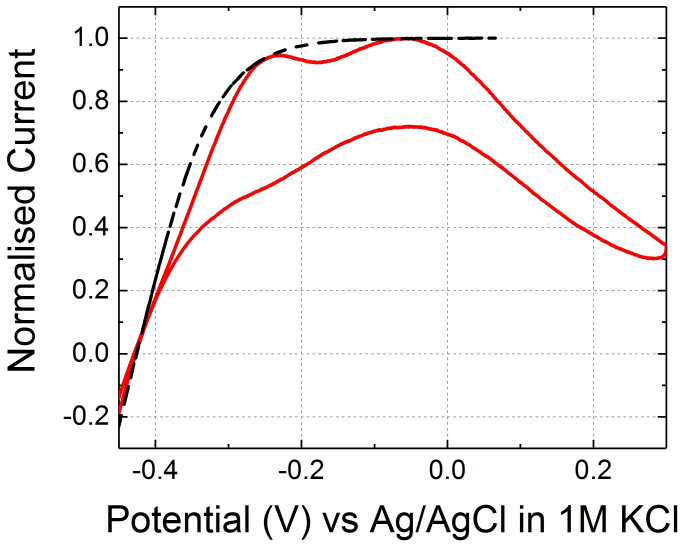

Figure B.3: Simulated response (black dash line) for the oxidation of hydrogen *via* the Tafel–Volmer mechanism at an isolated spherical PtNP in 1 mM $HClO_4$ and 19 mM $KClO_4$. Kinetic parameters used in the simulation are k_a, k_d and $k_{el} = 5.3 \times 10^7$ m^5 mol^{-2} s^{-1}, 5.3×10^7 m^2 mol^{-1} s^{-1} and 1.15×10^4 m^3 mol^{-1} s^{-1} respectively. Overlaid for comparison is the experimental response (CV of scan rate 200 mV s^{-1}) of a PtNP array at a gold microelectrode in equivalent to 1 mM $HClO_4$ and 19 mM $KClO_4$ (red line).

$k_{el} = 1.2 \times 10^4$ m^3 mol^{-1} s^{-1}.

B.2.3 Alkaline Case (20 mM KOH Electrolyte)

Simulation of the response under alkaline media is significantly more complicated due to the requirement of considering the conjugate base (water) as a source of protons, which means water decomposition must be taken into consideration. Hence, in the present work the evolution of hydrogen under these conditions is not considered. The adsorption rate constant k_a calculated from the nano-impact step current is about 5.9×10^6 m^5 mol^{-2} s^{-1}. To simulate the waveshape and the wave position, a small α value and an irreversible k_{el} are required. When assuming k_d also equal to 5.9×10^6 m^2 mol^{-1} s^{-1}, $k_{el} = 4.6$ m^3 mol^{-1} s^{-1} fits the position of the wave ($E_{sim} = E_{RHE} + \eta$). Figure B.4 shows a simulation with kinetic parameters $k_a = 5.9 \times 10^6$ m^5 mol^{-2} s^{-1}, $k_d = 5.9 \times 10^6$ m^2 mol^{-1} s^{-1} and $k_{el} = 4.6$ m^3 mol^{-1} s^{-1}.

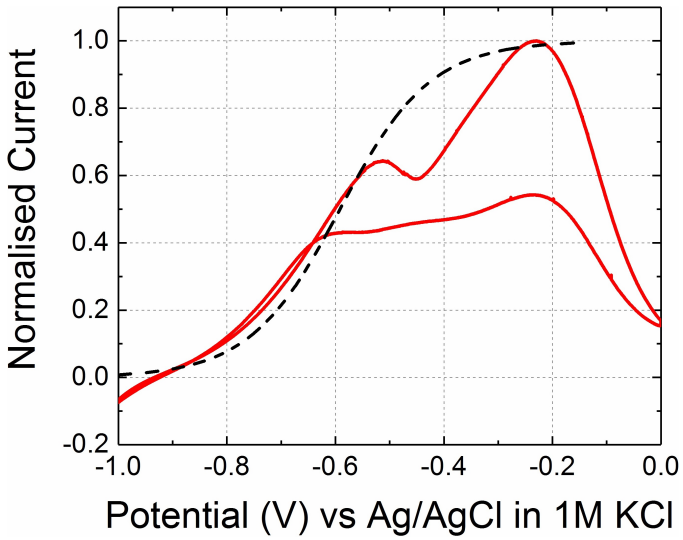

Figure B.4: Simulated response (black dash line) for the oxidation of hydrogen *via* the Tafel–Volmer mechanism at an isolated spherical PtNP in 20 mM KOH. Kinetic parameters used in the simulation are k_a, k_d and $k_{el} = 5.9 \times 10^6$ m^5 mol^{-2} s^{-1}, 5.9×10^6 m^2 mol^{-1} s^{-1} and 4.6 m^3 mol^{-1} s^{-1} respectively. Overlaid for comparison is the experimental response (CV of scan rate 200 mV s^{-1}) of a PtNP array at a gold microelectrode in equivalent to 20 mM KOH (red line).

B.3 Computational Modelling of Current Spike Shapes

Dr. Enno Kätelhön developed the models and carried out all the simulations as described below.

Four different models are considered for possible reaction mechanisms to establish the physical origins of the observed current spikes. Some of these theoretical models focus on aspects of the impact process that may take place concurrently and independently from each other, and may therefore be combined in joined models. A direct comparison between the theory and the experimental data enables further insight into the nature of the impact process and provides strong indications regarding the nature of the prevailing physical process.

The following section introduces the theoretical models, describes the computational model used for the signal processing *via* the analogue measurement equipment, details the parameters used in the calculations, and explains the computational methods used. Finally, the results of the different theoretical models are presented, discussed, and compared with experimental data.

B.3.1 Theoretical Models

Four different reaction mechanisms are considered that all give rise to different spike shapes in the current measurement. First, a solid spherical particle featuring a homogeneous surface concentration of surface-bound hydrogen and the immediate heterogeneous reaction of hydrogen to free protons upon the impact. Second, a porous spherical particle decorated with surface-bound hydrogen on all surfaces inside and outside of the particle, and immediate reaction kinetics for the oxidation of hydrogen to free protons. Third, the same porous particle is investigated for a case in which the reaction of the initially adsorbed hydrogen inside the particle is limited by the oxidation of adsorbed hydrogen at the particle surface. The reaction rate is herein determined by the effective diffusion of

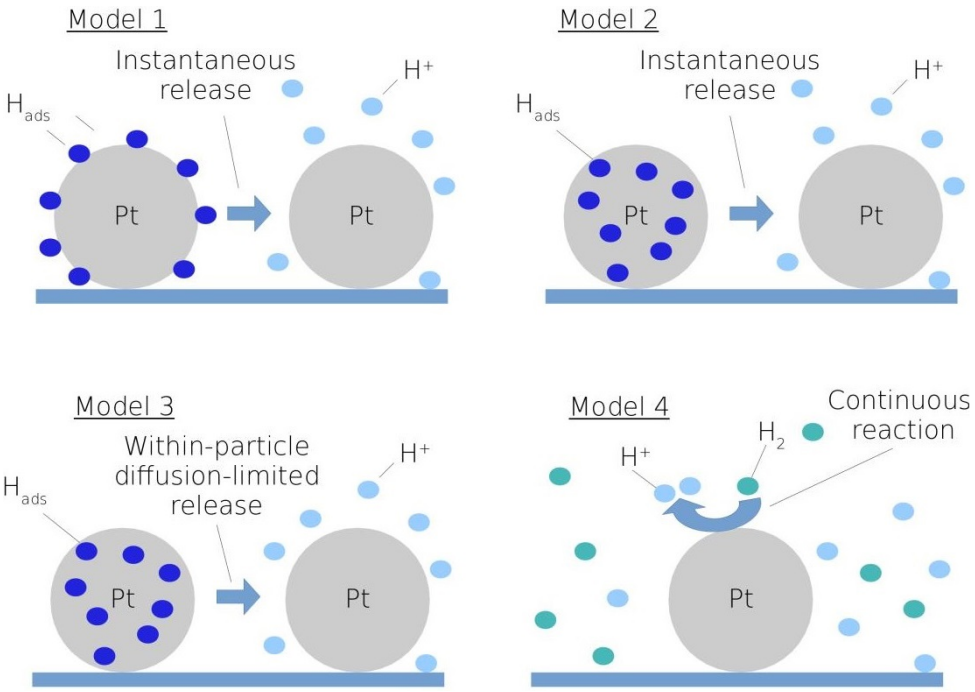

Figure B.5: Illustration of the considered reaction models one to four.

adsorbed hydrogen towards the particle surface where it is oxidized to a free proton. And fourth, a spherical solid or porous particle and a kinetically-limited reaction of dissolved hydrogen that diffusively reaches the particle from the solution and reacts at its surface. A schematic illustration of all models can be found in Figure B.5.

Solid Particle and Fast Proton Release

The first model describes the impact of a solid spherical nanoparticle. The particle features a layer of adsorbed hydrogen on its surface which can be described through a constant surface concentration $c_s(\mathrm{H_{ads}})$. Upon the impact of the particle at the electrode surface, the particle is assumed to instantaneously adopt the positive electrode potential. This change in potential triggers the equally instantaneous reaction to free protons alongside the simultaneous transfer of charge from the particle to the electrode. Assuming a constant total charge of the particle throughout the entire impact, the amount of charge transferred must herein equal the charge of the released protons. The corresponding electrode current

I_1 can hence be described as:

$$I_1(t) = q_s \delta(t - t_0) \tag{B.4}$$

where δ is the Dirac delta function, t_0 is the time of the impact, and q_s is the total charge all pre-adsorbed protons:

$$q_s = \int_S dA \; c_s(\mathrm{H_{ads}}) F = 4\pi {r_p}^2 c_s(\mathrm{H_{ads}}) F \tag{B.5}$$

where S and r_p signify the particle surface and radius, respectively.

Porous Particle and Fast Proton Release

The second model describes the impact of a spherical porous particle which is an aggregate of individual solid particles. These solid particles are assumed to be identical and to feature a homogeneous surface concentration $c_s(\mathrm{H_{ads}})$ of adsorbed hydrogen. The solid particles further arrange in the closest possible packing fashion within the aggregate, which hence features a packing density ρ_0 of 0.74. On the basis of the packing density, the average concentration of protons within a porous particle can be determined. The density of solid particles ρ_s can be calculated as:

$$\rho_s = \frac{\rho_0}{V_s'} = \frac{\rho_0}{\frac{4}{3}\pi (r_p')^3} \tag{B.6}$$

where V_s' and r_p' are the volume and the radius of the solid particles, respectively. The average charge density ρ_q of the porous particle can hence be calculated as:

$$\rho_q = \rho_s q_s'$$

with

$$q_s' = \int_{S'} dA \; c_s(\mathrm{H_{ads}}) F = 4\pi (r_p')^2 c_s(\mathrm{H_{ads}}) F \tag{B.7}$$

The total charge of all protons within the porous nanoparticle then amounts to:

$$q_p = \int_{V_p} dV \rho_q = \frac{4}{3}\pi {r_p}^3 \rho_q \tag{B.8}$$

In analogy with the previous section, it is assumed that all hydrogen reacts in the moment of the impact while an equal amount of charge is transferred from the electrode to the particle. The corresponding electrode current can then be written as:

$$I_2(t) = q_p \delta(t - t_0) \tag{B.9}$$

Porous Particle and Diffusive Proton Release

The third model considers the same porous particle as in the previous section featuring a homogeneous internal surface concentration of adsorbed hydrogen. In contrast to the second model, the release is however not instantaneous but limited by diffusion within the particle prior to electrolytic release. In addition, it is assumed that following the impact, the particle remains at the electrode until all protons are released.

The initial distribution of adsorbed hydrogen within the particle is approximated to a constant concentration:

$$c_\nu^*(\mathrm{H_{ads}}) = \frac{q_p}{F} \left(\frac{4}{3}\pi {r_p}^3 \right)^{-1} \tag{B.10}$$

The concentration of adsorbed hydrogen at the moment of the impact can then be written:

$$c_\nu(\mathrm{H_{ads}}, \vec{r}, t = t_0) = \begin{cases} c_\nu^*(\mathrm{H_{ads}}) & \text{for} \quad r < r_p \\ 0 & \text{for} \quad r_p < r \end{cases} \tag{B.11}$$

where r signifies the radial dimension in spherical coordinates with the origin set to the particle's centre of mass. Since the concentration of free protons outside the particle is much smaller and their diffusion much faster than inside the particle, it is further

approximated for all t:

$$c_\nu(\mathrm{H_{ads}}, r = r_p, t) = 0 \tag{B.12}$$

The model does not include any electrostatic effects and the mass transport of protons is described *via* diffusion equation:

$$\frac{\partial c_\nu(\mathrm{H_{ads}}, \vec{r}, t)}{\partial t} = D \overrightarrow{\nabla}^2 c_\nu(\mathrm{H_{ads}}, \vec{r}, t) \tag{B.13}$$

where D is the average diffusion coefficient of protons within the particle. Given the symmetry of the model, the partial differential equation can be simplified to:

$$\frac{\partial c_\nu(\mathrm{H_{ads}}, \vec{r}, t)}{\partial t} = D \left[\frac{\partial^2 c_\nu(\mathrm{H_{ads}}, \vec{r}, t)}{\partial r^2} + \frac{2}{r} \frac{\partial c_\nu(\mathrm{H_{ads}}, \vec{r}, t)}{\partial r} \right] \tag{B.14}$$

In analogy to the previous two models the change in the charge of the particle induced by the release of protons is compensated by the charge transfer between the electrode and the particle. This yields the following expression for the electrode current:

$$I_3 = -F \frac{d}{dt} \int_V dr \; c_\nu(\mathrm{H_{ads}}, \vec{r}, t) \tag{B.15}$$

The calculations are made along the lines of previous work,[53, 54] where related mathematical methods are detailed comprehensively.

Kinetically-Limited Hydrogen Oxidation at the Particle Surface

The fourth model describes the reaction of hydrogen at the surface of a solid or porous particle. It herein is assumed that in the moment of the impact the particle adsorbs at the electrode and adopts the electrode potential. Hydrogen diffusively reaches the particle from the solution and reacts in a kinetically-limited reaction, i.e. the reaction progresses slow enough that the concentration of hydrogen in the immediate surrounding

of the particle is not depleted. The electrode current is then proportional to the effective electrochemical rate constant k_0, the particle surface S, and the concentration $c_\nu(\mathrm{H_2})$ of hydrogen in solution:

$$I_4(t) = 4\pi r_p^2 k_0 n_e c_\nu(\mathrm{H_2})\Theta(t - t_0) \tag{B.16}$$

where Θ is the Heaviside step function and n_e equals two:

$$\Theta(t - t_0) = \int_{-\infty}^{t} dt' \; \delta(t' - t_0) \tag{B.17}$$

B.3.2 Computational Model of the Analogue Measurement Set-Up

Previous work[55] has established that the analogue circuitry of the potentiostat may dramatically alter the shape of measured spikes in nano-impact experiments. Features like the spike height or duration may differ by orders of magnitude if the actual charge transfer is compared with the measured one, while most implementations conserve only the overall charge transferred. It is therefore generally crucial to consider the influence of the potentiostat, i.e. its signal transfer function, in any analysis of the spike shape. For the experimental system modelled, the transfer characteristics are approximated as a first-order Butterworth low-pass filter and transform all depicted currents accordingly.

B.3.3 Parameters

The numerical calculations employ the parameters specified in Table B.1. Please note that the sampling frequency f_s is used as a convergence parameter in the numerical evaluation of the models. It describes the discretization of time, $1/f_s$, in the calculations and hence does not have a direct physical meaning.

Parameter	Symbol	Value
Particle radius	r_p	25 nm
Radius of individual solid particles in a porous particle	r_p'	2 nm
Surface concentration of adsorbed hydrogen	$c_s(\mathrm{H_{ads}})$	2.2×10^{-5} mol m^{-2}
Volume concentration of dissolve hydrogen in solution	$c_\nu(\mathrm{H_2})$	0.73 mol m^{-3}
Effective electrochemical rate constant	k_0	0.01 m s^{-1}
Filter cut-off frequency	f_c	100 Hz
Sampling frequency used in numerical calculations	f_s	≥ 1 MHz

Table B.1: Parameters used in numerical calculations.

B.3.4 Computational Methods

All code for numerical calculations is written in *Julia* and filters are implemented *via* Julia's *DSP* package.

Results and Comparison with Experimental Data

Figure B.6 compares the numerical results of the models one to four. All data was evaluated for the parameters shown in Table B.1 and include the transfer function of the potentiostat. The distinct features arising from the different models are discussed separately in the following.

The comparison between the simulated currents obtained *via* model one and two immediately reveals that both models yield identical but differently scaled spike shapes. This observation can be understood from the structure of the Equations B.4 and B.9 which both yield to current responses proportional to the Dirac delta function. This input signal, by definition, triggers the impulse response of the potentiostat. As the transfer function of the potentiostat is assumed to be linear and time invariant, both pulses must yield equal but differently scaled shapes.

A more detailed analysis of the data reveals that in model two and three equal amounts of charge are transferred between the electrode and the particle. This can be understood from the assumptions made in the design of the models: in both impact models of porous particles equal amounts of protons are initially adsorbed within the particle and released

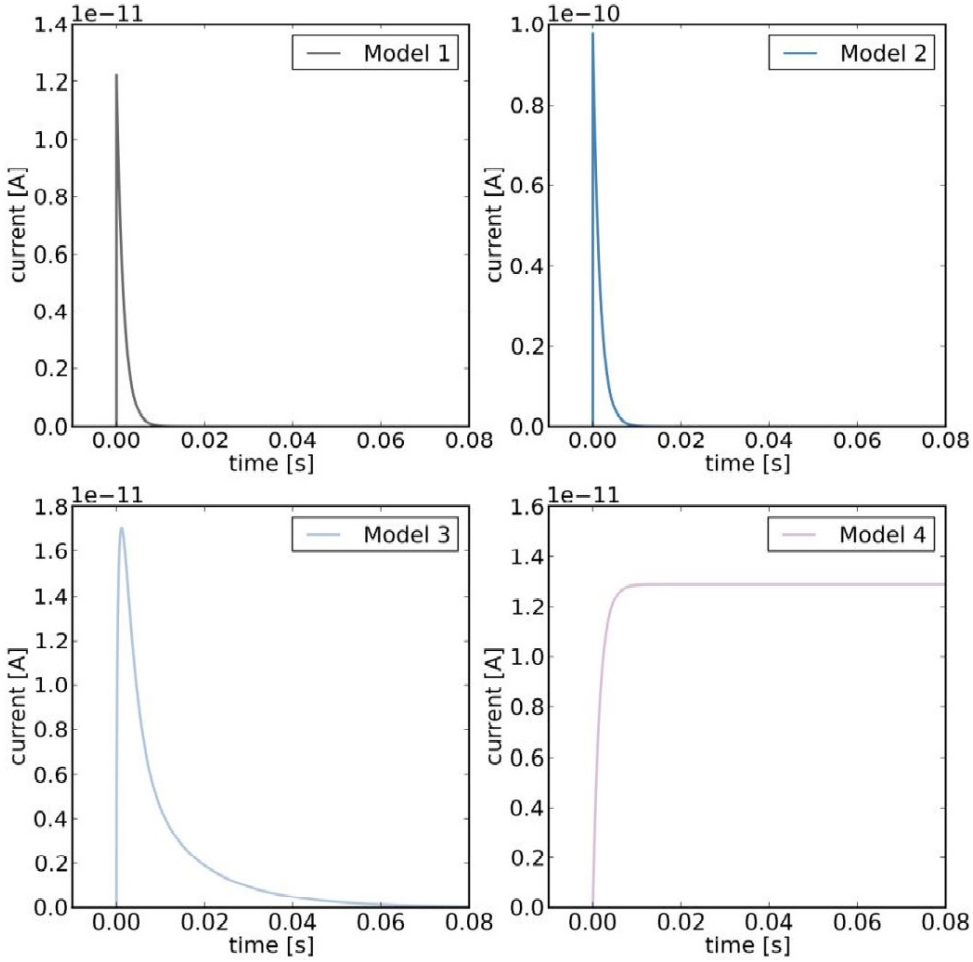

Figure B.6: Comparison of the above four numerical models for the spike shape. The third model was evaluated for a proton diffusion coefficient of 5×10^{-15} m^2 s^{-1}.

immediately or *via* a diffusive process. Model two hence renders the limiting case of model three if evaluated for an infinitely high diffusion coefficient.

Various of the above models can be combined to model the current response if multiple reaction processes take place simultaneously. While model one, two, and three describe the release of surface-bound hydrogen in form of free protons, model four is concerned with the oxidation of hydrogen in solution. If both processes are assumed to be independent, the models one to three can hence be combined with model four.

The spike shapes resulting from combined models are illustrated in Figure B.7. The figure reveals that for a solid particle, there is only little difference between the cases with and without pre-adsorbed hydrogen. For porous particles, however, the much larger

amount of preconcentrated protons within the particle leads to a distinct initial spike that cannot be seen in any of the two models for solid particles that consider the reaction of hydrogen. The different release kinetics of protons within the particle are reflected in the different durations of the onset spikes.

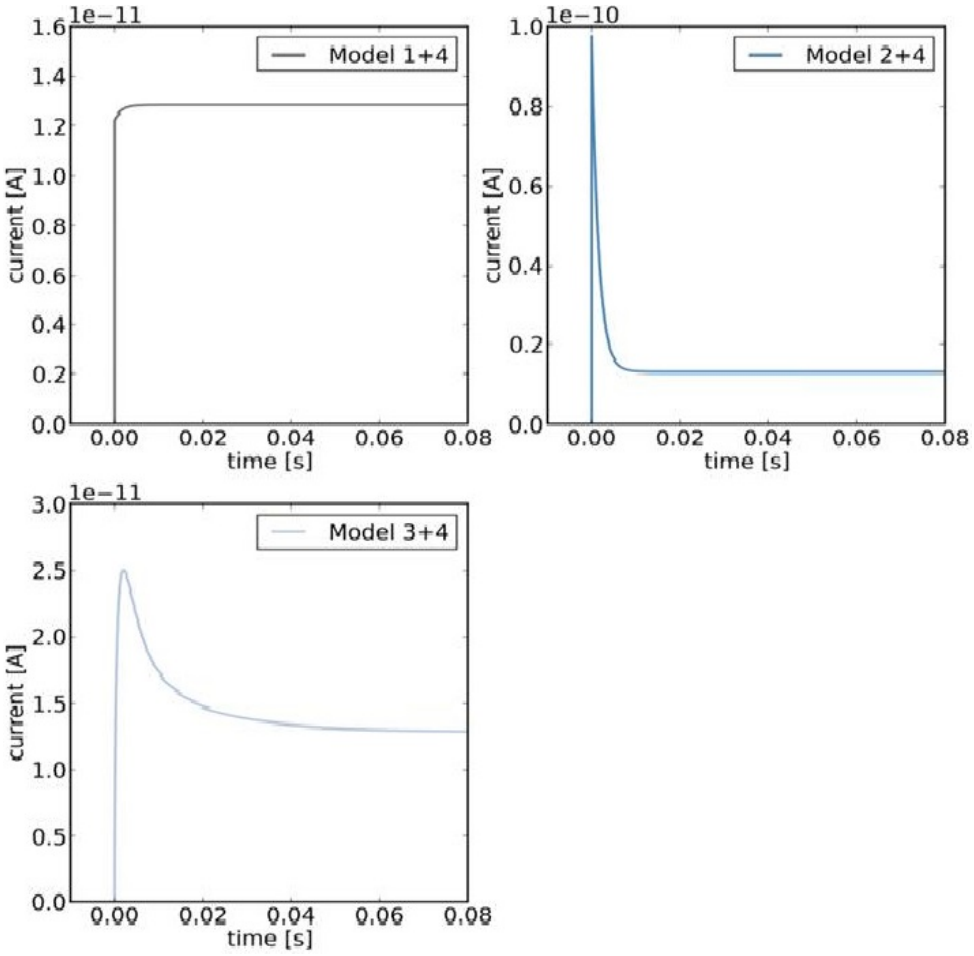

Figure B.7: Comparison of combined reacton models: (a) Impact of a solid nanoparticle. Pre-adorbed protons are immediately released upon the impact and trigger a simultaneous charge transfer between the electrode and the particle. Following the impact, the particle remains adsorbed to the electrode and enables the kinetically-limited reaction of hydrogen at it surface. (b) Equivalent to (a) evaluated for a porous nanoparticle and pre-adsorbed protons on all surfaces inside and outside the particle. (c) The previous case (b) is evaluated for a release of protons that is limited by the diffusion of pre-adsorbed protons out of the particle.

Bibliography

[1] Jiao, X.; Batchelor-McAuley, C.; Lin, C.; Kätelhön, E.; Tanner, E. E.; Young, N. P.; Compton, R. G. *ACS Catalysis* **2018**, *8*, 6192–6202.

[2] Snyder, J.; Fujita, T.; Chen, M.; Erlebacher, J. *Nature Materials* **2010**, *9*, 904–907.

[3] Marcus, R. A. *Journal of Chemical Physics* **1956**, *24*, 966–978.

[4] Hush, N. S. *Transactions of the Faraday Society* **1961**, *57*, 557–580.

[5] Hush, N. S. *Journal of Chemical Physics* **1958**, *28*, 962–972.

[6] Chidsey, C. E. *Science* **1991**, *251*, 919–922.

[7] Xiao, X.; Bard, A. J. *Journal of the American Chemical Society* **2007**, *129*, 9610–9612.

[8] Albrecht, T.; Horswell, S.; Allerston, L. K.; Rees, N. V.; Rodriguez, P. *Current Opinion in Electrochemistry* **2018**, *7*, 138–145.

[9] Dickinson, E. J. F.; Compton, R. G. *Journal of Electroanalytical Chemistry* **2011**, *661*, 198–212.

[10] Murray, R. W. *Chemical Reviews* **2008**, *108*, 2688–2720.

[11] Favaro, M.; Jeong, B.; Ross, P. N.; Yano, J.; Hussain, Z.; Liu, Z.; Crumlin, E. J. *Nature Communications* **2016**, *7*, 12695.

[12] Sheng, W.; Gasteiger, H. A.; Shao-Horn, Y. *Journal of the Electrochemical Society* **2010**, *157*, B1529–B1536.

[13] Markovića, N. M.; Sarraf, S. T.; Gasteiger, H. A.; Ross, P. N. *Journal of the Chemical Society, Faraday Transactions* **1996**, *92*, 3719–3725.

[14] Ledezma-Yanez, I.; Wallace, W. D. Z.; Sebastián-Pascual, P.; Climent, V.; Feliu, J. M.; Koper, M. *Nature Energy* **2017**, *2*, 17031.

[15] Frumkin, A. N.; Aikazyan, É. A. *Bulletin of the Academy of Sciences of the USSR, Division of Chemical Science* **1959**, *8*, 188–197.

[16] Zalitis, C.; Kucernak, A.; Sharman, J.; Wright, E. *Journal of Materials Chemistry A* **2017**, *5*, 23328–23338.

[17] Kongkanand, A.; Mathias, M. F. *Journal of Physical Chemistry Letters* **2016**, *7*, 1127–1137.

[18] These high rates are attained through the use of a gas diffusion electrode ensuring a rapid supply of material to the interface. Assuming an anode loading of 0.05 mg cm^{-2} with a catalyst electrochemical surface area of 50 m^2 g^{-1}, then with a current density of *cf.* 1 A $cm_{geo}{}^{-2}$ being drawn, the molecular turnover rate of hydrogen per surface area of the catalyst will be > 1000 nm^{-2} s^{-1}.

[19] Stephens, I. E. L.; Rossmeisl, J.; Chorkendorff, I. *Science* **2016**, *354*, 1378–1379.

[20] Bu, L.; Zhang, N.; Guo, S.; Zhang, X.; Li, J.; Yao, J.; Wu, T.; Lu, G.; Ma, J.-Y.; Su, D. *Science* **2016**, *354*, 1410–1414.

[21] Li, M.; Zhao, Z.; Cheng, T.; Fortunelli, A.; Chen, C.-Y.; Yu, R.; Zhang, Q.; Gu, L.; Merinov, B. V.; Lin, Z. *Science* **2016**, *354*, 1414–1419.

[22] Chen, C.; Kang, Y.; Huo, Z.; Zhu, Z.; Huang, W.; Xin, H. L.; Snyder, J. D.; Li, D.; Herron, J. A.; Mavrikakis, M. *Science* **2014**, *343*, 1339–1343.

[23] Higher rates are generally not limited by the onset of turbulence, but due to difficulties in fabrication of suitable high speed rotors.

[24] Masa, J.; Batchelor-McAuley, C.; Schuhmann, W.; Compton, R. G. *Nano Research* **2014**, *7*, 71–78.

[25] Zhou, R.; Zheng, Y.; Jaroniec, M.; Qiao, S.-Z. *ACS Catalysis* **2016**, *6*, 4720–4728.

[26] Treimer, S.; Tang, A.; Johnson, D. C. *Electroanalysis* **2002**, *14*, 165–171.

[27] Zalitis, C. M.; Kramer, D.; Kucernak, A. R. *Physical Chemistry Chemical Physics* **2013**, *15*, 4329–4340.

[28] Jiao, X.; Tanner, E. E. L.; Sokolov, S. V.; Palgrave, R. G.; Young, N. P.; Compton, R. G. *Physical Chemistry Chemical Physics* **2017**, *19*, 13547–13552.

[29] Jiao, X.; Lin, C.; Young, N. P.; Batchelor-McAuley, C.; Compton, R. G. *Journal of Physical Chemistry C* **2016**, *120*, 13148–13158.

[30] Ly, L. S. Y.; Batchelor-McAuley, C.; Tschulik, K.; Kätelhön, E.; Compton, R. G. *Journal of Physical Chemistry C* **2014**, *118*, 17756–17763.

[31] Xiang, Z.-P.; Deng, H.-Q.; Peljo, P.; Fu, Z.-Y.; Wang, S.-L.; Mandler, D.; Sun, G.-Q.; Liang, Z.-X. *Angewandte Chemie, International Edition* **2018**, *57*, 3464–3468.

[32] Kleijn, S. E. F.; Serrano-Bou, B.; Yanson, A. I.; Koper, M. T. M. *Langmuir* **2013**, *29*, 2054–2064.

[33] Sokolov, S. V.; Tschulik, K.; Batchelor-McAuley, C.; Jurkschat, K.; Compton, R. G. *Analytical Chemistry* **2015**, *87*, 10033–10039.

[34] Bond, A. M.; Fleischmann, M.; Robinson, J. *Journal of Electroanalytical Chemistry and Interfacial Electrochemistry* **1984**, *168*, 299–312.

[35] Li, X.; Batchelor-McAuley, C.; Laborda, E.; Compton, R. G. *Chemistry – A European Journal* **2017**, *23*, 15222–15226.

[36] Creighton, J. A.; Eadon, D. G. *Journal of the Chemical Society, Faraday Transactions* **1991**, *87*, 3881–3891.

[37] Jiao, X.; Sokolov, S. V.; Tanner, E. E. L.; Young, N. P.; Compton, R. G. *Physical Chemistry Chemical Physics* **2017**, *19*, 64–68.

[38] Sokolov, S. V.; Eloul, S.; Kätelhön, E.; Batchelor-McAuley, C.; Compton, R. G. *Physical Chemistry Chemical Physics* **2017**, *19*, 28–43.

[39] Bobbert, P. A.; Wind, M. M.; Vlieger, J. *Physica A: Statistical Mechanics and its Applications* **1987**, *141*, 58–72.

[40] Jiao, X.; Batchelor-McAuley, C.; Kätelhön, E.; Ellison, J.; Tschulik, K.; Compton, R. G. *Journal of Physical Chemistry C* **2015**, *119*, 9402–9410.

[41] Lin, C.; Jiao, X.; Tschulik, K.; Batchelor-McAuley, C.; Compton, R. G. *Journal of Physical Chemistry C* **2015**, *119*, 16121–16130.

[42] Lin, C.; Batchelor-McAuley, C.; Laborda, E.; Compton, R. G. *Journal of Physical Chemistry C* **2015**, *119*, 22415–22424.

[43] Compton, R. G.; Banks, C. E. *Understanding Voltammetry*, 2nd ed.; Imperial College Press, 2011.

[44] Macpherson, J. V.; Unwin, P. R. *Analytical Chemistry* **1997**, *69*, 2063–2069.

[45] Sheng, W.; Zhuang, Z.; Gao, M.; Zheng, J.; Chen, J. G.; Yan, Y. *Nature Communications* **2015**, *6*, 5848.

[46] Van der Niet, M. J. T. C.; Garcia-Araez, N.; Hernández, J.; Feliu, J. M.; Koper, M. T. M. *Catalysis Today* **2013**, *202*, 105–113.

[47] Conway, B.; Tilak, B. *Electrochimica Acta* **2002**, *47*, 3571–3594.

[48] The magnitude of the charge passed at +0.2 V indicates that in comparsion to the expected charge for a single monolayer of H_{upd} that the average agglomerate size per impact is maximally 2.

[49] Apelblat, A.; Barthel, J. *Zeitschrift für Naturforschung, A: Physical Sciences* **1991**, *46*, 131–140.

[50] A 25 nm long pore of radius 1 nm with a solution phase conductivity of 4.6 mS m^{-1} will have a resistance of approximately 1 TΩ, hence the passage of only tenths of a picoampere will lead to appreciable drops in potential along the structure.

[51] Guidelli, R.; Compton, R. G.; Feliu, J. M.; Gileadi, E.; Lipkowski, J.; Schmickler, W.; Trasatti, S. *Pure and Applied Chemistry* **2014**, *86*, 245–258.

[52] Guidelli, R.; Compton, R. G.; Feliu, J. M.; Gileadi, E.; Lipkowski, J.; Schmickler, W.; Trasatti, S. *Pure and Applied Chemistry* **2014**, *86*, 259–262.

[53] Kätelhön, E.; Feng, A.; Cheng, W.; Eloul, S.; Batchelor-McAuley, C.; Compton, R. G. *Journal of Physical Chemistry C* **2016**, *120*, 17029–17034.

[54] Zampardi, G.; Batchelor-McAuley, C.; Kätelhön, E.; Compton, R. G. *Angewandte Chemie, International Edition* **2017**, *56*, 641–644.

[55] Kätelhön, E.; Tanner, E. E.; Batchelor-McAuley, C.; Compton, R. G. *Electrochimica Acta* **2016**, *199*, 297–304.

Chapter 8

Simultaneous Activity and Surface Area Measurements on Single Mesoporous Nanoparticle Aggregates

The underpotential deposition and removal of hydrogen from a mesoporous platinum nanoparticle (PtNP) surface is shown to quantify the electrochemically active surface area (ECSA) of an *individual* nanoparticle. This surface area of the particle is concomitantly correlated with its individual catalytic activity (current density) towards the evolution of hydrogen. In addition, conclusions in this chapter are compared with the results in Chapters 4 and 5, showing consistency in all structural measurements of the particles.

This work has been published in *Physical Chemistry Chemical Physics*[1] and was performed in collaboration with Dr. Christopher Batchelor-McAuley and Dr. Neil P. Young (Department of Materials, University of Oxford). Dr. Christopher Batchelor-McAuley helped with the interpretation of the experimental results. Dr. Neil P. Young carried out the transmission electron microscopy (TEM) for the mesoporous PtNPs.

8.1 Introduction

Use of stochastic nanoparticle analysis methodologies enables the heterogeneity inherent in a sample population to be experimentally probed.[2] Over the preceding decade,

as outlined earlier in this thesis, the electrochemical study of individual nanoparticles has become an active area of development.[3–6] This work gives insight into the specific structure-activity relationship of the catalytic material. Although measurements are made on individual entities, correlation of this data with other information obtained *ex-situ* can generally only be achieved on a statistical basis. To overcome this challenge, work has sought to combine both optical[7] and electron[8] microscopy techniques to enable *in-situ* monitoring of reactions at the nanoscale. Current-time transients recorded for particle impacts on electrode allow the simultaneous measurement of catalytic activity and particle surface area.

As elaborated in Chapter 2, the technique of Faradaic single particle electrochemical impacts, also known as "nanoimpacts", may be broadly divided into two main types: *direct* and *mediated*.[9–11] These two approaches provide complementary information regarding the reactions occurring at the nanoscale.

A key factor in the study of heterogeneous redox reactions is knowledge of the electrochemically active surface area (ECSA).[12] For platinum surfaces at the macroscale, measurement of the ECSA is commonly attained by determining the charge passed when a monolayer of an electrosorbed species such as carbon monoxide, hydrogen or iodine is electrochemically removed from the metallic surface.[13] It is through the measurement of the ECSA of *ensembles* of particles that the *specific* current densities of new oxygen reduction reaction catalysts are routinely experimentally determined.[14, 15]

Many previous studies have reported the detection of single nanoparticles by collision with micoelectrodes including platinum particles.[16] However in this chapter, for the first time, it is demonstrated how a single nanoparticle current-transient response can *size* the ECSA of a *mesoporous* particle and concomitantly provide a measure of its *catalytic activity* (as quantified *via* the catalytic current density at a set overpotential). This technique is evidenced using the single mesoporous particle catalysis of the hydrogen

evolution reaction (HER).[9, 13, 14]

8.2 Experimental Section

8.2.1 Chemicals

Hydrogen ($\geq$ 99.98% H_2) was supplied from BOC, Surrey, U.K. Potassium nitrate ($\geq$ 99.0%, KNO_3), Potassium hydroxide were obtained from Fisher Scientific, Loughborough, U.K. Citrate-capped mesoporous platinum nanoparticles (PtNPs) were provided by nanoComposix, San Diego, CA, U.S.A., with a reported diameter 50 nm and concentration 3.3×10^{13} particles L^{-1}. All solutions were prepared with ultrapure water from Millipore, with a resistivity of not less than 18.2 MΩ cm at 298 K.

8.2.2 Characterization

The stock mesoporous PtNP samples were characterized *via* transmission electron microscopy (TEM) and ultraviolet–visible (UV–vis) spectroscopy.

TEM

Dr. Neil P. Young (Department of Materials, University of Oxford) conducted the TEM analysis for the mesoporous PtNPs as described below.

TEM (JEOL JEM-3000F FEGTEM, 300 kV accelerating voltage) was performed using conventional bright field imaging to determine the size of mesoporous PtNPs. Details of the sample preparation and analysis were given in Section 4.2.2 (Chapter 4). Clearly defined mesoporous PtNPs consisting of an aggregation of small particles were measured, and both radii calculated to give 23.1 ± 2.1 and 2.0 ± 0.3 nm, respectively. Example images of the particles and the corresponding size distributions were presented in Figures 7.1 and 7.2 (Chapter 7). From the geometry of such materials, assuming a close-packing

structure of the small particles (possibly leading to an overestimation of the ECSA), the total surface area of these mesoporous aggregates is found to be approximately 8.5 times greater than that of a solid sphere with an equivalent radius of 23.1 nm.

To clarify, in this work, the "mesoporous PtNP" refers to the mesoporous 23.1 nm particle, and the "small particles" are the 2 nm components of a mesoporous PtNP.

UV–Vis Spectroscopy

An important factor to consider is the extent to which these particles may be agglomerated in the electrochemical cell, plausibly encouraged by the presence of millimolar electrolyte concentrations.[17, 18] UV–vis (Shimadzu UV-1800 UV–vis spectrophotometer) measurements were conducted to evidence the stability of mesoporous PtNP colloids in bulk solution. The stock mesoporous PtNP sol was diluted by a factor of 2 with ultrapure water to obtain absorbance in an analytically meaningful range. Both deuterium and halogen light sources were used, with the sample being scanned from 900 to 250 nm. Figure 8.1 presents the variation of the platinum plasmon peak (*ca.* 300 nm)[19] as a

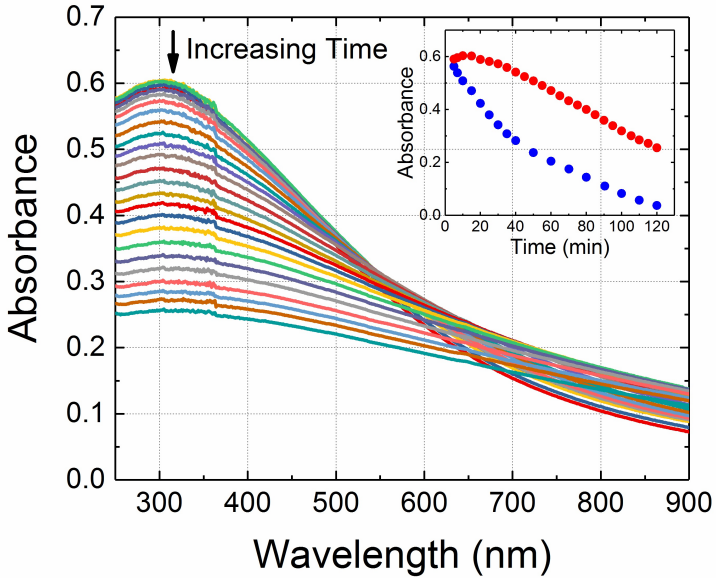

Figure 8.1: UV–vis spectrum of the mesoporous PtNPs in 20 mM KOH with H_2. Inlay: plot of the absorbance against the experimental time measured at a wavelength of 295 nm. Red circles and blue circles represent PtNPs in 20 mM KOH with H_2 and N_2, respectively.

function of time (over 2 hours) in the presence of 20 mM KOH and with hydrogen in solution. The inlay of Figure 8.1 shows the UV–vis absorbance measured at the peak (295 nm) against the experimental time under both hydrogen and nitrogen conditions. On the basis of these ensemble measurements it is concluded that the nanoparticle sol is metastable. Consequently, in order to *minimize* the influence of agglomeration upon the results, all experiments were restricted to being performed in the first 30 minutes after the electrolyte was added to the nanoparticle sol.

8.2.3 Electrochemistry

All electrochemical experiments were performed on a three-electrode system in a Faraday cage. The working electrode was a gold microdisc electrode of diameter 10 μm from ALS, Tokyo, Japan, and the electrode was polished with alumina powders from Buehler, Lake Bluff, IL, U.S.A., in a size sequence of 1.0, 0.3, and 0.05 μm. A leakless silver/silver chloride electrode [Ag/AgCl, 1.0 M KCl] from Cypress Systems, Lawrence, KS, U.S.A., functioned as a reference electrode (measured as -0.006 V vs saturated calomel electrode, SCE, [Hg/Hg_2Cl_2, KCl (saturated)], which is equivalent to +0.235 V vs SHE). A platinum foil from Goodfellow, Cambridge, U.K., acted as a counter electrode. All experiments were conducted under a hydrogen or nitrogen atmosphere. All electrochemical measurements were thermostated at 25 ± 0.5 °C.

Ensemble and Nano-Impact Experiments

Details of the in-house potentiostat can be found in Section 4.2.4 (Chapter 4).[20] The data acquisition (DAQ) was controlled by Python 3.5 (Canopy from Enthought, Austin, TX, U.S.A). The working electrode was running to ground where a low-noise current amplifier LCA-200-10G or LCA-4K-1G from FEMTO, Messtechnik GmbH, Germany was used to measure currents. The incoming analogue signal was oversampled and digitized by the

DAQ device at a stream rate of 100 kHz, and the digitised signal was subsequently filtered at a bandwidth of 100 Hz. To note again, in the context of nano-impact experiments the potentiostat conserves charge and therefore the integral of the current spikes is unaffected in their size analysis.[9]

8.3 Results and Discussion

In this chapter, first, the behavior and cyclic voltammetric responses of random nanoparticle arrays were outlined. Second, at the single particle scale, reductive responses arising from underpotential hydrogen deposition (H_{upd}) were revealed in an electrolyte saturated with nitrogen. These values were compared to measurements of the H_{upd} oxidation in the presence of hydrogen. Third, this H_{upd} signal was shown to give a direct measure of an individual entity's electrochemically active surface area (ECSA). The determined ECSA distribution for the impacting entities is in excellent agreement with the expected surface areas of individual particles as determined from TEM measurement and recognizing their porosity. This comparison indicates that 70-80% of the electrochemical events are associated with the arrival of *individual* particles. Finally, the work turned to consider the hydrogen evolution reaction (HER) at platinum nanoparticle (PtNP) surface. The ECSA of a mesoporous particle was measured simultaneously with its catalytic activity (current density) *via* a current transient.

8.3.1 Voltammetric and Nano-Impact Measurements

To characterize the activity and electrochemical behavior of the PtNPs, the electrochemical response of micro arrays of randomly distributed nanoparticles were first investigated. A gold microelectrode ($r = 5$ μm) was submerged into a PtNP sol (6.7 pM) containing 20 mM KOH and saturated with nitrogen. The gold electrode was selected due to the low

activity of the material towards the HER. In a degassed solution cyclic voltammetry was conducted from -1.0 to 0.0 V vs Ag/AgCl in 1M KCl (Figure 8.2 black lines). The freely diffusing PtNPs randomly collide with and adhere to the electrode. Note the nanoparticles have been previously shown to irreversibly adsorb to the electrode surface.[21] Over the course of multiple scans and as PtNP accumulate at the electrochemical substrate, a surface bound voltammetric feature becomes observable at *ca.* -0.49 V. This surface bound wave is associated with the underpotential deposition and removal of hydrogen (H_{upd}) at the platinum surface.[22, 23] Importantly, the nanoparticles employed in this work are citrate capped, which leads to a different H_{upd} response from that of a bare platinum surface.[17] During the course of the cyclic voltammetric scan reductive spikes in current are also observed. These spikes in current are associated with the arrival of new platinum entities to the electrode surface during the scan. The magnitude of these

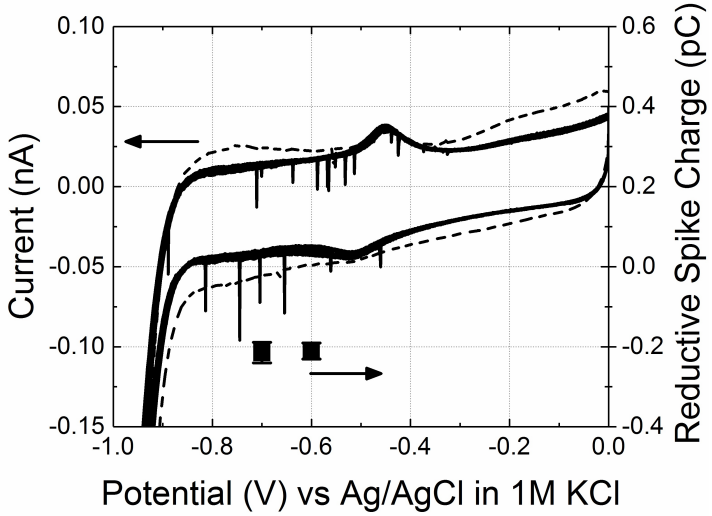

Figure 8.2: CVs for H_{upd} reduction (black lines) on an Au microelectrode with a random array of adsorbed mesoporous PtNPs (CV of scan rate 200 mV s^{-1}; nanoparticle of radius 23.1 nm, electrode of radius 5 μm). The initial scan is also shown in the diagram (dash line). Overlaid is the current response of individual mesoporous PtNPs as measured by chronoamperometry at -0.60 and -0.70 V (black squares) vs Ag/AgCl in 1 M KCl (measured from the time-current transients, 200 ms after the nanoparticle arrival). The electrolyte is 20 mM KOH saturated with N_2. Arrows indicate the left and right hand side axes, respectively, for the voltammograms and the impact charges.

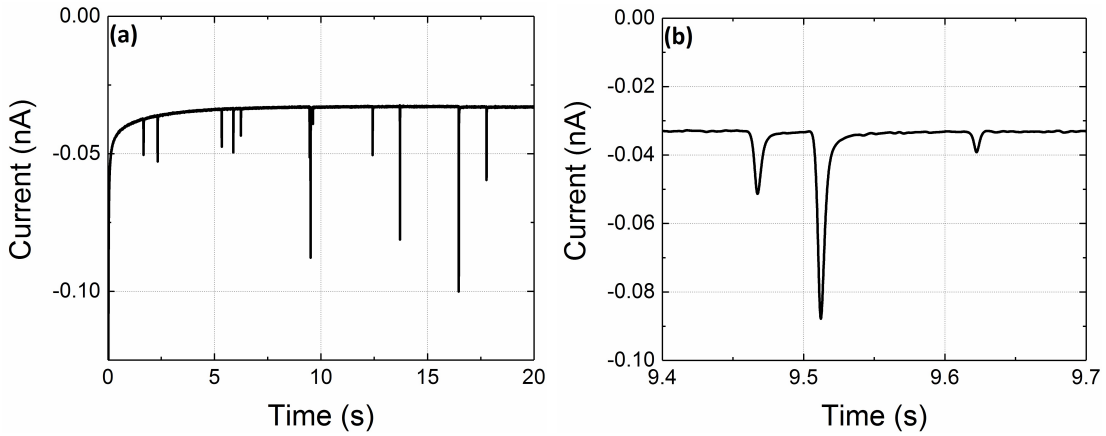

Figure 8.3: (a) CA of 6.7 pM mesoporous PtNPs in 20 mM KOH at an Au microelectrode with an applied potential of -0.60 V (vs Ag/AgCl in 1 M KCl). (b) Zoomed in plots of (a). The electrolyte is 20 mM KOH saturated with N_2.

features was investigated *via* chronamperometry at electrode potentials of -0.60 and -0.70 V (i.e. at potentials positive of the reversible hydrogen electrode, RHE). Examples of the raw current-time transients can be found in Figure 8.3. Also plotted are zoomed in versions of the current transients showing the individual spikes. Integration of these spikes allowed the charge passed per nano-event to be determined to be *ca.* 0.20 pC (as depicted on Figure 8.2).

These spikes in current are associated with the deposition of H_{upd} at the newly arriving nanoparticle surface. Upon arrival of a PtNP to a cathodically potentiostated electrode (below *ca.* -0.49 V vs Ag/AgCl in 1 M KCl), the following reaction is driven at the surface of the particle:

$$H_2O + e^- + M \rightleftharpoons Pt{-}H + OH^- \tag{8.1}$$

where M is an unoccupied platinum surface site. Hence, the magnitude of this process is sensitive to the nanoparticle's initial H_{upd} surface coverage and its total ECSA. A monolayer coverage of H_{upd} on a platinum surface corresponds to a charge of 210 μC cm^{-2}.[12] Consequently, the charge passed during a single entity reduction event can thus be converted to an effective surface area. Figure 8.4 shows the cumulative frequency of the measured ECSA per nano-event as measured from the reductive deposition of H_{upd}.

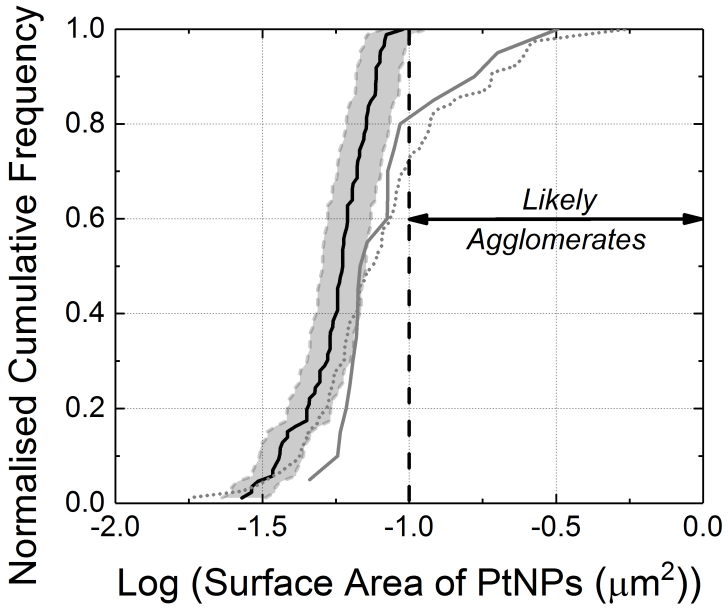

Figure 8.4: Plot of normalised cumulative frequency against surface area of PtNPs on a log scale from TEM (black solid line with grey dash lines to show the upper and lower error estimates), H_{upd} reduction at -0.60 V (nitrogen saturated, grey dot line) and oxidation at +0.15 V (hydrogen saturated, grey solid line). A vertical black dash line indicates the threshold above which the impacts may be due to agglomerates, as determined under an assumption of a complete monolayer of H_{upd} being added or removed during the course of the electrochemical process.

However, as illustrated by the UV-vis measurements (see Section 8.2.2), in the solution phase the mesoporous PtNP aggregates are only metastable in the presence of millimolar electrolyte concentrations; moreover, their stability is seemingly lower in the presence of nitrogen as opposed to hydrogen. In order to assess the extent to which the solution phase agglomeration level of the nanoparticle aggregates influences the electrochemical response the oxidation of H_{upd} was investigated. In a solution saturated with hydrogen the PtNPs become chemically modified with a surface layer of adsorbed H_{upd}, as driven by the reaction below:

$$H_2 + 2\,M \rightleftharpoons 2\,Pt{-}H \tag{8.2}$$

Consequently, by chemically tuning the surface functionality of the nanoparticles the influence of the presence of the hydrogen gas can be directly probed. To achieve this a gold microelectrode (10 μm diameter) was immersed under potentiostatic control into an

alkaline solution (20 mM KOH) containing mesoporous PtNPs (6.7 pM) saturated with hydrogen ($[H_2]_{sat}$ = 0.73 mM).[24] A potential of +0.15 V (vs Ag/AgCl in 1 M KCl) was selected for chronoamperometry. Upon impact of the nanoparticles to the electrode, small oxidative spikes were observed in the measured time-current profile. Examples of the voltamogram and the raw current-time transients can be found in the following text (Figures 8.5 and 8.6). These spikes correspond under these conditions to the oxidative removal of H_{upd} from the impacting nanoparticle surfaces. Again, the charge passed per impact event can be used to give an estimate of the total electroactive platinum surface area of the impacting entity. The resulting size distribution of the measured single entity platinum surface areas are also presented in Figure 8.4. The surface area size distribution measured from the oxidative removal of the H_{upd} is within experimental error to that obtained for the corresponding reductive deposition process. These two measurements have been performed in solutions containing hydrogen and nitrogen, respectively. This subsequently indicates that, over the experimental timescale (< 30 minutes), the presence of the gas does not lead to measurably different agglomeration levels of the *impacting* nanoparticles.

Underpotential Hydrogen Deposition (H_{upd}) Oxidation

First, micro arrays of nanoparticles were investigated to study the porosity of the PtNPs; a gold microelectrode (r = 5 μm) was submerged into a PtNP sol (6.7 pM) containing 20 mM KOH and saturated with hydrogen. Cyclic voltammetry was performed from -1.0 to 1.0 V vs Ag/AgCl in 1 M KCl (Figure 8.5 solid line). In the presence of hydrogen ($[H_2]_{sat}$ = 0.73 mM)[24] the voltammetric response of the gold electrode, modified *in-situ* by the solution-phase nanoparticles, shows a clear voltammetric peak at -0.5 V. The magnitude of this wave increases with exposure time of the electrode to the nanoparticle sol and is associated with the catalytic oxidation of hydrogen at the surface of the adsorbed

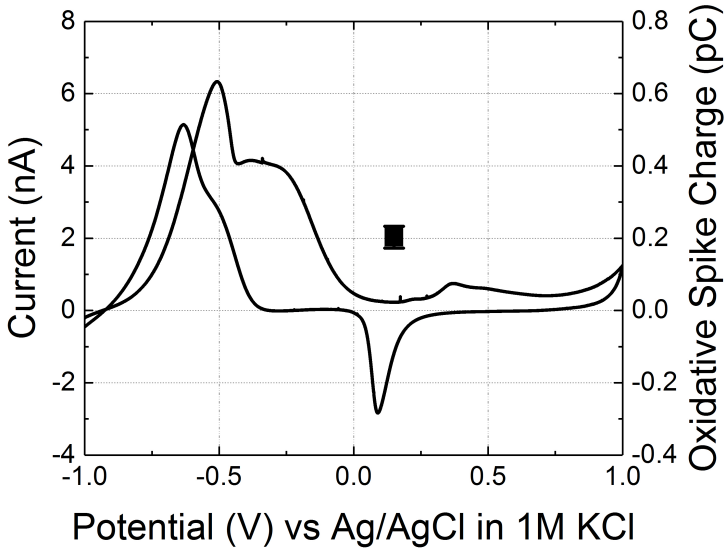

Figure 8.5: CVs for H_{upd} oxidation (solid line) on an Au microelectrode with a random array of adsorbed mesoporous PtNPs (CV of scan rate 200 mV s^{-1}; nanoparticle of radius 23.1 nm, electrode of radius 5 μm). Overlaid is the current response of individual mesoporous PtNPs at an applied potential of +0.15 V (black square) vs Ag/AgCl in 1 M KCl (measured from the time current transients, 200 ms after the nanoparticle arrival). The electrolyte is 20 mM KOH saturated with H_2.

PtNPs. In the absence of the PtNPs no oxidative wave is observed. Overall under alkali conditions the hydrogen oxidation is:

$$H_2 + 2\,OH^- \rightleftharpoons 2\,H_2O + 2\,e^- \tag{8.3}$$

Further, at platinum surfaces – as is seen in Figure 8.5 – the HOR becomes inhibited at high overpotentials, this reportedly arises due to specific anion adsorption.[25] Also noted is the voltammetric feature shown in Figure 8.5 with a forward peak at +0.37 V and a reverse peak at 0.09 V which is associated with the oxidation of the micro gold electrode substrate and is seen in the absence of PtNPs.

Second, the responses of individual particles impacting at the gold substrate were considered; upon impact of the nanoparticles to an electrode potentiostated above 0.0 V (vs Ag/AgCl in 1M KCl) – such that the oxidation of solution phase hydrogen is inhibited – oxidative spikes in current are observed, corresponding to the removal of the adsorped

H_{upd} layer from the platinum surface. Therefore, to study the H_{upd} oxidation a potential of +0.15 V (vs Ag/AgCl in 1 M KCl) is selected for chronoamperometry (*vide infra*) to avoid any influence caused by the hydrogen oxidation occurred at more negative potentials.

A gold microelectrode (10 μm diameter) is immersed under potentiostatic control into an alkaline solution (20 mM KOH) containing mesoporous PtNPs (6.7 pM), resulting in the observation of small spikes in the measured time-current profile. Figure 8.6 depicts representative chronoamperograms (CAs) where the gold working electrode has been held at a potential of +0.15 V (vs Ag/AgCl in 1M KCl) under hydrogen condition. The size of spikes detected varies as the PtNPs have a size distribution. Also plotted are zoomed in versions of the current transients showing the individual spikes.

For CAs conducted at +0.15 V the magnitude of these current spikes are determined (overlay in Figure 8.5) to give a mean value of *ca.* 0.2 pC. These resulting spikes correspond to the arrival of individual nanoparticle entities to the electrode, whence upon electrical contact with the electrified interface the nanoparticles are modified by the oxidation of H_{upd} to water, and therefore give a direct measure of the internal structure of the individual particle entities. To note these average oxidative charges passed (*ca.* 0.2 pC) are directly comparable in magnitude to those found reductively (see above).

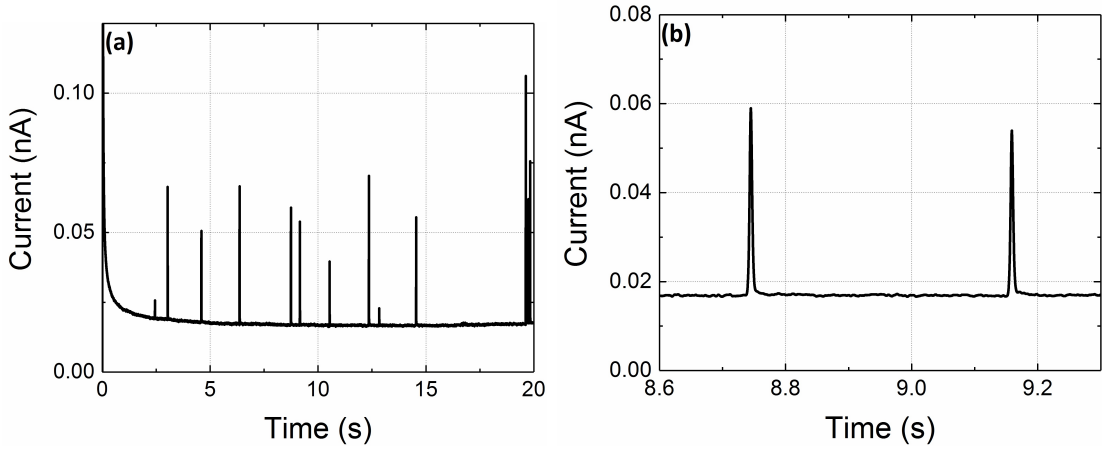

Figure 8.6: (a) CA of 6.7 pM mesoporous PtNPs in 20 mM KOH at an Au microelectrode with an applied potential of +0.15 V (vs Ag/AgCl in 1 M KCl). (b) Zoomed in plots of (a). The electrolyte is 20 mM KOH saturated with H_2.

To what extent do these single entity surface area measurements reflect the arrival of *individual* nanoparticle aggregates? Figure 8.4 depicts the predicted surface area cumulative frequency plot for the *individual* nanoparticle aggregates as determined from TEM. This estimation has been made on the basis of fully accounting for the internal surface area of the mesoporous nanoparticle *ca.* 8.5 times larger surface area than that of a solid sphere of equivalent radius. Once the particles mesoporous structure is considered, good agreement is found between the particle surface area distributions as measured *via* TEM and the nano-impact techniques.[21] This result, first, indicates that the *entire* nanoparticle surface area (internal and external) is electroactive and contributes to the charge passed during spike of the impact event (see the following for further details on electrochemical particle surface area measurements). Second, the likely extent of the nanoparticle agglomeration of the *impacting* platinum entities can be evidenced. The electrochemically measured area per entity is marginally higher than that predicted from TEM for a single nanoparticle aggregate (here a single mesoporous particle of radius 23.1 nm is referred). On the basis of the data shown in Figure 8.4, it is estimated that over the course of these experiments the impact results are fully consistent with 70-80% of the events being due to the arrival of a single particle aggregate.

Mesoporous Platinum Nanoparticle (PtNP) Electrochemically Active Surface Area (ECSA) Measurements

As a result of the mesoporous structure of the nanoparticles, to what extent is the internal structures of this material electrochemically accessible? Table 8.1 presents a summary of the charge measured *via* the nano-impact technique utilising H_{upd} – both reductive and oxidative – and from previous work as measured *via* nitro group reduction[20] (Chapter 4) and surface platinum oxidation[26] (Chapter 5). In all cases presented in Table 8.1

Experiment	Average Charge per PtNP impact (pC)	Number of Electron Transfer per RAG	Area per RAG (A^2)
Nitro Group Reduction	0.094	4	45.5
Surface Platinum Oxidation	0.15	1.1	7.8
H_{upd} Reduction	0.21	1	4.4
H_{upd} Oxidation	0.20	1	4.6

Table 8.1: Surface area measurements per RAG: nitro group reduction, surface platinum oxidation, H_{upd} reduction and oxidation (at -0.60 and +0.15 V vs Ag/AgCl in 1 M KCl). Area per RAG is calculated on the basis of the surface area of one mesoporous PtNP obtained from TEM.

these measurements have been made using the same mesoporous PtNPs and performed in the presence of millimolar electrolyte concentrations. Moreover all of these processes are surface reactions and the magnitude of the charge passed per event is proportional to the particle's electroactive area. The reported areas per redox active group (RAG) have been calculated on the assumption that the total surface area of a single particle is $(5.7 \pm 1.6) \times 10^{-2}$ μm^2 (for H_{upd} reduction and oxidation) or $(6.7 \pm 1.4) \times 10^{-2}$ μm^2 (for nitro group reduction and surface platinum oxidation). This discrepancy of surface area results from the slightly difference size of PtNP aggregates based on the TEM measurement. For comparison the surface coverage of 4-nitrothiophenol (NTP) on a gold surface has been previously reported to be 48.3 Å^2[27] and the area per platinum atom on a polycrystalline platinum surface is approximately 7.6 Å^2 (as calculated on the basis of H_{upd} signal of 210 μC cm^{-2} and assuming one hydrogen atom per platinum). The H_{upd} area calculated from experimental results (Table 8.1) is smaller than the literature value. This is because in the calculation one spike is assumed to correlate to impact of one single nanoparticle aggregate and do not account for agglomeration of the PtNP aggregates. From the cumulative frequency plot (Figure 8.4), a 20-30% agglomeration of the nanoparticles is observed in the experiment time scale. Consequently, the areas per RAG as measured on a *per particle*

basis strongly indicate that the *entire* nanoparticle surface is electroactive. In the case of the H_{upd} measurements, the influence of particle agglomeration on the reported effective area per RAG is considered.

At more negative electrode potentials ($E_{RHE} = -0.96$ V vs Ag/AgCl in 1 M KCl at pH 12.27), the HER can be driven to occur at the individual catalytic PtNPs. To study this catalytic process a gold microelectrode was submerged into a nanoparticle sol containing 20 mM KOH and either saturated with nitrogen or hydrogen. PtNPs diffuse, freely collide with and stick on to the gold substrate. CAs were recorded at a potential of -1.30 V vs Ag/AgCl in 1M KCl. At this potential no significant hydrogen evolution occurs on the bare gold substrate (see Figure 8.8 in the following text). The arrival and impact of a nanoparticle entity at the interface leads to measured steps in the time-current transient. The raw data is shown below. From these individual events the "average" response of

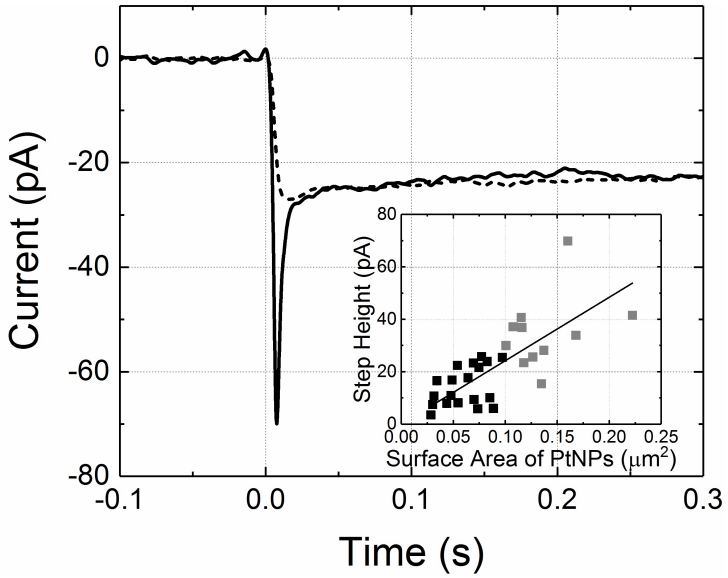

Figure 8.7: Overlay of the averaged HER response of individual mesoporous PtNPs upon arrival, and electrical contact with, a potentiostated Au microelectrode with an applied potential of -1.30 V (vs Ag/AgCl in 1 M KCl). The electrolyte is 20 mM KOH saturated with H_2 (dash line) or N_2 (solid line). Current responses given as a function of time where $t = 0$ is taken as the nanoparticle arrival and is associated with the step in current. Inset: plot of surface area of single PtNPs (as calculated on the basis of H_{upd} signal of 210 μC cm^{-2}) against step height of individual impacts (black squares: measured at the time-current transients). Linear fitting of 30 measurements has been forced to pass 0 (black line) with a R^2 value of 0.86.

multiple individual nano-impact events can be determined, as presented in Figure 8.7. In both the presence of hydrogen and nitrogen a step in current is recorded which after approximately 200 ms has a steady-state current of *ca.* 25 pA. This steady-state current gives a direct measure of the rate of catalytic reduction of water at this high pH. At the individual PtNP surfaces the corresponding reaction is:

$$2\,H_2O + 2\,e^- \rightleftharpoons H_2 + 2\,OH^- \tag{8.4}$$

The magnitude of this steady-state catalytic current is sensitive to the applied electrode potential.

Hydrogen Evolution Reaction (HER) under Nitrogen or Hydrogen Condition

To investigate the porosity and activity of the PtNP aggregates, the HER was studied with the solution saturated with either nitrogen or hydrogen. First, a gold microelectrode (10 μm diameter) was immersed into an alkaline solution (20 mM KOH) under nitrogen condition. HER signal is observed at potentials negative to -1.20 V vs Ag/AgCl in 1

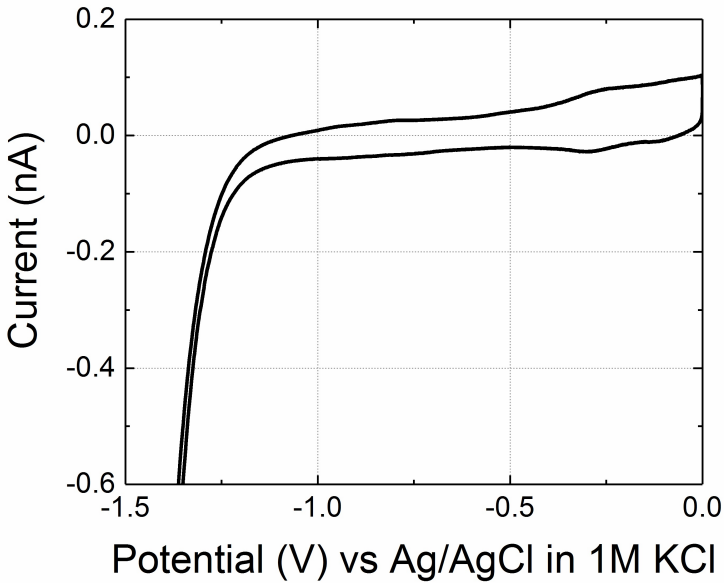

Figure 8.8: CV for HER on an Au microelectrode (CV of scan rate 200 mV s^{-1}; electrode of radius 5 μm). The electrolyte is 20 mM KOH saturated with N_2.

M KCl, as shown in Figure 8.8. To further study the HER on the platinum surface a potential of -1.30 V (vs Ag/AgCl in 1 M KCl) is selected for chronoamperometry (*vide infra*) because at this potential no significant hydrogen evolution occurs on the bare gold substrate based on Figure 8.8. However HER is significantly observed in Figure 8.2 (see above) on PtNP surfaces. This 0.3 V difference in the onset of hydrogen evolution potentials in Figures 8.2 and 8.8 is due to the presence of PtNPs on the gold electrode surface in the voltammogram presented in Figure 8.2.

Second, immersion of the gold working electrode under potentiostatic control into an alkaline solution (20 mM KOH) containing mesoporous PtNPs (6.7 pM) results in the observation of small steps in the measured time-current profile. Figure 8.9 and 8.10 depict representative CAs where the gold electrode has been held at a potential of -1.30 V (vs Ag/AgCl in 1M KCl) under nitrogen and hydrogen conditions, respectively. Also plotted are zoomed in versions of the current transient showing the individual steps in current. The current steps are found to be around a few picoampere in magnitude and correspond to the arrival of individual nanoparticle entities to the electrode, whence upon electrical contact with the potentiostatted interface the nanoparticles serve to catalyze the reduction of water to hydrogen. The resulting step gives a direct measure of the reaction

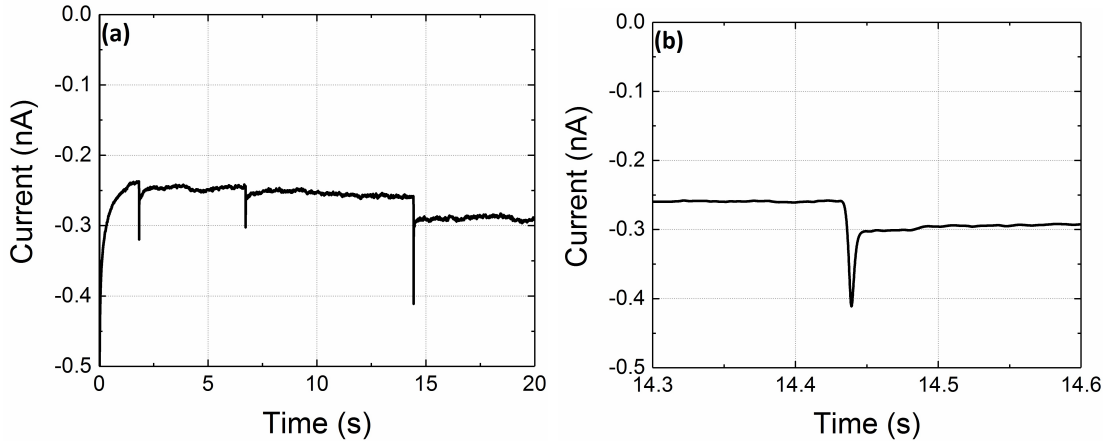

Figure 8.9: (a) CA of 6.7 pM mesoporous PtNPs in 20 mM KOH at an Au microelectrode with an applied potential of -1.30 V (vs Ag/AgCl in 1 M KCl). (b) Zoomed in plots of (a). The electrolyte is 20 mM KOH saturated with N_2.

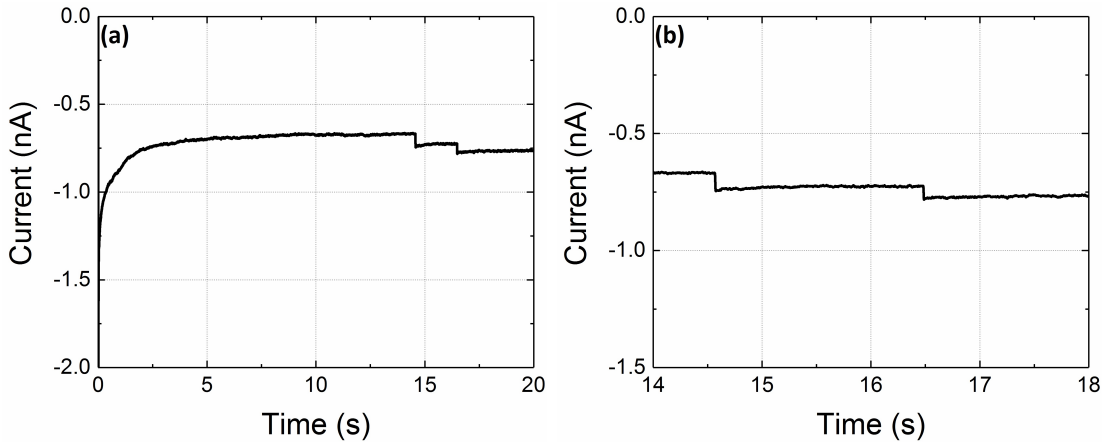

Figure 8.10: (a) CA of 6.7 pM mesoporous PtNPs in 20 mM KOH at an Au microelectrode with an applied potential of -1.30 V (vs Ag/AgCl in 1 M KCl). (b) Zoomed in plots of (a). The electrolyte is 20 mM KOH saturated with H_2.

rate occurring at the individual particle entities.

Notably, as seen in Figure 8.7, in the absence of solution phase hydrogen an initial spike in current is observed at the onset of the individual catalytic event (Figure 8.9). The addition of hydrogen to the nanoparticle sol suppresses this initial peak in current (Figure 8.10). This occurs as, in the solution phase and in the presence of H_2, the nanoparticles become pre-modified with a monolayer of H_{upd} as formed by the chemisorption of the gas to the catalytic surface, as discussed earlier (Equation 8.2). Consequently, in the absence of solution phase hydrogen this initial spike in current can be used to provide a *direct* measure of an individual impacting entity's ECSA. The inlay of Figure 8.7 depicts for individual nano-impact events the magnitude of the initial spike in current as compared to the resulting catalytic current step size. A strong ($R^2 = 0.86$) positive correlation between these two features is found. For a single PtNP, the maximum surface area predicted is $\sim$0.1 μm^2, consequently nano-impact events with an initial spike larger than this threshold are ascribed as occurring due to the arrival of agglomerated material, as indicated visually in the inlay of Figure 8.7.

Through controlling the reaction conditions and undertaking single nanoparticle catalytic reduction reactions either in the presence or absence of hydrogen gas, the surface

functionality of the nanoparticles in solution can be chemically altered. By exploiting this control it is directly evidenced that the initial reductive spike in current, as observed for individual nanoparticles, can be unambiguously identified as relating to the formation of a monolayer coverage of H_{upd}. Hence, the magnitude of this peak gives a direct measure of the nanoparticle's ECSA. At an intrinsic level such a method, providing simultaneous sizing and activity information, yields a route by which nanoparticulate *specific* activity may be identified in a stochastic manner. In the present case at -1.30 V ($E_{\mathrm{RHE}} = -0.96$ V vs Ag/AgCl in 1M KCl), the average catalytic *specific* current density for the alkaline evolution of hydrogen at the single particle is determined to be 242 ± 18 A m^{-2} as estimated from the slope of the linear fitting line in the inlay of Figure 8.7. This is in contrast with the current density on bulk platinum which has been measured to be 352 A m^{-2} at -1.30 V (vs Ag/AgCl in 1M KCl) under these experimental conditions (see the following text). This lower activity of the nanoparticulate material may either reflect the nanoparticlulate material being inherently lower in activity, be a result of particle's local porous structure, or relate to the electrical connectivity[28] of the particle. Specifically, the reported activity (current density) for the mesoporous particle is a measure of the average rate over the entire nanoparticle structure, including internal and external surfaces. The platinum surface at the centre of the particle is not as accessible as the outer edge of the particle. Hence, there will likely be concentration and potential gradients through the porous structure of the nanoparticle, plausibly leading, for a given electrode potential, to a lower activity of the platinum at the centre of the mesoporous structure. Alternatively, this apparently lower activity may result from electron transport issues either to or within the particle itself.

Current Density of Hydrogen Evolution Reaction (HER) on Platinum Bulk

The activity (current density) of the HER at a platinum bulk electrode is investigated in this section. First, a platinum microelectrode (10 μm diameter) was immersed into an acidic solution (1 mM $HClO_4$ and 19 mM $KClO_4$) under nitrogen. H_{upd} reduction and oxidation signals were observed at -0.20 V vs Ag/AgCl in 3.4 M KCl, as shown in Figure 8.11. The charge of H_{upd} on platinum bulk was determined to be 5.0×10^{-10} C by integrating the current underneath the cyclic voltammogram (-0.34 to -0.00 V). This charge value dividing by the geometric area of the electrode gives a charge density of $\sim$6.4 C m^{-2}. By comparing with the literature value, taking the monolayer coverage of H_{upd} on a platinum surface (2.1 C m^{-2}),[12] the electrode surface roughness of the polycrystalline platinum estimated to be factor of 3.0. Therefore, the electroactive area of the electrode is triple that of the geometric area.

Second, a platinum microelectrode (10 μm diameter) was immersed into an alkaline solution (20 mM KOH) under nitrogen condition. HER signal was observed at potentials negative to -0.90 V vs Ag/AgCl in 3.4 M KCl, as shown in Figure 8.12. The current density

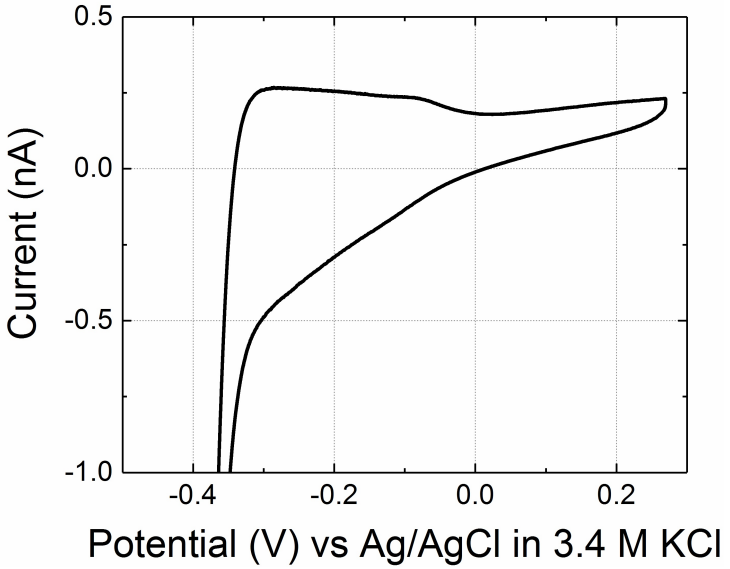

Figure 8.11: CV of H_{upd} reduction on a Pt microelectrode (CV of scan rate 200 mV s^{-1}; electrode of radius 5 μm). The electrolyte is 1 mM $HClO_4$ and 19 mM $KClO_4$ saturated with N_2.

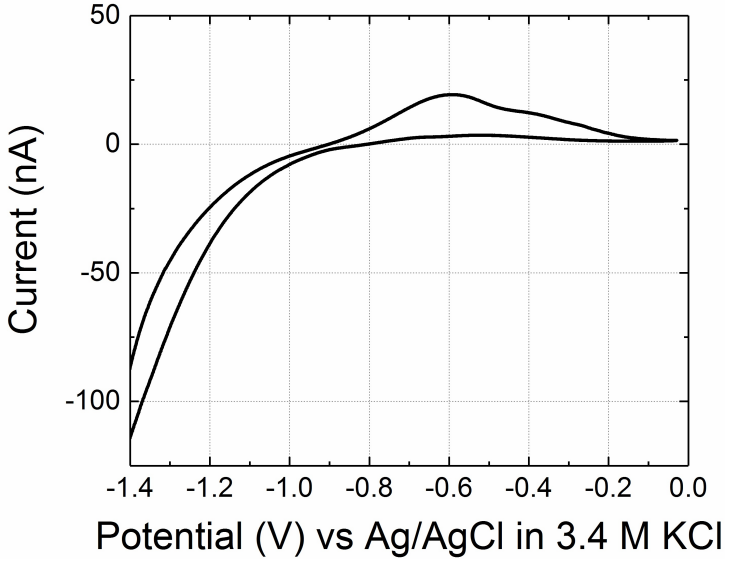

Figure 8.12: CV of HER on a Pt microelectrode (CV of scan rate 200 mV s $^{-1}$; electrode of radius 5 μm). The electrolyte is 20 mM KOH saturated with N_2.

of HER on platinum bulk at -1.33 V (vs Ag/AgCl in 3.4 M KCl) can be calculated using the current measured at this potential (-83 nA) divided by the electroactive area of the electrode, giving a value of $\sim$352 A m^{-2}.

8.3.2 Conclusions

The H_{upd} oxidation and reduction were employed to quantify the ECSA of individual mesoporous PtNP aggregates *via* nanoimpacts. The results achieved are in close agreement with those in Chapters 4 and 5, showing consistency of all the experimental findings. Using the evolution of hydrogen, for the first time, this chapter demonstrates how a current-transient response of a single nanoparticle aggregate gives information regarding the size of a particle's ECSA and concomitantly provides a measure of its catalytic activity. The direct correlation of the two indicates in this case that the total mesoporous nanoparticle surface area, both *internally* and *externally*, is active towards the HER. In addition, the current density of the evolution of hydrogen on the mesoporous PtNP aggregate was found to be 242 ± 18 A m^{-2}, which is smaller than that of a platinum bulk electrode (352 A m^{-2}) due to the porosity of the particles.

Bibliography

[1] Jiao, X.; Batchelor-McAuley, C.; Young, N. P.; Compton, R. G. *Physical Chemistry Chemical Physics* **2018**, *20*, 23847–23850.

[2] Gooding, J. J. *Angewandte Chemie, International Edition* **2016**, *55*, 12956–12958.

[3] Xiao, X.; Bard, A. J. *Journal of the American Chemical Society* **2007**, *129*, 9610–9612.

[4] Stevenson, K. J.; Tschulik, K. *Current Opinion in Electrochemistry* **2017**, *6*, 38–45.

[5] Imaoka, T.; Akanuma, Y.; Haruta, N.; Tsuchiya, S.; Ishihara, K.; Okayasu, T.; Chun, W.-J.; Takahashi, M.; Yamamoto, K. *Nature Communications* **2017**, *8*, 688.

[6] Tahmasebi, S.; Jerkiewicz, G.; Baranton, S.; Coutanceau, C.; Furuya, Y.; Ohma, A. *Journal of Physical Chemistry C* **2018**, *122*, 11765–11776.

[7] Wang, W. *Chemical Society Reviews* **2018**, *47*, 2485–2508.

[8] Wu, Y. A.; Yin, Z.; Farmand, M.; Yu, Y.-S.; Shapiro, D. A.; Liao, H.-G.; Liang, W.-I.; Chu, Y.-H.; Zheng, H. *Scientific Reports* **2017**, *7*, 42527.

[9] Sokolov, S. V.; Eloul, S.; Kätelhön, E.; Batchelor-McAuley, C.; Compton, R. G. *Physical Chemistry Chemical Physics* **2017**, *19*, 28–43.

[10] Albrecht, T.; Horswell, S.; Allerston, L. K.; Rees, N. V.; Rodriguez, P. *Current Opinion in Electrochemistry* **2018**, *7*, 138–145.

[11] Pumera, M. *ACS Nano* **2014**, *8*, 7555–7558.

[12] Trasatti, S.; Petrii, O. A. *Pure and Applied Chemistry* **1991**, *63*, 711–734.

[13] Climent, V.; Feliu, J. M. *Journal of Solid State Electrochemistry* **2011**, *15*, 1297–1315.

[14] Jackson, C.; Smith, G. T.; Inwood, D. W.; Leach, A. S.; Whalley, P. S.; Callisti, M.; Polcar, T.; Russell, A. E.; Levecque, P.; Kramer, D. *Nature Communications* **2017**, *8*, 15802.

[15] He, D.; Zhang, L.; He, D.; Zhou, G.; Lin, Y.; Deng, Z.; Hong, X.; Wu, Y.; Chen, C.; Li, Y. *Nature Communications* **2016**, *7*, 12362.

[16] Dasari, R.; Robinson, D. A.; Stevenson, K. J. *Journal of the American Chemical Society* **2013**, *135*, 570–573.

[17] Kleijn, S. E. F.; Serrano-Bou, B.; Yanson, A. I.; Koper, M. T. M. *Langmuir* **2013**, *29*, 2054–2064.

[18] Furlong, D. N.; Launikonis, A.; Sasse, W. H. F.; Sanders, J. V. *Journal of the Chemical Society, Faraday Transactions 1: Physical Chemistry in Condensed Phases* **1984**, *80*, 571–588.

[19] Creighton, J. A.; Eadon, D. G. *Journal of the Chemical Society, Faraday Transactions* **1991**, *87*, 3881–3891.

[20] Jiao, X.; Sokolov, S. V.; Tanner, E. E. L.; Young, N. P.; Compton, R. G. *Physical Chemistry Chemical Physics* **2017**, *19*, 64–68.

[21] Jiao, X.; Batchelor-McAuley, C.; Lin, C.; Kätelhön, E.; Tanner, E. E.; Young, N. P.; Compton, R. G. *ACS Catalysis* **2018**, *8*, 6192–6202.

[22] Sheng, W.; Zhuang, Z.; Gao, M.; Zheng, J.; Chen, J. G.; Yan, Y. *Nature Communications* **2015**, *6*, 5848.

[23] Herrero, E.; Buller, L. J.; Abruña, H. D. *Chemical Reviews* **2001**, *101*, 1897–1930.

[24] Wilhelm, E.; Battino, R.; Wilcock, R. J. *Chemical Reviews* **1977**, *77*, 219–262.

[25] Zalitis, C.; Kucernak, A.; Sharman, J.; Wright, E. *Journal of Materials Chemistry A* **2017**, *5*, 23328–23338.

[26] Jiao, X.; Tanner, E. E. L.; Sokolov, S. V.; Palgrave, R. G.; Young, N. P.; Compton, R. G. *Physical Chemistry Chemical Physics* **2017**, *19*, 13547–13552.

[27] Nielsen, J. U.; Esplandiu, M. J.; Kolb, D. M. *Langmuir* **2001**, *17*, 3454–3459.

[28] Li, X.; Batchelor-McAuley, C.; Shao, L.; Sokolov, S. V.; Young, N. P.; Compton, R. G. *Journal of Physical Chemistry Letters* **2017**, *8*, 507–511.

Chapter 9

Conclusions

This thesis has investigated the porosity of platinum nanoparticles (PtNPs) comprised of an aggregate of many ($10^2 - 10^3$) much smaller particles. Their internal surfaces were shown to be available for electrocatalytic reaction, and accessible to the solution in which the particles are suspended. The results obtained from the tag-redox coulometry (TRC) were consistent with those measured *via* direct electrochemical redox reaction, supporting the accuracy of the experimental measurements using both techniques. In particular, nanoimpacts provide a methodology for the *in-situ* detection of the "active surface area" of the particles, which is essential in understanding the origin of any catalytic behavior shown by the nanoparticles.

Next, voltammetric and nano-impact approaches were employed to study the hydrogen oxidation reaction (HOR) on platinum. The adsorption rate constant of the HOR was found to be larger at PtNPs than on bulk platinum electrodes, likely due to the high effective surface area of the nanoparticles. The kinetic parameter obtained from PtNP ensembles (*ca.* 0.007 m s^{-1}) was smaller than that at individual PtNPs (*ca.* 0.02 m s^{-1}). This was attributed to the aggregation or loss of particles in the drop-casting experiments. Nanoimpacts were concluded to allow a more accurate and comprehensive study of the kinetics for electrocatalytic reactions.

Even at the single particle scale, the material's catalytic activity towards the HOR is sensitive to the applied potential and exhibits two maxima in activity. These peaks in

activity were directly reflected in the electrochemical current measured at both individual particles and sparse arrays of material. At different proton concentrations, the position of the first minimum was shown to directly correlate with the oxidation potential of underpotential hydrogen deposition (H_{upd}). The rate of adsorption of hydrogen to the interface is consequently highly sensitive to the interfacial structure, where at higher potentials the HOR is likely inhibited by specific anion adsorption. This was further evidenced by the shape of the single particle time-current signals, where at low potentials the activity of PtNPs dynamically decreases with time as H_{upd} is removed from the particle's interface. Specifically, the shape of the resulting nano-impact transients relates to the structure of the nanomaterial. For the mesoporous PtNPs, the activity of their internal structure towards the HOR was confirmed *via* comparison with solid particles.

Finally, the H_{upd} oxidation and reduction were employed to quantify the electrochemically active surface area (ECSA) of individual mesoporous PtNP aggregates *via* nanoimpacts. The results achieved were in close agreement with those of nitro group reduction and surface platinum oxidation, showing consistency of *all* the experimental findings. Using the evolution of hydrogen, current-transient responses of a single nanoparticle aggregate provided information about the particle's ECSA and concomitantly about its catalytic activity. The direct correlation of the two indicated that the total mesoporous nanoparticle surface area, both *internally* and *externally*, is active towards the hydrogen evolution reaction (HER). In addition, the current density of the evolution of hydrogen on the mesoporous PtNP aggregate was found to be 242 ± 18 A m^{-2}, which is smaller than that of a platinum bulk electrode (352 A m^{-2}) due to the porosity of the particles.

To summarize, the particle porosity is essential to fully and correctly understand catalytic properties.